



DISS: ETH NO. 25341

# A Timing Detector based on Scintillating Fibres for the Mu3e Experiment

## Prototyping, Simulation and Integration

A thesis submitted to attain the degree of

DOCTOR OF SCIENCES OF ETH ZURICH

(Dr. sc. ETH Zurich)

presented by

**Simon Corrodi**

MSc. ETH Physik

born on 27.01.1988

citizen of Marthalen ZH

accepted on the recommendation of

Prof. Dr. Christophorus Grab

Prof. Dr. Niklaus Berger

Prof. Dr. Klaus Kirch

2018

©2018 – SIMON CORRODI

DOI 10.3929/ETHZ-B-000299260

## ABSTRACT

MU3E is a dedicated experiment searching for the rare charged lepton flavour violating decay  $\mu \rightarrow eee$ , aiming, in a first stage, for a single event sensitivity of  $2 \cdot 10^{-15}$ ; this is a three order of magnitude improvement over the previous results. In consequence of the heavy suppression of this process in the Standard Model of particle physics to an unobservable level, any observation is a sign of new physics. Achieving this sensitivity requires a combination of high muon rates and a detector with a large acceptance, excellent momentum, vertex and time resolution. The MU3E Scintillating Fibre sub-detector provides time resolution better than 350 ps together with minimal momentum resolution degradation and high efficiencies.

This thesis describes the path towards this sub-detector. The combination of the presented fibre and fibre ribbon characterization measurements and the described simulation of the sub-detector in the framework of the full MU3E experiment determined the detector design. In this context, the sub-detector's response is integrated into the experiment's reconstruction and analysis framework. This allows the study of expected combinatorial background suppression and rejection of mis-reconstructed track candidates due to the time information from the timing detectors.

The scintillating fibre ribbons are read out on both sides by SiPM column arrays. The requirements and results from test measurements of detector components and simulation led to the development of a dedicated readout chip, the MU<sub>TRIG</sub>. In this thesis, the feasibility of operating this ASIC at a single-photon level at rates up to 300 kHz/channel is demonstrated. Results obtained by digitization of the full waveform are reproduced with MU<sub>TRIG</sub>. The mechanical and electrical integration of the sub-detector into the experiment is presented.

## ZUSAMMENFASSUNG

MU3E ist ein Experiment zur Suche nach dem seltenen Leptonflavor verletzenden Zerfall  $\mu \rightarrow eee$ , das in einer ersten Phase eine Einzelereignisempfindlichkeit von  $2 \cdot 10^{-15}$  anstrebt. Dies ist eine Verbesserung um drei Grössenordnungen gegenüber den vorherigen Ergebnissen.

Aufgrund der starken Unterdrückung dieses Prozesses im Standardmodell der Teilchenphysik auf ein nicht beobachtbares Niveau ist jede Beobachtung ein Zeichen für neue Physik. Um diese Empfindlichkeit zu erreichen, ist eine Kombination aus hohen Myonraten und einem Detektor mit grosser Akzeptanz, exzellenter Impuls-, Vertex- und Zeitauflösung erforderlich. Der MU3E szintillierende Fasern-Detektor erzielt eine Zeitauflösung von besser als 350 ps bei minimalem Impulsaufklärungsverlust und hoher Effizienz.

Diese Arbeit beschreibt den Weg zu diesem Subdetektor. Die Kombination der präsentierten Messungen zur Faser- und Faser-Ribbon-Charakterisierung so wie die beschriebene Simulation des Subdetektors im Experimentframework bestimmt das Detektordesign. In diesem Zusammenhang wurde das Verhalten des Subdetektors in die Rekonstruktions- und Analysesoftware des Experiments integriert. Dies ermöglicht die Untersuchung der zu erwartenden Unterdrückung von Untergrundprozessen so wie der Aussortierung von falsch rekonstruierten Spurkandidaten aufgrund der Zeitinformation der Zeitdetektoren.

Die Ribbons aus szintillierenden Fasern werden beidseitig von SiPM Spaltenarrays ausgelesen. Die Anforderungen und Ergebnisse aus Testmessungen von Detektorkomponenten und Simulationen führten zur Entwicklung eines speziellen Auslesechips, dem MuTRiG. Diese Arbeit weist die Machbarkeit des Betriebs dieses ASICs auf einem Level von einzelnen Photonen mit Raten bis zu 300 kHz/Kanal nach. Ergebnisse, welche durch die Digitalisierung der gesamten Wellenform erlangt werden, sind mit dem MuTRiG reproduzierbar. Die mechanische und elektrische Integration des Subdetektors in das Experiment wird vorgestellt.

# Contents

<b>I</b>	<b>The Search for Charged Lepton Flavour Violating Decays</b>	<b>1</b>
1	CHARGED LEPTON FLAVOUR VIOLATION	3
1.1	Charged Lepton Flavour Violation . . . . .	4
1.1.1	Model Independent View: Effective Field Theory . . . . .	5
1.2	Experimental Status and Outlook . . . . .	7
1.3	Hints at New Physics . . . . .	9
2	THE MU3E EXPERIMENT	11
2.1	Muon Decays: Signal and Background Topologies . . . . .	11
2.1.1	The Signal Decay: $\mu \rightarrow eee$ . . . . .	12
2.1.2	Internal Conversion: $\mu \rightarrow eee\nu\nu$ . . . . .	12
2.1.3	Radiative Decay: $\mu \rightarrow e\gamma\nu\nu$ . . . . .	13
2.1.4	Accidental Background . . . . .	13
2.2	Experimental Concept . . . . .	15
2.2.1	Optimization for Momentum Resolution . . . . .	17
2.2.2	Implications of High Muon Rates . . . . .	19
2.3	Beamline and Stopping Target . . . . .	19
2.4	Tracking . . . . .	20
2.4.1	The Sensors: HV-MAPS . . . . .	20
2.4.2	The Tracker Support Structure . . . . .	21
2.4.3	Triplet-Based Track Finding . . . . .	21
2.5	The Timing Detectors . . . . .	23
2.6	Data Acquisition System . . . . .	23
2.6.1	The MIDAS Framework . . . . .	23
2.7	Mechanical Support, Magnet and Cooling . . . . .	25
3	SCINTILLATING FIBRE DETECTOR CONCEPT	27
3.1	Requirements of the Sub-Detector . . . . .	27
3.2	The Sub-Detector's Design . . . . .	28
3.3	Particle Rates and Distributions in the Scintillating Fibre Detector . . . . .	30
<b>II</b>	<b>Scintillating Fibres and Silicon Photomultipliers</b>	<b>35</b>
4	SCINTILLATING FIBRES	37

4.1	Organic Scintillators . . . . .	37
4.1.1	Scintillator Molecules . . . . .	37
4.1.2	The Emission Spectrum of Plastic Scintillators . . . . .	39
4.2	Fibres: Photon Guides . . . . .	40
4.2.1	Capture Efficiency . . . . .	41
4.2.2	Attenuation Length . . . . .	42
<b>5</b>	<b>SILICON PHOTO DETECTORS</b>	<b>43</b>
5.1	Working Principle . . . . .	43
5.2	Silicon Photomultiplier . . . . .	45
5.2.1	Detection Efficiency . . . . .	46
5.2.2	Dark Count Rate . . . . .	46
5.2.3	Crosstalk . . . . .	47
5.2.4	Time Resolution . . . . .	49
5.3	SiPM Column Arrays . . . . .	49
5.4	Radiation Damage in Silicon Photomultipliers . . . . .	51
5.4.1	Expected Radiation Damage from Literature . . . . .	54
5.4.2	Observations . . . . .	54
<b>6</b>	<b>SiPM READOUT ELECTRONICS</b>	<b>57</b>
6.1	State of the Art SiPM Readout Electronics . . . . .	57
6.2	The DRS4 ASIC . . . . .	58
6.3	The STiC and MuTRiG ASICs . . . . .	59
6.3.1	The Analogue Part . . . . .	60
6.3.2	Time-to-Digital Converter . . . . .	60
6.3.3	Data Transmission and Slow Control . . . . .	61
6.3.4	Reset Scheme . . . . .	61
<b>III</b>	<b>Prototypes, Measurements and Simulated Performance</b>	<b>63</b>
<b>7</b>	<b>SCINTILLATING FIBRE RIBBONS</b>	<b>65</b>
7.1	Scintillating Fibre Ribbon Constraints . . . . .	65
7.2	Scintillating Fibre Ribbon Prototypes . . . . .	69
7.2.1	Construction of Scintillating Fibre Ribbons . . . . .	71
7.3	Characterization of Scintillating Fibre Ribbons . . . . .	71
7.3.1	The Ribbon Characterization Setup . . . . .	71
7.3.2	The SiPM Readout Scheme . . . . .	75
7.3.3	Testbeam Area $\pi M1$ . . . . .	77
7.3.4	Analysis Procedure and Physical Property Extraction . . . . .	78
7.3.5	Characterisation Results . . . . .	89
7.4	Impact and Comparison with Earlier Results . . . . .	92

8	SIMULATION OF A SINGLE SCINTILLATING FIBRE	95
8.1	Single Fibre Simulation Configuration	95
8.2	Simulation of Photon Generation and Propagation	96
8.3	Cross-Check of the Single Fibre Simulation	96
8.4	Extraction of Single Fibre Properties	96
8.4.1	Photon Exit Positions	96
8.4.2	Photon Exit Angles	99
8.4.3	Photon Positions on the Detector Surface	99
8.4.4	Photon Path Lengths in Fibres	100
8.4.5	Exploitation of the Obtained Properties	100
9	THE SCINTILLATING FIBRE DETECTOR IN THE MU3E SIMULATION FRAMEWORK	101
9.1	The Sub-Detector in the Framework	101
9.1.1	Dimensions of the Fibre Ribbons	101
9.1.2	Dimensions of the Support Structure	103
9.2	Simulation of the Scintillating Fibre Detector's Response	103
9.2.1	Parametrization in Energy and Position	103
9.2.2	Number of Photons Emitted by the Fibres	103
9.2.3	Photon Distribution at the Sensors Surface	106
9.2.4	The Photon Distribution over Time	108
9.2.5	Sensor and Readout Electronic Response	109
9.3	Simulation Settings and Validation	109
9.4	Simulated Performance of the Scintillating Fibre Detector	113
10	TIMING IN THE RECONSTRUCTION AND ANALYSIS FRAMEWORK	117
10.1	Time-to-Track Matching	117
10.1.1	Fibre Detector Hit Clustering	118
10.1.2	Fibre Detector Cluster to Track Candidate Matching	118
10.1.3	Pixel and Tile Detector Time Matching	120
10.1.4	Track Candidate Timing	120
10.2	Vertexfit: Signal Candidates	121
10.2.1	Signal Candidate Timing Cuts	121
10.3	Impact of the Scintillating Fibre Detector	122
10.3.1	Background Suppression by Time Information	122
10.3.2	Mis-Reconstruction Identification by Time Information	126
10.3.3	Scintillating Fibre Detector Impact on Momentum Resolution and Re- construction Efficiency	128
<b>IV DAQ and Integration</b>		<b>131</b>
11	MuTRiG	133
11.1	MuTRiG Setup and DAQ	133
11.1.1	MuTRiG Electrical Connectivity	134

11.1.2	Evaluation Boards . . . . .	137
11.1.3	Ribbon and Sensor Connection . . . . .	139
11.1.4	PCIe based Data Acquisition System . . . . .	140
11.2	Measurement and Analysis Procedure: A User's Guide . . . . .	143
11.2.1	PLL Validation . . . . .	143
11.2.2	Threshold Determination . . . . .	146
11.2.3	Clustering and Time Resolution Extraction . . . . .	153
11.3	MuTRiG Performance . . . . .	155
11.3.1	Hit Validation by the External Trigger . . . . .	156
11.3.2	Coincidence between Channels . . . . .	156
11.3.3	Cluster Sizes measured with MuTRiG . . . . .	159
11.3.4	Time Resolution measured with MuTRiG . . . . .	159
<b>12</b>	<b>MECHANICAL AND ELECTRICAL INTEGRATION</b>	<b>167</b>
12.1	Constraints and Requirements . . . . .	167
12.1.1	The Available Volume . . . . .	167
12.1.2	The Environment of the Detector . . . . .	169
12.1.3	Mechanical Requirements . . . . .	169
12.2	Detector Integration Concept . . . . .	170
12.2.1	Electrical Connection . . . . .	173
12.2.2	The Readout Board: Scifi Board . . . . .	175
12.2.3	The Detectors Cooling . . . . .	177
<b>13</b>	<b>DAQ</b>	<b>181</b>
13.1	The Expected Data Rates . . . . .	181
13.1.1	Data Rates from the Scifi Board . . . . .	181
13.1.2	Sorting and Packaging in the Front-End . . . . .	182
13.1.3	Expected Final Data Rates . . . . .	184
13.2	The Available Link Bandwidth . . . . .	185
13.2.1	Alternative DAQ Scheme . . . . .	185
<b>V</b>	<b>Summary and Outlook</b>	<b>187</b>
<b>14</b>	<b>SUMMARY AND OUTLOOK</b>	<b>189</b>
14.1	Proposed Sensor and MuTRiG Operation Mode . . . . .	190
14.2	Outlook and Upcoming Issues . . . . .	190
	<b>APPENDICES</b>	<b>192</b>
	<b>ACKNOWLEDGMENTS</b>	<b>231</b>
	<b>ACRONYMS</b>	<b>231</b>

LIST OF FIGURES	234
LIST OF TABLES	238
BIBLIOGRAPHY	240



## **Part I**

# **The Search for Charged Lepton Flavour Violating Decays**



# 1

## Charged Lepton Flavour Violation

The field of Particle Physics is in the exceptional position to possess a single theory describing nearly all phenomena of its object of research, matter's building blocks and the interactions among them. This Standard Model of Particle Physics (SM) is a quantum field theory describing all known particles and three of the four fundamental forces: electromagnetic, weak and strong. Renormalizable field theory can not describe the gravitational interaction. Matter consists of fermions: leptons and quarks. As experimentally found they exist in three flavour families, three copies of the same gauge representation. Transitions between different families in the quark sector as well as in the neutral lepton sector have been observed.

Despite the enormous success in stringent tests, the SM is known to be incomplete in the sense of being a low energy limit of a broader theory of physics Beyond Standard Model (BSM). Besides omitting the gravitational force, the SM fails to describe several of phenomena. Rotation patterns of galaxies, the expansion speed of the universe as well as observations of the Cosmological Microwave Background (CMB) indicate that only about 5 % of the universe's energy density arises from particles described by the SM [1, 2]. Dark Matter, which the SM fails to provide suitable candidates for, accounts for another 26 % completed by 69 % Dark Energy. Furthermore, the SM does not offer a substantial enough charge and parity (CP) symmetry breaking to explain today's dominance of matter over anti-matter in the universe [3]. It also lacks a theoretical motivation for the unnaturally small Higgs boson mass with respect to other energy scales, in particular, the scale of gravity. Also, the existence of three families is included in the SM but by no means predicted from first principles.

A vast variety of BSM theories exist. Only experimental observations of new phenomena provide a handle to identify the set of theories realized by nature. Experiments sensitive to such observations can be grouped into three categories. *Direct search* for new particles which requires particle collisions at the highest possible centre of mass energies would allow investigating a new particle's properties most straightforwardly. The currently accessible energy scale of up to 13 TeV is set by the Large Hadron Collider (LHC), the most energetic particle accelerator at present. Complementary searches are performed in *precision experiments* where deviations from SM predictions would indicate new physics indirectly up to much higher en-

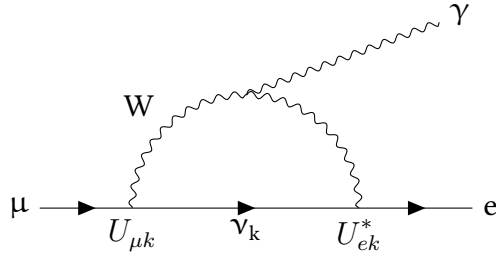


**Figure 1.1:** Dominant SM diagram with neutrino oscillation ( $\nu_k$ ) contributing to the decay  $\mu \rightarrow e\gamma$ .

ergy scales. Such experiments usually require an excellent control of backgrounds and high particle rates. Furthermore, particles from a *cosmic origin*, typically highly energetic or secondaries, are studied to explore the nature of dark matter.

Precision experiments investigating flavour have proven to be particularly successful in providing hints at new physics in the past [4]. The observation of neutrino oscillations [5–7], evidence for non-vanishing neutrino masses, led to the most recent modifications of the Minimal Standard Model sometimes referred to as  $\nu$ SM<sup>1</sup>. With this observation, Flavour Violation (FV) is not only present in the quark sector expressed by the Cabibbo-Kobayashi-Maskawa (CKM) matrix but also in the neutral leptons, the neutrinos. Charged Lepton Flavour Violation (cLFV) seems to be natural. However, does cLFV exist? If not, why? A small set of precision experiments have made it their goal to answer this exact question.

## 1.1 CHARGED LEPTON FLAVOUR VIOLATION

In contrast to most of the other conserved quantities in the SM, the conservation of lepton flavour in the (minimal) SM is not caused by a symmetry under gauge transformations. The concept of different flavours is not theoretically motivated, it was triggered by the nonobservation of  $\mu \rightarrow e\gamma$  in the 1950's [8]. Nevertheless, this accidental conservation can be expressed by a  $U(1)$  rotation associated with each lepton family which leads to three conserved charges:  $L_e, L_\mu, L_\tau$  which are defined as +1 for negatively charged leptons and neutrinos of the corresponding generation. For the corresponding anti-particles, positively charged leptons and anti-neutrinos of a generation, the charges are defined as -1 and as 0 otherwise.

Lepton Flavour Violation of neutrinos is described by the Pontecorvo-Maki-Nakagawa-Sakata (PMNS) matrix ( $U_{ij}$ ) which describes the rotation between the mass eigenstates  $\nu_1, \nu_2, \nu_3$ , relevant for free propagation, and the flavour eigenstates  $\nu_e, \nu_\mu, \nu_\tau$ , relevant for weak interactions. Although charged lepton flavour is conserved at lowest order (tree level) diagrams within the SM, neutrino oscillations in loops permit cLFV decays like  $\mu \rightarrow e\gamma$  or  $\mu \rightarrow eee$ . Figure 1.1 shows such a diagram. However, the branching fraction of such decays is heavily suppressed due to the absence of flavour changing neutral currents at tree level, and the tiny neutrino masses, more specifically their mass-squared differences  $\Delta m_{i1}^2$ . This is proportional

<sup>1</sup>Note that in this thesis I include  $\nu$ SM in SM.

to

$$\mathcal{B}_{SM}(\mu \rightarrow eee) \sim \mathcal{B}_{SM}(\mu \rightarrow e\gamma) \approx \frac{3\alpha}{32\pi} \left| \sum_{i=2,3} U_{\mu i}^* U_{ei} \frac{\Delta m_{i1}^2}{m_W^2} \right|^2 < 10^{-54}, \quad (1.1)$$

where  $\alpha$  is the fine structure constant and  $m_W$  the mass of the W-boson [9]. cLFV induced by neutrino masses is roughly forty orders of magnitudes smaller than the sensitivity of current state of the art experiments. Which in turn means that any experimental observation of cLFV would be an unambiguous sign of physics beyond the Standard Model of Particle Physics.

As a result of the fact that lepton flavour is more an accidental than a fundamental conserved quantity, many BSM models predict violations at an experimentally accessible level [9]. To distinguish between models, complementary measurements in different lepton flavour violating channels are required. If cLFV is not observed at all by next-generation experiments, this sets stringent constraints on them. Examples of classes for such theories are extended Higgs sectors [10, 11], unified [12], left-right symmetry [13] and neutral  $Z'$  [14] models.

From an experimental point of view, it is attractive to use model-independent approaches to classify and compare different cLFV processes.

### 1.1.1 MODEL INDEPENDENT VIEW: EFFECTIVE FIELD THEORY

Effective Field Theories (EFTs) are theories which only describe the physics below a mass scale  $\Lambda$ , whereby in the considered case  $m_W \geq \Lambda \gg m_b$  [15]. At energies well below  $\Lambda$  the effective Lagrangian can be expanded in  $1/\Lambda$  including the SM  $\mathcal{L}_{SM}$  to

$$\mathcal{L} = \mathcal{L}_{SM} + \frac{1}{\Lambda} \sum_k C_k^{(5)} Q_k^{(5)} + \frac{1}{\Lambda^2} \sum_k C_k^{(6)} Q_k^{(6)} + \dots \quad (1.2)$$

with the operators  $Q_k^{(D)}$  and the corresponding Wilson coefficients  $C_k^{(D)}$ , where  $D$  is the relevant dimensionality in mass. The index  $k$  runs over all possible operators involving only SM fields and respecting their gauge symmetries. At the low energies of the considered experiments, interactions with new particles are described by point-like interactions. Note that the running of the couplings (coefficients) can be expressed by the Renormalization-Group Evolution (RGE) between this energy scale and the energy scale of potential new BSM theories [15]. This is analogous to the Fermi theory of weak interactions. The only allowed operators with  $D = 5$  generate neutrino masses and lead only to the negligible cLFV described in Equation 1.1. Nineteen of the possible  $D = 6$  operators can induce cLFV process either directly or at loop level [9].

These considerations provide a tool to compare the power to constrain coefficients of different observables, e.g. cLFV decays. Experiments constrain these decays which can be translated into bounds on the various operators at the experiments' energy scale ( $C(\mu_m u)$ ). To better understand the impact of these bounds for possible new physics requires a translation to the corresponding high energy scale ( $C(\Lambda)$ ). This scaling by RGEs mixes various operators among each other.

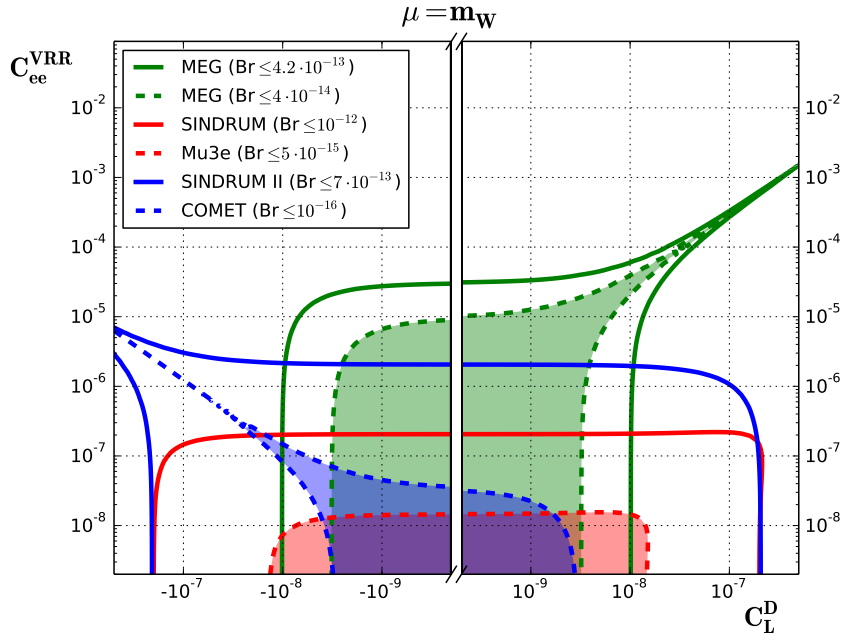


**Figure 1.2:** Bounds on dipole  $C_L^D$  and four-lepton  $C_{ee}^{VRR}$  operators provided by current (solid) and future (dashed) cLFV muon decay experiments (MEG:  $\mu \rightarrow e\gamma$ , SINDRUM, Mu3e:  $\mu \rightarrow eee$ , SINDRUM II, COMET:  $\mu N \rightarrow eN$ ) evaluated at energy scale  $\Lambda = m_W$  [15].

## 1.2. EXPERIMENTAL STATUS AND OUTLOOK

**Table 1.1:** Current upper limits (90 % confidence level) of cLFV muon decays and the year of the last publication.

Process	Experiment	Bound	Year	Reference
$\mu^+ \rightarrow e^+ \gamma$	MEG	$4.2 \cdot 10^{-13}$	2016	[27]
$\mu^+ \rightarrow e^+ e^- e^+$	SINDRUM	$1.0 \cdot 10^{-12}$	1988	[28]
$\mu^- \text{Ti} \rightarrow e^- \text{Ti}$	SINDRUM II	$4.3 \cdot 10^{-12}$	1998	[29]
$\mu^- \text{Ti} \rightarrow e^+ \text{Ca}^*$	SINDRUM II	$3.6 \cdot 10^{-11}$	1998	[30]
$\mu^- \text{Pb} \rightarrow e^- \text{Pb}$	SINDRUM II	$4.6 \cdot 10^{-11}$	1996	[31]
$\mu^- \text{Au} \rightarrow e^- \text{Au}$	SINDRUM II	$7 \cdot 10^{-13}$	2006	[32]

An EFT approach with scaling by RGEs allows, for example, a close look at the cLFV muon decays:  $\mu \rightarrow e\gamma$ ,  $\mu \rightarrow eee$  and  $\mu N \rightarrow eN$  in the vicinity of a nucleus. While the decays  $\mu \rightarrow e\gamma$  at tree level impose only constraints to the dipole operators ( $C_L^D, C_R^D$ ), the process  $\mu \rightarrow eee$  is also sensitive to the four-lepton operators (scalars  $C_{ee}^{SLL}, C_{ee}^{SRR}, C_{ee}^{SLR}, C_{ee}^{SRL}$  and vectors  $C_{ee}^{VLL}, C_{ee}^{VRR}$ ). Through RGEs,  $\mu \rightarrow e\gamma$  is likewise sensitive to other operators than dipole and  $\mu \rightarrow eee$  is sensitive to operators involving quarks or other leptons. The process  $\mu N \rightarrow eN$  is already sensitive to dipole, vector and scalar operators at the tree level, with a dependency on the involved nucleus (N) [16]. The processes  $\mu \rightarrow e\gamma$  and  $\mu \rightarrow eee$  have been compared under the mentioned conditions by [17] using current and predicted experimental limits, see section 1.2. The authors of [17] presented an explicit example of a correlation between dipole ( $C_L^D$ ) and four-fermion vector effective couplings ( $C_{ee}^{VLL}$ ) at an energy scale  $\Lambda = m_W$ , shown in Figure 1.2. This study was performed under the assumption that they are the only two non-vanishing couplings generated by a possible BSM theory. It illustrates the complementarity of the planned searches.

## 1.2 EXPERIMENTAL STATUS AND OUTLOOK

At present, there is no evidence for Charged Lepton Flavour Violation, despite a wide variety of searches for such processes. Historically, these experiments can be grouped into three categories. Until the fifties, processes in cosmic ray muons [18, 19] were studied, followed by an epoch during which stopped pion beams provided muons to study. Since the seventies stopped muon beams and collider experiments are the main base for cLFV search. Muon decays give the most stringent bounds. The current experimental upper limits of the three processes  $\mu \rightarrow e\gamma$ ,  $\mu \rightarrow eee$  and  $\mu N \rightarrow eN$  are summarized in Table 1.1. All three process types are at present constrained by experiments hosted at the Paul Scherrer Institute (PSI) in Villigen, Switzerland. The most stringent limits for cLFV in tau decays, which are all in the order of  $\mathcal{O}(10^{-8})$ , are set by BaBar [20, 21] and Belle [22–24]. More recently, the CMS experiment succeeded to set first upper bounds on cLFV Higgs boson decays  $\mathcal{B}(H \rightarrow e\mu) < 3.5 \cdot 10^{-4}$  [25],  $\mathcal{B}(H \rightarrow \tau\mu) < 2.5 \cdot 10^{-3}$  and  $\mathcal{B}(H \rightarrow \tau e) < 6.1 \cdot 10^{-3}$  (95 % C.L.) [26]. Moreover, an extensive amount of cLFV meson and Z-boson decays have been studied and constrained by various experiments. A comprehensive overview can be found in [9].

**Table 1.2:** Projected Single Event Sensitivities (SESs) ( $S$ ) or 90 % confidence level ( $B$ ) of planned  $\text{cLFV}$  experiments with muons and the corresponding host institutes. PRIME is potential next generation conversion experiment at Japan Proton Accelerator Research Complex (J-PARC). The stopping target material is not yet defined; therefore  $N$  stands for a generic nucleus.

Process	Experiment	Sensitivity	Facility	Reference
$\mu^+ \rightarrow e^+ \gamma$	MEG II	$6 \cdot 10^{-14}$ ( $B$ )	PSI	[33]
$\mu^+ \rightarrow e^+ e^- e^+$	MU3E Phase I	$2 \cdot 10^{-15}$ ( $S$ )	PSI	[34]
	MU3E Phase II	$\sim 1 \cdot 10^{-16}$ ( $S$ )	PSI	[34]
$\mu^- \text{SiC} \rightarrow e^- \text{SiC}$	DEEMe	$2 \cdot 10^{-14}$ ( $S$ )	J-PARC	[35]
$\mu^- \text{Al} \rightarrow e^- \text{Al}$	COMET Phase I	$3 \cdot 10^{-15}$ ( $S$ )	J-PARC	[36]
	COMET Phase II	$2.6 \cdot 10^{-17}$ ( $S$ )	J-PARC	[36]
	MU2E	$2.9 \cdot 10^{-17}$ ( $S$ )	FNAL	[37]
$\mu^- N \rightarrow e^- N$	PRIME	$\sim 1 \cdot 10^{-18}$ ( $S$ )		[38]

As pointed out in subsection 1.1.1, the pure observed branching ratio is inadequate to compare the potential to constrain new physics models by different experiments or channels. A model-independent approach like EFT provides a possible handle but on the downside hides new physics phenomena behind, potentially multiple, operators. In principle, tau decays would be more sensitive to  $\text{cLFV}$  than muon decays due to stronger couplings to new physics. The present availability of considerable muon beam rates in the order of  $10^7$  up to  $10^{10}$  muons per second cause  $\mu$ -channels to provide the best constraints to date to possible BSMs. However, even between muon channels, the comparison is not trivial. Depending on the nature of new physics, the different channels show a different sensitivity.  $\mu \rightarrow eee$  is roughly

$$\frac{\mathcal{B}(\mu \rightarrow eee)}{\mathcal{B}(\mu \rightarrow e\gamma)} = \frac{\alpha}{3\pi} \left( \log \frac{m_\mu^2}{m_e^2} - 3 \right) \approx 0.006 \quad (1.3)$$

less sensitive to new physics induced by dipole operators (e. g. loop diagrams) than  $\mu \rightarrow e\gamma$  due to the additional vertex. Then again  $\mu \rightarrow eee$  is sensitive to more operators (see subsection 1.1.1), which significantly enhances the sensitivity for tree-level processes involving new particles as over  $\mu \rightarrow e\gamma$ . It is crucial to measure multiple channels, in order to distinguish between potential models.

Due to the feasibility, partially also availability, of high-intensity low-momentum muon beams, sensitivity enhancements of up to four orders of magnitudes can be expected in the next years. Dedicated experiments for all three muon channels are foreseen. Their expected Single Event Sensitivities (SESs) are summarized in Table 1.2 along their host facilities. While the searches for  $\mu \rightarrow e\gamma$  and  $\mu \rightarrow eee$  utilize continuous muon beams, available for example at PSI, the hunts for  $\mu N \rightarrow eN$  exploit pulsed beams, as at Japan Proton Accelerator Research Complex (J-PARC) and Fermi National Accelerator Laboratory (FNAL). The SES is the branching ratio at which a background-free experiment expects precisely one event. Under the assumption of negligible background in the signal region, a 90 % confidence level (C.L.) of an upper

limit can be estimated as  $\mathcal{B}_{90\% \text{ C.L.}} = 2.30 \times SES^2$  assuming pure Poisson statistics. MEG II is an upgrade to the MEG experiment at PSI with the aim to improve the sensitivity for  $\mu \rightarrow e\gamma$  by one order of magnitude. At that level, it will be limited by accidental background due to the limited photon energy resolution of the design [39]. MU3E is a novel dedicated experiment for the search of  $\mu \rightarrow eee$ , also located at PSI, in fact, it shares in its phase I the beamline with MEG II. Ultimately, in a second phase, it targets a sensitivity improvement by four orders of magnitudes with respect to the present limit. MU3E is presented in more detail in chapter 2. Out of the three dedicated searches for  $\mu N \rightarrow eN$  the DEEME experiment at J-PARC is the smallest and simplest setup allowing for an earlier start. Compared to the others its sensitivity is moderate, but still aiming for more than one order of magnitude of improvement with respect to current bounds. The DEEME muon production target, which consists in the first phase of graphite followed by silicon carbide in a second phase, serves at the same time as the converter. The COMET experiment at J-PARC and the MU2E experiment at FNAL both aim for an ultimate sensitivity improvement by four orders of magnitude. In contrast to DEEME the muon stopping targets and the production target out of aluminium are separated; In case of MU2E by an S-shaped transport solenoid whereas at COMET by a C-shaped solenoid. COMET follows a staged approach. In a first phase, the production target and detectors are placed already after a  $90^\circ$  bend of the solenoid. In the second phase, the C-shape is completed, and an additional curved solenoid is used after the stopping target to remove low energy electrons. PRIME is a potential next-generation conversion experiment at J-PARC that could also be realised at FNAL.

### 1.3 HINTS AT NEW PHYSICS

I would like to draw particular attention to two classes of experiments which show potential signs for physics beyond the SM, possibly related to cLFV searches.

The first class probes lepton flavour universality in B-physics. If this concept is heavily broken, cLFV effects are to be expected to some extent [40]. In charged-current processes like  $b \rightarrow cl\nu$  BaBar [41], Belle [42] and LHCb [43], whose data were averaged in [44], measured an approximately  $4\sigma$  deviation in the ratios

$$R_D = \frac{\mathcal{B}(B \rightarrow D\tau\bar{\nu})_{\text{exp}}/\mathcal{B}(B \rightarrow D\tau\bar{\nu})_{\text{SM}}}{\mathcal{B}(B \rightarrow Dl\bar{\nu})_{\text{exp}}/\mathcal{B}(B \rightarrow Dl\bar{\nu})_{\text{SM}}} = 1.34 \pm 0.17, \quad (1.4)$$

and the same for  $R_{D^*}$ , the analogy for  $B \rightarrow D^*\tau\bar{\nu}$  where  $l = e, \mu$ . Deviations in neutral-current processes are less interesting concerning cLFV searches but worth mentioning because of a possible joint explanation ([45]) with the effects in the above stated charged-current processes. Deviations are observed by the LHCb collaboration [46] in processes like  $b \rightarrow sl^+l^-$ . The ratio

$$R_K = \frac{\mathcal{B}(B^+ \rightarrow K^+\mu^+\mu^-)}{\mathcal{B}(B^+ \rightarrow K^+e^+e^-)} = 0.745_{-0.074}^{+0.090} \pm 0.036, \quad (1.5)$$

---

<sup>2</sup>  $\int_0^{\tilde{\xi}} \text{Pois}(0|\xi) d\xi = \int_0^{\tilde{\xi}} e^{-\xi} d\xi = 0.9.$

is predicted by the SM to deviate by less than 1% from unity [47]. Similar deviations on a  $3\sigma$  level are observed in the decays  $B^0 \rightarrow K^{*0} \mu^+ \mu^-$ ,  $B \rightarrow K^* \mu^+ \mu^-$  and  $B_s^0 \rightarrow \phi \mu^+ \mu^-$  [48–50].

The second class are anomalies in the muon sector. The probably most prominent deviation is the muon's anomalous magnetic moment  $a_\mu = (g_\mu - 2)/2$ , the  $(g_\mu - 2)$  anomaly, a  $3.5\sigma$  deviation from SM predictions originally measured at Brookhaven National Laboratory (BNL) [51]. A new experiment at FNAL aiming for an uncertainty reduction by a factor four, thus allowing a potential  $> 5\sigma$  discovery, is running [52]. The second anomaly is the proton radius puzzle, the discrepancy of the proton charge radius of muonic hydrogen determined at PSI through Lamb shift [53] and the radius of normal hydrogen extracted from nuclear scattering at MAMI [54] and through spectroscopy [55].

# 2

## The Mu3e Experiment

Mu3E is a dedicated experiment searching for the rare Charged Lepton Flavour Violation (cLFV) decay  $\mu^+ \rightarrow e^+ e^- e^+$  [34]. In consequence of the heavy suppression of this process in the SM to a branching ratio below  $10^{-54}$  (see Equation 1.1), any observation above this is a sign for new physics. The goal of a two-stage approach is to achieve in a first phase a Single Event Sensitivity (SES) of  $2 \cdot 10^{-15}$  at the existing beamline  $\pi E5$  at PSI (see section 2.3), which provides up to  $10^8$  stopped muons per second on to the target. This sensitivity represents already three orders of magnitude improvement with respect to the current limit [28]. The ultimate SES goal of the second phase is  $1 \cdot 10^{-16}$  and requires an upgraded or novel beamline capable of providing  $\mathcal{O}(10^9)$  muons per second and significant detector upgrades. Such high muon beam rates are required to accumulate the desired numbers of muons, translating into a SES, within a reasonable time, thus demanding excellent discrimination of signal from background processes and rate capability.

Section 2.1 describes the topologies of these signal and background processes in more detail, followed by a general description of the experimental concept used to measure them in section 2.2. The experiment's components such as beamline and stopping target, the particle tracking, the timing detectors, as well as the experiment's Data Acquisition System (DAQ) and mechanical design, cooling and magnetic field, are outlined in the following sections 2.3 to 2.7.

### 2.1 MUON DECAYS: SIGNAL AND BACKGROUND TOPOLOGIES

The muon mass is  $m_\mu = (105.658\,374\,5 \pm 0.000\,002\,4) \text{ MeV}/c^2$  [56, 57] and its lifetime is  $\tau_\mu = (2.196\,981\,1 \pm 0.000\,002\,2) \mu\text{s}$  [56, 58]. It decays predominantly in the process  $\mu \rightarrow e \bar{\nu}_e \nu_\mu$ . We denote this process Michel decay. In the rest frame of the muon, the electron's momentum distribution can be described by eponymous Michel parameters. The values of these parameters, thus the shape of the distribution, are potentially sensitive to new physics.

In the SM, the momentum and angular distribution for anti-muon decays is proportional to

$$\frac{d^2\Gamma}{dx \, d\cos\theta} \sim x^2 [(3 - 2x) - P_\mu \cos\theta(1 - 2x)], \quad (2.1)$$

where  $x = \frac{E_x}{E_x^{\max}}$ ,  $P_\mu$  is the muon polarisation and  $\theta$  is the angle between the directions of the muon spin and positron momentum [59]. Expression 2.1 neglects the electron and neutrino masses and radiative corrections.

### 2.1.1 THE SIGNAL DECAY: $\mu \rightarrow eee$

The signature of  $\mu^+ \rightarrow e^+e^-e^+$  consists of two positrons and one electron in a plane in the anti-muon rest frame from a common vertex in space and in coincidence in time. The sum of the three daughter particles' momenta ( $\vec{p}_i$ ) vanishes:

$$\vec{p}_{\text{tot}} = \sum_{i=1}^3 \vec{p}_i = 0 \quad (2.2)$$

Furthermore, the energy of the three electron-like particles ( $E_i$ ) sums up to the muon mass:

$$E_{\text{tot}} = \sum_{i=1}^3 E_i = m_\mu. \quad (2.3)$$

The decay dynamics depend on the underlying nature of the cLFV process. A general parametrized Lagrangian is presented in [60], that allows studying different signal models organized by different coupling types, such as dipole, scalar or vector-like couplings.

### 2.1.2 INTERNAL CONVERSION: $\mu \rightarrow eee\nu\nu$

Relatively rare, with a branching fraction of  $(3.4 \pm 0.4) \cdot 10^{-5}$ , a muon decays in the process  $\mu^+ \rightarrow e^+e^-e^+\bar{\nu}_e\nu_\mu$  [61]. We denote this process Internal Conversion (IC) since it proceeds in the SM through the emission of an off-shell photon with subsequent internal conversion into a  $e^+e^-$  pair. If the undetectable neutrinos carry away only little energy, this process mimics the topology of  $\mu \rightarrow eee$ . Nevertheless, the energy carried away by the neutrinos,  $E_{\text{miss}}$ , can be exploited to distinguish between the two decays. Two independent differential Next-to-Leading Order (NLO) calculations have been presented recently [62, 63]. In principle, the differential branching ratio in the momentum fraction distribution and in the angular distribution provide a tool to distinguish between possible BSM models. In Figure 2.1, the branching ratio as a function of  $E_{\text{miss}}$  is given for a MU3E like scenario. The presented calculation imposes an energy cut on the positrons and electrons of  $E_i > 10$  MeV, an acceptance of  $|\cos\theta| < 0.8$ , where  $\theta$  is the angle between the direction of the beam and the individual daughter particle's momentum, and a polarisation of 0.85 in upstream direction. To achieve an irreducible background suppression at the order of  $\mathcal{O}(10^{-15})$ , the aimed SES for phase I, the experimental resolution for

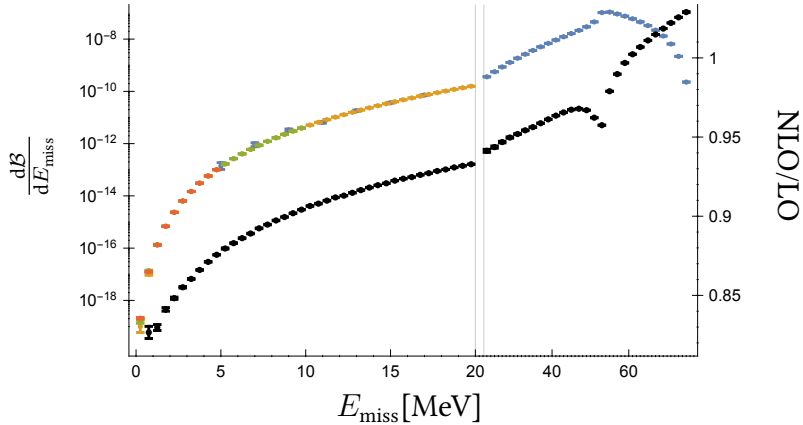


**Figure 2.1:** The differential IC decay distribution as a function of the invisible energy  $E_{\text{miss}}$  at NLO in blue, orange, green and red and the factor NLO/LO in black. The different colours encode different cuts on  $E_{\text{miss}}$  in the calculation which allow to focus on the distribution’s low energy tail. The scaling is broken at  $E_{\text{miss}} = 20$  MeV, to emphasize this tail. Taken from [63].

the missing energy is required to be below 1.0 MeV for a  $2\sigma$  cut and purely Gaussian distributed resolution. For the phase II goal, roughly half the mass resolution will be required. This assumes a Gaussian momentum resolution, in particular without tails towards high momenta. This translates directly into the combined momentum resolution of the two positrons and the electron  $\vec{p}_{(e^+e^-e^+)}$  respectively the mass resolution  $m_{\mu\text{rec}}$ .

### 2.1.3 RADIATIVE DECAY: $\mu \rightarrow e\gamma\nu\nu$

The third significant lepton flavour conserving muon decay in the SM is  $\mu^+ \rightarrow e^+\gamma\nu\bar{\nu}$  with a branching ratio of  $(1.4 \pm 0.4) \cdot 10^{-2}$  imposing  $E_\gamma > 10$  MeV [64] or of  $(6.03 \pm 0.14(\text{stat.}) \pm 0.53(\text{sys.})) \cdot 10^{-8}$  imposing  $E_\gamma > 40$  MeV and  $E_{e^+} > 45$  MeV [65] respectively. If the photon converts in the target to an  $e^+e^-$  pair, it could mimic the topology of the IC. If the conversions take place outside of the target or displaced from the initial decay, vertex reconstruction provides an excellent handle for its discrimination. The radiative muon decay is also background for BSM searches.

### 2.1.4 ACCIDENTAL BACKGROUND

Besides the irreducible backgrounds mentioned above, a second category consists of a superposition of two positrons and an electron track candidate that accidentally resemble the signal topology. In general, this background category is suppressed on the one hand again by the tight cuts on the reconstructed muon mass  $m_{\mu\text{rec}}$  and on the other hand by the requirement of a common vertex in space and time. While plenty of positrons are present from the ordinary Michel decay, the primary source for electrons is Bhabha scattering on electrons in the stopping target material. Other potential sources of positron-electron pairs are the conversion of

photons, e.g. from the radiative decay, or a pair from IC. Single electron track candidates can originate from Compton scattering or mis-reconstruction. The fake  $\mu \rightarrow eee$  signals comprise either one positron from a Michel decay and an  $e^+e^-$  pair or two Michel positrons and a single electron track candidate.

The probability of an  $e^+e^-$  pair or electron and one or two positrons to manifest like a signal can be approximated by

$$\varepsilon_t^p \approx \varepsilon_{\text{kinematic}}^{p,t} \times \varepsilon_{\text{vertex}}^t \times \varepsilon_{\text{coincidence}}^t, \quad (2.4)$$

where type  $t$  stands either for the pair or the single electron case.  $\varepsilon_{\text{kinematic}}^{p,t}$  describes the probability of the three particles, where the positron-electron pair or the electron ( $t$ ) are produced through a given process  $p$  to fulfil the kinematic selection criteria for the signal decay. It depends mainly on the momentum resolution of the experiment.  $\varepsilon_{\text{vertex}}^t$  and  $\varepsilon_{\text{coincidence}}^t$  describe the probability of them to occur from a common vertex in space and time within the experiment's vertex and time resolution. In general, all three factors can depend on the position of the stopped muon. Moreover, the latter two also depend on the kinematics of the three particles. Naturally, this introduces correlations. The number of accidental background events within a certain time frame ( $ABG$ ) including either an  $e^+e^-$  pair or a single electron from a given process  $p$  is approximated by

$$ABG_{\text{pair}}^p \sim \binom{N}{2} \times \varepsilon_{\text{pair}}^p \times (2\varepsilon_p) \times \varepsilon_{\text{acceptance}}^{3e} \times \varepsilon_{\text{reconstruction}}^{3e} \quad (2.5)$$

$$ABG_{\text{single}}^p \sim \binom{N}{3} \times \varepsilon_{\text{single}}^p \times (3\varepsilon_p) \times \varepsilon_{\text{acceptance}}^{3e} \times \varepsilon_{\text{reconstruction}}^{3e}, \quad (2.6)$$

where the number of stopped muons within the time frame  $N$  is proportional to the muon rate,  $\varepsilon_p$  is the probability of producing a positron-electron pair or an electron by the considered process in the target,  $\varepsilon_{\text{acceptance}}^{3e}$  the geometrical acceptance and  $\varepsilon_{\text{reconstruction}}^{3e}$  the reconstruction efficiency of all three tracks ( $3e$ ). The last two factors depend again on the kinematics of the particles. Hence, the total number of accidental background events of the first type, containing a positron-electron pair, scale quadratically<sup>1</sup> with the muon rate. The second type, comprising two independent muons from Michel decay and an electron from a given process, scales cubically<sup>2</sup> with this rate. Considering the linear scaling of signal events in the muon rate, this leads to a linear, respectively quadratic, scaling of accidental background with respect to the signal (BG/S). The respective accidental background probability per stopped muon scales analogously. To take into account all correlations that are neglected here, extensive Monte Carlo simulations are required.

### POSITRON-ELECTRON PAIRS FROM BHABHA SCATTERING

Positron-electron pairs generated through Bhabha scattering of positrons from muon decay on electrons at rest have a characteristic invariant mass spectrum with a sharp cut-off at

---

<sup>1</sup> $\binom{N}{2} = \frac{1}{2}(N-1)N.$

<sup>2</sup> $\binom{N}{3} = \frac{1}{6}(N-2)(N-1)N.$

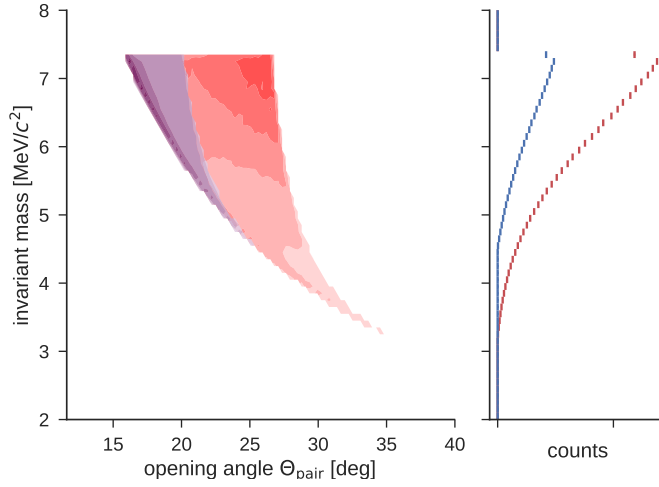


**Figure 2.2:** The invariant mass and opening angles for positron-electron pairs generated through Bhabha scattering of a positron from muon (Michel) decay and an electron at rest. Both particles are required to have a momentum larger than 5  $\text{MeV}/c$  ( $\rightarrow$ ), respectively 10  $\text{MeV}/c$  ( $\rightarrow$ ).

$7.3 \text{ MeV}/c^2$  caused by the Michel edge. Figure 2.2 shows this spectrum for pairs where both particles have a momentum  $p > 5 \text{ MeV}/c$  and  $p > 10 \text{ MeV}/c$ , respectively, in combination with the opening angles between the particles of the pairs. The cross section for Bhabha scattering is proportional to the path length of the positron in a material and its ratio  $Z/A$  of the atomic number and mass. The characteristic invariant mass and opening angle could be exploited to further suppress combinatorial background by sacrificing this parts of the phase space.

## 2.2 EXPERIMENTAL CONCEPT

The design of the MU3E experiment aims for the best possible discrimination between signal and background topologies, and the ability to measure  $\mathcal{O}(10^{16})$  muon decays within few hundred days of beam time. This requires, on the one hand, excellent energy, i.e. total momentum, resolution in a range from a few  $\text{MeV}/c$  up to  $\sim 53 \text{ MeV}/c$  and on the other hand the ability to run at high muon rates. Figure 2.3 illustrates the main components of the cylindrical phase I detector cut along the beam direction and transverse planes. The experiment is embedded in a helium atmosphere and a homogeneous magnetic field with a field strength of 1 T parallel to the beam axis. A monochromatic continuous muon beam is injected through the beamline into the experiment's centre. The long lifetime of the muon of  $2.2 \mu\text{s}$  allows a scheme where the particles decay at rest in a defined volume, such as the hollow double cone Mylar stopping target in the centre. This leads to very clear signal topology. Cylinder-like thin silicon-based tracking double layers with a radial offset of roughly 1 cm and a length of 34 cm, respectively 36 cm, are located concentrically around the centre at radii between 7 cm to 8 cm. Each layer consists of single sensors with an active area of  $2 \text{ cm} \times 2 \text{ cm}$ . This tracker is duplicated both

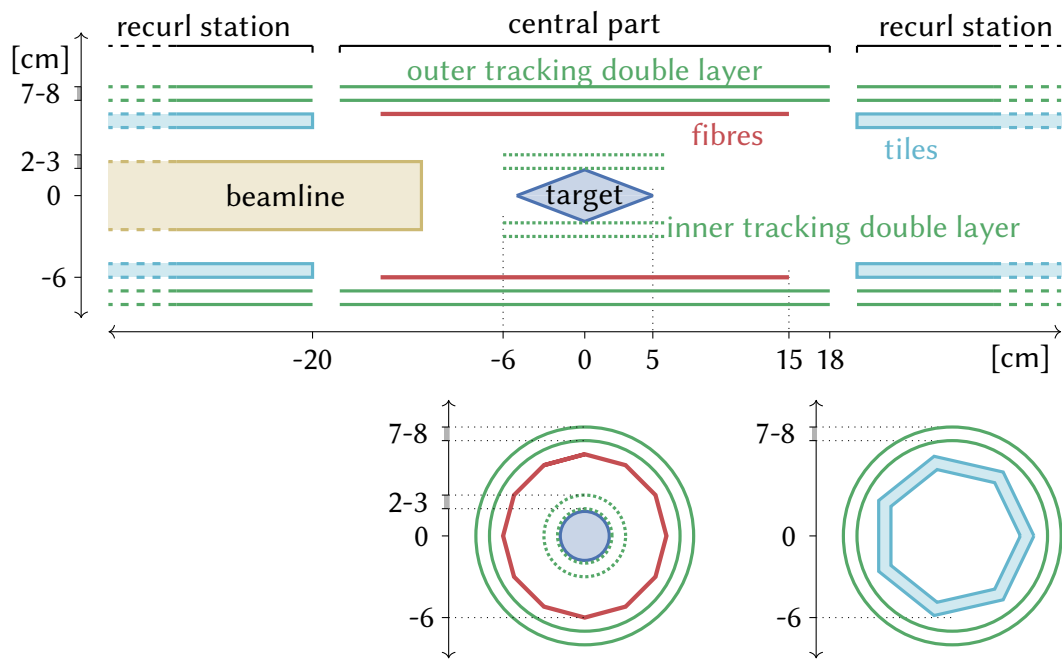


**Figure 2.3:** The MU3E detector components: beamline (—), hollow double cone muon stopping target (—), thin silicon based tracking inner (···) and outer (—) double layers, scintillating fibre (—) and scintillating tile (—) detectors. The phase I experiment comprises of a central part and recurl stations up- and downstream. In the top part, the components are shown in a cut following the beam direction. In the bottom part, transverse projections of the different regions are shown.

up- and downstream in the so-called recurl stations. Furthermore, a supplementary shorter tracking double layer envelopes the target at a radius between 2 cm to 3 cm with a length of 12 cm. The central part is equipped with a 30 cm long cylindrical scintillating fibre detector at a radius of 6 cm. A scintillating tile detector is located at the same radius in the recurl stations.

Helices describe the electron trajectories in the homogeneous magnetic field. The particles loop and eventually recurl at least a second time into the outer tracking double layer. As long as the particles' trajectories avoid thick material such as the beamline, the scintillating tiles or mechanical structures the helices are only modified slightly by multiple Coulomb scattering and small energy losses in the thin detector layers. The electrons can complete multiple turns. The elongated detector design with its recurl stations provides high acceptance, particularly for second hits of electrons with high axial momentum components in the outer tracking double layer.

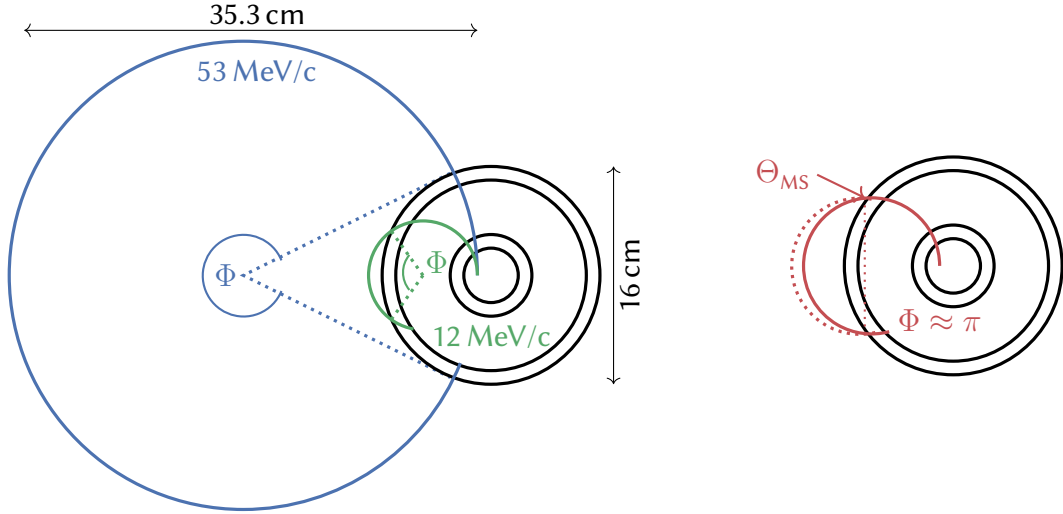
### 2.2.1 OPTIMIZATION FOR MOMENTUM RESOLUTION

State-of-the-art calorimeters provide neither the required resolution nor granularity to handle the required occupancies. Therefore, the electron's momentum is determined by exploiting their track bending in the presence of a magnetic field. In the simplest case of a uniform solenoid field, the trajectories are helical. Neglecting the spatial resolution of the tracking systems, at least three space points are required to determine the three-dimensional trajectory of a single track unambiguously. Particles traversing matter undergo multiple Coulomb scattering. The scattering angle net distribution can be represented by a Gaussian component for small angles in combinations with long tails from large angle scattering [56]. The three-dimensional angle  $\theta_{1/e}$  at which this distribution has fallen by  $1/e$  is given by [66]

$$\theta_{1/e} = \frac{17.5 \text{ MeV}}{\beta c p} \sqrt{\frac{x}{X_0}} [1 + \varepsilon], \quad (2.7)$$

where  $p$  is the momentum of the traversing particle,  $\beta c$  is the velocity and  $x/X_0$  is the thickness of the scattering medium in units of its radiation length.  $\varepsilon$  is a small correction factor depending on  $\ln(x/X_0)$ . The relevant total momentum range below half the muon mass is in a regime of significant multiple Coulomb scattering even for very thin tracking layers in the order of 0.1 %  $X_0$ .

If a very low material tracker is employed, the particle's interaction with the material of the tracking layers alters to first order only momentum's direction but not the amplitude, respectively the total energy. This introduces two additional parameters in the helix based momentum determination, a transverse and axial scattering angle in the second of the three tracking points. Including these, three space points, which are called triplet, define precisely two helices with the same radius and the scattering in between them as mentioned above. Such triplets are combined to track candidates. An non-iterative solution of such a three-dimensional triplet fit using a linearization ansatz can be found in [67]. The relative uncertainty of the helix radius, directly connected to the momentum of a particle, is roughly proportional to  $\theta_{1/e}/\Phi$  where  $\Phi$  is the trajectory bending angle between the points. Combining multiple triplets reduces the uncertainty further.



(a) Tracks with the maximal transverse momentum of 53 MeV/c (—) and tracks with  $p_t = 12$  MeV/c (—) penetrate all four tracking layers.

(b) The tangential position offset at first recurling caused by the scattering  $\Theta_{MS}$  cancels to the first order if  $\Phi \approx \pi$ .

**Figure 2.4:** The tracker in a transverse cut. The projection of different particle trajectories with different transverse momenta projected to the cut plane is shown. The shown trajectories originate in the target at a radial offset of 1 cm from the beam axis in the presence of a homogeneous magnetic field with  $B = 1$  T parallel to the beam.

Three design considerations optimize the momentum resolution. Firstly, the experiment is conducted in a *helium atmosphere* to limit multiple scattering and energy loss of particles almost uniquely to the detector layers and the target. Secondly, the *minimization of material* in all trajectories in the acceptance up to the point of an adequate momentum measurement reduces the energy smearing due to the stochastic nature of energy deposition. Furthermore, very thin tracking layers with low radiation length reduce the multiple scattering and hence increase the relative momentum resolution. Thirdly, the radial position of the tracking layers are chosen to *maximize the total bending angles*  $\Phi$  of the triplets based tracks as shown in Figure 2.4a. A cylindrical design with two tracking double layers performs best<sup>3</sup>. In particular, the extended material-free path length during the recurling of particles allow for an excellent momentum resolution. Furthermore, if the bending angle is  $\Phi \approx \pi$ , the azimuthal position offset in the recurling tracking layer due to multiple scattering in the outgoing layer, cancels to first order. This effect is illustrated in Figure 2.4b. The magnetic field strength of 1 T and the radii of the outer tracking double layer of 7 cm to 8 cm are chosen in such a way that electrons in the transverse momentum range from 15 MeV up to 53 MeV penetrate this layer at least twice. On the other hand, all tracks are contained in a volume with a radius below 38 cm around the beam axis. This is a feasible volume for a homogeneous magnet.

<sup>3</sup>An alternative scheme consists of tangential tracking double layers.

## 2.2.2 IMPLICATIONS OF HIGH MUON RATES

Accidental background, as described in subsection 2.1.4, is the primary challenge high muon rates evoke. Moreover, the higher the rates are, the more care has to be taken to keep detector occupancies at feasible levels.

The pileup of decay products of several stopped muons is tackled in two ways, based on a four-dimensional vertex reconstruction, a spatially extended target and the beam structure. Firstly, a system to distinguish between different vertices, the four-dimensional muon decay coordinates, in space and time is deployed. It consists on one hand of a cylindrical tracking double layer surrounding the muon target, which provides together with the outer tracking double layers vertexing in space. On the other hand two timing detectors, a scintillating fibre detector in the central part and scintillating tile detector in the recurl stations provide a precise time measurement which is used for vertexing in time. The thin hollow double cone Mylar target with a maximal radius of 1.9 cm and a total length of 10 cm maximizes the spatial spread of the vertices. This design keeps at the same time, the material budget as low as possible to minimize multiple scattering and energy loss, as well as to reduce the production of secondary particles which contribute potentially in accidental background.

Secondly, the use of a continuous beam spreads the muon decays uniformly over time. This reduces the accidental background and is beneficial for the detector's occupancy. Potential  $\mu \rightarrow eee$  signal candidates are identified only after a full event reconstruction. The decay topology does not provide a handle for a trigger without full track reconstruction. In a pulsed scheme, the detector readout could be reduced to a defined time window after a fixed offset with respect to the muon beam pulse. The muon lifetime of  $2.2 \mu\text{s}$  would have to be taken into account. The continuous beam rate is only fully exploited if neither the detector readout nor the reconstruction introduces dead time. This leads to the requirement of a trigger-less continuous readout with an online event reconstruction.

## 2.3 BEAMLIN AND STOPPING TARGET

The MU3E experiment exploits  $\mu^+$  from the PSI high-rate beam channel in the area  $\pi\text{E5}$ . A primary 2.2 mA beam of protons with an energy of 590 MeV interacts with a pion production target made of polycrystalline graphite. Pions which stop inside the target close to the surface generate monochromatic ( $p_\mu=29.8 \text{ MeV}/c$ ) fully polarized muons which are extracted backwards under  $165^\circ$ . The native  $\pi\text{E5}$  channel, some MEG-beamline elements and the Compact Muon Beam Line (CMBL) [68], shown in Figure 2.5, transports the particles from the production target to the experiment. For positron suppression, this beamline contains a particle separator which filters velocity over energy by a combined orthogonal  $E \times B$ -field. The delivery of  $8 \cdot 10^7 \mu^+/\text{s}$  at a primary beam current of 2.2 mA at the final focus was demonstrated [68]. This corresponds to about  $5 \cdot 10^7 \mu^+/\text{s}$  stopped in the target. The MEG and the MU3E experiments share parts of the beamline, up to the Triplet II. Only one experiment is supplied with muons at the time.

A 600  $\mu\text{m}$  Mylar degrader and the 35  $\mu\text{m}$  thick Mylar beam window reduce the muon momenta so that 90 % stop in the hollow double cone Mylar target. The target has a total length

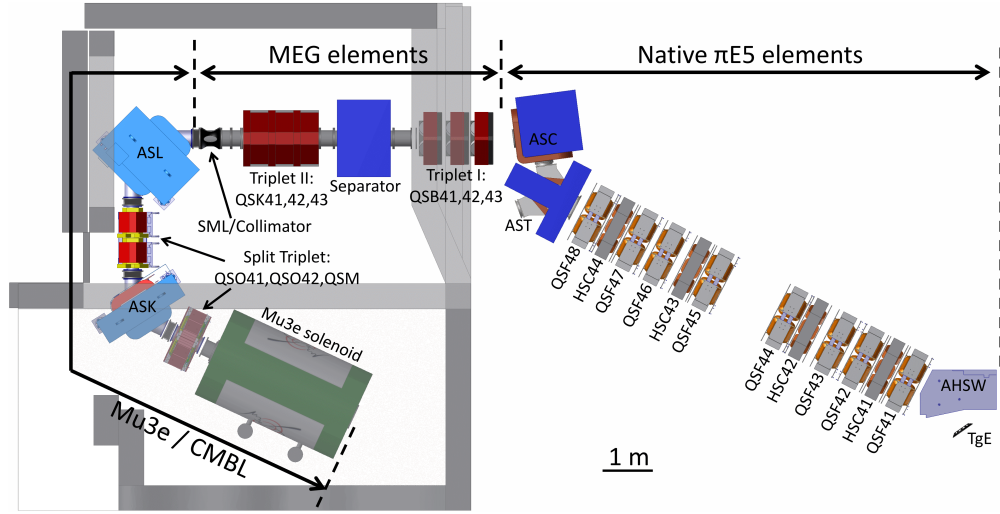


**Figure 2.5:** The high-rate  $\mu^+$  beam channel at PSI used for the first phase of the Mu3E experiment. Surface muons are transported from the target (TgE) by the native  $\pi$ E5 elements and components shared with the MEG experiment which contains a particle separator. The CMBL transfers the particles into the Mu3E solenoid magnet. Modified from [68].

of 10 cm and a maximal radius of 19 mm. The upstream side is  $70\ \mu\text{m}$  and the downstream side  $80\ \mu\text{m}$  thick. The chosen target shape and dimensions provide good stopping efficiency and reduce combinatorial background by distributing the decay vertices over a large area and minimizing Bhabha scattering in the target material (see Equation 2.1.4).

## 2.4 TRACKING

The Mu3E tracker faces the challenge of high particle rates and the need to minimize the material budget along the particles trajectories. Novel silicon High-Voltage Monolithic Active Pixel Sensor (HV-MAPS) which can be thinned down provide time resolutions in the order of nanoseconds and good spacial resolution. Hence, they are an ideal choice for the experiment's tracker.

### 2.4.1 THE SENSORS: HV-MAPS

In HV-MAPS, transistors are integrated into the diode which provides almost full fill factor. This low voltage part is shielded by deep N-wells from the charge-collecting diodes. Order of 60 V reverse biasing of the diodes results in thin, about  $10\ \mu\text{m}$  thick, depleted regions with high electric drift fields. This leads to fast charge collection of  $\mathcal{O}(1\ \text{ns})$  and allows to thin down the substrate to  $50\ \mu\text{m}$ .

## THE MUPIX SENSOR

A dedicated HV-MAPS is being developed for the Mu3E experiment [34]. This MuPix sensor is fabricated currently in the commercial AMS H18 180 nm High-Voltage CMOS process. Its design goal has an active area of roughly  $2\text{ cm} \times 2\text{ cm}$  with pixel size of about  $80\text{ }\mu\text{m} \times 80\text{ }\mu\text{m}$ . At least the first amplification stage is located inside the pixel, potentially also the comparator stage. Each pixel is connected to the periphery which hosts the signal processing and digital state machine. A 8 ns timestamp is assigned to each pixel hit. Up to four 1.25 Gbps Low Voltage Differential Signalling (LVDS) links per chip transmit the zero-suppressed pixel data. A low number of signal and slow control lines is required to reduce the material budget of sensor's support structure. A power consumption below  $300\text{ mW/cm}^2$  is targeted.

MuPix8, the sensor's most recent R&D version, has an active size of  $2\text{ cm} \times 1\text{ cm}$  and hosts different matrices for the signal propagation from pixel to the periphery. High efficiencies above 99% at negligible noise rates below 1 Hz/pixel have been demonstrated [69]. This sensor shows a time resolution of  $\mathcal{O}(14\text{ ns})$  which is consistent to its predecessors [69, 70].

### 2.4.2 THE TRACKER SUPPORT STRUCTURE

The pixel sensors are tab-bonded onto Kapton-aluminium flex print High Density Interconnect (HDI) which provides power together with signal and slow control lines. Multiple sensors along the beam direction are combined to a ladder on the same HDI. The ladders are reinforced with  $25\text{ }\mu\text{m}$  thick polyimide foil. In the outer two tracking layers additional v-folds are added to enhance the mechanical stability. At the same time, they are used as channels for additional flow of gaseous Helium which is used to cool the sensors. The radiation length of the combination of the sensors with the support structure of one layer is projected to be about  $0.1\% X_0$ .

The pixel ladders are combined to modules which are mounted between support rings on both sides.

### 2.4.3 TRIPLET-BASED TRACK FINDING

The track finding in the experiment is based on triplets of pixel hits which are combined to actual tracks in a second step.

## TRIPLETS

Due to the small pixel size and low particle momenta, the tracking uncertainties are dominated by Multiple Scattering (MS) (see Equation 2.7). Furthermore almost all material, which causes scattering, is located around the tracking planes. Motivated by these two observations, a helix fit which treats MS in the pixel detector planes as the only uncertainty has been developed by the Mu3E collaboration [67, 71]. Variations of the same algorithm are employed for online reconstruction required for event filtering and offline data analysis. The algorithm is based on triplets of hits, which can be fit in parallel. Thus the method is suited for online track finding.

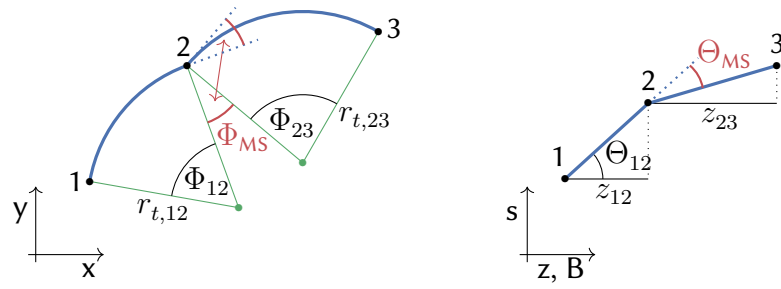


**Figure 2.6:** Two helices through a hit triplet (1,2,3) with scattering angles  $\Phi_{MS}$  and  $\Theta_{MS}$  in the material in the plane of the central (2) hit. The magnetic field is parallel to the z-axis which is aligned with the beam direction. The left side shows a projection in a transverse plane, the right side a projection on the longitudinal (z-s) plane, where s is the path length along the trajectories. Adapted from [67].

The reconstructed tracks consist of combinations of multiple triplets of hits in successive detector layers. Figure 2.6 illustrates two helices through the triplet hits with scattering in the material in the plane of the central hit (2). In first order, multiple scattering in the material of thin tracking layers only alters a particle momentum's direction but not the amplitude, thus the total energy. Hence the three-dimensional bending radius in the homogeneous magnetic field

$$R_{3D}^2 = r_{t,12}^2 + \frac{z_{12}^2}{\Phi_{12}^2} = r_{t,23}^2 + \frac{z_{23}^2}{\Phi_{23}^2} \quad (2.8)$$

is conserved. The scattering is expressed by the scattering angles  $\Phi_{MS}$  and  $\Theta_{MS}$  in the transversal and longitudinal plane respectively. According to MS theory (see subsection 2.2.1), the scattering angles distribute around zero with variances of  $\sigma_\theta^2 = \sigma_{MS}^2$  and  $\sigma_\phi^2 = \sigma_{MS}^2 / \sin^2 \theta$ . The algorithm minimizes

$$\chi^2(R_{3D}) = \frac{\Phi_{MS}(R_{3D})^2}{\sigma_\phi^2} + \frac{\Theta_{MS}(R_{3D})^2}{\sigma_\theta^2} \quad (2.9)$$

by using a linearization around an approximate solution with  $r_{t,12} = r_{t,23}$ . More than one solution exists for different numbers of half turns of the helix.

## TRACK FINDING

The triplets are built from pre-selected hits in a reconstruction time frame. Currently, reconstruction frames of 50 ns are used, which is roughly aligned to the silicon pixel's time resolution of  $\mathcal{O}(14 \text{ ns})$ . Track candidates are built by combining valid multiple triplets which yields a common

$$\chi_{\text{track}}^2(\bar{R}) = \sum_{i=1}^{n_{\text{triplets}}} \chi_i^2(R_i), \quad (2.10)$$

where  $n_{\text{triplets}} = n_{\text{hits}} - 2$  and  $\chi_i^2(R_i)$  corresponds to Equation 2.9 of the i-th triplet.  $\bar{R}$ , which translates directly into a particle's momentum, is the weighted average of all triplet radii  $R_i$ .

## 2.5 THE TIMING DETECTORS

The two timing detectors consist of plastic scintillators read out by Silicon Photomultiplier (SiPM). In the central detector region, the material in the particles trajectories has to be minimized. Hence thin scintillating fibres are used in this part. Chapter 3 describes the design in more detail. Particles which reach the tile detector in the outer detector barrels have recurred; they penetrated the outer tracking double-layer twice. Hence their momentum is already measured as precise as possible. There is no need to minimize the material other than from space constraints. The plastic scintillator tiles consist of EJ-228<sup>4</sup> and have a size of  $\sim 6.3 \text{ mm} \times 6.2 \text{ mm} \times 5 \text{ mm}$ . They are wrapped into Enhanced Specular Reflector ESR foil. The detector consists of 56 rings along the beam direction which each contains 56 tiles. They are grouped into sub-modules of 4 tiles along the beam direction and 8 tiles in the transverse plane. 7 sub-modules along the beam-direction assemble into one module.

The tiles are read out by  $3 \text{ mm} \times 3 \text{ mm}$  SiPMs whose signal is digitised by the same Application-Specific Integrated Circuit (ASIC) as deployed for the scintillating fibre detector.

Prototypes tested in test beams yield a time resolution of  $\mathcal{O}(50 \text{ ps})$  [72].

## 2.6 DATA ACQUISITION SYSTEM

The trigger-less DAQ system is built in such a way that each reconstruction computer receives the data from the full detector of a time slice. A total data rate in the order of  $\mathcal{O}(80 \text{ Gbps})$  is expected at a muon stopping rate of  $1 \cdot 10^8 \text{ Hz}$  [73]. Figure 2.7 gives an overview of the whole system. 1.25 Gbps LVDS links connect the pixel sensors and the timing readout ASICs to the front-end Field Programmable Gate Arrays (FPGAs) inside the magnet. The front-end boards transmit the merged data stream optically outside the magnet to the switching boards which further merge the data and forward it to the online reconstruction computer farm. These computers receive the data from the whole detector of a time slice. A data collector manages the storage of selected reconstruction frames. A detailed description of the fibre sub-detector DAQ is given in chapter 13.

### 2.6.1 THE MIDAS FRAMEWORK

The MU3E experiment's DAQ is integrated into the Maximum Integrated Data Acquisition System (MIDAS) [74], which is developed at PSI and TRIUMF. It is in use in a vast variety of experiments, and it is PSI's standard DAQ system. This framework offers run control, event building and logging, slow control and history systems and also online monitoring. The system offers multi-user access through a web interface.

---

<sup>4</sup>from ELJEN TECHNOLOGY

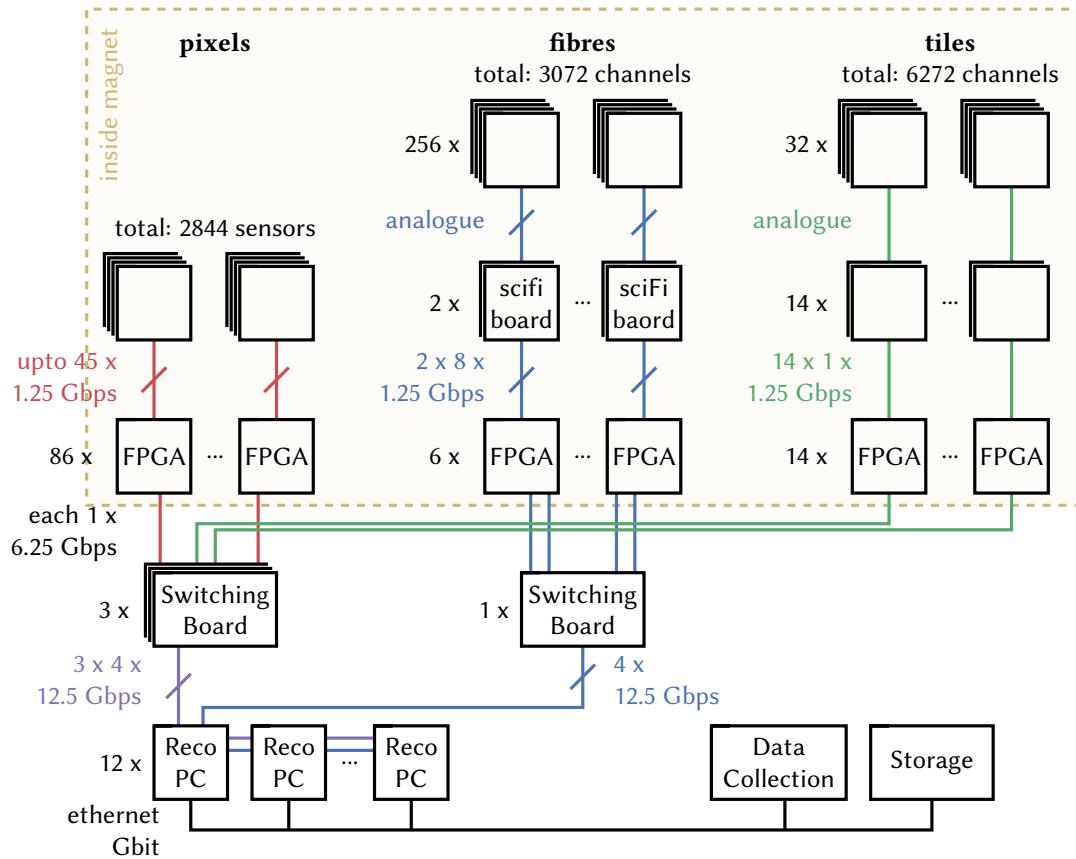


**Figure 2.7:** The trigger-less data acquisition system of the MU3E experiment. 1.25 Gbps LVDS links connect the pixel sensors and timing readout ASICs with the front-end FPGAs. The switching boards collect all data stream and route them to the reconstruction (Reco) computers. Two SiPM arrays, each attached to one fibre ribbon and comprising 128 channels, with a total of 256 channels are connected to one SCIFI BOARD. Two SCIFI BOARDS are connected to one experiment FPGA front-end board; all six such boards are connected to a common switching board. This sums up to  $256 \times 2 \times 6 = 3072$  channels for the fibre sub-detector.

### 2.7 MECHANICAL SUPPORT, MAGNET AND COOLING

The cylindrically shaped detector with a total length of  $\sim 1.2$  m, a detector diameter of  $\sim 17$  cm and a diameter of the active volume where particles recur of  $\sim 80$  cm is located inside a superconducting magnet which provides a homogeneous 1 T magnetic field parallel to the beam axis. The detector is mounted on a cage which is inserted into the magnet. The magnet's warm bore has a diameter of 1 m. The calculated homogeneity along the beam axis is 0.1 %, the uniformity in the transverse plane at the radius of 35 cm is 3 ppm [75].

The detector is cooled on one hand by a global gaseous helium flow through the whole magnet bore. Furthermore, gaseous helium is fed to the volume between the pixels layers as well as the volume between scintillating fibre detector and the pixel layer outside. In addition, a fast gas flow is injected in the v-folds of the pixel support structure. Simulations of the planned scheme show a temperature gradient of up to  $40^{\circ}\text{C}$  at the outer two pixel layers [75]. Helium temperatures slightly above  $0^{\circ}\text{C}$  are foreseen. The fibre and tile sub-detector's ASIC are cooled by additional liquid cooling systems (see chapter 12).



# 3

## Scintillating Fibre Detector Concept

The cylindrically shaped scintillating fibre detector is located in the central part of the experiment. Scintillating fibres are used to measure the precise time of passing particles with minimal material in the particle trajectories. Scattering in the material spoils the momentum resolution. This chapter starts with the requirements of the sub-detector determined in the scope of this thesis. Followed by the detector's design. The presented CAD<sup>1</sup> models and renderings are results of this work. In a third part, the expected particle rates and distributions inside the sub-detector are discussed based on the integration of the fibre sub-detector into the experiment's simulation framework which is described in more detail in chapter 9.

### 3.1 REQUIREMENTS OF THE SUB-DETECTOR

The sub-detector provides additional time information to the pixel sensors. On the one hand, the timing is used to suppress combinatorial background and on the other hand to reject misreconstructed track candidates, particularly wrong charge assignment. The latter requires a time resolution per particle crossing of better than 350 ps and an efficiency close to one. This allows resolving the sense of rotation from two sub-detector hits of tracks with  $p > 20$  MeV/c which recurl at least  $\Phi > 90^\circ$  (see Figure 2.4b) better than 95 %.

The fibre detector is required to resolve particle crossings at a total rate of 255 MHz in the whole detector.

At the same time, the material budget has to be as small as possible to maintain the excellent momentum resolution. A too thin detector's efficiency is insufficient. A plastic scintillator detector with a thickness  $\lesssim 1$  mm is a trade-off between these two constraints. Figure 3.1 shows the scattering of crossing particles in the fibre detector as a function of their momentum.

---

<sup>1</sup>Computer-Aided Design.

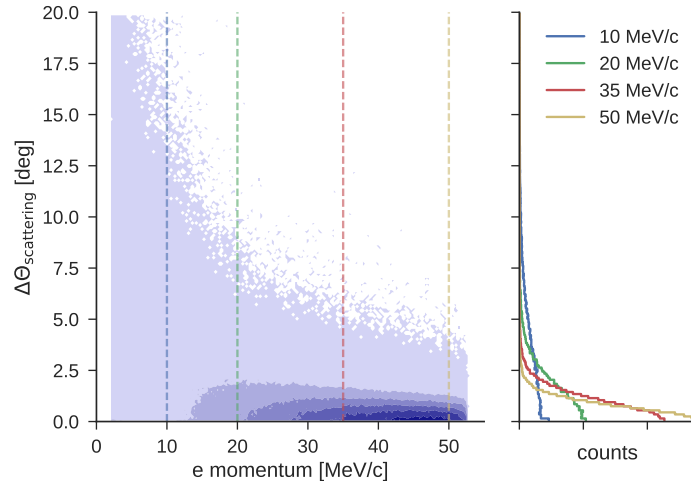


**Figure 3.1:** Simulated scattering at a fibre ribbon consisting of 4 layers of 250  $\mu\text{m}$  thick round fibres as a function of the particle's momentum. The path length inside the fibre ribbon depends on the particles inclination angle.

### 3.2 THE SUB-DETECTOR'S DESIGN

The cylindrically shaped detector is located in the central part of the experiment at a radius of about 6 cm and has a sensitive length of roughly 29 cm. Three considerations determine the sub-detector location. Firstly, no material should be placed outside of the fourth pixel layer where the main momentum measurement is performed. Secondly, it has to be in close vicinity to a pixel layer. The utilized track finding algorithm considers scattering alone in these layers. And thirdly, the larger the radius is, the smaller the sub-detectors occupancy and consequent pile-up.

The detector consists of round, double clad, 250  $\mu\text{m}$  thick scintillating fibres. The fibres are assembled to ribbons consisting of 3 or 4 layers which each consist of about 126 fibres. The fibres of different layers are offset by the fibre radius. As shown in subsection 10.3.3, four or fewer layers are feasible regarding the experiment's momentum resolution and reconstruction efficiency. On the other hand, ribbon prototypes consisting of 3 layers fulfil the sub-detector's requirements as presented in chapter 7. Both options will be tested in full-scale prototypes. The fibre ribbons have a width of 32 mm, a thickness of 0.9 mm<sup>2</sup> and a length of 288 mm. Twelve ribbons form the full scintillating fibre detector.

The fibres are read out on both sides by SiPM column arrays which are described in more detail in section 5.3. The sensors are bonded on flex prints which connects them with the readout electronics (see section 6.3) and provide bias voltage. The sensors are attached directly to the polished fibre ends without the use of any additional optical grease or glue. Figure 3.2 shows the details of this assembly, which is spring loaded in the whole detector to account

<sup>2</sup>4 layer ribbons.

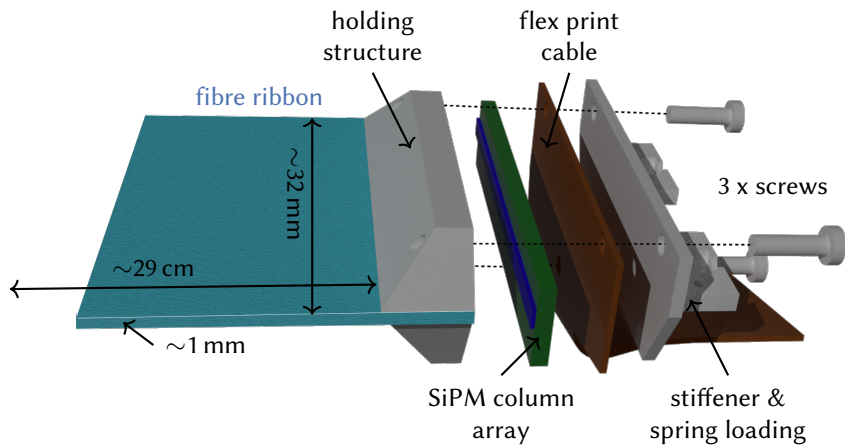


**Figure 3.2:** Schematic overview of the fibre ribbon coupling to SiPM column array readout sensors present on both ribbon sides. The sensors are bonded onto flexprint cables. The assembly is fixed with three screws and a stiffener.

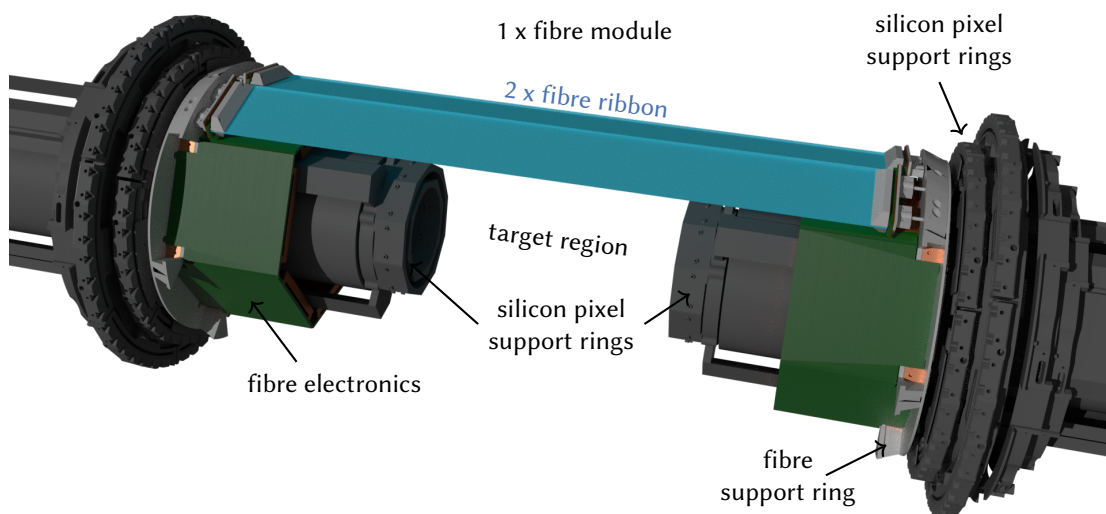


**Figure 3.3:** A fibre module, consisting of two ribbons, located in the central part of the experiment. The full fibre detector comprises 6 modules, respectively 12 ribbons. Furthermore the fibre support structure including the support rings and fibre electronic boards are shown inside the experiment's support structure.

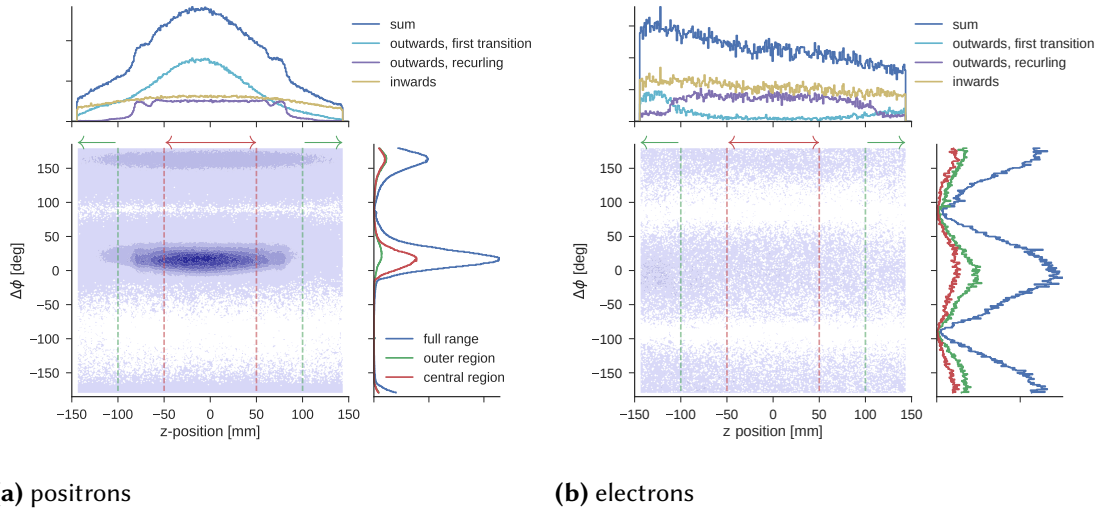


**Figure 3.4:** The simulated angle of the particle momentum direction with respect to the outward pointing fibre ribbon normal projected to the transverse plane for positrons (a) and electrons (b) as a functions of the particle's incident position along the beam (z) direction. The outer region ( $\leftarrow$ ) is defined as  $|z| > 100$  mm and the central region ( $\rightarrow$ ) as  $|z| < 50$  mm. Out going particles ( $\leftarrow$ ,  $\rightarrow$ ) penetrate the fibre ribbons from smaller to larger radii, vice versa for the recurling (inwards,  $\rightarrow$ ) ones.

for the fibres thermal expansion. Figure 3.3 shows one module and the experiment's support structure. A more detailed description of the detectors mechanics is given in chapter 12.

### 3.3 PARTICLE RATES AND DISTRIBUTIONS IN THE SCINTILLATING FIBRE DETECTOR

Table 3.1 summarizes the expected particle rates at a muon stopping rate of  $1 \cdot 10^8$  Hz. Particles crossing the detector outwards for the first time, recurling particles and those passing the detector inwards are distinguished. Figure 3.4 shows the distribution of positrons and electrons along the beam (z) direction and the particles inclination angle in the transverse plane. The inclination angle of a crossing particle is the angle between the particle's momentum direction and the outward normal of the fibre ribbons.  $\Delta\Phi$  is its projection to the transverse plane, where  $\Delta\Theta$  is its projection to the longitudinal plane which is shown in Figure 3.5. The different inclination angles correspond to varying path lengths inside the detector. Their distribution is presented in Figure B.1.

Figure 3.6 shows the total momentum and transverse momentum distributions of the particles crossing the fibre detector for the first time outwards, inwards and for further recurling particles. The transverse momentum is linear to the two-dimensional helix radii. The number of detector transitions is shown in Figure 3.7 and the vertex of the particles crossing the fibre detector in Figure 3.8. Only about 70 % of the positrons and 0.5 % of the electrons detected in the fibre detector originate from the target volume (see Table 3.1).

### 3.3. PARTICLE RATES AND DISTRIBUTIONS IN THE SCINTILLATING FIBRE DETECTOR

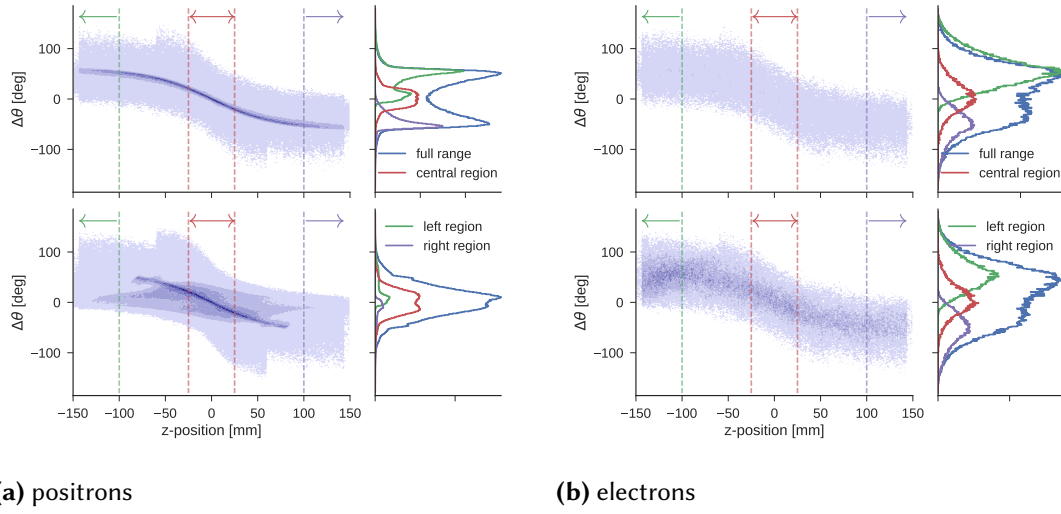


**Figure 3.5:** The simulated angle of the particle momentum direction with respect to the outward pointing fibre ribbon normal projected to the longitudinal plane for outwards (top) and inwards (bottom) propagating positrons (a) and electrons (b) as functions of the particle’s incident position along the beam (z) direction. The upstream region ( $\leftarrow$ ) is defined as  $z < -100$  mm, the central region ( $\rightarrow$ ) as  $|z| < 25$  mm and the downstream region ( $\rightarrow$ ) as  $z > 100$  mm.

**Table 3.1:** Expected rates in the fibre detector at a muon stopping rate of  $1 \cdot 10^8$  Hz in the target. The rates are divided into the detector crossings from positrons and electron, and their direction: inwards and outwards for the first time and all subsequent recurling hits. Furthermore, the particle which originate from a vertex within  $r < 20$  mm and  $|z| < 55$  mm are listed separately as *from the target region*.

particle	type	rate		
		from target total [MHz]	total [MHz]	total per fibre [kHz]
positrons	outwards, first transition	79	107	69.3
	outwards, recurling	39	56	36.4
	inwards	54	77	50.4
	<i>total</i>	<i>172</i>	<i>240</i>	<i>156.1</i>
electrons	outwards, first transition	0.02	7	4.7
	outwards, recurling	0.03	2	1.0
	inwards	0.03	6	3.9
	<i>total</i>	<i>0.08</i>	<i>15</i>	<i>9.6</i>
<b>total</b>	<b>172</b>	<b>255</b>	<b>165.7</b>	

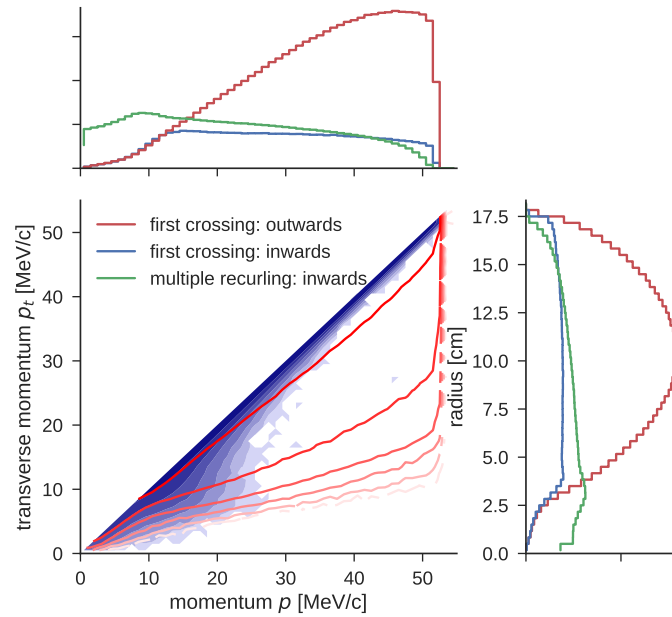


**Figure 3.6:** Simulated total momentum distribution and its transverse component, corresponding to the projection of the trajectory onto the transverse plane, of particles crossing the fibre detector at the first crossing outwards ( $\rightarrow$ ), at the first crossing inwards ( $\leftarrow$ ) and during all further recurlings ( $\leftarrow$ ).

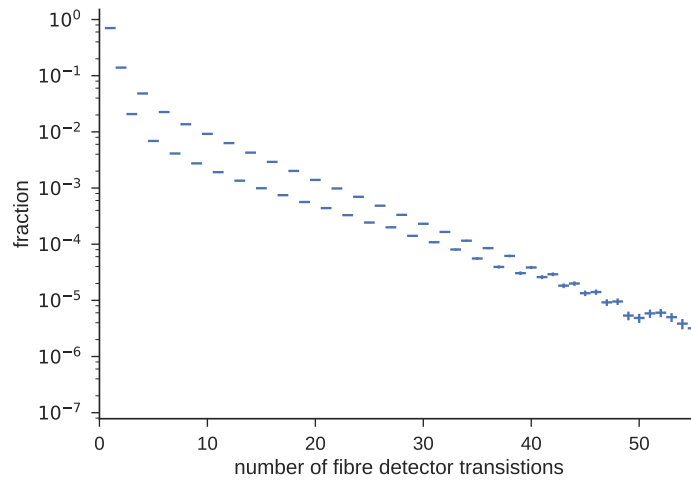


**Figure 3.7:** Simulated distribution of the number of fibre detector crossing of positrons and electrons. The spectrum is dominated by positrons due to their abundance from the decay of the stopped  $\mu^+$ . One full revolution comprises two detector crossings.

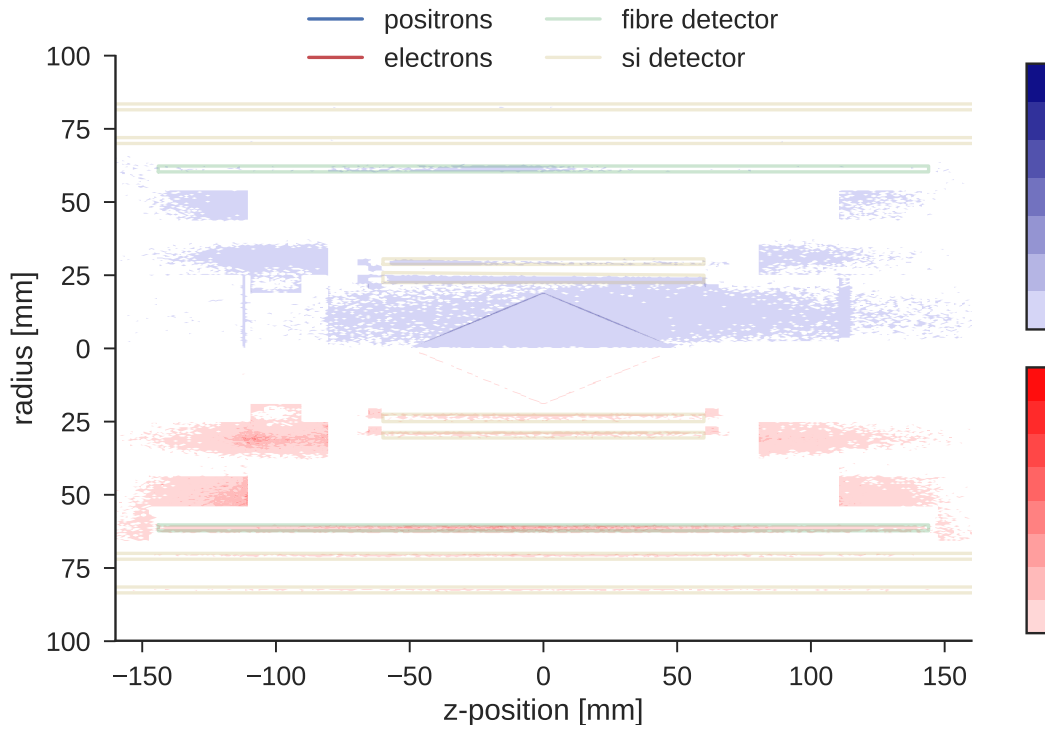


**Figure 3.8:** The simulated vertex distribution in a longitudinal projection (z-r) of positrons ( $\rightarrow$ ), in the top, and electrons ( $\leftarrow$ ), in the bottom, crossing the fibre detector ( $\rightarrow$ ). The stopped muons decay predominantly in  $\mu \rightarrow e\nu\nu$ . The fibre detector and the silicon tracking layers are indicated for better orientation ( $\rightarrow$ ). The distribution of positron's vertices is dominated by the volume of the very thin hollow target which manifests triangular in this projection. The positron and electron vertex density are shown in different scales; the latter is enhanced by a factor of 250.



**Part II**

**Scintillating Fibres and Silicon  
Photomultipliers**



# 4

## Scintillating Fibres

Scintillating fibres combine the detection of charged particles and the propagation of their response outwards in one single volume, hence optimizing the active volume. In this chapter, the working principle of organic scintillators is introduced following [76, 77], completed by a description of fibres as photon guides.

### 4.1 ORGANIC SCINTILLATORS

Scintillation describes the emission of light in a medium by the passage of a particle. Typical organic scintillators consist of a carrier substance, for example polystyrene, with two additive dyes. The largest fraction of the deposited energy of a passing particle is deposited in the carrier substance and part of it needs to be transferred to the primary scintillator molecules, the activators. In plastic scintillators with a typical concentration of  $\mathcal{O}(10 \text{ g/L})$  this energy transfer between adjacent molecules is non-radiative. Wavelength shifting dyes can increase the attenuation length and adjust the scintillator's emittance spectrum for particular applications.

#### 4.1.1 SCINTILLATOR MOLECULES

In organic scintillators, molecules excited by the passing particles emit light in a subsequent de-excitation process. They consist of aromatic hydrocarbon compounds made of benzene ring molecules ( $\text{C}_6\text{H}_6$ ). Three out of the four valence electrons, one 2s and three 2p orbitals, of each carbon atom bind one hydrogen and two neighbouring carbon atoms in covalent  $\sigma$  bonds. These three  $\text{sp}^2$  hybrid orbitals lead to the ring structure shown in Figure 4.1. The remaining electrons, orbitals, form  $\pi$  bonds resulting in charge clouds below and above the carbon ring plane. The individual electrons cannot be assigned to a specific atom, they are delocalized. The scintillation properties arise from the energy levels of this  $\pi$ -electrons, illustrated in Figure 4.2. The energy difference between  $S_0$  and  $S_1$  states is in the order of 3 eV to 4 eV, corresponds to wavelengths of 300 nm to 400 nm. Furthermore, each level reveals sub-levels with a spacing of  $\mathcal{O}(0.16 \text{ eV})$  due to vibrational modes. Energy absorption from an ionizing particle leads to

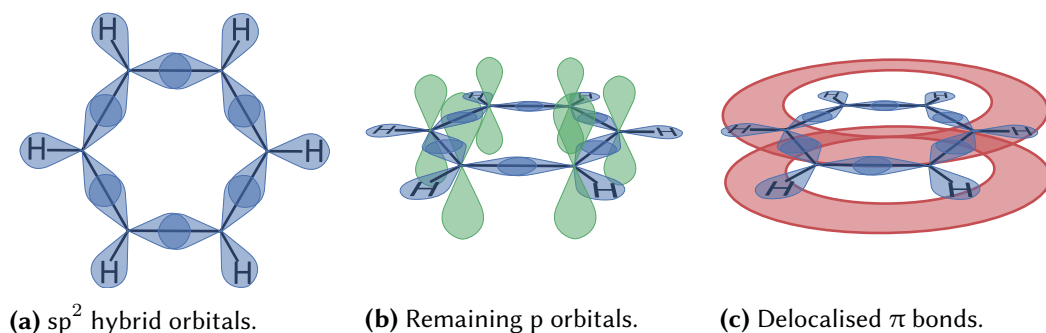


**Figure 4.1:** Structure of benzene ring ( $C_6H_6$ ) with its covalent  $\sigma$  bonds between C and H atoms, the remaining p orbitals resulting in delocalized  $\pi$  bonds. Adapted from [78].

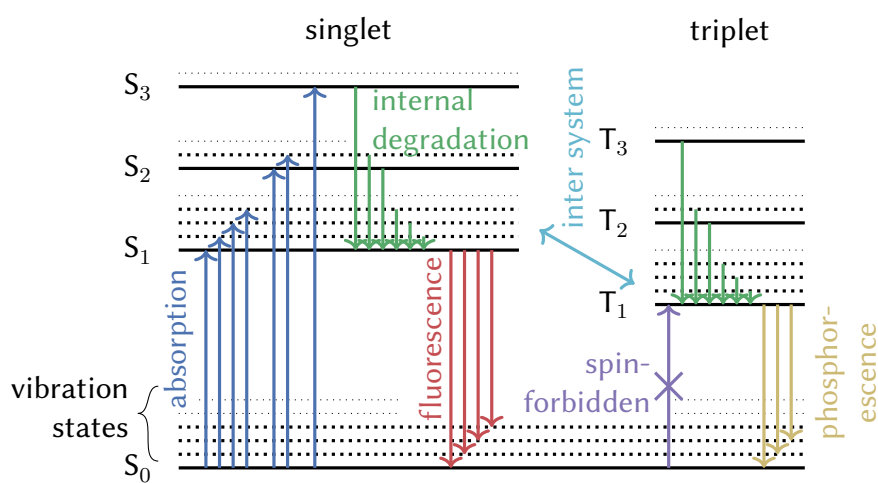


**Figure 4.2:** Schematic view of the  $\pi$ -electron energy levels of a scintillating material and the different processes: photon absorption, radiation-less internal degradation to the  $S_1$  energy level, subsequent fluorescence with photon emission, internal system crossings from singlet to the triplet states and phosphorescence. Adapted from [76].

excitation of  $\pi$ -electron and vibrational modes. The excitation into a triplet state is forbidden due to spin conservation. States in energy levels above  $S_1$  decay very quickly, in less than 10 ps, radiation-less through internal degradation unto this ground state. Within the order of 1 ns, states in the  $S_1$  energy level decay into a vibration mode state of  $S_0$ . This process emits a photon and is called *fluorescence*. Due to the vibrational modes the energy of the emitted light is smaller than the minimal energy required to excite an electron from the  $S_0$  ground state into at least the  $S_1$  state. This suppresses the immediate re-absorption of the photons and makes the material transparent for its emitted light. This shift between the absorbed and emitted light is called *Stokes shift*.

It is possible that electrons transit in a radiationless process, called inter-system crossing, to the triplet state. The lowest triplet energy state  $T_1$  is metastable, which causes decay times in the order of milliseconds. The emission of light in the decay from this state into a vibration state of the ground state is called *phosphorescence* and adds a delayed scintillation component [76].

#### 4.1.2 THE EMISSION SPECTRUM OF PLASTIC SCINTILLATORS

In general shorter wavelengths are more affected by scattering and absorption processes in the material. Therefore the ultraviolet photons emitted by the primary scintillator molecules are converted by absorption and re-emission by spectral shifter luminophores into lower energy photons. This results in longer attenuation lengths and better matching to the wavelength sensitivities of the photodetectors.

In conventional plastic scintillators the wavelength up-shifting is realized in a multi-step process, hence lacks efficiency. Very recently introduced Nanostructured Organosilicon Luminophore (NOL) bond the activator and spectral shifter through silicon atoms into one molecule. This provides a more efficient non-radiative energy transfer from activators to spectral shifters resulting in a faster spectrum transformation [79]. Such NOL fibres are not yet commercially available. Figure 7.1 shows typical emission spectra of scintillating fibres tuned to match SiPM's most sensitive wavelengths.

The photon distribution over time can be described by a swift rise of the emitted signal in the order of 100 ps and the combination of two exponential decays. As described in section 4.1, the decay consists of a fast component  $\mathcal{O}(\text{ns})$  and a slow component. The relative strength of the two components depends on the scintillator material.

#### LIGHT YIELD OF PLASTIC SCINTILLATORS

The efficiencies of all processes involved in the scintillation can be combined into a scintillation efficiency. For Minimum Ionizing Particles (MIPs), the amount of light emitted is proportional to the energy deposited in the material by a crossing particle [76]. Therefore, the light yield  $Y$  is expressed in terms of total number of emitted photon, integrated over the whole spectrum, per deposited energy. Typical values are in the order of 10 photons/keV. In the case of highly ionizing particles, the light yield suffers from quenching due to lack of molecules in the ground state. The light is emitted isotropically along the particle path.

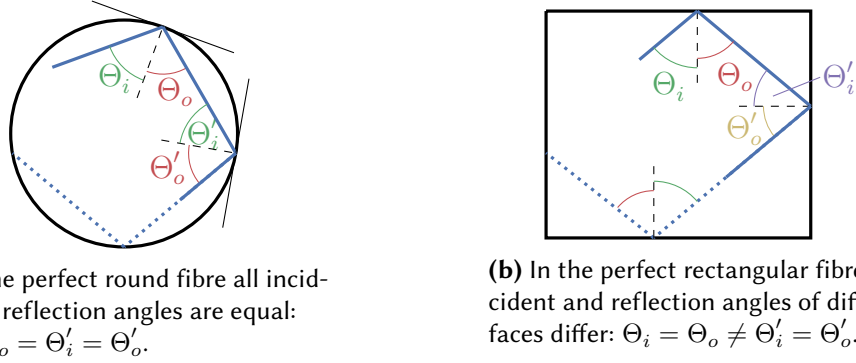


**Figure 4.3:** Repetitive internal total reflection in fibres guiding the photons. Transverse cuts perpendicular to the fibre axis of round and square fibres are shown.

Scintillation consists of statistical processes, the number of emitted photons shows Poisson-like fluctuations.

## 4.2 FIBRES: PHOTON GUIDES

Plastic scintillating fibres act as guides for photons due to total internal reflection. These fibres are available in different geometries, of which round and square cross sections are most common. In general, they consist of a core material and a cladding material with a refractive index  $n_{\text{core}} > n_{\text{cladding}}$ . The incident angle  $\Theta$  of a photon is described with respect to the normal of the interface between the two materials. If the incident angle of a photon is larger than a critical angle

$$\Theta_c = \arcsin\left(\frac{n_{\text{cladding}}}{n_{\text{core}}}\right), \quad (4.1)$$

the photons are totally internally reflected. The absolute value of the incident and reflected angle are equivalent. In the case of perfectly round fibres, this leads to continuous internal reflection with a constant incident angle of the photon with respect to the interface surface, as shown in Figure 4.3a. In the case of square or rectangular fibres, shown in Figure 4.3b, the angles at different faces differ. Photons are only guided inside such a fibre by repetitive reflections if the angles at both ends fulfil the total internal reflection criterion.

The use of additional claddings with progressive smaller refractive index decreases the critical angle  $\Theta_c$ , thus increases the collection of scintillation light emitted in the core material. Even though the total internal reflection angle is in principle determined only by the ratio of the refractive index of the outermost (smallest  $n$ ) layer and the core material, multiple layers are required for the mechanical stability of the claddings.

A typical multi-clad scintillating fibre, as shown in Figure 4.4, consist of a polystyrene (PS) core with a refractive index of  $n_{\text{core}} = 1.59$ , cladded with polymethyl methacrylate (PMMA) and a fluorinated polymer (FP) with refractive indices of  $n_{\text{clad}}^{\text{PMMA}} = 1.49$  and  $n_{\text{clad}}^{\text{FP}} = 1.42$ . Fluorescent dopants are mixed into the core material only, hence this is the scintillating active volume. The claddings have a typical combined thickness in the order of 3% of the fibre

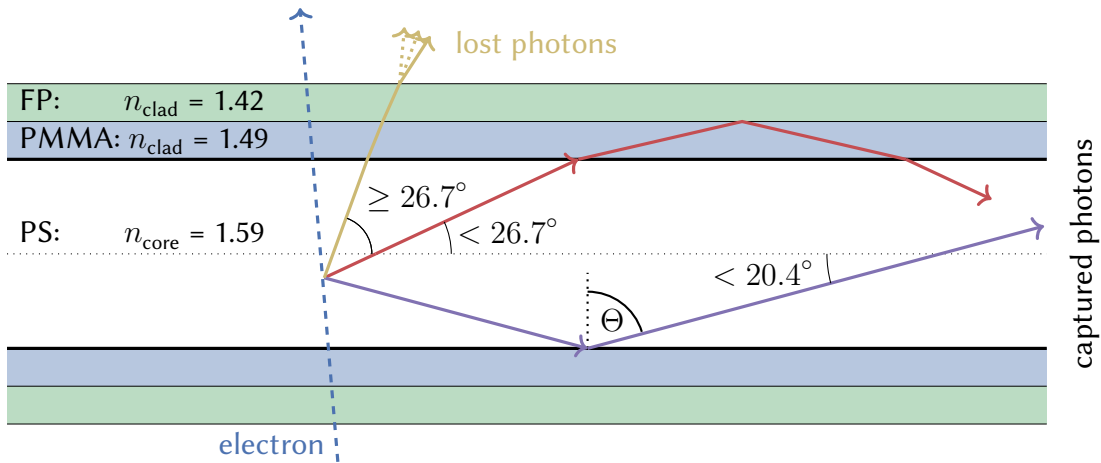


**Figure 4.4:** Capture of scintillation photons in a typical fibre by internal total reflection at the interface between core and PMMA cladding ( $\leftarrow$ ) or at the interface between PMMA and FP cladding ( $\rightarrow$ ). Photons with an angle larger  $\Theta_c$  ( $\leftarrow$ ) leave the fibre and are lost. The photon exit angles depend on the refractive index of the surrounding material.

**Table 4.1:** Capture Efficiency (CE) per hemisphere for round and square fibres at the first and second cladding and in the ideal case of a fibre embedded in air or vacuum ( $n \approx 1$ ). The angle is defined with respect to the fibre axis.

total reflection at	1 <sup>st</sup> clad	2 <sup>nd</sup> clad	air
angle [deg]	21.4	27.4	51.3
CE round [%]	3.4	5.6	18.7
CE square [%]	4.4	7.3	28.0

diameter. Due to mechanical stability, it is not possible to use only one FP cladding. The fibres are produced in a preform drawing method which takes special care of the molecular orientation of the polystyrene core polymer. A higher degree of molecular orientation reduces its optical transparency<sup>1</sup> [79]. Plastic scintillating fibres are available with diameters from 250  $\mu\text{m}$  up to 2 mm.

#### 4.2.1 CAPTURE EFFICIENCY

The efficiency to collect scintillating photons emitted in the fibre core and guide them to the fibre ends is determined by internal total reflection and their attenuation along the propagation path. Table 4.1 summarises the capture efficiency of round and square fibres for single and double claddings. The reflection at the interface of the second cladding and the surrounding is determined by the surface roughness and the embedding medium's refractive index. In prin-

<sup>1</sup>but increases the mechanical stability.

ciple, the best results could be achieved with a bare fibre in air ( $n_{\text{air}} \approx 1$ ). In most applications the fibres are embedded in epoxy resins with typical refractive indices larger than  $n_{\text{clad}}^{\text{FP}}$ . In this case most of the photons entering the second cladding are lost. The propagation of photons with small incident angles involves many reflections and hence results in long path lengths with respect to photons with larger incident angles. Photons with longer path lengths through the fibre are more prone to attenuation.

#### 4.2.2 ATTENUATION LENGTH

Losses of scintillation photons during the propagation along the fibre are characterized by a wavelength dependent attenuation length  $\Lambda(\lambda)$  defined as the distance along the fibre at which a fraction of  $1/e$  of the initial photons with a wavelength  $\lambda$  are remaining. Note that this distance does not correspond to the covered pathlength of propagating photons which is angle dependent. Causes for attenuation are absorption of the scintillating material, impurities and traps as well as imperfections in the interfaces. Total reflections at the different interfaces and different emission angles lead to a variety of photon propagation modes. For example more meridional rays which pass by the fibre axis closely between every reflection or more helical skew rays. This results in multiple attenuation length components. Typically the light intensity  $I(\lambda, d)$  at a certain wavelength  $\lambda$  at a distance  $d$  along the fibre can be described by

$$I(\lambda, d) = I_0^{\text{long}}(\lambda)e^{\frac{-d}{\Lambda_{\text{long}}(\lambda)}} + I_0^{\text{short}}(\lambda)e^{\frac{-d}{\Lambda_{\text{short}}(\lambda)}}, \quad (4.2)$$

where  $I_0^{\text{long}}(\lambda) + I_0^{\text{short}}(\lambda) = I_0(\lambda)$  is the initial intensity at the wavelength  $\lambda$ .  $\Lambda_{\text{short}}$ , relevant for the Mu3E experiment, is around 20 cm to 30 cm [80] whereas  $\Lambda_{\text{long}}$  is in the order of 3 m [81].

#### APPROXIMATIONS IN THE MU3E REGIME

The emission spectrum  $I_{\text{interaction}}(\lambda)$  at the interaction position  $d$  yields a total light intensity at the photons exit position at the fibre end of

$$I_{\text{exit}}(d) = \int \exp\left(\frac{-d}{\Lambda(\lambda)}\right) I_{\text{interaction}}(\lambda) d\lambda. \quad (4.3)$$

Measurements showed [80] that for the relevant wavelengths of 400 nm to 550 nm (see Figure 7.1) and distances of 0 cm to 30 cm

$$I_{\text{exit}}(d) \approx \exp\left(\frac{-d}{\Lambda_{\text{attenuation}}}\right) \int I_{\text{interaction}}(\lambda) d\lambda. \quad (4.4)$$

This corresponds to a roughly constant  $\Lambda(\lambda)$  in the considered range.

# 5

## Silicon Photo Detectors

Silicon-based photon detectors combine the low-light detection capabilities of traditional Photomultiplier Tubes (PMTs) with the advantages of solid-state devices. They offer relatively low-voltage operation in the order of few 10 V, mechanical robustness, small form and large fill factors, insensitivity to magnetic fields, and uniform responses. Following [72, 77, 82–84], this chapter firstly introduces the working principle of silicon photodetectors followed by a more detailed description of SiPMs in section 5.2. Supplemented by a detailed description of the sensors which will be used in the fibre detector in section 5.3 and preliminary irradiation studies in the context of the MU3E experiment and this thesis in section 5.4.

### 5.1 WORKING PRINCIPLE

Silicon absorbs photons passing through. Energy is transferred to a bound electron which is moved from the valence into the conducting band producing an electron-hole pair. The absorption depth, the silicon thickness at which  $1 - 1/e$  photons have been absorbed, is highly photon energy dependent. It ranges from  $4 \cdot 10^{-3} \mu\text{m}$  at wavelengths of 280 nm up to  $30 \mu\text{m}$  at a wavelength of 900 nm. For photon energies below the band gap of 1.12 eV it becomes basically transparent.

In the interface region between a p-type and n-type doped semiconductors, a p-n junction, the mobile charge carriers diffuse into the opposite site and recombine. This layer is depleted from mobile charge carriers and leads to the build-up of oppositely charged regions. Thereof a local electrical field forms which stops, in the end, the charge carrier exchange in an equilibrium between this force and the diffusion “pressure”. An external voltage across this structure causes a current flow in one direction and heavily suppresses it in the opposite one. Elements with this property are called diode. Forward biasing, where the resulting field opposes the intrinsic one, neutralizes the depletion zone and leads to a current flow above a threshold voltage  $V_d$ . Reversely biased, the depletion zone is extended causing a high resistance to the flow of charge carriers. The depletion zone breaks down if the electric field is above a critical level caused by external potential larger  $U_{br}$ . Breakdown processes, either tunnelling of electrons

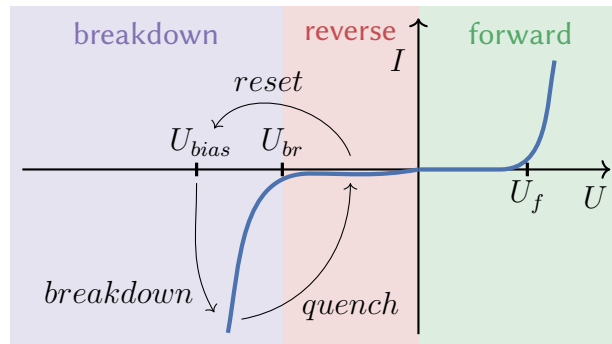


**Figure 5.1:** Typical diode  $I$ - $V$  diagram. Three operation regions exist: **forward** or **reverse** biased and **breakdown**. SiPMs are operated at  $U_{bias}$  in the breakdown region; a quenching resistor is required to interrupt the current flow and subsequently reset the pixel.

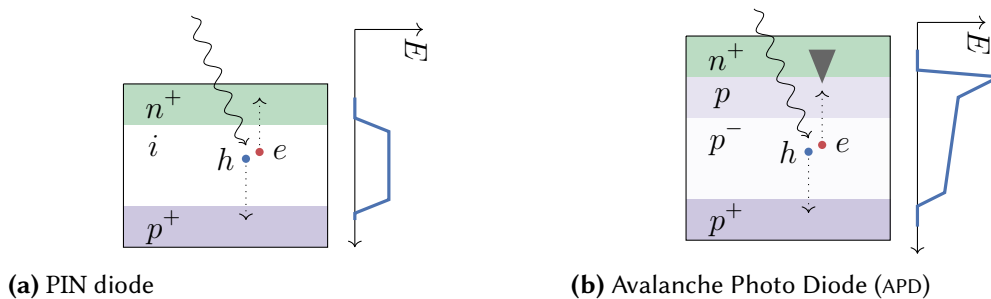


**Figure 5.2:** Doping and electric field structure of PIN diode (5.2a) and APD (5.2b).

from valence into conducting bands or avalanches, are reversible as long as no thermal damage is caused.

If a photon is absorbed in the depleted region, the charge carriers, i.e. the electron and the hole, drift in the electric field in opposite directions creating a net current.

## PIN DIODE

To increase the active volume of a sensor an intrinsic silicon layer can be added in between the heavily doped  $p^+$  and  $n^+$  layers. A small reverse bias is enough to extend the depletion zone over the full intrinsic layer and form a uniform electric field in this zone (see Figure 5.2a). The induced current of such a PIN diode is proportional to the incoming photon flux and stable with respect to temperature and bias voltage variations. The absence of an internal gain, one absorbed photon sources one hole and one electron, makes the detection of single photons practically impossible.

### AVALANCHE PHOTO DIODE

APDs allow the measurement of single photons by exploiting an internal gain mechanism. This gain can be achieved if charge carriers acquire enough energy due to high electric fields ( $> 5 \cdot 10^5$  V/cm) to create secondary electron-hole pairs via impact ionisation. Such fields are obtained by high doping gradients at the p-n interface. With respect to PIN diodes the active volume is shifted to a  $p^+-i-p$  region as illustrated in Figure 5.2b. In order to extend the depletion over this volume reverse bias close to the  $U_{br}$  is used. Incident photons produce electron-hole pairs whereby the electrons drift in the moderate electric field towards the amplification layer in the junction. Due to the higher ionisation coefficient of electrons over holes, only the first participate in the amplification avalanche. The avalanche propagates in one direction until the electrons leave the high field region. In this operation mode, the number of electrons in the anode is proportional to the number of initial electron-hole pairs, gains up to 1000 can be achieved.

Even higher gain is achieved if the APDs are operated above  $U_{br}$  in the so-called *Geiger mode*. In this mode, the electric field is large enough so that also the holes participate in the avalanche amplification process. This leads to a self-sustaining breakdown with significant current flow which needs to be quenched. A passive quench resistor of a few 100 k $\Omega$  stops the avalanche by reducing the effective voltage below  $U_{breakdown}$  due to a voltage drop at the same. Consequently, the voltage across the diode recharges and resets the sensor. The time needed for this process is called recovery time. Figure 5.1 illustrates this process of breakdown, quenching and subsequent resetting. In this mode, the gain, up to  $1 \cdot 10^6$ , is a constant, given by the difference between the operation voltage  $U_{bias}$  and  $U_{br}$ . This voltage difference is called overvoltage  $U_{over}$ . Once an avalanche is triggered, the signal is independent of the number of absorbed photons. Thermal electrons in the active volume can also trigger an avalanche. Due to the unity gain, the signal of this so-called dark counts is not distinguishable from signals caused by photons. The increased gain comes at the expense of photon counting capability.

A typical current signal can be envisaged as the discharge of the pixel capacitance  $C_d$ , initially biased by  $U_{bias}$ , through the small pixel resistance  $R_S$ . The capacity  $C_d$  depends on the pixel size. A large enough resistance  $R_q$  in the bias leg quenches the discharging current flow. Thus, the signal's rise time is given by  $t_{rise} = R_S C_d$ . The maximal current is determined by  $U_{over}/R_q$ , consequently the gain is linear in  $U_{over}$ . The avalanche process determines the pixel resistance. Hence it rises with the exponential decrease of  $U_{over}$  due to the discharge. The signal decay time, which is at the same time the recovery time of the pixel, is given by  $C_d R_q$ .

### 5.2 SILICON PHOTOMULTIPLIER

Silicon Photomultiplier (SiPM) refers to multi-pixel array APDs operated in the *Geiger mode* [85]. The combination of small individual pixels, typical dimensions range from 10  $\mu\text{m}$  to 100  $\mu\text{m}$ , with individual quench resistors restores the photon counting capability and still provides high gains. Figure 5.3 shows a typical pixel structure. The signal of a single triggered pixel does not depend on the number of incident photons. The individual pixels are connected in

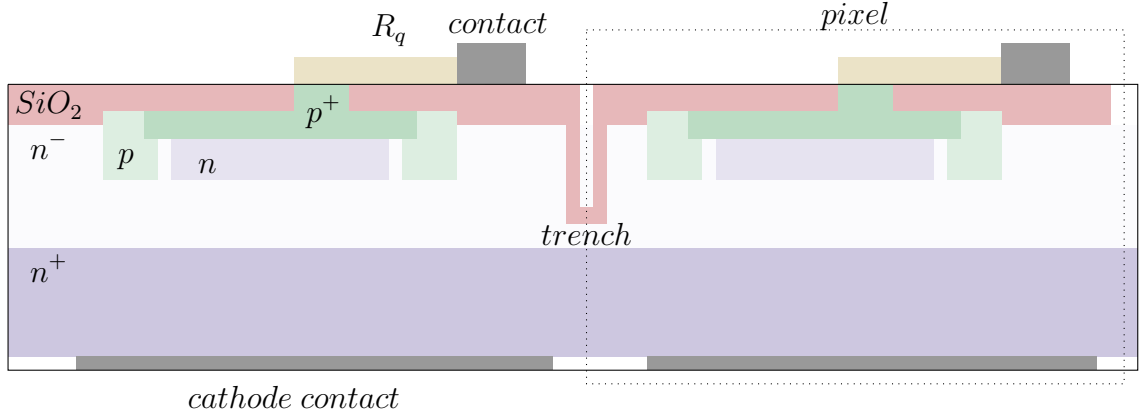


**Figure 5.3:** Structure of a typical SiPM pixel: APD structure with additional silicon oxide layer, guard rings, quench resistor  $R_q$  and trenches between pixels. Adapted from [82].

parallel. Hence, the device's signal is a binary combination of all pixels with discrete signal levels for the number of triggered pixels. During the discharge of one or multiple pixels, see Figure 5.1, all the others remain fully charged. Table 5.1 summarizes typical values and the dependencies of typical SiPM properties which are described in the following.

### 5.2.1 DETECTION EFFICIENCY

The fraction of the surface sensitive to light is called fill factor. The separation of the individual pixels, the quench resistors and connection lines reduces this area. The dead area's size is almost independent of the pixel size, therefore the fill factor increases for sensors with large pixels. A typical fill factor  $\epsilon_{\text{fill}}$  for SiPM with pixels size of  $50 \mu\text{m} \times 50 \mu\text{m}$  are in the order of 70 % to 80 %. The Photon Detection Efficiency (PDE) is given by

$$PDE(U_{\text{over}}, \lambda) = \epsilon_q(\lambda) \cdot \epsilon_{\text{fill}} \cdot \epsilon_{\text{avalanche}}(U_{\text{over}}) \quad (5.1)$$

where  $\epsilon_q(\lambda)$  is the photon wavelength-dependent quantum efficiency of silicon, the probability that such a photon produces an electron-hole pair.  $\epsilon_{\text{avalanche}}(U_{\text{over}})$  is the overvoltage-dependant probability that a free charge carrier triggers an avalanche. In normal SiPM operation modes the sensor is fully depleted, hence the avalanche probability approaches  $\epsilon_{\text{avalanche}} \rightarrow 1$ . The wavelength dependency of PDE is shown in Figure 7.1.

### 5.2.2 DARK COUNT RATE

Each pixel shows a similar dark count behaviour as a single APD in *Geiger mode*. If SiPMs are used to detect single photons, dark counts are the main noise contribution. As in the case of a single Geiger mode APD, avalanches from single pixels triggered by incidence photons cannot be distinguished from these provoked by thermal electrons. The Dark Count Rate (DCR) is the

rate of such dark counts per sensor. This definition introduces a linear dependency on the SiPM area. Two sources of thermal electrons exist. Firstly, electrons transfer from the valence to the conducting band via an additional state, a trap, within the band gap. This process is sensitive to the temperature and trap density. Secondly, the tunnelling between the bands which is a function of the electric field and only weakly temperature dependent [82]. The first process dominates above a cross-over temperature typically below 0 °C. Typical values of DCR at room temperature (25 °C) are in the order of 50 kHz/mm<sup>2</sup> with a factor two increase approximately every 5 °C.

The current, in the absence of photon-induced signals is called *dark current*  $I_{\text{dark}}$  and consists of two components: A bulk current due to thermal charge carriers and a surface current due to defects in the silicon oxide interface [83]. Both contributions are functions of  $U_{\text{bias}}$ . A significant increase of dark current occurs when  $U_{\text{bias}}$  approaches  $U_{\text{br}}$ . In fact, the later is defined by

$$\left. \frac{dI_{\text{dark}}}{dU_{\text{bias}}} \right|_{U_{\text{br}}} = 0. \quad (5.2)$$

For bias voltages above  $U_{\text{br}}$ , the dark current is dominated by the dark counts  $I_{\text{dark}} \approx DCR \cdot \text{gain} \cdot \frac{1}{1 - \epsilon_{\text{crosstalk}}}$ . A second significant increase of dark current is observed at bias voltages well above breakdown voltage at the point where the quench resistance becomes too small to stop an avalanche. In this regime, the sensor behaves like an ohmic resistor. Typically, DCR is quoted at a signal threshold of 0.5 photoelectrons. 1.0 photoelectrons correspond to the signal caused by exactly one SiPM pixel.

### 5.2.3 CROSSTALK

The combination of multiple pixels, single Geiger mode APDs, to one sensor leads to cross-talk between them. The accelerated charge carriers of an avalanche emit  $2.5 \cdot 10^{-5}$  photons/electron<sup>1</sup> with a wavelength between 500 nm and 1600 nm [86]. The absorption length in silicon of such near infrared photons is in the order of mm, hence the produced photons travel considerable distances. Either directly or reflected at the entrance window or at the back side of the substrate, they can reach a neighbouring pixel where they potentially create an electron-hole pair and subsequently trigger an avalanche. Since the number of produced infrared photons is proportional to the gain, the cross-talk is also.

If the charge carrier pair is created inside the active region, the secondary pixel fires within the order of 100 ps. The sensor's signal amplitude doubles, it mimics precisely a two-photon signal. The cross-talk probability determines the number of dark count signals with an amplitude  $> n$  pixel with respect to the signals  $\geq n$  triggered pixels. Figure 5.4 shows the measured DCR dependent on the applied threshold. The rate at threshold  $t$  corresponds to all signals with a voltage amplitude  $\geq t$ , hence the plateaus correspond to the rate of all signals  $\geq n$  pixel levels. The ratio of two plateaus corresponds to the prompt cross-talk probability.

If the charge carrier pair is created in the bulk substrate they can drift to the active region and trigger an avalanche. Since drift is a rather slow process, this correlated cross-talk can

<sup>1</sup>Hamamatsu S10362-11-100U operated at a voltage above quenching at 23.5 °C room temperature.

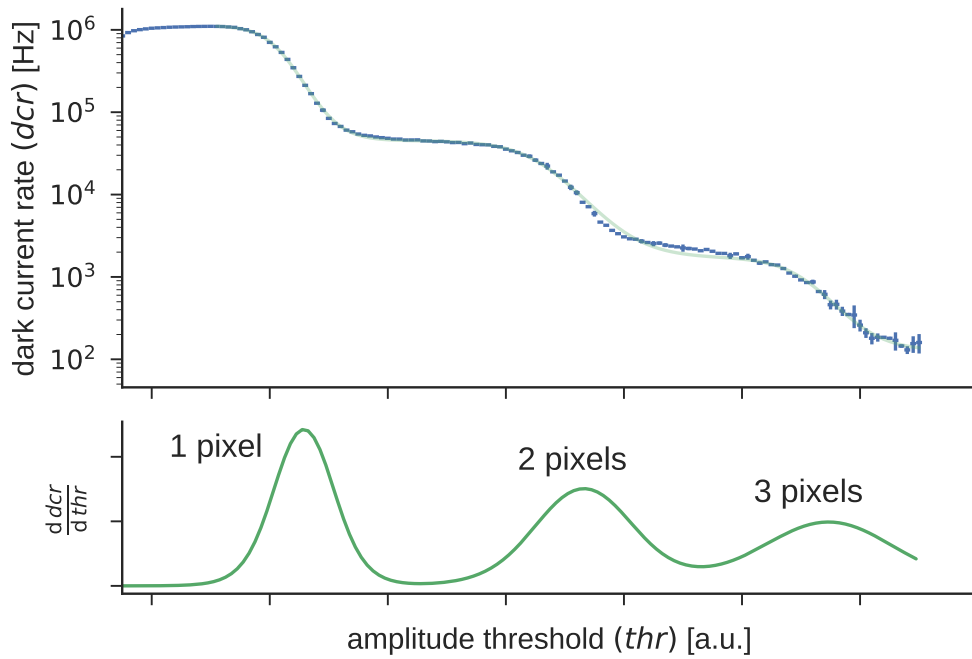


**Figure 5.4:** The DCR of a Hamamatsu S13360-1350PE with an active area of  $1.3 \text{ mm} \times 1.3 \text{ mm}$  at 3 V above its breakdown voltage at  $20^\circ \text{C}$  as a function of the applied amplitude threshold. Multiple sigmoid functions are fitted to emphasize the step structure ( $\text{—}$ ). Peaks in its derivative, shown in the bottom part, highlight the discrete amplitudes of one, two and three-pixel signal. Crosstalk causes multiple pixel signals.

**Table 5.1:** SiPM properties and their dependencies in combination with typical values for a Hamamatsu S13360 sensor with a pixel size of  $50\ \mu\text{m} \times 50\ \mu\text{m}$  operated at  $U_{\text{over}} = 3\ \text{V}$  at room temperature of  $25\ ^\circ\text{C}$ .

property	dependencies	typical values
$U_{\text{breakdown}}$	$\propto T$	54 mV/K
gain	$C_d \cdot U_{\text{over}}$	$(53 \pm 5)\ \text{V}$
DCR	$\frac{d\text{DCR}}{dT} \approx T, \propto U_{\text{over}}$	$1.7 \cdot 10^6$
PDE	$\frac{\times 2}{5\ \text{K}}$	50 kc/s/mm <sup>2</sup>
cross-talk	$U_{\text{over}}$	40 %
after pulse	$U_{\text{over}}$	3 %
SPTR	$U_{\text{over}}$	< 1 %
		FWHM : $\mathcal{O}(200\ \text{ps})$

occur with a delay in the order of several 10 ns.

Cross-talk in SiPM is reduced by the introduction of trenches between pixels which are opaque for the infrared photons.

#### AFTER PULSES

If charge carriers are trapped during an avalanche and released during the recovery of the pixel, signals with non-unity gain occur. The signal amplitude in the same pixel depends on the pixel's recovery state.

#### 5.2.4 TIME RESOLUTION

The stochastic nature of SiPM signal generation, as well as non-uniformities in and between individual pixels, lead to an intrinsic time resolution for single photons. This Single Photon Time Resolution (SPTR) depends mainly on  $U_{\text{over}}$  and weakly on the photon's incident position within a pixel [87]. Measurements performed with the STiC ASIC of a Hamamatsu S13360 SiPM with a pixel size of  $50\ \mu\text{m} \times 50\ \mu\text{m}$  yield a time resolution of  $\text{FWHM} = (158 \pm 7)\ \text{ps}$  [88] at high overvoltage  $\mathcal{O}(10\ \text{V})$ .

### 5.3 SiPM COLUMN ARRAYS

Multi-channel SiPMs out of two dies each with 64 channel arranged in a one-dimensional array are utilized in the experiment to detect the scintillation light from the fibres. Each channel consists of 104 pixels with a size of  $57.5\ \mu\text{m} \times 62.5\ \mu\text{m}$  arranged by a  $4 \times 26$  grid resulting in a channel area of  $230\ \mu\text{m} \times 1625\ \mu\text{m}$ . Figure 5.5 presents an equivalent circuit of one channel with  $N$  individual pixels [90]. They are separated by trenches of the fifth generation Hamamatsu low-crosstalk development (LCT5). The channels have a pitch of  $250\ \mu\text{m}$ , and a gap of  $220\ \mu\text{m}$  separates the two dies in the centre of the sensor. They share a common cathode. The

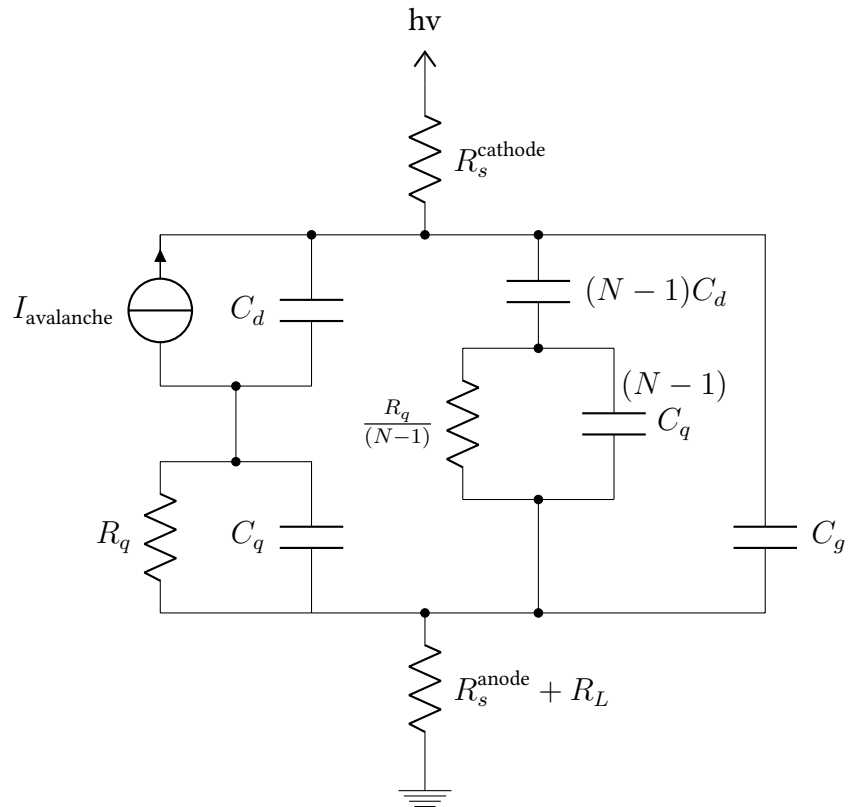


**Figure 5.5:** Equivalent circuit of a SiPM resulting from a large number of  $N$  parallel-connected Geiger mode APD cells from [89]. For Hamamatsu S13552 the variables show the following values:  $N = 104$ ,  $C_d = 115$  fF,  $C_1 = 18$  fF,  $C_g = 1$  pF,  $R_q = 470$  k $\Omega$ ,  $C_s^{\text{cathode}} = 0.5$   $\Omega$  and  $C_s^{\text{anode}} = 1.5$   $\Omega$  from [90].

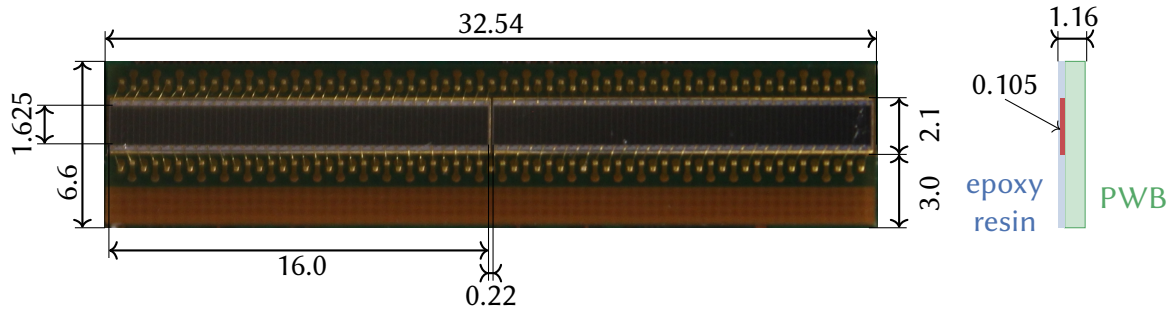


**Figure 5.6:** Picture of a Hamamatsu S13552-HRQ SiPM column array (left) and a schematic side view (right). All dimensions are given in units of mm. 24 such sensors are used in the Mu3E fibre detector.

sensors are delivered wire bonded to a Printed Wiring Board (PWB) with solder pads on the backside and covered with a 105  $\mu\text{m}$  thick epoxy resin. Figure 5.6 shows such an assembly.

The Hamamatsu 11.2016 S13552-HRQ SiPM was developed by a collaboration of HAMAMATSU, the LHCb collaboration and CERN for the LHCb scintillating fibre tracker. The LHCb collaboration characterised this sensor in great details [91]. Table 5.2 summarizes its key numbers.

#### 5.4 RADIATION DAMAGE IN SILICON PHOTOMULTIPLIERS

Radiation damages silicon-based detectors through two different mechanisms. Locally distorted silicon lattice in the bulk causes states with new energy levels. The most common displacement is the displacement of an atom from a regular lattice position to a usually not occupied spot, called Frenkel displacement. In silicon, the energy of this pair, the vacancy and the atom at an interstitial site, is 21 eV. This increases the dark count rate and the after-pulsing due to changes in the charge collection. Damage of this type is proportional to the non-ionizing energy loss (NIEL) in the bulk material, which is a small fraction of the energy loss of low energy, a few MeV, electrons. Photons with energy below 300 keV and electrons with energy below 255 keV generate no damage in the bulk. The effects of ionisation, the much larger fraction, is fully reversible in the conducting bulk and causes no damage.

The second damage mechanism occurs on the sensor surface in the thin dielectric silicon oxide layer where ionisation creates electron-hole pairs. Not all pairs recombine, but the electrons escape the oxide which causes an accumulation of positive charge. Some of the remaining holes accumulate at the silicon to silicon oxide interface and generate traps. This leads to additional surface currents, which increases the leakage current. Surface damage is proportional to the ionisation energy loss in this layer.

The extrapolation of radiation damage from measurements to the device performance in the experiment has to be separated in bulk and surface damage due to their very different mechanisms. The deposited dose in the thin, a few to hundred nanometers thick, silicon dioxide layer causes surface damage. Bulk damage extrapolation bases on NIEL in the full, roughly 300  $\mu\text{m}$  thick, silicon crystal. The damage in the lattice, consisting of displacement of atoms, is

**Table 5.2:** SiPM (S13552-HRQ) characteristics at  $\Delta T = 3.5 \text{ V}$  and  $T = 25 \text{ }^\circ\text{C}$  from [91].

characteristic	value
breakdown	51.0 V
variation per sensor	$\pm 250 \text{ mV}$
variation between sensors	$\pm 500 \text{ mV}$
temperature coefficient	53.7 mV/K
gain	$3.8 \cdot 10^6$
direct crosstalk	3 %
delayed crosstalk	2.5 %
after-pulse	0 %
peak PDE	48 %
max PDE wavelength	450 nm
mean quench resistance $R_Q$	490 k $\Omega$ at 25 $^\circ\text{C}$
recovery time $\tau_{\text{recovery}}$	$(68.9 \pm 2.1) \text{ ns}$
short component $\tau_{\text{short}}$	$< 1 \text{ ns}$
long component $\tau_{\text{long}}$	$(50.1 \pm 4.1) \text{ ns}$

caused by Primary Knock-on Atom (PKA) with recoil energy  $E_R$  below  ${}^2E_R^{\text{max}}$ . In the case of electrons, Coulomb scattering is the main PKA production process. The lattice damage caused by them can be expressed by the displacement damage function [92]

$$D(E) = \sum_{\nu} \sigma_{\nu}(E) \cdot \int_0^{E_R^{\text{max}}} f_{\nu}(E, E_R) P(E_R) dE_R, \quad (5.3)$$

where  $\nu$  are all possible interactions of a particle with the energy  $E$  leading to a displacement of an atom in the silicon lattice.  $\sigma_{\nu}$  is the cross section for such a process,  $f_{\nu}(E, E_R)$  the probability for a PKA with the energy  $E_R$ . The Lindhard partition function  $P(E_R)$  describes the portion of recoil energy that is deposited in the form of displacement damage [93]. It is conventional to express bulk damage relative to the damage that would be caused by a given flux of 1 MeV neutrons ( $n_{\text{eq}}$ ), which show total kinetic energy release in silicon of 95 MeVmb. Figure 5.7 shows the damage function of electrons as a function of kinetic energy.

Under the assumption of a 100 nm thick silicon oxide layer and a bulk thickness of 300  $\mu\text{m}$  the deposited energy dose in the oxide layer and the NIEL in the Mu3E fibre detector's SiPM bulk is extracted from simulation. This is needed to extrapolate the detectors performance during operation. At a muon stopping rate of  $1.0 \cdot 10^8$  muon/s, the sensors experience a particle rate through their volume of  $(116 \pm 10) \cdot 10^3/\text{s}$  in the upstream located sensors respectively  $(82 \pm 8) \cdot 10^3/\text{s}$  in the ones located downstream consisting of one third electrons, two thirds positrons and below 0.2 % photons. This rate divides over the sensors 128 channels respectively

---

${}^2E_R^{\text{max}} = 2 \frac{E_k + 2m_p c^2}{M c^2} E_k$  where  $E_k$  is the kinetic energy of the incoming particle,  $M$  the mass of the silicon atom and  $m_p$  its rest mass.

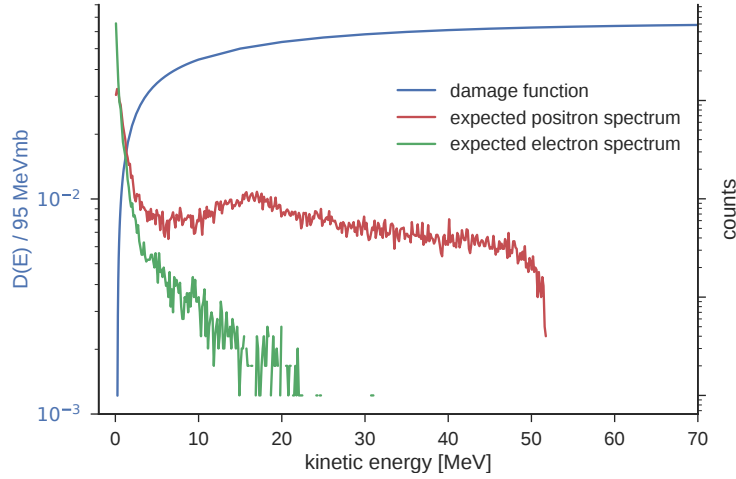


**Figure 5.7:** The relative bulk damage ( $\rightarrow$ ) due to lattice displacements with respect to 1 Mev neutrons ( $n_{eq}$ ) as a function of the particles kinetic energy from [94] in combination with the expected energy spectrum of electrons ( $\rightarrow$ ) and positrons ( $\rightarrow$ ) in the fibre detector's SiPM arrays.

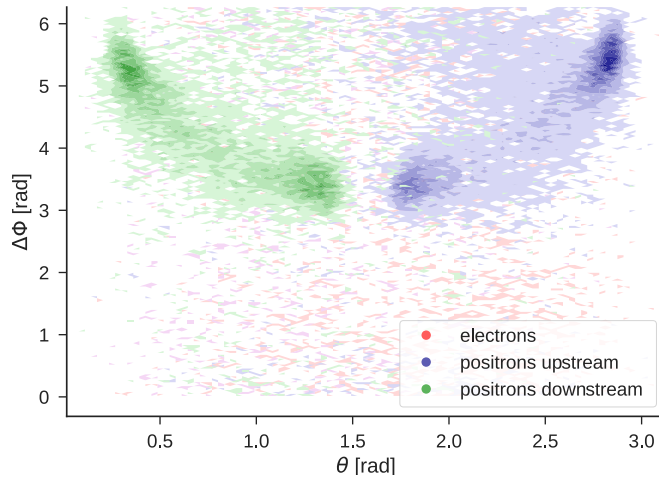


**Figure 5.8:** Expected incident angles of electrons ( $\bullet$ ) and positrons on the up ( $\bullet$ ,  $\Theta > \pi/2$ ) and down stream ( $\bullet$ ,  $\Theta < \pi/2$ ) side in the SiPMs.  $\Delta\Phi$  is given with respect to the sensor's column orientation.

an area of  $32 \text{ mm} \times 1.6 \text{ mm} = 51.2 \text{ mm}^2$ . Due to the location of sensors and the experiment's event topologies, most of the tracks penetrate the SiPMs not perpendicular to the active surface. Figure 5.8 shows the expected incident angles of electrons and positrons. The particle's kinetic energy spectrum is presented in Figure 5.7. In  $1 \cdot 10^7 \text{ s}$ , corresponding to 116 d, of beam time, roughly one year of operation, a dose of  $(263 \pm 71) \text{ Gy}$ ,  $(184 \pm 68) \text{ Gy}$  respectively, is accumulated in the silicon oxide layer. In the same time period the neutron equivalent fluence<sup>3</sup> of  $(3.45 \pm 0.18) \cdot 10^{10} n_{\text{eq}}/\text{cm}^2$ ,  $(2.45 \pm 0.07) \cdot 10^{10} n_{\text{eq}}/\text{cm}^2$  respectively, through the bulk is acquired.

#### 5.4.1 EXPECTED RADIATION DAMAGE FROM LITERATURE

Whereas in most SiPM applications with significant radiation either signals of hundreds of photons are detected or the sensors are operated well below room temperature, in Mu3E single photons are detected at room temperature. Many irradiation studies have been conducted by different groups with different applications in mind. For applications with hundreds of photons the focus is on dark current behaviour as a function of irradiation. Due to the fact that radiation damage in the oxide layer increases the leakage current but does not increase the dark current rate, but displacement damage in the bulk increases both, the extrapolation from dark current to dark count rate, even with known gain, is not possible. The irradiation of Hamamatsu S10362-11-050C with x-rays below 300 keV, causing only damages in the oxide layer, shows a significant increase of dark current but no significant increase of the dark count rate, below 10 %, up to an irradiation dose of 20 kGy [95]. For higher doses, up to 20 MGy, significant dark count rate was observed. It has been demonstrated that the increase in dark current is independent if the sensors are biased or not during irradiation for Hamamatsu devices [96]. Furthermore, the dark count rate as a function of overvoltage scales globally with irradiation, it shows the same dependency [96]. The annealing with respect to the dark current shows an exponential behaviour in temperature of  $\tau_{\text{annealing},0^\circ} = 40 \text{ d}$  at  $0^\circ \text{C}$  and a decay constant of  $\lambda = -0.096 \text{ d}/^\circ\text{C}$  [96]. The signal degradation is below 10 % for irradiations up to  $1 \cdot 10^{10} n_{\text{eq}}/\text{cm}^2$  [97]. It is observed that irradiation degrades the uniform gain of all pixels [98, 99], which corrupts the characteristic step behaviour of the dark count rate as a function of the threshold, used for calibration. In comparison of different sensor vendors, Hamamatsu devices usually perform best with respect to dark current as a function of irradiation [96, 100, 101]. No significant drop in PDE is observed. The LHCb collaboration performed extensive irradiation studies with the same sensors used in the Mu3E experiment. The characterisation, in particular dark current measurements, are performed around  $-40^\circ \text{C}$ , far below the operation temperature in Mu3E. Thus, an extrapolation is not trivial.

#### 5.4.2 OBSERVATIONS

First irradiations with a MBq  $^{90}\text{Sr}$  source show a linear dependency of DCR. Figure 5.9 show this dependency as a function of 1 MeV neutron equivalent fluence. As expected, the irradiation with x-rays with an energy below 60 MeV cause no increase in DCR. The rate is obtained

<sup>3</sup>integrated flux.

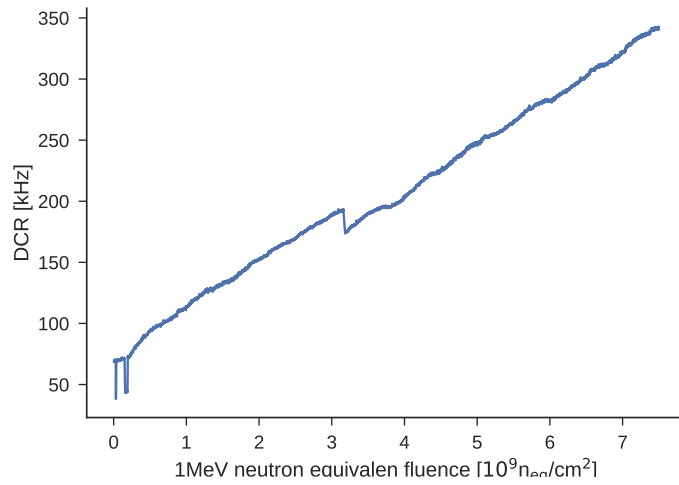


**Figure 5.9:** DCR of Hamamatsu S13360-1350PE as a function of irradiation by a  $^{90}\text{Sr}$  source at room temperature. The presented rate is corrected for temperature variations; the bias voltage is kept constant. At  $\sim 3.2 \cdot 10^9 n_{eq}/cm^2$  the sensors annealed at room temperature for  $\sim 10$  days. Courtesy of L. Gerritzen.

by a discriminator with a fixed threshold at the 0.5 photoelectron level of the not irradiated sensor. No significant loss in signal amplitude is observed.



# 6

## SiPM Readout Electronics

The electrical signals from SiPM are either pre-amplified and read out by application-suited digitizers or directly by dedicated ASICs. For detector R&D the combination of pre-amplifier and waveform digitizers, for example, the Domino Ring Sampler (DRS4) chip (see section 6.2), provide the most insight into the investigated systems. Dedicated ASICs allow in general to build more compact and power-efficient multi-channel systems tailored to an experiment's needs.

This chapter gives an overview of available SiPM readout ASICs followed by a more detailed description of DRS4, STiC and MuTRiG ASICs which are used in the scope of this thesis.

### 6.1 STATE OF THE ART SiPM READOUT ELECTRONICS

The available SiPM readout electronics can be grouped in two main classes. Firstly, chips that comprise only the front-end which typically contains amplification stages and consequent discrimination. These chips need additional digitization; pre-amplification might be required. Secondly, mixed-mode ASICs which combine the front-end with signal processing, digitization and fast serial transmission. It is very challenging to suppress common mode noise from digital chip parts in the analogue input-stages. Mixed-mode chips for Time of Arrival (ToA), Time over Threshold (ToT) and charge measurement exists. Table 6.1 lists different available SiPM readout ASICs.

#### READOUT ELECTRONICS FOR THE SCINTILLATING FIBRE DETECTOR

The Mu3E scintillating fibre detector requires the digitization of the ToA at a single photon level where very little space is available. Furthermore, the readout electronics has to cope with 650 MHz signal from particles crossing the detector in combination with up to about 300 MHz DCR on a single photoelectron trigger level. Due to the space constraints, the usage of a mixed-mode ASIC is required. None of the available chips was initially able to handle the required rates. MuTRiG was developed within the Mu3E collaboration based on STiC to fulfil

**Table 6.1:** Overview-of-state of the art SiPM readout ASICs. The abbreviations  $T_{0A}$  and  $T_{0T}$  stand for Time of Arrival, respectively Time over Threshold. The ASICs are grouped according to their field of application.

type	ASIC family	description/comment
ToA & ToT	STiC/MuTRiG [102, 103] PETA [104–106] TRIROC [107]	MuTRiG evolved for Mu3E for PET, sensor-ASIC hybrids available limited rate capability
ToA & charge charge integration	TOFASIC [108, 109] KLauS [110, 111] VATA [112] SPIROC [113]	focus on PET, max 600 kHz/channel  no sufficient time information
only front-ends	BASIC [114] FLEXTOT [115] PETRIROC [116, 117] NINO [118, 119] CITIROC [117] DRS4 [120]	additional ADCs required    waveform sampling

the detectors requirement and is described in more detail in section 6.3. The tile sub-detector uses the same SiPM readout chip.

## 6.2 THE DRS4 ASIC

The DRS4 [120] chip is a switched capacitor array based digitizer chip with nine input channels able to handle up to 5 gigasamples per second with an array depth of 1024 capacitors. It has an input bandwidth of 850 MHz. Samples of the analogue waveforms are stored in a series of capacitors which are enabled successively. The so-called Domino Wave, generated by the delay of a series of inverters, opens the switches to the 1024 capacitance of one channel in circular sequence. Small internal mismatches of capacitances in the inverters introduce cell-dependent variations in the sampling bin widths. The speed of this wave is locked via a Phase Locked Loop (PLL) to an external reference clock. A trigger stops the propagation of the Domino Wave and therefore the sampling. An external Analog to Digital Converter (ADC), typically an octal AD9222 operating at 64 Msps, is used to digitise the waveforms. Flexible cascading schemes allow combining multiple channels and chips to increase the waveform depths. Furthermore, one of the nine channels is usually used to digitise a global reference clock for calibration [120].

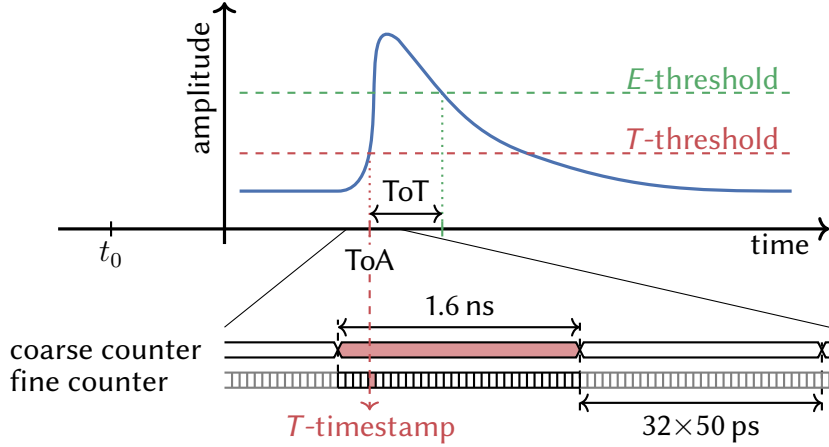


**Figure 6.1:** Sketch of the STiC and MuTRiG functionality. The analogue signal from a SiPM (—) is discriminated by a “time”  $T$ - and an “energy”  $E$ -threshold. The ASIC digitizes the relative time with respect to a common reset  $t_0$  of the rising edge at the  $T$ -threshold and the falling edge at the  $E$ -threshold into a  $T$ - and an  $E$ -timestamp. These timestamps comprise a 1.6 ns course counter which is divided into 32 fine counter states, corresponding to bins with a mean width of 50 ps. The  $T$ -timestamp corresponds to the signal’s Time of Arrival ( $T_{oA}$ ). The difference of the two timestamps provides a linearized Time over Threshold ( $T_{oT}$ ). It is possible to suppress signals which do not pass the  $E$ -threshold.

### 6.3 THE STiC AND MuTRiG ASICS

STiC and MuTRiG are custom mixed-mode ASIC in  $0.18\ \mu\text{m}$  CMOS<sup>1</sup> technology developed at the Kirchhoff Institute for Physics at the University of Heidelberg. The chip was originally developed under the name STiC (v3) for Positron Emission Tomography (PET) applications within the scope of the ENDOFOPET-US project. Its successor MuTRiG consists of the identical analogue front-end and Time-to-Digital Converter (TDC) in combination with a new digital part adjusted to the requirements of the Mu3E experiment, in particular, faster digital links.

Figure 6.1 sketches the functionality of this ASIC. The analogue signals from SiPM is discriminated by a lower “time”  $T$ - and an higher “energy”  $E$ -threshold. The ASIC digitizes the relative time with respect to a common reset  $t_0$  of the rising edge at the lower  $T$  threshold and the time of the falling edge at the higher  $E$ -threshold into a  $T$ - and an  $E$ -timestamp. The  $T$  timestamp corresponds to the signal’s  $T_{oA}$ . The difference of the two timestamps provides a linearized  $T_{oT}$ . These two timestamps are the output of the ASIC. In the MuTRiG version, it is possible to substitute the  $E$ -timestamp by a single flag which indicates if the signal has passed the  $E$  threshold. This reduces the size of a MuTRiG event which allows for higher event rate at same link speed, in particular to reach the required  $1.1\ \text{MHz/channel}$ <sup>2</sup>. Since the ASIC was initially developed for PET applications, with large signals and the need to suppress single photon noise, a optional signal validation by the  $E$ -threshold can be imposed. In this case, only

<sup>1</sup>Complementary metal-oxide-semiconductor.

<sup>2</sup>Before  $\sim 40\ \text{kHz/channel}$

signals passing this threshold are processed in the digital part and transmitted off-chip. This suppresses the sensors' dark signals.

The chips provide a single 8b/10b [121] encoded LVDS link running at 160 Mbps in the case of STiC and at 1.25 Gbps for MuTRiG.

### 6.3.1 THE ANALOGUE PART

The ASICs comprise a current sensitive low impedance analogue front-end which allows for a differential or single-ended connection scheme of detectors and positive as well as negative signal polarities. The voltage at the positive input terminal can be adjusted in a range from 100 mV to 900 mV with respect to ground which allows a individual adjustment of the bias voltage of attached SiPM. Subsection C.1.1 provides a detailed description of the analogue front-end.

The  $T$ -threshold can be adjusted around the single photon level, whereas the  $E$ -threshold covers a much larger range up to typical SiPM saturation levels. Both thresholds can be used for both signal polarities. Subsection C.1.2 describes the implementation of the thresholds in the ASIC.

### 6.3.2 TIME-TO-DIGITAL CONVERTER

The  $T$ - and the  $E$ -timestamps are digitized by the same Time-to-Digital Converter (TDC) unit. They comprise a 1.6 ns course counter part which is divided into 32 fine counter states. An example of a timestamp is presented in Figure 6.1.

The STiC's and MuTRiG's TDC, developed and characterized by [122], is based on a Phase Locked Loop with a 16-stage Voltage Controlled Oscillator. The coarse counter is driven by the PLL output, whereas the fine counter part is defined by the Voltage Controlled Oscillator (VCO) state. The logic signal propagation through the 16 delay cells with a mean delay of  $\hat{\tau}_d$  each, is inverted at the last element and fed back. This results in a coarse counter clock of  $32 \hat{\tau}_d$  and 32 different VCO states. In this way, the fine counter divides each coarse counter bin into 32 sub-bins. If the TDC is triggered, the coarse counter, as well as the VCO state, are latched. To stabilize the PLL and allow for the synchronization of multiple such devices, it is locked to an external reference clock.

STiC, with its 64 channels, comprises two PLLs, one for 32 channels each. The 32-channel MuTRiG contains only one. In both cases, the VCO is designed for a frequency of 625 MHz. This results in coarse counter bin width of 1.6 ns and mean fine bin width of 50 ps. Figure 6.1 shows an example of a timestamp consisting of this two counters. It is possible to trigger the TDCs by an external pulse. The dead time of the TDC is  $\sim 40$  ns (see subsection 11.2.2).

### THE COARSE COUNTER

The coarse counter is a 15 bit Linear Feedback Shift Register (LFSR). Since the coarse counter is in principal unstable during the switching of two states, two states are always latched. One at the rising and one at the falling edge of the coarse counter clock. Depending on the fine counter state, the stable state is selected in the chip's digital part.

### THE FINE COUNTER: DIFFERENTIAL NON-LINEARITY

Although the VCO keeps the sum of all delay elements  $\sum_i \tau_{d,i} = 32 \cdot \hat{\tau}_d$  very stable, the individual delay of each cell varies from cell to cell. This corresponds to different fine bin width for each state. This difference of an individual cell concerning the mean is called Differential Non-Linearity (DNL). The misalignment of a specific bin  $i$  is given by the sum of the  $DNL_i$  of all previous delay cells.

In the digital part of the ASIC, the 32 bit VCO state, represented by a unary code counter, is mapped to a 5 bit binary number. If the code is invalid, in detail, if it comprises not of a single consecutive sequence of ones followed by zeros, a flag (bad hit) is raised.

### 6.3.3 DATA TRANSMISSION AND SLOW CONTROL

In standard MU3E fibre detector operation mode event validation by passing the  $E$ -threshold is switched off. A detailed description of the on-chip event building and arbitration is given in subsection C.1.3.

The STIC and MUTRIG data transmission is frame based. Default events comprising a  $T$ - and an  $E$ -timestamp and have a size of 48 bits, whereas short MUTRIG events consisting of a  $T$ -timestamp and an  $E$ -flag have a reduced size of 27 bits. The latter is used for the fibre sub-detector. A description of the data format of the frames can be found in subsection C.1.5. Both ASICs are configured through a Serial Peripheral Interface (SPI) interface. In MUTRIG, an additional slow control interface allows to read out the number of events per channel per millisecond, which is latched in the Channel Event Counter (CEC).

### 6.3.4 RESET SCHEME

The current version of MUTRIG has two single-ended reset lines. The CHANNEL RESET which sets the coarse counter to zero as long as active. This reset can be exploited for synchronization of multiple ASICs and sub-systems. The CHIP RESET's effect depends on its length. A reset signal which is active for only one system cycle, e.g. 8 ns has the same behaviour as the CHANNEL RESET; it resets all the coarse counters. If it is active longer, it also resets the digital part, e.g. all the finite-state machines as well as the PLL.

Currently, the reset is synchronised to an internal 125 MHz system clock derived from the 625 MHz reference clock. Unfortunately, this leads to eight possible phases of the reset with respect to the input clock. It is foreseen to align the reset to the reference clock in future developments of the ASIC.



## **Part III**

# **Prototypes, Measurements and Simulated Performance**



# 7

## Scintillating Fibre Ribbons

To achieve the optimal design for the fibre detector, we have investigated different fibre materials, coatings and geometrical setups. In a first part, the requirements and constraints for the fibre ribbons are summarized in section 7.1. In a second part in section 7.2, this chapter briefly summarizes studies performed in the past which led to the latest set of prototypes. A third part describes in section 7.3 the characterization of this prototypes in a test beam in the scope of this thesis with the goal to find the optimal fibre, coating and setup for the experiment and extract properties required to extrapolate the sub-detector's response in the experiments simulation framework. This is followed by section 7.4 which discusses the impact of the presented measurements and provides a comparison with earlier results.

Different scintillating fibres types from two leading vendors, Kuraray and Saint-Gobain are available. A summary is given in Table 7.1. The emission spectra of two Kuraray types, SCSF-78 and SCSF-81, and one Saint-Gobain type, BCF-12, match the SiPM sensitivity spectra well and provide at the same time high light yield and long attenuation lengths. Furthermore, a novel R&D fibre, NOL-11, is investigated. The main differences deducible from the specifications between the fibre types are on the one hand the decay times which spread out from 1.1 ns for the novel NOL fibre up to 3.2 ns for BCF-12. On the other hand, square double-clad fibres are only available from Saint-Gobain. But as it turns out, light yield differences, which is not evident from the specification or literature, is more important than shape.

### 7.1 SCINTILLATING FIBRE RIBBON CONSTRAINTS

The MU3E fibre detector bundles the individual fibres to ribbons (see section 3.2) which are required to fulfil the requirements described in section 3.1. A time resolution better than 350 ps at very high efficiencies and as little material, more specifically low radiation length, as possible are targeted.

The use of high purity double clad fibres allows detecting sufficient photons for the required time resolution and high efficiencies. Both mentioned vendors provide such round fibres with a diameter of 250  $\mu\text{m}$ , 500  $\mu\text{m}$  and larger. Table 7.2 lists the fill factor inside a fibre ribbon for

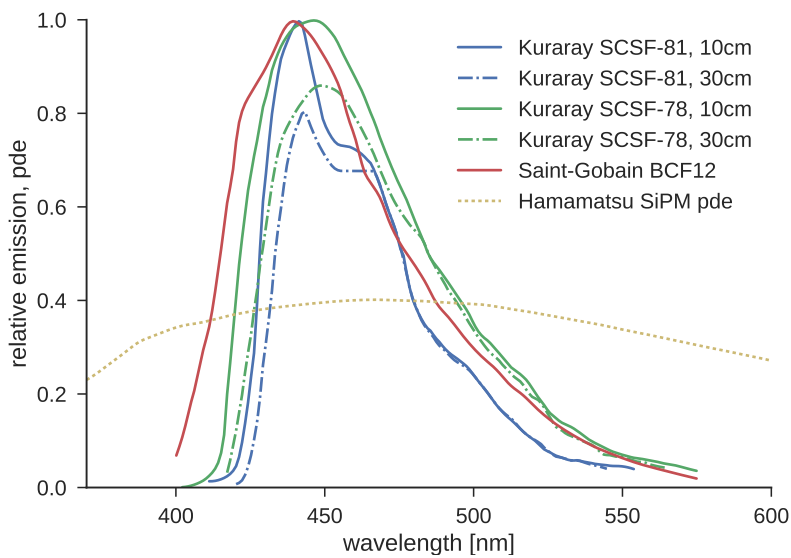


**Figure 7.1:** The emission spectrum of different fibres normalized to the peak amplitude of the closest measurement of each type. For Kuraray SCSF-81 (—) and SCSF-78 (—) the spectrum of 1 mm thick fibres at 10 cm (—) and 30 cm (---), which are presented *relative* to the first one, under an excitation by 370 nm and 350 nm, respectively [81]. The emission spectrum of Saint-Gobain BCF-12 is shown in (—) [123]. As a reference the photon detection efficiency of a Hamamatsu SiPM (S13360-50PE) at  $V_{\text{over}} = 3\text{ V}$  is overlaid (···) on the same axis [83].

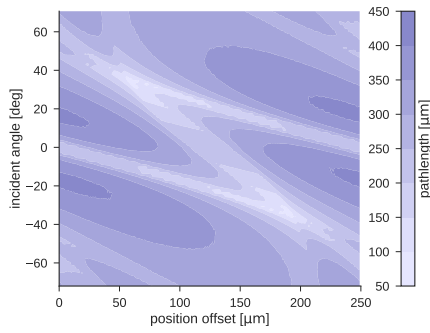
## 7.1. SCINTILLATING FIBRE RIBBON CONSTRAINTS

**Table 7.1:** Properties of different fibre types from Kuraray and Saint Gobain [81, 123]. NOL-11 is a R&D fibre with Kuraray involvement. Its properties are assumed to be very similar to the other Kuraray fibres. Light yield is only quoted by Saint-Gobain, whereas Kuraray characterises SCSF-78 and NOL-11 as “high light yield” fibres.

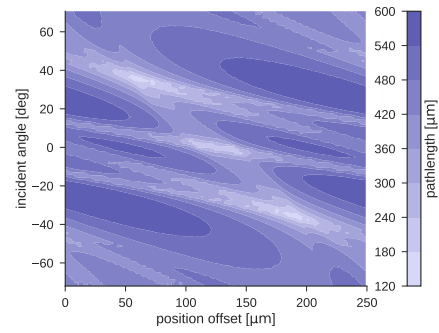
company type		Saint-Gobain	Kuraray		R&D
		BCF-12	SCSF-81MJ	SCSF-78MJ	NOL-11
emission peak	[nm]	435	437	450	
decay time	[ns]	3.2	2.4	2.8	1.1
attenuation length	[m]	>2.7	>3.5	>4.0	
light yield	[ph/MeV]	~8000		high	high
refractive index		1.60/1.49/1.42	1.59/1.49/1.42		
density	[g/cm <sup>3</sup> ]	1.05	1.05/1.19/1.43		
available shapes		round & square	round		round
cladding round	[%]	3/1	3/3		
square	[%]	4/2	-	-	-
trapping round	[%]	≥5.6	5.4		
square	[%]	7.3	-	-	-
core			Polystyrene (PS)		
inner cladding			Acrylic (PMMA)		
outer cladding			Fluor-acrylic (FP)		

**Table 7.2:** Ribbon fill factor of the fibres and the active core with respect to the full ribbon in different configurations.

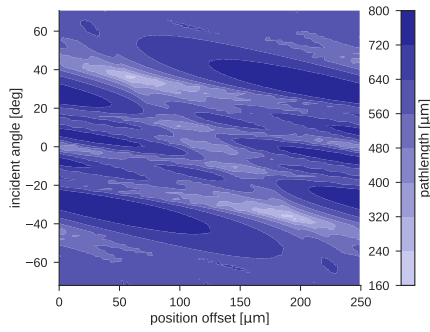
configuration layers	fibre $d$ [ $\mu\text{m}$ ]	fill factor [%]	
		fibres	active
2	250	84.2	74.4
3	250	85.8	75.8
4	250	86.6	76.5
2	500	84.2	74.4



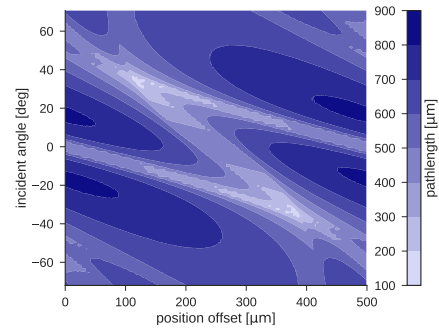
(a) 2 layers of 250  $\mu\text{m}$



(b) 3 layers of 250  $\mu\text{m}$



(c) 4 layers of 250  $\mu\text{m}$



(d) 2 layers of 500  $\mu\text{m}$

**Figure 7.2:** The particle's path length in the active fibre volume for different position offsets with respect to the fibre centre in the first layer and different inclination angles. The inclination angle is defined between a particle momentum direction and the ribbon's normal.

**Table 7.3:** Overview of scintillating fibre prototypes divided by class: square or round, and readout concept: a fan-out scheme to read out single fibres or the direct connection of a SiPM column array.

class	type		single fibre readout	SiPM column array
square	BCF-12	(bcf12)	[124]	[125, 126]
round	SCSF-81	(mj81)	[77]	here, [126]
	SCSF-78	(mj78)	-	here, [126]
	NOL-11	(nol11)	-	here, [126]
	BCF-12	(bcf12)	-	here, [126]

different configurations. The fill factor describes the ratio of the considered material, either the fibres or only the active scintillating core, to the total fibre ribbon volume. The particle path length inside the active volume is illustrated in Figure 7.2 as a function of the incident offset from the the centre of a peripheral fibre and incident angle in the transverse plane for different configurations assuming straight trajectories. The non uniform path lengths depending on incident position and angle are expected lead to non uniform fibre ribbon efficiencies. In the case of round fibres, the layers are offset by the fibre radius. This prevents particle trajectories entirely outside of the scintillation cores, optimizes the fill factor and simplifies the ribbon production. If square fibres would be used, different stacking configurations could be considered.

The utilization of fibres with a diameter of 250  $\mu\text{m}$  allows more flexibility in the design, in particular, 3 layer-configurations. The fibre ribbon design is described in more detail in section 3.2.

## 7.2 SCINTILLATING FIBRE RIBBON PROTOTYPES

The ribbon characterisation studies involve two different readout strategies and two different types of fibres prototypes, partially performed by different groups. In the earlier setups, the properties of single fibres within a ribbon were studied by individual readout of each fibre. Their performance was extrapolated to potential detector designs. A fan-out to individual detached SiPMs was required. Very detailed information can be found in [77, 124]. The second approach is the test of fibre ribbons directly attached to SiPMs column arrays. This allows the characterization of the detector as used in the experiment and concurrently simplifies the prototype production due to the omitted fan-out. On the downside, no insight into single fibre properties such as crosstalk nor simple extrapolation to alternative detector designs is obtained.

Three SiPM column array versions are used for the setup scheme where the scintillating fibre ribbons are directly attached to it; the Hamamatsu S10943-3183(x) [127], S13552 [128] and its successor S13552-HRQ [91]. The results presented in this thesis are obtained with the latter. This sensor is described in more detail in section 5.3. Even though S13552-HRQ

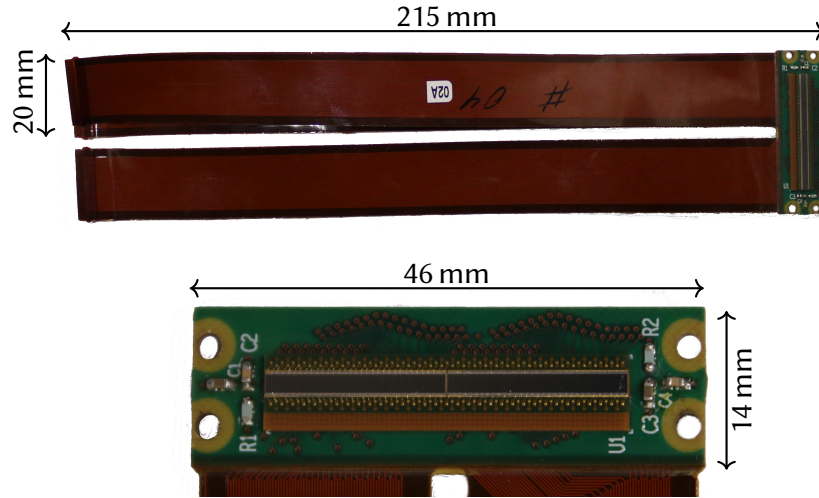


**Figure 7.3:** SiPM arrays bonded on a carrier PCB with integrated flex print cables. In the bottom part, the filter capacitors ( $C1$ - $C4$ ) and current limit resistors  $R1$  and  $R2$  are visible.

is the SiPM array version which will be used in the experiment<sup>1</sup>, the carrier Printed Circuit Board (PCB) with attached flex print is not. This flex print board on which the sensors are soldered is developed initially for a scintillating fibre tracker for incoming proton and heavy ion (Ar, Xe, Pb) beam particles in the NA61/SHINE experiment [129, 130]. Figure 7.3 shows the SiPM column arrays soldered on the flex print PCBs.

Furthermore, two different classes of prototypes have been investigated. A group based at PSI produced and characterised ribbons consisting of square fibres. This choice is driven by synergies with a feasibility study of an active target for the MEG experiment [131]. In general, square fibres show a better trapping efficiency and can be packed more densely. Since such square fibres are available only from Saint-Gobain, BCF-12 is the best-suited type for 250  $\mu\text{m}$  thick fibres with high light yield. Alternative BCF-20 could also be considered with an emission peak shifted by 57 nm with respect to BCF-12 into green at 492 nm, a decay time of 2.7 ns instead of 3.2 ns and an attenuation length  $>3.7$  m compared to 2.7 m [132]. Very detailed descriptions and characterizations of these prototypes consisting of square fibres with a single fibre readout can be found in [124]. In section 7.4 the results are summarized briefly and compared to other prototypes. Prototypes consisting of square fibres directly coupled to SiPM column arrays are under investigation. First results can be found in [126].

The second class of prototypes consists of round double-clad fibres. These ribbons are produced at the University of Geneva and consist of Kuraray fibres. The choice of Kuraray over Saint-Gobain is based on the experience with wavelength shifting fibres where Kuraray fibres are known to perform in general better. In a first approach SCSF-81MJ, the one with the shortest decay time of 2.4 ns at that time, were used. NOL fibres, which show an even shorter decay time of  $\mathcal{O}(1$  ns), became available only recently. These prototypes were tested in a

<sup>1</sup>and the LHCb experiment.

fanned-out configuration where single fibres are read out. A detailed description and studies can be found in [77]. A wider range of different fibre types such as Kuraray SCSF-81MJ, SCSF-81MJ, the novel R&D NOL-11 as well as round Saint-Gobain BCF-12 are tested in prototypes directly attached to SiPM column arrays. Table 7.3 gives an overview of the different prototypes divided by class, square or round, and readout concept: fan-out scheme to read out single fibres or the direct connection to a SiPM column arrays.

### 7.2.1 CONSTRUCTION OF SCINTILLATING FIBRE RIBBONS

Parallel to the fibre and fibre ribbon R&D, also the ribbon production has been optimized. Based on the tools and experience from the prototype production the final ribbons will be built.

Fibre ribbons consisting of round fibres are produced at the University of Geneva. A detailed description can be found in [126]. Two ribbons at the time are produced on a winding tool. The fibres are rewound from a large spool into Teflon coated U-channel where the fibres of the same layer are aligned next to each other. The ribbons are built up layer-by-layer. The amount of used glue, currently Araldite 2020, is minimized to increase the fibre ribbons fill factor. A holding structure (see section 3.2) is glued onto the fibre ends. The ribbons are cut and polished by diamond tools.

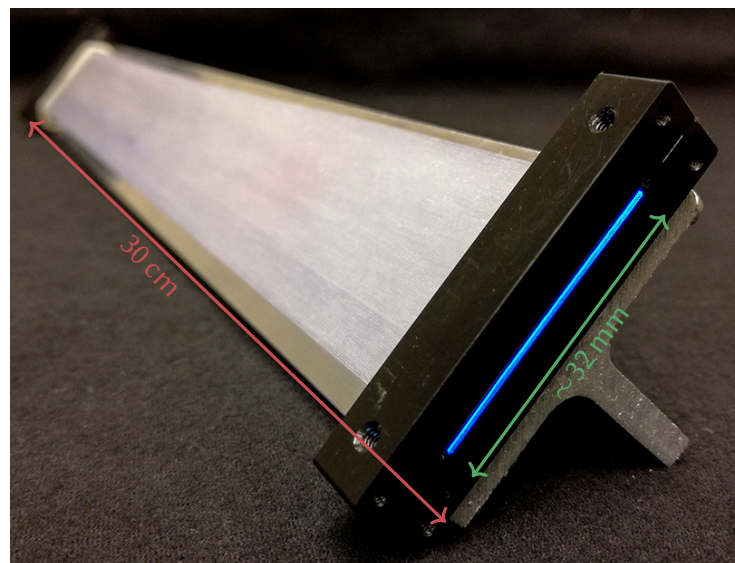
Figure 7.4 shows a full fibre ribbon prototype with dimensions close to the final ribbons in the experiment.

## 7.3 CHARACTERIZATION OF SCINTILLATING FIBRE RIBBONS

As described above, the MU3E fibre group has put a lot of effort into the characterization of fibres and fibre ribbons over the last years. This path led to the final design. Such most recent prototypes are directly, without any fan-out, coupled to the same SiPM column arrays which will also be deployed in the experiment. In the following, the characterization of such latest-version prototypes consisting of different fibre types in different configurations is described and their performance is extracted and compared.

### 7.3.1 THE RIBBON CHARACTERIZATION SETUP

The setup for ribbon characterization at the  $\pi M1$  beam line at PSI is depicted in Figure 7.5. It consists of scintillating fibre ribbons of different types, with different number of layers with a width of at least 8 mm, which corresponds to 32 fibres with a thickness of 250  $\mu\text{m}$ . The ribbons have a length of 30 cm. On both sides, they are directly coupled to SiPM column arrays of type S13552-HRQ. The geometric overlap of the 1.625 mm high sensor columns ensures the full coverage of the ribbon, which has a thickness below 1 mm. The edges of the ribbons are avoided by the trigger size in combination with a good alignment. The sensors are pressed slightly against the polished ribbons by four screws. No glue or additional grease is used for the fibre-sensor coupling.



(a) Full fibre ribbon prototype with preliminary holding structure.



(b) Front view of ribbon prototype with  $120 \times 3$  fibres round fibres of  $250 \mu\text{m}$  diameter.

**Figure 7.4:** Fibre ribbon prototype with dimensions close to final ribbons in the experiment. Picture from A. Damyanova.

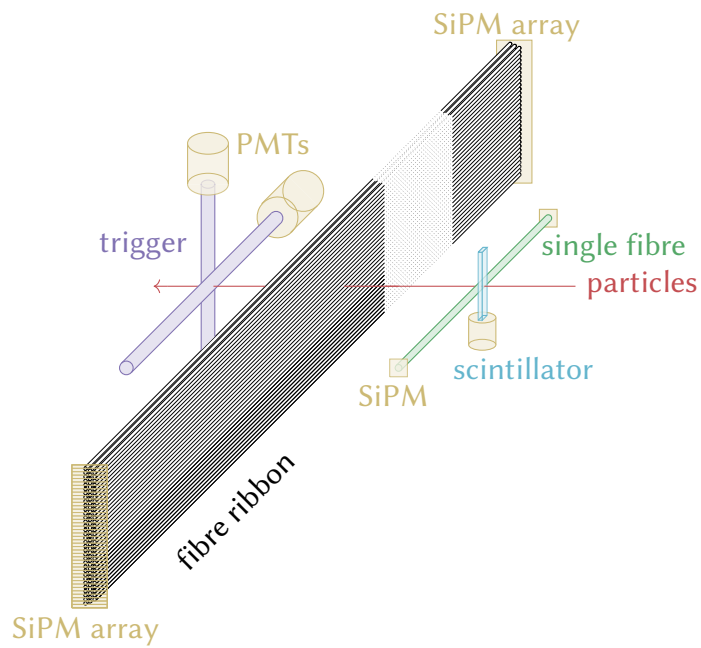


**Figure 7.5:** Scintillating fibre ribbon characterisation setup consisting of: the fibre ribbon (→) readout on both sides by SiPM column arrays (→), a trigger (→) out of 1 mm scintillating fibres read out by PMTs (→), a single 0.5 mm fibre (→) read out by single SiPM (→) and supplementary scintillator (→).

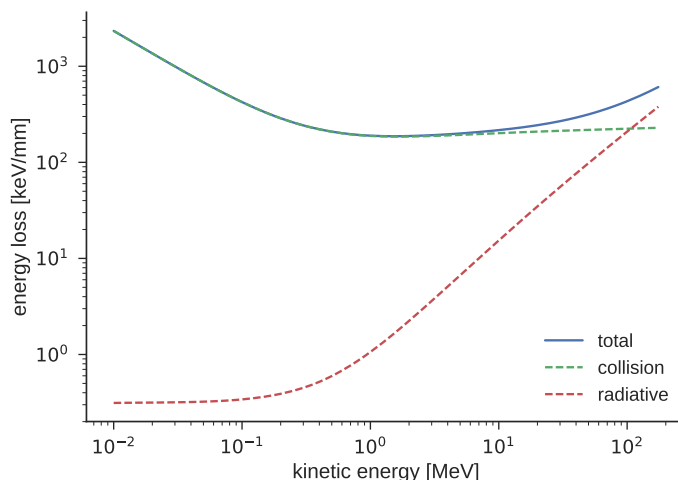


**Figure 7.6:** Energy loss, due to radiative effects (—), collisions (—), and total (—), of electrons in Polystyrene (PS) based scintillating fibres as a function of kinetic energy [133].

#### THE SELECTION OF MINIMUM IONIZING PARTICLES

The trigger consists of two crossed 1 mm thick round fibres read out by PMT located  $\approx 6$  cm behind the ribbon. The geometrical acceptance of  $\approx 1$  mm  $\times$  1 mm is much smaller than the readout width of the ribbon. This allows for scanning through the ribbon.

This additional scintillator behind the fibre ribbon ensures that particles from the beam penetrate the ribbon fully. The rejection of particles which stop in the ribbon ensures their MIP behaviour. Figure 7.6 shows the electron's energy loss per distance in Polystyrene, the core material of the used fibres. As long as the electrons or positrons penetrate the ribbon, their energy loss due to collisions, which leads to excitation and hence scintillation, scales linearly between 187 keV/mm for kinetic energies of 1.75 MeV up to 229 keV/mm at 150 MeV. The scintillation behaviour is almost uniform.

#### TELESCOPE CONFIGURATION

Optionally a single 0.5 mm thick round fibre read out on both sides by a single SiPM of type S13360-1375CS with an active area of 1.3 mm  $\times$  1.3 mm, as well as a small 5 mm wide scintillator read out by one sensor of the same type, is present  $\approx 3$  cm in the beam before the ribbon. These supplementary scintillators in front and the trigger behind the ribbon prototype with a small form factor, or a coincidence of multiple scintillators with a small geometrical overlap respectively, provide a vestigial telescope which allows for the extraction of efficiencies. It is possible to move the ribbon together with the supplementary scintillator vertically with respect to the trigger, what allows to scan through the ribbon. On the other hand, the trigger can be moved horizontally. The whole setup is horizontally movable to be aligned with the beam.

Note that, if the particle's kinetic energy is low, as in the case of radioactive sources, this method suffers from enhanced multiple Coulomb scattering and stopping of the particles.

### 7.3.2 THE SiPM READOUT SCHEME

In the setups where the full waveforms are digitised, fast transistor based three-stage common emitter circuit amplifiers developed in collaboration by UNIVERSITY OF GENEVA and UNIVERSITY OF ZURICH are used. In a single-ended readout scheme, a shunt resistor of  $R_{\text{shunt}} = 39 \Omega$  converts the SiPM's current signal into a voltage which is AC-coupled by a  $C = 100 \text{ nF}$  capacitance to the amplification stages. Simulations of the amplifier show a cut-off frequency of 400 MHz [77]. A variable gain in the order of 35 dB provides single photo-electron amplitudes of roughly 100 mV. Typical SiPM signals show a rise time of approximately 1 ns.

The waveforms are digitised with the DRS4 chip developed at PSI (see section 6.2). Either multiple daisy-chained four-channel evaluation boards also developed at PSI or a custom-made Versa Module Europa (VME) board designed by the UNIVERSITY OF GENEVA are utilized.

An example waveform from a ribbon consisting of 3 layer NOL-11 fibres without any additional  $\text{TiO}_2$  in the glue directly attached to a SiPM column array (S13552-HRQ) read out with the VME based DRS4 boards is shown in Figure 7.7. The raw ADC values of the 1024 sampling points are displayed on top. The bin width of each sampling cell is calibrated with a sinusoidal signal. The bin widths of the matching cells are shown right below. Furthermore, each cell is voltage calibrated. The corresponding voltage is given by

$$U = \frac{\text{adc} - \text{offset}}{\text{scaling}}. \quad (7.1)$$

The resulting calibrated waveform is plotted on top of the ADC values and corresponds to the response of a multiphoton event.

The need for cell wise calibration is illustrated in Figure 7.8 which shows a channel without a SiPM signal. On top, the raw ADC values are displayed. In the centre, this waveform is shown in the case where a constant bin width, as well as a cell independent voltage calibration, is applied. The baseline shows large fluctuations and two distinct levels. A cell-by-cell calibration, shown in the bottom, significantly reduces the noise levels and smooths the waveform. Different features are visible only in the calibrated waveforms. First, right before 25 ns, crosstalk induced from adjacent channels is observed. As shown in Figure 7.10 this position corresponds to the delay of SiPM signals with respect to the trigger. This crosstalk is assumed to be caused by a not optimal grounding scheme of the custom VME card. Second, two spikes around 50 ns and 80 ns can be observed. Such pairs of spikes with a fixed distance to each other are a known DRS4 feature and can be corrected for. Third, around 170 ns, calibration artefacts at the border of the ring buffer occur.

### DAQ JITTER AND COMMON REFERENCE SIGNALS

Discrete Nuclear Instrumentation Module (NIM) units discriminate the trigger signals from the PMT at a  $-50 \text{ mV}$  level. The logical AND of the two signals with a gate length of  $\approx 8 \text{ ns}$  is

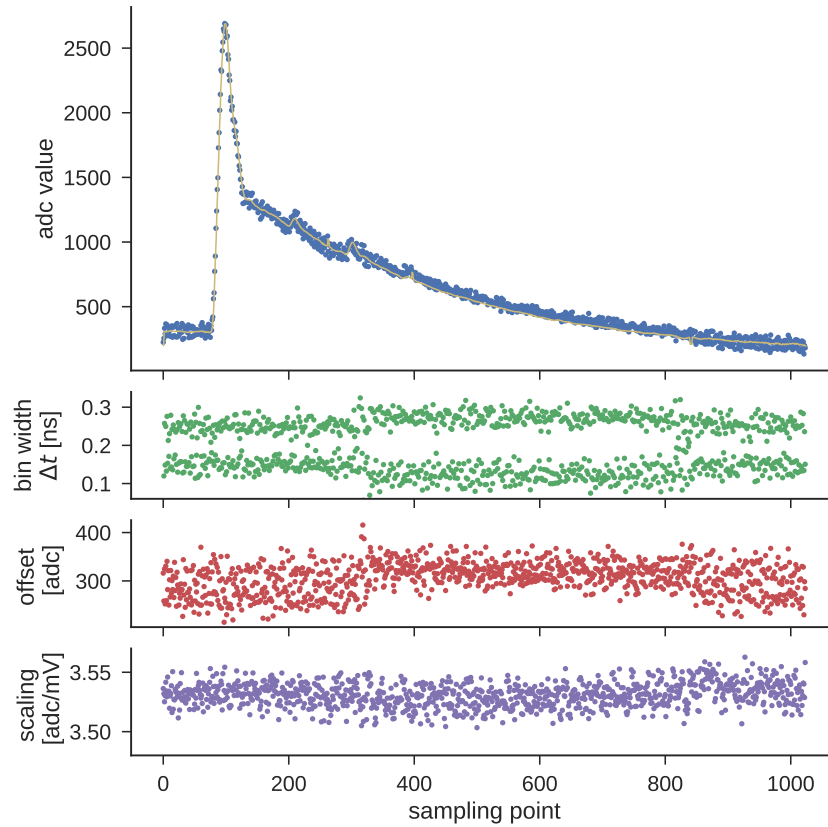


**Figure 7.7:** The ADC values of an exemplary 1024 sampling points long waveform containing a SiPM signal are shown on top ( $\bullet$ ). The corresponding calibrations are shown below: the bin width of each sampling point  $\Delta t$  ( $\bullet$ ) and the offset ( $\bullet$ ) along with the scaling ( $\bullet$ ) of the, per bin, ADC value to voltage calibration. For reference, the calibrated waveform ( $\text{—}$ ) is superimposed in the top figure.

**Table 7.4:** Jitter performance of the DRS4 based DAQ. One VME board hosts four ASICs. The time of the reference signal is extracted at 50% constant fractions.

type	jitter between	$\sqrt{\text{var}}$ [ps]
channel	trigger cell to reference signal (trigger)	$1139 \pm 10$
inter-board	reference signals of different VME boards	$1529 \pm 46$
same board	reference signals of different ASICs on the same board	$120 \pm 12$

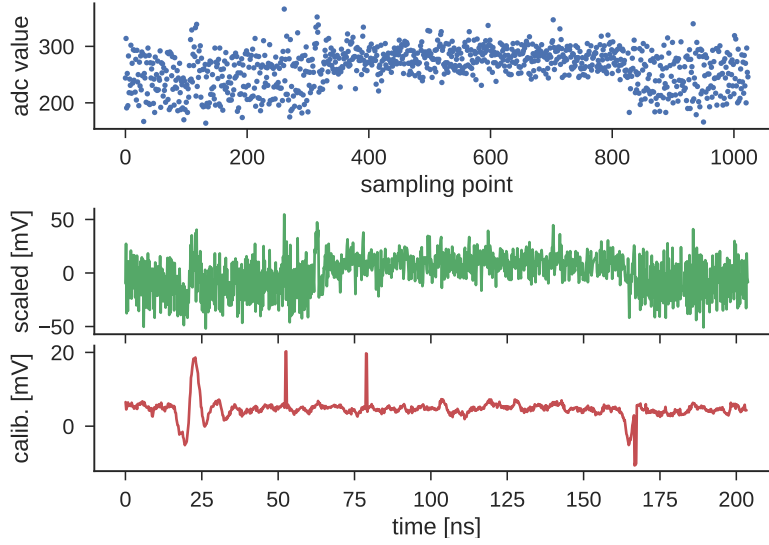
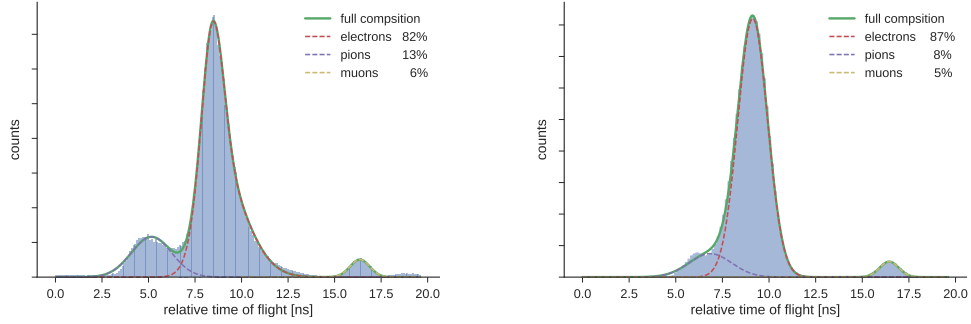


**Figure 7.8:** The ADC values for an exemplary baseline waveform without signal are shown on top (•). In the centre, the derived waveform (—) is shown, whereby a common scaling and offset are used for all 1024 bins. The same waveform exploiting a per bin calibration scheme is shown in the bottom (—).

used to trigger the DRS4-based DAQ. To ensure a consistent timing of this coincidence, one of the signals is delayed by 2 ns. The short gates reduce the probability of pile up at high beam rates. Without beam, the trigger rate is negligible. The signals from the SiPM are amplified and digitised as described in subsection 7.3.2. The actively split discriminated coincidence signal of the trigger is fed in one of the eight available channels of each DRS4 chip to provide a stable time reference. The jitter of the board internal synchronisation between the ASICs is summarized in Table 7.4. The time of the reference signal is extracted at 50 % constant fraction. The usage of split reference signals is essential for the extraction of time information below 1 ns resolution.

### 7.3.3 TESTBEAM AREA $\pi$ M1

$\pi$ M1 is a beamline with a nominal momentum range from 100 MeV/c up to 500 MeV/c, which provides electrons, muons and pions of both polarities. At an extraction angle of  $22^\circ$  particles are extracted from TARGET M in the PSI proton beam [134]. At low momentum, electrons and positrons dominate over pions. For negatively charged particles, the crossover is around 210 MeV/c, whereas for positive particles around 170 MeV/c. The muon contamination is below 5 % for  $\mu^-$ , respectively below 15 % for  $\mu^+$  [135]. The ribbon characterisation is performed with a beam momentum of 161 MeV/c of positive particles. At this energy 55 %  $e^+$ , 30 %  $\pi^+$  and 15 %  $\mu^+$  are expected. Protons are efficiently suppressed by a plastic block in the beam line. The distance from TARGET M to the setup is 21 m. The different time of flight of different



(a) testbeam 2017: discriminated RF signal      (b) testbeam 2015: sinusoidal RF signal [77]

**Figure 7.9:** Time of flight based particle type identification of pions (—), electrons (—) and muons (—) at a beam momentum of 161 MeV/c. The position of 0 is arbitrary.

particle types is exploited to distinguish them by recording the 50.63 MHz RF sinusoidal signal of the proton cyclotron’s accelerating cavities. This is illustrated in Figure 7.9 where the distribution of the time difference between the trigger signal and the RF is shown. Due to the cyclotron frequency, the pattern has a length of 19.74 ns with an arbitrary phase. The different particles are identified by the expected abundance. In the 2017 test beam campaign the discriminated RF signal is recorded, whereas in 2015 the sinusoidal signal was directly digitised. In Figure 7.9a an asymmetric combination of two Gaussian distributions is used to fit the electrons following [77]. All other contributions are fitted with a single Gaussian distribution.

### 7.3.4 ANALYSIS PROCEDURE AND PHYSICAL PROPERTY EXTRACTION

The recorded signals of a typical event of one ribbon side are presented in Figure 7.10. Five consecutive SiPM channels arranged around the cluster centre in channel 13 are shown. The majority of the photons arrive in coincidence and cause steep rising edges (*primary photons*). A few *late arriving photons* are visible in the signal tails (e.g. channel 14 at 75 ns) and also in the rising edges (e.g. channels 12 and 14). Furthermore, the sensors’ two different decay components manifest in all channels with a signal with a *kink*. *Crosstalk* from the high amplitude channels to all others channels causes the concurrent dip in channels 11 and 15 at the signal peak position around 20 ns. The timing of all channels on one DRS4 ASIC is determined with respect to a reference signal (ref) consisting of a copy of the split trigger signal. Spikes at the beginning of the waveforms, as in the reference signal, are a known DRS4 feature. The first and last ten cells are ignored in the analysis.

### DETERMINATION OF THRESHOLD LEVELS

The thresholds on signal amplitudes for each individual channels are calibrated with respect to number of detected photons relative to an event-wise baseline. The baseline consists of the mean of the waveform between 2 ns and 10 ns. The waveforms are integrated between

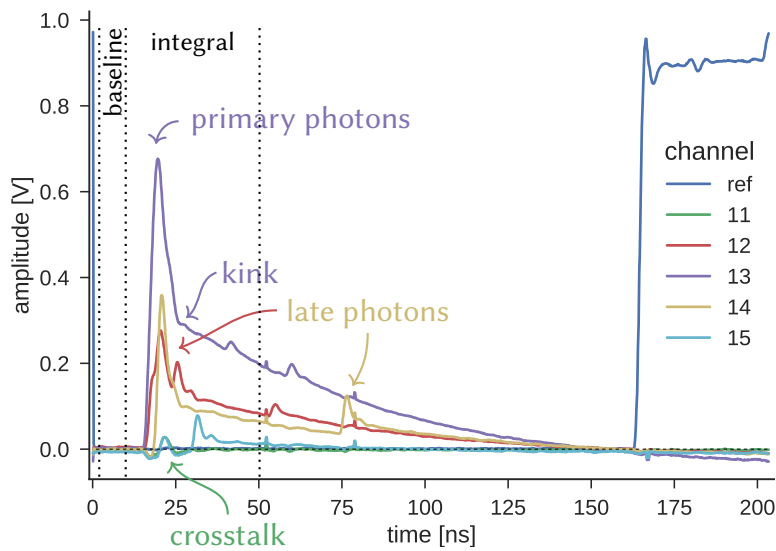


**Figure 7.10:** An exemplary event of a 3 layer NOL ribbon without additional coating at PSI test beam. The figure shows the calibrated waveforms of five consecutive SiPM array channels (11 to 15) arranged around the cluster centre in channel 13 (—) attached to one side of the ribbon, in combination with their reference signal (—) (i.e. trigger signal). The ranges in which the *baseline* and the *integral* are extracted are indicated.

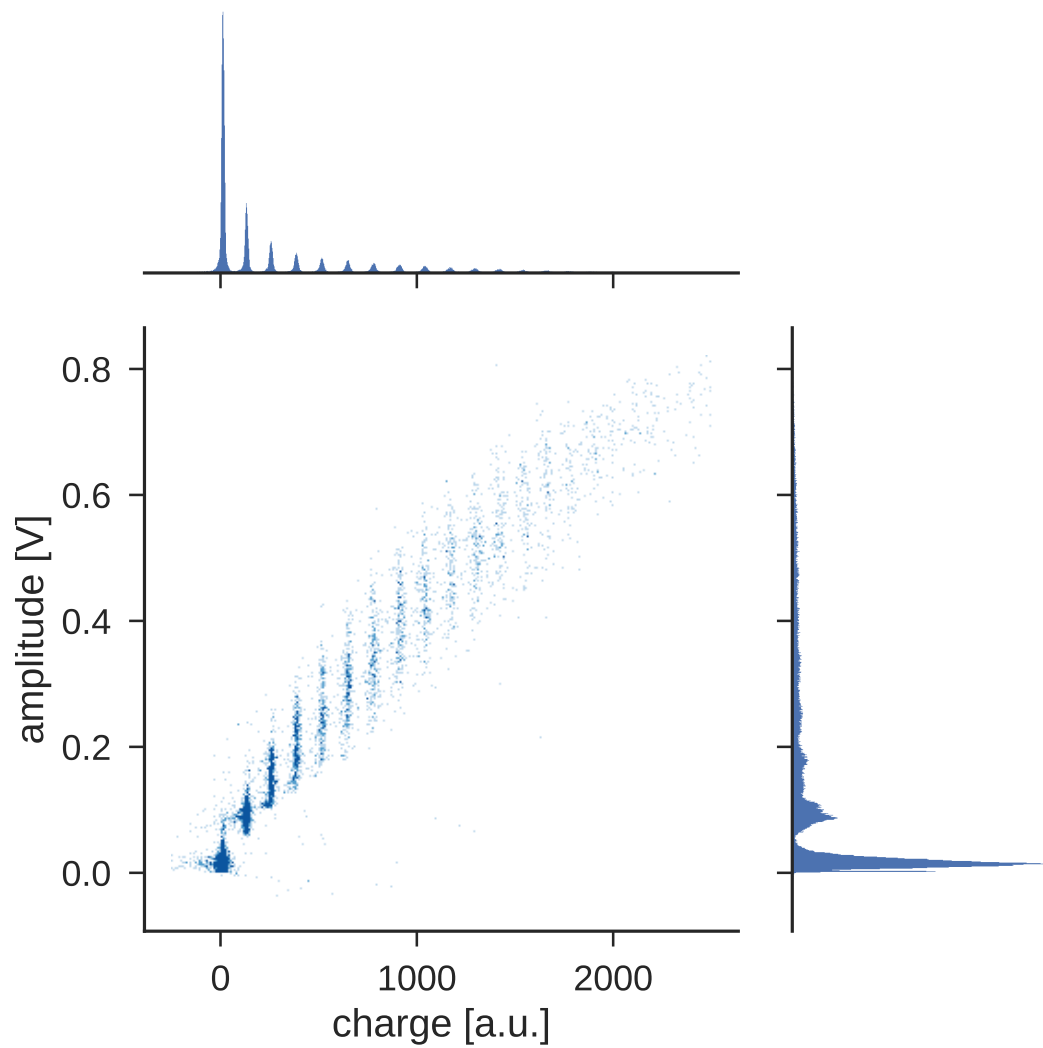


**Figure 7.11:** The 2D plot shows the charge versus amplitude distribution of a single SiPM channel (13) attached to one side of the ribbon. The fibre, to which this channel is attached to, is located inside the acceptance of the used trigger. On top and on the right side the respective projections are shown.

10 ns and 50 ns to obtain the charge. Both ranges are indicated in Figure 7.10. The strong correlation between the charge and the amplitude, as shown in Figure 7.11, is exploited to filter the amplitude spectra used for the threshold determination. Based on the charge, events with a certain number of photons are selected, thereby a Gaussian fit of the amplitude spectra yields the corresponding signal level. For a randomly selected run, a NOL ribbon with 3 layers and no additional coating, the amplitude uniformity between channels of the amplifiers on the board of one side is 5.3 % and 10.7 % on the other side. This is most likely caused by small variations in the amplifier bias voltages. The charge per detected photon, corresponding to the combined gain of the sensor and the amplifier, is determined by a linear fit of the “charge peak” positions, which are in turn extracted by fitting a Gaussian distribution to each individual peak. This procedure is applied to each channel. The residuals to the linear fit which show a standard deviation of 3.0 %, validate the linearity. The gain between channels shows an overall uniformity of 8.0 %. Based on this procedure the amplitude thresholds for 0.5 and 1.5 photoelectrons are determined per channel.

#### CLUSTERING AND TIME EXTRACTION

The scintillating light from a single particle crossing is spread over multiple SiPM columns. This effect causes signals in multiple neighbouring channels, see as example Figure 7.10 where all channels around 13 also show multiple photoelectron signals. Based on the thresholds of 0.5 or 1.5 photoelectrons, clusters are constructed out of adjacent channels which show an amplitude above the respective threshold. Although the extracted charge would provide a better discrimination of the number of detected photons, the amplitude is used to mimic the behaviour of the designated readout electronic of the experiment, the MuTRiG ASIC. Furthermore, the Time of Arrival (ToA) is extracted at the crossing of the same threshold as used for the clustering. The waveform is linearly interpolated between the closest sampling points on both sides of the threshold crossing. The best cluster time is given by the first detected photon, which corresponds to the smallest time within a cluster.

#### FIBRE RIBBON TIME RESOLUTION

The time resolution of a ribbon is determined by the distribution of the difference of the cluster time from both sides of the fibres  $t_{\text{left}} - t_{\text{right}}$ . This scheme allows measurement without an additional time reference. If the time resolution would show a purely uncorrelated Gaussian behaviour, the time resolution of a single side is given by

$$\sigma(t_{\text{side}}) = \frac{\sigma(t_{\text{left}} - t_{\text{right}})}{\sqrt{2}}. \quad (7.2)$$

If, moreover, the hit position in the fibre ribbon is known, for instance from pixel-based tracking or an external trigger, the propagation time in the fibres can be corrected for in first order ( $t'_{\text{side}}$ ). This yields a time resolution of the ribbon, assuming signals on both sides, of

$$\sigma_{\text{ribbon}} = \sigma\left(\frac{t_{\text{left}} + t_{\text{right}}}{2}\right) = \frac{\sigma(t_{\text{side}})}{\sqrt{2}} = \frac{\sigma(t_{\text{left}} - t_{\text{right}})}{2}. \quad (7.3)$$

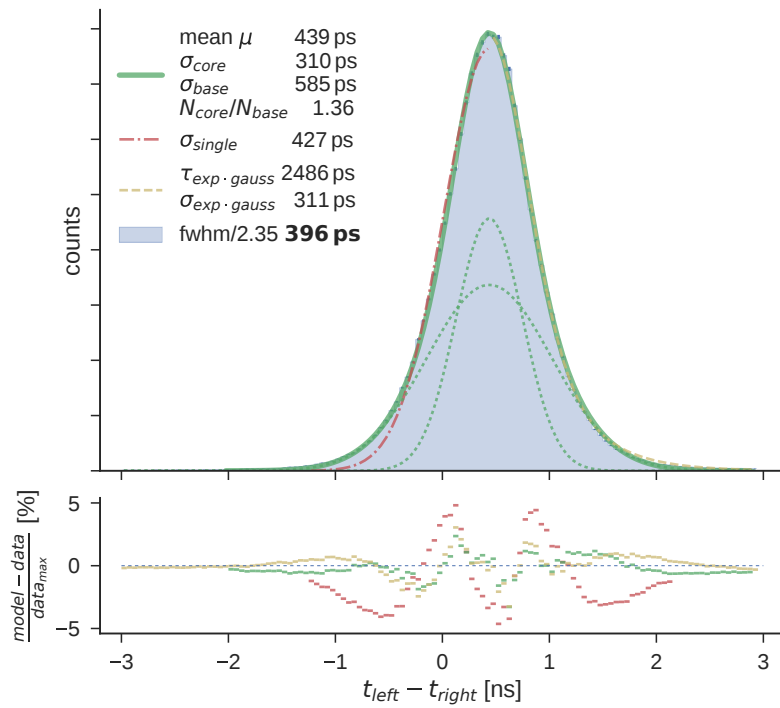


**Figure 7.12:** The distribution of the time difference between the left and the right ribbons side of matched clusters is shown in combination with different fit models: (—) a double Gaussian distribution with a common mean, the superposed distributions are also shown (⋯), (—) a single Gaussian distribution fitted within  $\pm 4\sigma$  around its mean, (—) an exponential distribution convoluted with a Gaussian one. The latter two are fitted symmetrically around the mean but are shown only on one half to enhance clarity.

### 7.3. CHARACTERIZATION OF SCINTILLATING FIBRE RIBBONS

**Table 7.5:** Time resolution of a 3 layer NOL-11 fibre without any additional coating extracted through different models and cuts: FWHM, a single Gaussian and the sum of two Gaussian with the same mean position with  $\sigma_{\text{core}}$  and  $\sigma_{\text{base}}$  in the ratio  $N_{\text{core}}/N_{\text{base}}$ . The time resolution depends on the applied amplitude threshold  $th$ , the required number of columns of each cluster per side  $cl$  and different timing extractions. The timing is determined either by leading edge  $le$  at 0.5 or 1.5 photoelectrons or constant fraction  $cf$  at 20 % or 50 %. In the last lines,  $cl$  mean, the cluster timing is extracted by averaging over all involved SiPM columns weighted by the number of photons ( $w$ ) and non-weighted.

th [phe]	cl ≤	timing	$\frac{\text{FWHM}}{2.35}$ [ps]	$\sigma_{\text{single}}$ [ps]	$\sigma_{\text{core}}, \sigma_{\text{base}}$ [ps]	$N_{\text{core}}/N_{\text{base}}$
0.5	1	le 0.5 phe	396	427	310, 585	1.36
0.5	2	le 0.5 phe	395	426	307, 578	1.30
1.5	1	le 0.5 phe	399	433	310, 601	1.37
1.5	1	le 1.5 phe	482	553	392, 763	1.31
1.5	2	le 0.5 phe	399	434	311, 606	1.41
1.5	2	le 1.5 phe	482	552	390, 758	1.12
0.5	1	le 0.25 phe	441	468	382, 659	2.13
0.5	1	cf 20 %	465	496	435, 756	3.85
0.5	2	cf 20 %	466	495	432, 738	3.55
0.5	1	cf 50 %	679	747	721, 1447	20.86
0.5	2	cf 50 %	679	746	722, 1444	20.81
0.5	1	cl mean (w)	405	429	337, 617	1.97
1.5	1	cl mean (w)	603	686	530, 1151	2.65
0.5	1	cl mean	1131	1292	835, 1883	1.17
1.5	1	cl mean	747	778	660, 1179	3.11

The distribution of the time difference of a 3 layer NOL-11 fibre ribbon without any additional coating is presented in Figure 7.12. The simplest quantisation of the distribution's width is presented as the Full Width at Half Maximum (FWHM) divided by a factor of 2.35. In a purely Gaussian case, this corresponds to the standard deviation of the distribution. Furthermore, different models describing the distributions are compared. A single Gaussian, fitted within  $\pm 4$  sigma around the peak position, fails to model the tails correctly. The sum of two Gaussian distributions with a common mean position describes the distribution well but fails in quantifying the time resolution in a single number. This model is fitted within  $\pm 8$  sigma of the core distribution. Both fits are stable with respect to larger fitting ranges. Furthermore, the convolution of a Gaussian distribution with an exponential with the decay time  $\tau_{\text{exp}}$  is presented. This model is motivated by the exponential nature of the scintillation process as described in chapter 4. The offset of 439 ps is caused by the not-perfect central alignment of the ribbon with respect to the beam and trigger and subordinately by slightly different signal trace lengths.

The effects of different cuts are summarized in Table 7.5. Both, amplitude thresholds of 0.5 or 1.5 photoelectrons are used to discriminate the waveforms. All clusters or only such with

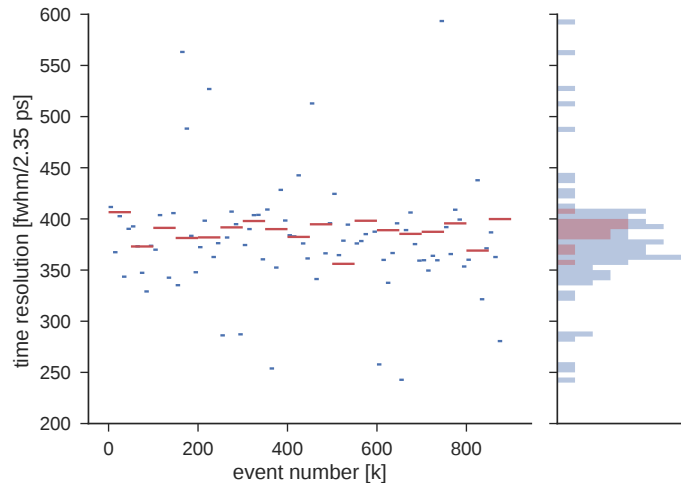


**Figure 7.13:** Time resolution of a 3 layer NOL-11 ribbon without any additional coating extracted in different subsets of 10k (—) and 50k (—) events from the full collection.

at least two SiPM columns are used. Although the ASIC used in the experiment provides the timing at the threshold level, the effects of other combinations are presented here. Furthermore, time extraction by constant fraction at 20 % and 50 % are studied. For comparison, the time resolution of weighted and non-weighted mean cluster times are shown for the different cuts. The effects of cluster size cuts are found to be negligible. As long as the cluster time is extracted by the smallest time, this is also true for the different thresholds for signal discrimination. Higher thresholds used for the ToA determination worsen the time resolution. Note, that the two thresholds are identical in the experiment. If a 1.5 photoelectrons timing threshold is deployed, the chances to catch the earliest photons decreases. In principle, a timing threshold of 0.25 photoelectrons could provide better resolution; but noise and crosstalk effects start to dominate in the used system. The non-uniform arrival time of the photons at the detectors cause non-uniform signal rise times which is the reason for the worse performance of constant fraction time extraction. At lower levels, e.g. 20 %, this effects reduces due to the relative low number of photons per channel in the order of five. The use of cluster mean time yields worse time resolution if no weighting by the number of detected photons is available. The operation mode foreseen for the MuTRiG ASIC does not provide a resolved amplitude information, thus weighting will not be possible. The feasible cluster mean time is very prone to noise, hence its performance is worse at low discrimination thresholds.

#### SYSTEMATICS: MEASUREMENT STABILITY OVER TIME

Figure 7.13 shows the time resolution as a function of the event number of a 3 layers NOL-11 ribbon recorded over 4.75 hour from 0:40 until 5:26 grouped in 10k and 50k event buckets. The time resolution is very stable over time, no trend can be identified, and it shows a spread with a standard deviation of 12 ps for both presented bucket sizes. Scans along the width of a

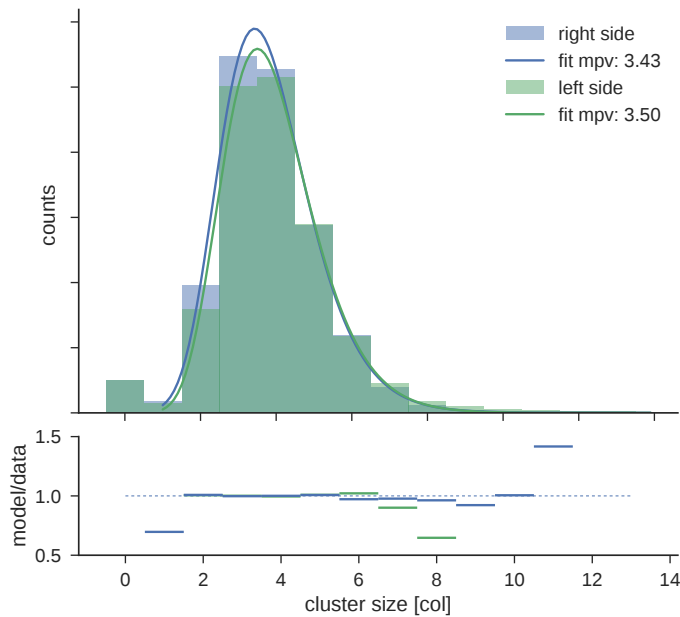


**Figure 7.14:** Cluster size of both sides of a 3 layer NOL-11 ribbon without any additional coating fitted with the convolution of a Landau and a Poisson distribution.

ribbon show consistent fluctuations with a standard deviation of 12 ps. This spread describes the systematic uncertainty of the time resolution extraction.

#### CLUSTER SIZES

Based on the previously described cluster definition, a cluster consists of all consecutive sensor columns, corresponding to SiPM channels, with an amplitude larger than a specific threshold, the cluster size for both sides is extracted. An exemplary distribution at a threshold of 0.5 photoelectrons of a 3 layers NOL-11 ribbon without any additional coating is shown in Figure 7.14, overlaid by the convolution of a Landau and Poisson distribution, which is fitted to the presented data. The fit shows good agreement around the Most Probable Value (MPV) which is used for comparison between different datasets. The difference of cluster sizes between both sides is probably caused by slightly different couplings of the ribbons to the SiPM arrays.

#### NUMBER OF DETECTED PHOTONS

The number of photons detected by a SiPM column is determined by the integral of the waveforms as described in Figure 7.3.4 discriminated based on the channel wise calibration for the photon number. Due to the utilization of the MuTRiG, this information will not be accessible in the experiment. The detected photons of all columns of a cluster from both sides are summed

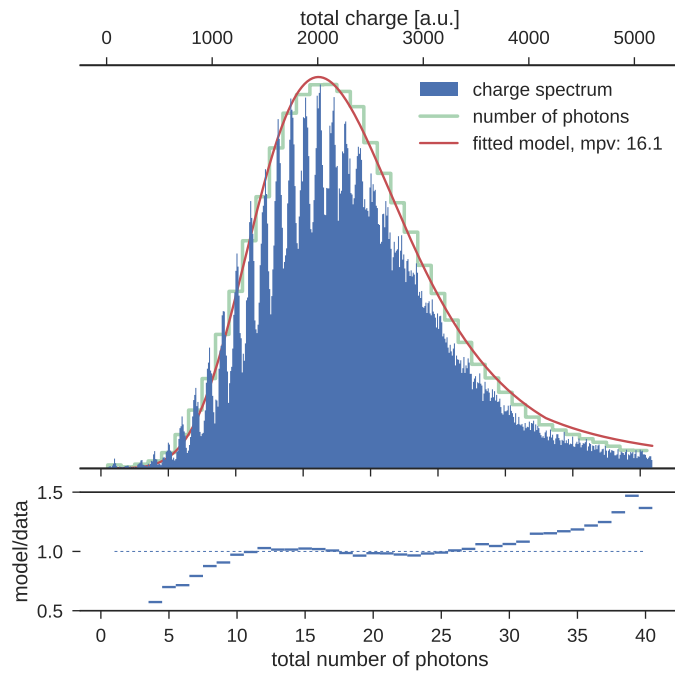


**Figure 7.15:** Detected charge (—), respectively number of photons (—), of one side of a 3 layer NOL-11 ribbon without any additional coating. The number of photons distribution is fitted with a convolution of Landau and a Poisson distribution (—).

to extract the light yield  $Y$  of a ribbon under test. Figure 7.15 shows both the total charge of the clusters, where the single photons can be identified, and the total number of detected photons in the clusters of both sides. The discrete distribution of the number of photons is fitted with the convolution of a Landau and a Poisson distribution. The fit shows good agreement around the MPV which is extracted for comparison of different prototypes.

The stability over time of the extracted ribbon quantities is demonstrated in Figure 7.16 where the quantities are extracted in buckets of 10 kevents and presented as a function of event number, corresponding to the measurement time. The same data set of 3 layer NOL-11 based ribbon without any additional coating, taken over 4.75 h, as in Figure 7.13 is presented. The cluster position of both sides is presented relative to the mean of the first 200 kevents. Around event number 400k the position jumps around  $250 \mu\text{m}$ , which corresponds to one SiPM column, probably due to a movement of the mechanic support structure which is adjustable in height. Since the SiPM arrays at the two sides are mounted rotated by  $180^\circ$  with respect to each other, the movement causes an offset in opposite direction. This small change of positions has almost no effect on the other quantities. In the MPV of the cluster sizes and in the number of detected photons, as well as in the value of the maximal amplitude, no trend is visible. The distributions of the first two show a standard deviation of  $\sigma_{\text{cluster size}} = 0.2$ , respectively  $\sigma_{\text{photons}} = 1.4$ . The position of the peak position of the time differences of the two sides, corresponding to an offset from the central position of the trigger along the fibre direction, shows a small jump correlated with the position jump but no trend in the two individual segments. The standard deviation of the overall distribution is  $\sigma_{\Delta t, \text{offset}} = 6.6 \text{ ps}$ . The spread in the here presented quantities are used to extract the uncertainties of the extracted ribbon quantities.

### EXTRACTION OF EFFICIENCIES

The efficiency of a ribbon under test is determined with respect to the additional scintillators in the setup (see Figure 7.5). The simplest pseudo-telescope like configuration is given by the beam and the trigger consisting of two crossed 1 mm thick round fibres. This confines the particle tracks to a geometrical area of  $\approx 1 \text{ mm} \times 1 \text{ mm}$  at  $\approx 4 \text{ cm}$  behind the ribbon and approximately to the beam size in the order of 1 cm. Divergence of the beam and scattering of particles allow for particle penetrating the trigger but not the fibre ribbon. To confine the particle trajectories further an additional 0.25 mm thick single fibre is added  $\approx 2 \text{ cm}$  in front of the ribbon. A supplementary thin plastic scintillator with a width of 5 mm can be used to constrain the particles further in the horizontal fibre direction. Particles scattering in the fibre ribbon, thus leaving the pseudo-telescope structure, don't enter in the denominator of the efficiency extraction. Efficiencies are extracted at thresholds of 0.5 and 1.5 photoelectrons by accepting all clusters or requiring at least two SiPM columns. In an AND configuration such a cluster is required on both sides where in an OR configuration a cluster on either side is sufficient. Since only 8 mm of the ribbon are instrumented and the pseudo-telescope has an acceptance in ribbon height direction of 1 mm no further spatial requirement is applied. The efficiencies  $\varepsilon$  are given by the number of events fulfilling the required conditions divided by

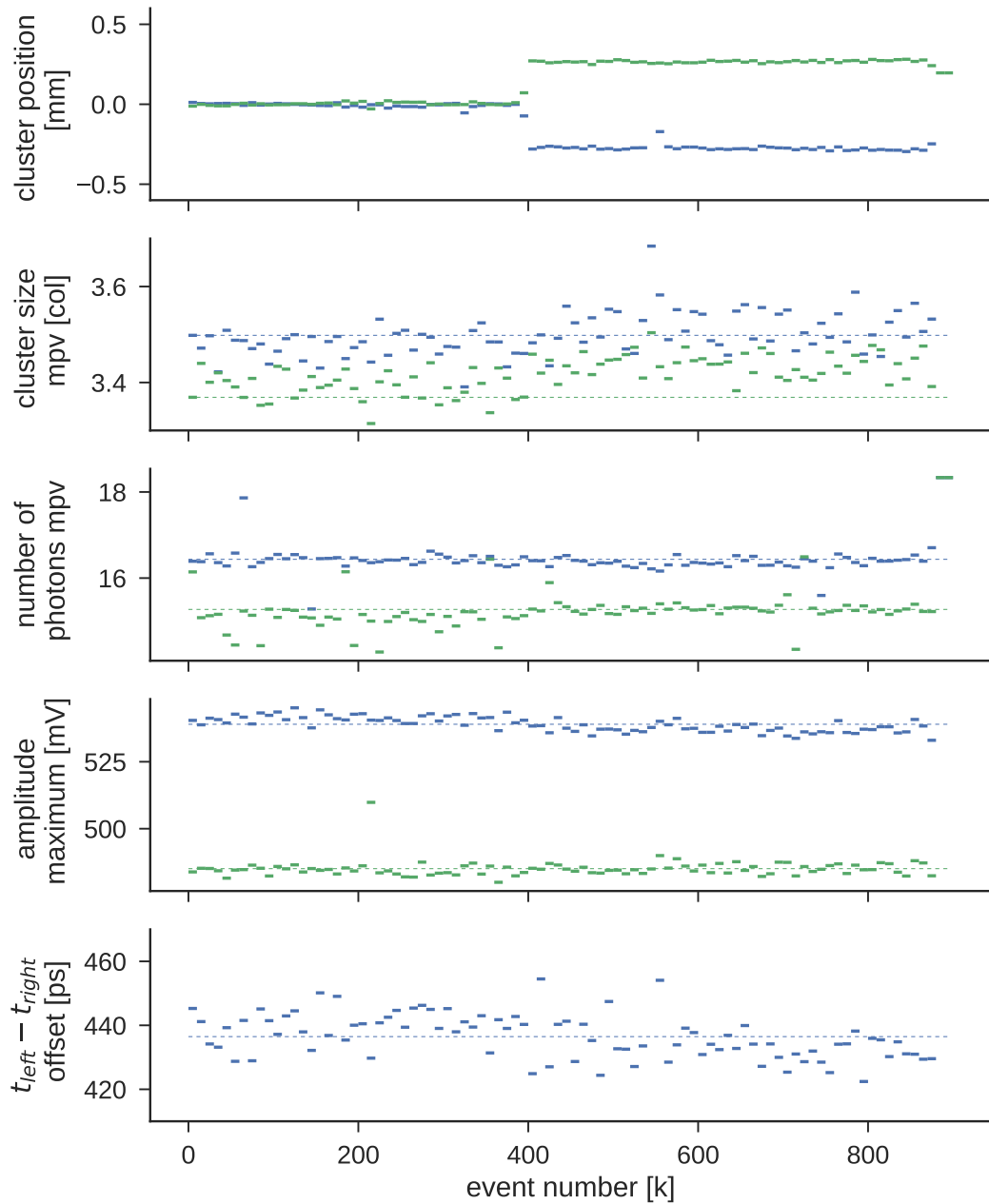


**Figure 7.16:** Time dependency of various observables: cluster position, Most Probable Value (MPV) of the cluster size (relative to the initial position), MPV of the number of detected photons, the maximal amplitude of a cluster in each case for the left ( $\rightarrow$ ) and the right ( $\leftarrow$ ) side and the offset of the time difference. The dataset of a 3 layer NOL-11 ribbon without any additional coating, recorded over 4.75 hour, is divided into 10k buckets of about 3 min.

the number of events which fulfil the pseudo-telescope conditions as defined in the following.

$$\varepsilon(\text{ribbon}) = \frac{\text{num}\left(\text{sig}(\text{ribbon}) \wedge \text{sig}(\text{trigger})\right)}{\text{num}\left(\text{sig}(\text{trigger})\right)}, \quad (7.4)$$

$$\varepsilon_{\text{add sci}}(\text{ribbon}) = \frac{\text{num}\left(\text{sig}(\text{ribbon}) \wedge \text{sig}(\text{trigger}) \wedge \text{sig}(\text{add sci})\right)}{\text{num}\left(\text{sig}(\text{trigger}) \wedge \text{sig}(\text{add sci})\right)}, \quad (7.5)$$

where  $\text{num}(X)$  are the number of events which fulfil  $X$ ,  $\text{sig}(Y)$  are the definition of a signal for the event type  $Y$ .  $\text{Sig}(\text{ribbon})$  is defined by the different trigger levels, coincidence and cluster size conditions;  $\text{sig}(\text{trigger})$  and  $\text{sig}(\text{add sci})$  are the corresponding discriminated scintillator signals in coincidence. The additional scintillators (add sci) are not present for all data sets, therefore the efficiencies with respect to the pure trigger are also stated for better comparison. The extraction of the efficiency by only the latter lacks good particle track confinement. The uncertainty of the efficiency determination is given for a 68.3% central confidence interval exploiting the Fisher-Snedecor distribution [136] as recommended by [56].

### 7.3.5 CHARACTERISATION RESULTS

The performance of the different tested scintillating fibre ribbons concerning a usage in the  $\text{Mu3E}$  experiment are summarised in Table 7.6. The values are extracted for a threshold of 0.5 photoelectrons, for both hit validation and time measurement, and cluster sizes of at least two columns are required. The timing is extracted at FWHM of the time difference distribution from both sides ( $t_{\text{left}} - t_{\text{right}}$ ). For cluster size and number of detected photons, the MPV of the measured distribution for each side is quoted, the full distributions can be found in appendix A. The presented efficiencies are determined in an AND configuration. Figure 7.18 visualizes the efficiencies of the different fibre ribbon prototypes for the different efficiency extraction schemes: threshold levels of 0.5 and 1.5 photoelectrons, cluster sizes of  $n > 0$  and  $n > 1$ , AND and OR configuration, and usage of different additional scintillators for the pseudo-telescope configuration. The setup without additional scintillators provides no sufficient pseudo-telescope track constraints for reliable absolute efficiency extraction. A relative comparison between the different conditions is possible. Lower photon yield, as in ribbon prototypes with only two layers or consisting of BCF-12, manifests in an efficiency drop in more demanding conditions. Ribbons comprised at least 3 layers and Kuraray fibres show significant higher efficiencies, sufficiently high for the  $\text{Mu3E}$  sub-detector.

The three most important quantities for the experiment, time resolution, efficiency and cluster size, of the different fibre types in the different prototypes, are visualized for a better comparison in Figure 7.17. As expected, the time resolution and the efficiency show a strong correlation to the light yield. The more photons are generated and detected, the better the timing and the efficiency.

**Table 7.6:** Overview of measured fibre ribbon prototype properties. Thresholds of 0.5 photoelectrons are used, and clusters are required to be at least 2 columns wide. The efficiencies are quoted for the same conditions in an AND configuration. The distributions can be found in appendix Figure A. Fibre nol11<sup>(1)</sup> after exposure to direct sunlight for a couple of days.

material	layers	coating	time resolution FWHM/2.35 [ps]		cluster size		photons [MPV]		efficiency
			left	right	left	right	left	right	
mj81	4	TiO <sub>2</sub>	558±26	2.99±0.02	3.06±0.02	2.99±0.02	12.6±0.6	11.90±0.1	92.9 <sup>+0.1</sup> <sub>-0.1</sub>
mj78	4	TiO <sub>2</sub>	361±23	3.26±0.02	3.26±0.02	3.26±0.02	22.6±0.3	22.06±0.3	96.1 <sup>+0.0</sup> <sub>-0.0</sub>
nol11	3	-	398±25	3.40±0.03	3.48±0.03	3.40±0.03	16.5±0.4	15.21±0.4	95.9 <sup>+0.0</sup> <sub>-0.0</sub>
nol11	4	-	354±17	3.94±0.02	3.89±0.02	3.94±0.02	22.6±0.7	23.01±0.7	97.0 <sup>+0.0</sup> <sub>-0.0</sub>
nol11 <sup>(1)</sup>	4	-	438±25	3.98±0.02	4.03±0.03	3.98±0.02	16.9±0.2	16.30±0.2	96.3 <sup>+0.0</sup> <sub>-0.0</sub>
nol11	3	TiO <sub>2</sub>	904±38	3.86±0.04	3.82±0.05	3.86±0.04	18.3±0.3	18.31±0.3	88.5 <sup>+0.1</sup> <sub>-0.1</sub>
nol11	3	TiO <sub>2</sub>	364±28	3.76±0.03	3.81±0.04	3.76±0.03	18.2±0.2	17.77±0.2	93.1 <sup>+0.1</sup> <sub>-0.1</sub>
nol11	2	TiO <sub>2</sub>	434±30	3.06±0.02	3.00±0.03	3.06±0.02	11.3±0.2	11.14±0.2	91.0 <sup>+0.1</sup> <sub>-0.1</sub>
nol11	2	TiO <sub>2</sub>	409±32	3.08±0.02	3.06±0.02	3.08±0.02	11.2±0.1	10.94±0.1	88.4 <sup>+0.1</sup> <sub>-0.1</sub>
nol11	4	TiO <sub>2</sub>	1024±37	3.75±0.06	3.67±0.11	3.75±0.06	21.5±1.1	22.07±1.1	87.9 <sup>+0.1</sup> <sub>-0.1</sub>
bcf12	4	TiO <sub>2</sub>	940±47	1.91±0.06	1.62±0.06	1.91±0.06	2.6±0.1	3.20±0.1	46.5 <sup>+0.1</sup> <sub>-0.1</sub>
bcf12	4	TiO <sub>2</sub>	801±42	1.78±0.03	1.66±0.03	1.78±0.03	3.7±0.1	3.70±0.1	50.6 <sup>+0.1</sup> <sub>-0.1</sub>

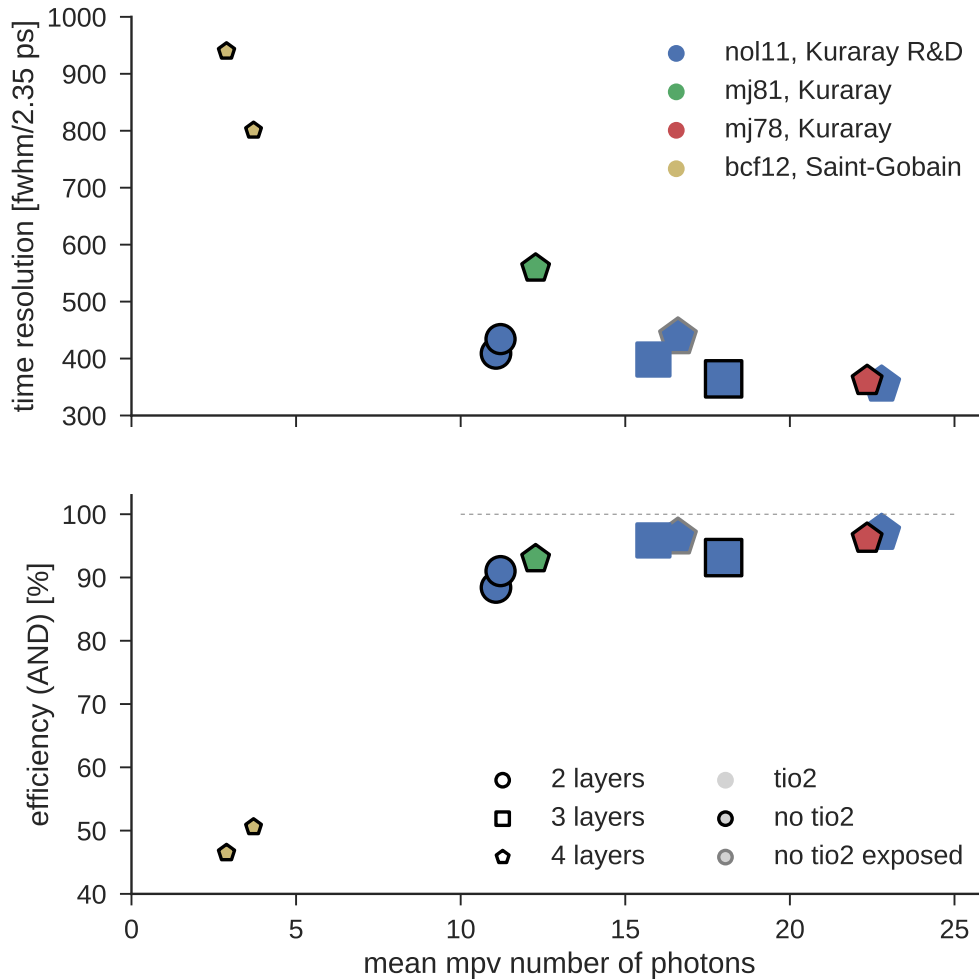


**Figure 7.17:** Time resolution and efficiency of the different fibre prototypes as a function of light yield. The light yield is given by the mean of the MPV from both fibre sides. The time resolution is quoted in terms of the FWHM/2.35 of the distribution of the cluster time differences from both ribbon sides. The efficiencies are obtained in an AND configuration by the setup without additional scintillators, requiring a cluster size of  $n > 2$  on each side. These efficiencies are to be understood for relative comparison and lower limits. The marker size represents the measured mean of the cluster sizes from both sides.

### 7.4 IMPACT AND COMPARISON WITH EARLIER RESULTS

All tested fibre ribbon prototypes consisting of Kuraray fibres with at least 3 layers show sufficient time resolution and efficiencies for the  $\text{Mu3E}$  scintillating fibre detector. Out of the commercially available fibres, the SCSF-78 performs better than SCSF-81 in all aspects. The novel R&D NOL-11 fibres are very promising for potential future upgrades.

In the past [77, 124] the  $\text{Mu3E}$  fibre group R&D activities focused on the behaviour of individual fibres within a ribbon. The performance of the ribbons connected to SiPM column arrays, as presented here, was extrapolated.

Compared to these earlier results, the presented round Kuraray fibre's light yield is increased significantly. The fibre spools<sup>2</sup> out of which the older round prototypes consist is believed to have been exposed to UV-light. Furthermore, the production procedure improved with each prototype iteration, and the fibres in a fan-outed scheme are much more likely to be damaged than the ones directly connected to a sensor array.

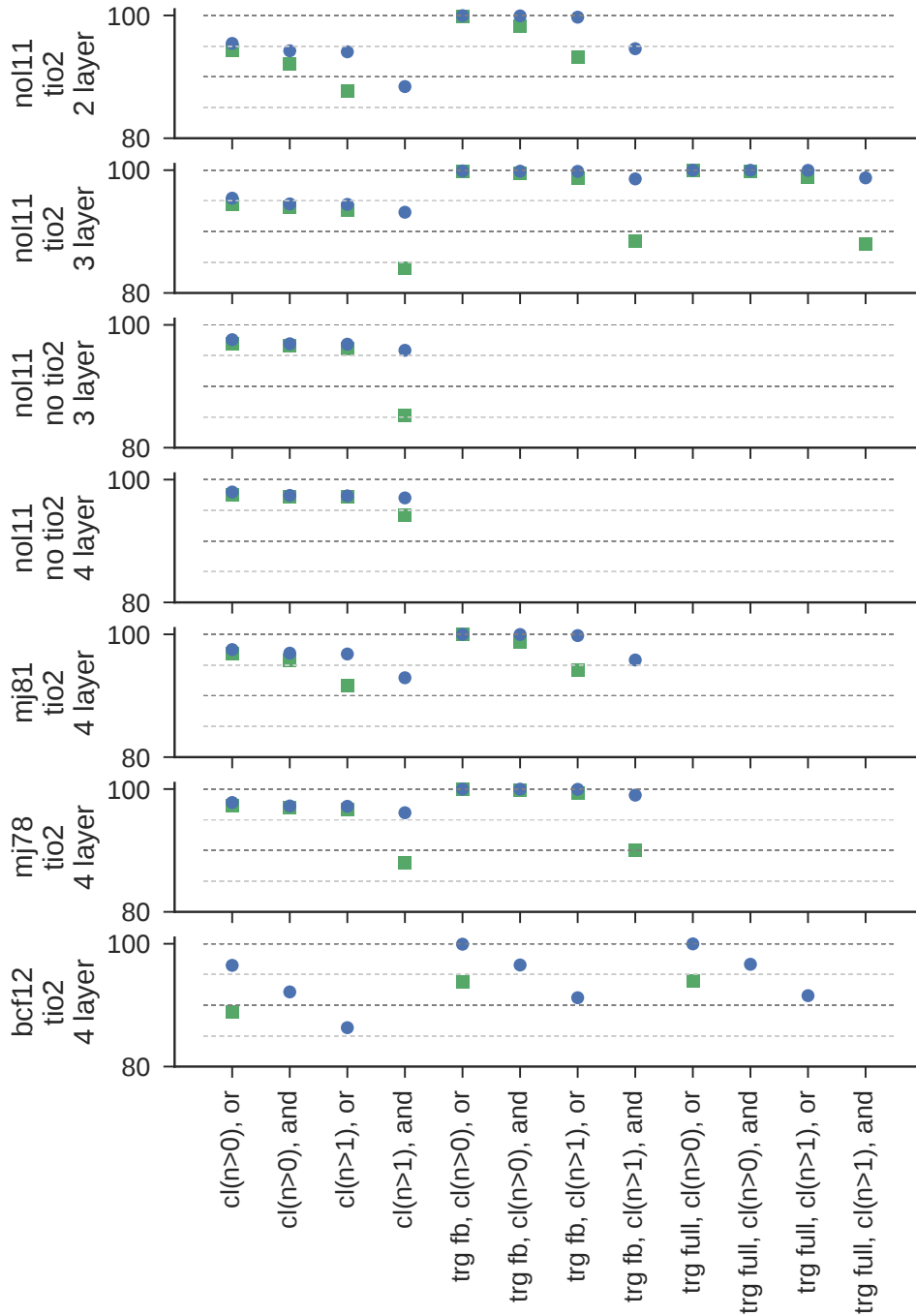
The extrapolations from the square Saint Gobain fibres based ribbon prototypes agree well with the new prototypes [125].

---

<sup>2</sup>Kuraray SCSF-81 fibres.

## 7.4. IMPACT AND COMPARISON WITH EARLIER RESULTS

**Figure 7.18:** Efficiencies of the different fibre ribbon prototypes in different configurations. In an AND configuration a cluster with the given multiplicity,  $n > 0$  or  $n > 1$ , is required on each side, whereas in an OR configuration a cluster on either side is sufficient. The abbreviation *trg fb* stands for the setup with an additional 250  $\mu\text{m}$  thick fibre horizontally in front of the ribbon under test, whereas in the *trg full* setup also a further 5 mm thick scintillator is added in front to confine the measurement horizontally. Furthermore, thresholds of 0.5 (●) and 1.5 photoelectrons (■) are applied.





# 8

## Simulation of a Single Scintillating Fibre

The simulation of single scintillating fibres in various configurations provides a method to study and compare their properties and helps to develop an intuition for such detectors. A dedicated simulation framework, based on the GEANT4 [137–139] toolkit, addresses the scintillation response of the detector material, photon propagation inside a fibre up to the potential detection in an attached detector. In the scope of this thesis, fibre properties, which are difficult to access experimentally, are extracted from this dedicated single fibre simulation for use in the experiment’s main simulation framework. For example, the framework requires the scintillation photon distribution on the sensor surface which is covered by 100  $\mu\text{m}$  thick epoxy resin (see subsection 9.2.3). This distribution is extrapolated for different fibre configurations by this dedicated simulation including photon propagation.

This chapter describes the simulation’s setup in section 8.1 and its working principle in section 8.2, followed by a validation by a dedicated measurement in section 8.3. The extracted single fibre properties are summarized in the last part in section 8.4.

### 8.1 SINGLE FIBRE SIMULATION CONFIGURATION

The simulation framework contains simulation of a scintillating fibre core, round or square, encased by up to two claddings, a potential additional coating, and all covered in glue. At both fibre ends, photon detection layers are located at a configurable distance along the fibre direction.

The material and thicknesses of the different volumes follow the fibres studied for the experiment. Their properties are summarized in Table 7.1. Additional fibre coating is ignored. A 100  $\mu\text{m}$  thick region between the photon detector and the end of the 30 cm long fibre is filled with epoxy resin (Bisphenol-A-diglycidylether (BADGE)) with a constant refractive index of  $n_{\text{BADGE}} \approx 1.5$ .

## 8.2 SIMULATION OF PHOTON GENERATION AND PROPAGATION

Scintillation photons are created according to the emission spectrum shown in Figure 7.1, whereby the overall light yield is an adjustable parameter. In the GEANT4 toolkit, these *optical photons* are treated as electromagnetic waves. Hence, at the boundaries between two dielectric media, they are transmitted or reflected. The photon propagation follows the laws of optics in combination with wavelength dependent absorption. Micro facets can roughen the interfaces between different materials. In this case, the direction of the surface normal is smeared statistically, i.e. sampled for each interaction from a Gaussian distribution with a specified standard deviation, corresponding to the roughness of the interface. A more detailed description can be found in [77]. The precise knowledge about the surfaces is difficult to access experimentally and the combination of surface roughness and attenuation length span a large parameter space [140]. The baseline configuration in this simulation uses perfectly polished surfaces.

## 8.3 CROSS-CHECK OF THE SINGLE FIBRE SIMULATION

Whereas the simulation provides no absolute light yield estimate from first principles, the fibre dimensions and the sensor's plane distance determine the photon spatial distribution on a sensor plane. The latter is used to cross-check the simulation. Figure 8.1a shows the light intensity profile of a 2 mm thick round double clad scintillating fibre coupled to a Light Emitting Diode (LED). The integrated photon flux is measured at a distance of 7 mm with a camera sensor, i.e. by the  $2592 \times 1728$  green pixels of a  $22.3 \text{ mm} \times 14.9 \text{ mm}$  Complementary Metal-Oxide-Semiconductor (CMOS) image sensor<sup>1</sup>. Figure 8.1b shows a projection of a horizontal cut of this intensity profile averaged between pixel 350 and 550 in combination with the simulated result of the identical setup. The measured distribution is reproduced well by the simulation.

## 8.4 EXTRACTION OF SINGLE FIBRE PROPERTIES

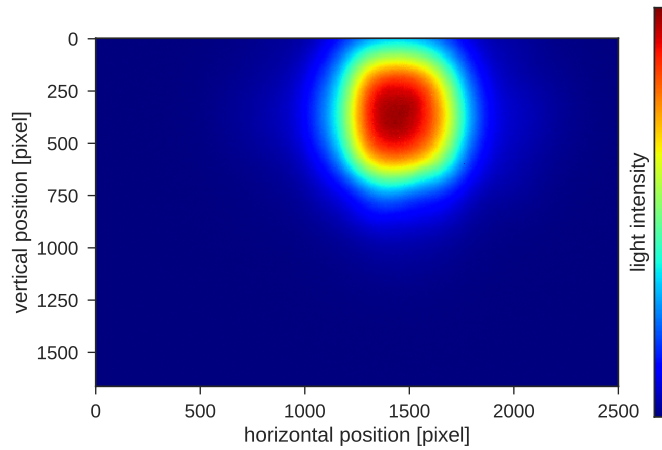
Light yield and the attenuation length are used to tune the simulation; therefore they can not be extracted from this simulation. This type of simulation only provides a tool for interpolation between different configurations. However, the simulation yields the photon's exit position and angle, which allow the extrapolation of the photon distribution on a detector layer. The cross-check, discussed above, demonstrates this feature.

### 8.4.1 PHOTON EXIT POSITIONS

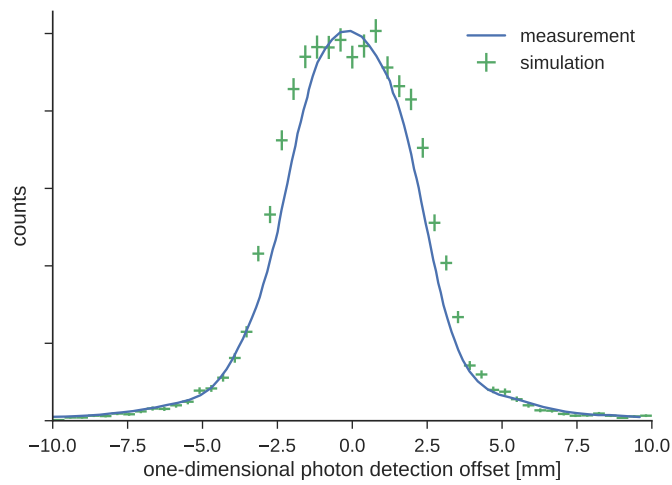
Figure 8.2 and Figure B.2 show the photon exit position of double-clad  $250 \mu\text{m}$  thick round and square fibres with perfectly polished surfaces. Subfigures (a) and (b) show these distributions for photons which are totally reflected only at the core-cladding interface or at the cladding-cladding interfaces respectively. Subfigures (c) show the combination of the two

---

<sup>1</sup>CMOS APS-C sensor in a CANON EOS 1200D camera.



(a) Light intensity profile measured by a  $22.3 \text{ mm} \times 14.9 \text{ mm}$  large CMOS image sensor. The intensity profile reveals the distortion of the round fibre. Measurement performed by D. Ge.



(b) Horizontal projection of Figure 8.1a averaged between pixels 350 and 550 (—) in combination of simulation (+) of the identical setup.

**Figure 8.1:** Light output from a 2 mm thick round fibre coupled to an LED detected at a distance of 7 mm from the fibre end.

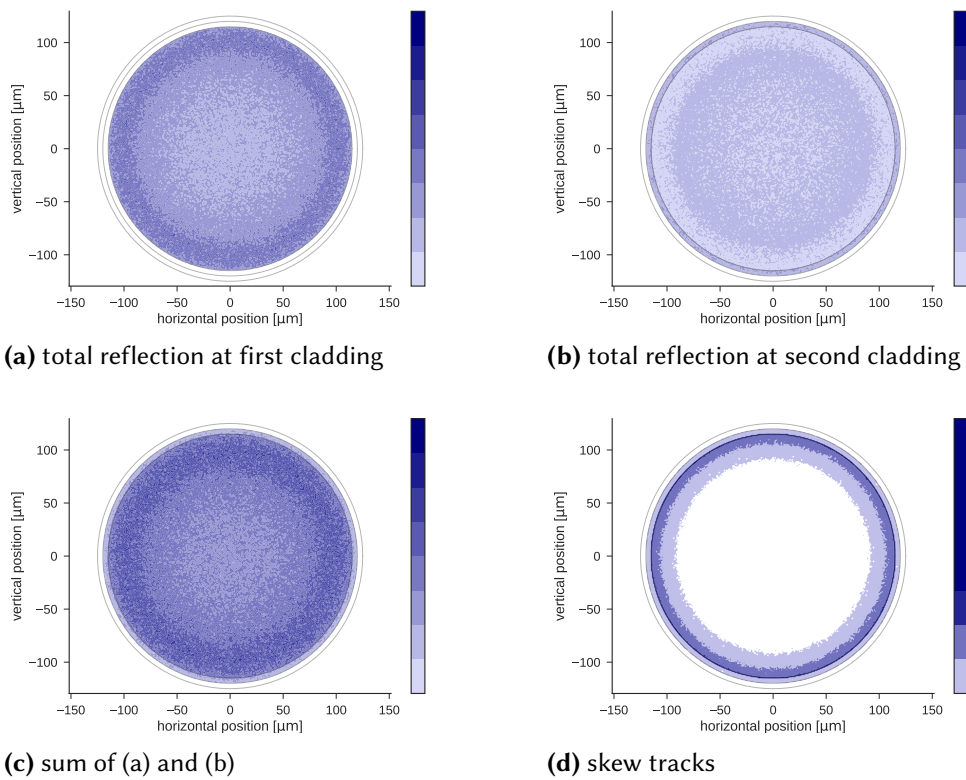


**Figure 8.2:** Simulated photon exit position in 250  $\mu\text{m}$  thick double clad round fibres with perfect polished interfaces. Photons with skew trajectories are suppressed in subfigures (a) - (c) by limiting the number of reflections to below 1000. The interfaces between core, cladding and surrounding material are indicated for better orientation.

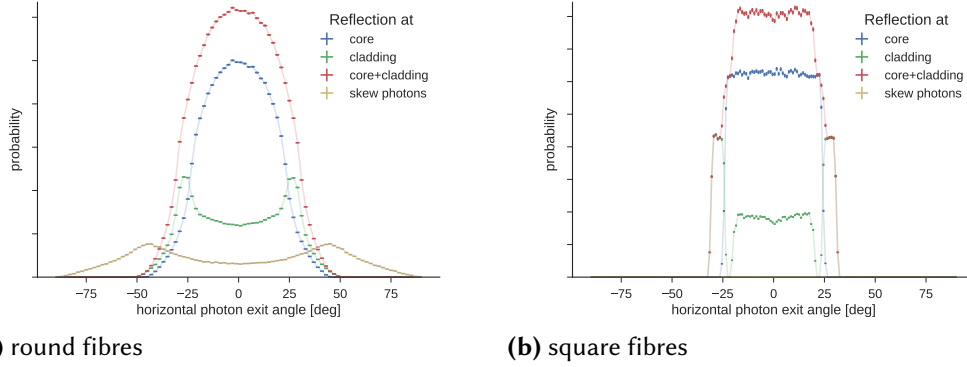


**Figure 8.3:** Simulated distribution of photon exit angles with respect to the fibre axis projected to one plane of perfect 250  $\mu\text{m}$  thick double clad fibres. The angular distributions for photons which undergo total reflection at the core-cladding interface ( $\text{---}$ ), at the cladding-cladding interface ( $\text{---}$ ), the combination of the two ( $\text{---}$ ) and in the case of round fibres, skew trajectories ( $\text{---}$ ) are shown separately.

contributions. In the case of the round fibres, un-physical skew tracks (see chapter 4) are suppressed by limiting the number of reflections to 1000. These skew trajectories, which run along the core-cladding interface, only exist in perfectly round fibres with polished interfaces. The smallest surface impurity destroys these highly helical photon paths. Figure 8.2d shows the hypothetical exit positions of such photons.

#### 8.4.2 PHOTON EXIT ANGLES

Figure 8.3 shows the photons exit angle distribution with respect to the fibre axis projected on the horizontal plane ( $\varphi_x$ ) for the same configurations as described above. The horizontal plane is defined as the x-axis of a Cartesian coordinate system with its z-axis aligned to the fibre axis and, in case of square fibres, axes parallel to the fibre surfaces. The refraction due to the refractive index ratio between the fibre material and the employed epoxy resin between the fibre end and sensors is taken into account. The distributions are again divided into a part which is reflected at the core-cladding interface, a part which is reflected at the cladding-cladding interface, the sum of the two and, in case of round fibres, a hypothetical part consisting of photons with skew trajectories. Due to the cross-section of square fibres, their distribution of the projection of the photon exit angles is very flat.

#### 8.4.3 PHOTON POSITIONS ON THE DETECTOR SURFACE

The combination of the photons' exit positions, angles and the refractive index of the material covering the sensors results in the position distribution at a detector layer. Such distributions are utilized in the main simulation framework (see subsection 9.2.3). Figure 9.5 shows these distributions for round and square fibres in the presence of a 100  $\mu\text{m}$  thick epoxy resin between the fibre ends and detector surface.

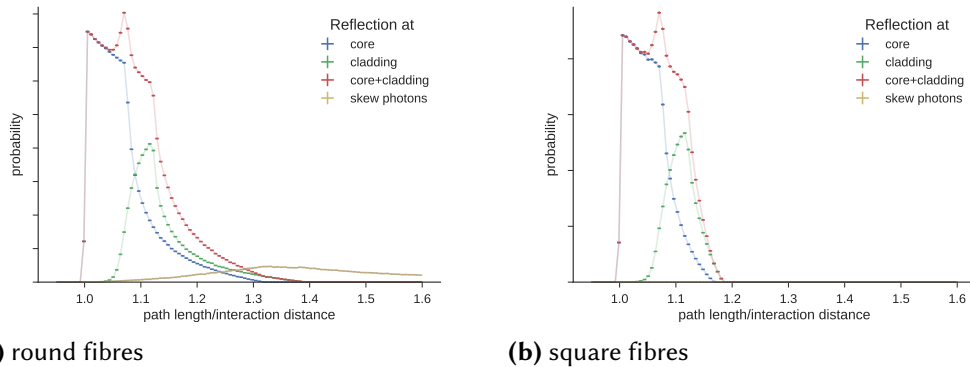


**Figure 8.4:** Simulated distribution of photon path lengths normalized to the interaction distance of perfect  $250\ \mu\text{m}$  thick double clad fibres. The distributions for photons which undergo total reflection at the core-cladding interface ( $\rightarrow$ ), at the cladding-cladding interface ( $\leftarrow$ ), the combination of the two ( $\leftrightarrow$ ) and helical skew trajectories ( $\dashrightarrow$ ) are shown separately.

#### 8.4.4 PHOTON PATH LENGTHS IN FIBRES

Figure 8.4 shows the path length distribution of scintillation photons inside the same fibres presented above, normalized to the distance of the particle interaction from the fibre end. The same components as previously, including the helical skew tracks in case of round fibres, are presented. These distributions match simple geometrical considerations. The superposition of the path length distributions of photons reflected at the core-cladding and the cladding-cladding interfaces produces a peak around 1.07 relative length where the two distributions overlap. An approximation of these distributions is used in the main simulation framework (see subsection 9.2.4).

#### 8.4.5 EXPLOITATION OF THE OBTAINED PROPERTIES

The distribution of the photon position on the detector surface (see subsection 8.4.3) is required by the experiment simulation framework to map the scintillation photons of the individual fibres to their corresponding SiPM column (see subsection 9.2.3). Furthermore, the distribution of the photon path lengths in the fibres is used to parametrize the arrival time of the individual scintillation photons at the sensors (see subsection 9.2.4).

# 9

## The Scintillating Fibre Detector in the MU3E Simulation Framework

The MU3E software framework consists of a GEANT4 [137–139] toolkit based simulation and a custom reconstruction software. The scintillating fibre detector is included in the simulation, and its simulated sensor response was made available in the reconstruction and analysis framework in the scope of this thesis. The response to particles passing the sub-detector is modelled by sampling parametrized distributions. The parametrization explained in this chapter depends on the deposited energy in the scintillating volume and the interaction position.

This chapter starts with a description of the improved fibre detector in the simulation framework in section 9.1, followed by the description of its response to passing particles, which was optimised in the scope of this work, in section 9.2. The simulation settings are described and a validation is presented in section 9.3. The chapter closes with a discussion of the extrapolated fibre detector performance in section 9.4 based on the measurements presented in chapter 7.

### 9.1 THE SUB-DETECTOR IN THE FRAMEWORK

Different fibre detector configurations are available in the MU3E simulation framework. The fibre volumes depend upon the choice of the fibre shape, length and diameter. Figure 9.1 shows a cut through the fibres. The material and relative thickness of the two claddings are implemented according to the vendor’s specifications listed in Table 7.1. An optional aluminium coating of the fibres is available. Note that the relative thickness of the claddings depends on the fibre geometry.

#### 9.1.1 DIMENSIONS OF THE FIBRE RIBBONS

In the baseline configuration, as described in Table B.1, the scintillating fibre detector consists of 12 ribbons with a maximum 126 fibres per ribbon separated by 5  $\mu\text{m}$  epoxy resin in 4 layers

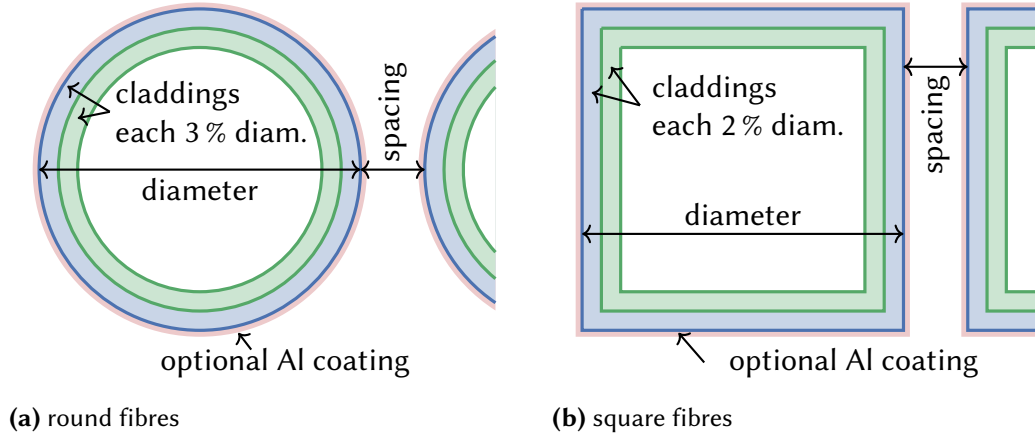


**Figure 9.1:** Transverse cut of the fibres as implemented in the GEANT4 simulation. The shown dimensions are not to scale. The cladding thickness is 3% (2%) of the fibre diameter for round (square) fibres. An optional aluminium coating of a few 100 nm can be added.

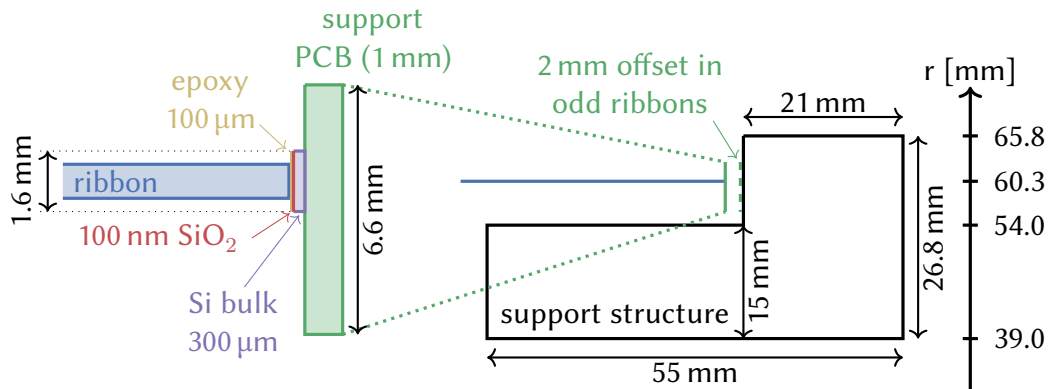


**Figure 9.2:** SiPM and fibre detector support volumes in the experiment's simulation framework. The support structure is rotationally symmetric.

and no additional aluminium coating. The distance between ribbons, specified as shown in Figure B.5, is 180  $\mu\text{m}$ . This results in ribbons with dimensions of 32.13 mm  $\times$  0.91 mm  $\times$  287.75 mm at a minimal radius of 60.28 mm, and a maximal radius of 63.27 mm.

The volume between the individual fibres inside such a ribbon is filled with BADGE, with the chemical formula  $\text{C}_{21}\text{H}_{24}\text{O}_4$ , and a density of 1.15 g/cm<sup>3</sup>. Typical epoxy resins, such as ARALDITE 2020, employed for ribbon production consist of BADGE with a refractive index  $n_{\text{BADGE}} \approx 1.53$ .

Figure B.3 and Figure B.4 show the numbering scheme of the fibre volumes.

### 9.1.2 DIMENSIONS OF THE SUPPORT STRUCTURE

The passive support structure is modelled as aluminium rings with the following dimensions: The ribbon holding structure between the ribbon's ends and the pixel support with a thickness of 21.1 mm, an outer radius of 65.8 mm and an inner radius of 39 mm, and a support structure below the ribbons with a length of 55 mm with the same inner radius and a height of 15 mm. Figure 9.2 shows an overview of these volumes.

SiPM, consisting of a 300  $\mu\text{m}$  silicon bulk and a 100 nm thin silicon oxide layer covered with 100  $\mu\text{m}$  epoxy, on a 1 mm thick PCB on each side of a fibre ribbon allow to study the radiation dose in the sensors. The sensors have an area of 1.6 mm  $\times$  32.5 mm whereas the support PCB has a height of 6.6 mm, as shown in Figure 5.6.

## 9.2 SIMULATION OF THE SCINTILLATING FIBRE DETECTOR'S RESPONSE

The scintillating fibre detector's response to crossing particles is simulated by sampling parametrized distributions. No single scintillation photon propagation inside the fibres is simulated to keep the *MU3E* simulation speed high. It bases on the concept presented in [77]. The parametrizations are extended and modified for the usage of SiPM arrays and adjusted for newer results.

The full information of the simulated particles can be stored and is linked to the detector responses through the full simulation and reconstruction chain.

### 9.2.1 PARAMETRIZATION IN ENERGY AND POSITION

The scintillating fibre response is parametrized as a function of the summed deposited energy  $E_{\text{dep}}$  of a crossing particle in the active part of a fibre and the interaction position. A detailed discussion of the used range cuts is given in [77]. The deposited energy of all crossing particles within a time window<sup>1</sup>  $t_{\text{fb\_pileup}} = 3 \text{ ns}$  is merged. This fibre pileup time, the time span in which the scintillation photons from two crossing particles can not be distinguished, is in the order of the scintillation time of a plastic scintillator fibre  $\tau_{\text{scintillation}}$ . At the same time, crosstalk to neighbouring fibres can be simulated.

### 9.2.2 NUMBER OF PHOTONS EMITTED BY THE FIBRES

The total deposited energy  $E_{\text{dep}}$  determines the number of potentially detectable photons per fibre. The material characteristic light yield  $Y \approx 8000 \text{ photons/MeV}$  and the intrinsic resolution  $\sigma_1$  determine the number of scintillation photons. Both, the light yield and the intrinsic resolution, are empirical parameters and depend on the material choice. For each particle crossing, the number of scintillation photons  $n_{\text{scint}}$  is sampled from a Gaussian distribution as

---

<sup>1</sup> $t_{\text{fb\_pileup}}$  can be specified in the configuration file.

described below.

$$n_{\text{scint}} \sim \mathcal{N}(\mu, \sigma_i^2), \quad (9.1)$$

$$\mu = E_{\text{dep}} \cdot Y, \quad (9.2)$$

$$\sigma_i = y \cdot \sqrt{E_{\text{dep}} \cdot Y}, \quad (9.3)$$

where  $y = 1$  is a resolution scale [141]. The usage of a Gaussian distribution over a Poisson distribution is motivated by the possibility to use a non-unit resolution scale ( $y \neq 1$ ). A Gaussian distribution is chosen over a Poisson to If a scale of  $y = 1$  is used, a Poisson distribution should be used. The combination of  $n_{\text{scint}}$  with the fibre's capture efficiency  $\varepsilon_{\text{capture}}$  (see subsection 4.2.1), the sensors' PDE  $\varepsilon_{\text{pde}}$  (see subsection 5.2.1) and the attenuation length  $\Lambda_{\text{attenuation}}$  along the fibre determine the number of the potentially detectable photons  $n_{\text{det}}$  per side.

In principle, PDE and the attenuation length are wavelength  $\lambda$  dependant. As described in subsection 4.2.2 and Equation 4.2.2, the attenuation length consists typically of two components where only the short one, which is of the order of the fibre length compared to several metres for the long component, is relevant for the sub-detector. It is approximated by a constant  $\Lambda_{\text{attenuation}}$ , which is wavelength independent. The same approximation as in Equation 4.3 is used for

$$\varepsilon_{\text{pde}} = \frac{\int \varepsilon_{\text{pde}}(\lambda) \cdot I_{\text{exit}}(\lambda) d\lambda}{\int I_{\text{exit}}(\lambda) d\lambda} \quad (9.4)$$

The number of photons that reach the sensor surfaces  $n_{\text{det}}$  is sampled per ribbon side, based on the common  $n_{\text{scint}}$ , from a Poisson distribution:

$$n_{\text{det}} \sim \mathcal{P}(\mu), \quad (9.5)$$

$$\mu(n_{\text{scint}}, d_{\text{side}}) = \varepsilon_{\text{capture}} \cdot \varepsilon_{\text{pde}} \cdot \exp\left(\frac{-d_{\text{side}}}{\Lambda_{\text{attenuation}}}\right) \cdot n_{\text{scint}}, \quad (9.6)$$

where  $d_{\text{side}}$  is the distance from the interaction position to the corresponding fibre ribbon end.

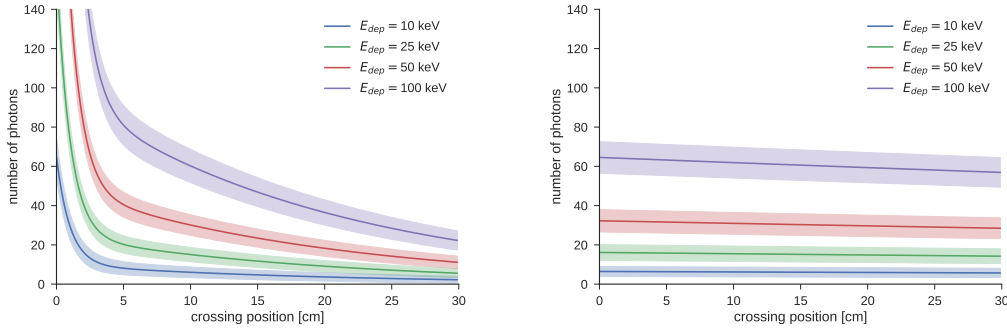
#### ALTERNATIVE PARAMETRIZATION BY STAND-ALONE SIMULATIONS

Alternatively, the number of detected photons is sampled from a Gaussian distribution with parametrized mean and standard deviation, which are extracted from stand-alone, GEANT4 based single fibre simulations with full photon propagation as described in chapter 8. Typical parametrizations show the same expression as in Equation 9.1 and Equation 9.5 for the distribution's mean, whereas the standard deviation consists of an  $E_{\text{dep}}$  independent and an  $E_{\text{dep}}$  dependent part:

$$\mu_n(E_{\text{dep}}, d_{\text{side}}) = E_{\text{dep}} \cdot (Y \cdot \varepsilon_{\text{pde}} \cdot \varepsilon_{\text{capture}}) \cdot \exp\left(\frac{-d_{\text{side}}}{\Lambda_{\text{attenuation}}}\right), \quad (9.7)$$

$$\sigma_n(E_{\text{dep}}, d_{\text{side}}) = E_{\text{dep}} \cdot y' \cdot \exp\left(\frac{-d}{\Lambda'}\right) + E_0 \cdot \exp\left(\frac{-d_{\text{side}}}{\Lambda''}\right) \quad (9.8)$$

In both approaches, it is possible to add a second attenuation length component. The stand-alone simulation's parameters are tuned to the same quantities, photon yield  $Y$  and attenuation length, used in above. Figure 9.3 shows the parametrization extracted by two different



(a) Simulation with rough surface. From [77]. (b) Simulation with perfect surface.

**Figure 9.3:** Two different parametrizations based on stand-alone GEANT4 simulations including photon propagation tuned to different data sets and with different surface roughness.

simulations, whereby the one shown in Figure 9.3a is tuned to an older data set with shorter attenuation length. Furthermore, it employs rough surfaces between the fibre core and the claddings [77]. This results in an enhanced component with a short attenuation length in the order of 1 cm caused by helical skew rays. This effect is neglected in more recent simulations because it is not observed in test beam and lab measurements [77, 80]. Although the stand-alone simulations are a more fundamental approach, they provide not more information about the number of emitted photons than that used to tune them. Hence, the direct parametrization is preferred.

#### VALIDATION OF THE NUMBER OF PHOTONS PER FIBRE

The parametrization values, such as light yield  $Y$ , resolution scale  $y$ , efficiencies  $\varepsilon$  and the attenuation length  $\Lambda_{\text{attenuation}}$  are tuned according to measurements. Figure 9.4 shows a simulated distribution of the number of photons summed from both sides tuned to a measurement of MIP passing at the centre of a prototype consisting of 250  $\mu\text{m}$  square Saint-Gobain fibres. The shape of the distribution of the simulation describes the shape of the data's distribution well. Furthermore, the presented parametrization reproduces also the measured efficiencies in an OR and AND trigger configuration of the two fibre sides for thresholds of 0.5 photoelectrons and 1.5 photoelectrons within 2% at statistical uncertainties of the measurements of 1% [124]. With the exception of the AND configuration at 1.5 photoelectrons, which shows an absolute deviation of 11%. The excellent agreement of the shape of the distribution of the simulated and the measured number of photons in combination with the acceptable modelling of the efficiencies in different trigger configurations validates the employed parametrization scheme.

The attenuation length is set according to dedicated measurements. Note, that for tuning and validation of the simulation at this level, prototypes with single fibre readout are required. But most recent fibre ribbon prototypes (see section 7.2) are read out without fan-out by SiPM arrays. Thus, tuning and validation of the simulation at the single fibre level are not possible.

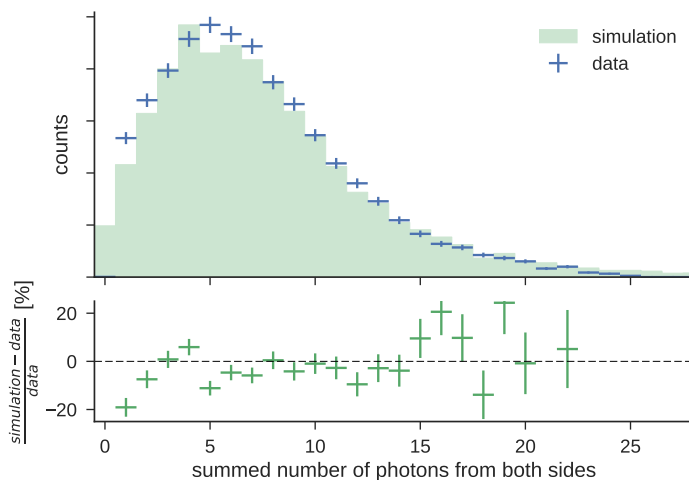


**Figure 9.4:** Number of detected photons summed over both fibre ends. Data (+) and simulation (—) tuned to MIP passing in the centre of a prototype consisting of 250  $\mu\text{m}$  thick square fibres with individual fibre readout. The lower figure shows the relative deviation of the simulation to data. Data extracted from [142].

### 9.2.3 PHOTON DISTRIBUTION AT THE SENSORS SURFACE

Photons exit the fibres under different angles with respect to the fibre axis. The sensors employ a 100  $\mu\text{m}$  thick epoxy resin on top of the active area to protect the sensors and the wire bonds. The exit angular distribution, the exit position from the fibre end, and the thickness and refractive index of this protective layer determine a photon's detection position on the detector surface. The used SiPM array's columns are, with a dimension of 1.625 mm, much larger than the ribbon thickness which is in the order of 0.9 mm. Thus the photon spread in the column ( $y$ )<sup>2</sup> direction is not simulated because the photons are detected independently of their spread in this direction. Figure 9.5 shows the probability density of photons to end up at a specific offset in column-to-column ( $x$ ) direction with respect to the fibre centre at the sensor's surface. The probability distributions for round and square fibres in the presence of 100  $\mu\text{m}$  thick epoxy resin is shown. The position on the sensor surface in the  $x$ -direction is sampled from the corresponding distribution for each photon. One SiPM column collects photons from different fibres.

### EXIT POSITION TO SENSOR COLUMN MATCHING

In a second step, the photon detection position is mapped to a SiPM column as illustrated in Figure 9.6. One-to-one mapping is not possible due to the different pitch of the ribbons, of  $\sim 255 \mu\text{m}$  and the sensor columns of 250  $\mu\text{m}$ . The offset between the sensor and ribbon

<sup>2</sup>See Figure 9.6 for coordinate system.

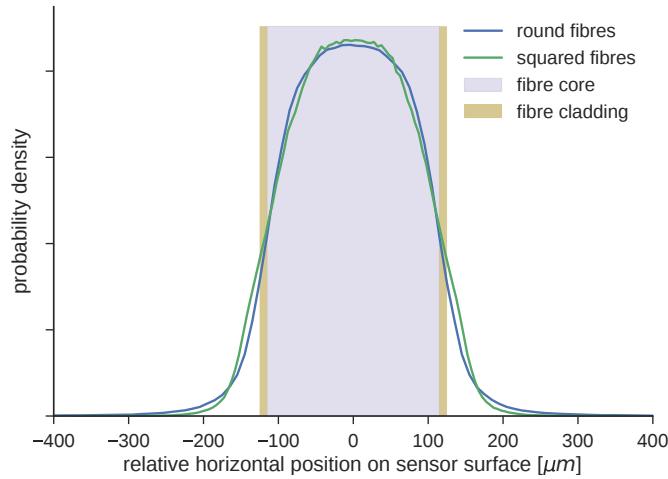


**Figure 9.5:** The probability density for photons to end up at a relative offset with respect to the fibre centre at the sensor surface. The relative offset along the SiPM column-to-column direction is shown in the presence of 100  $\mu\text{m}$  thick epoxy resin between the fibre and the active sensor surface for round (—) and square (—) fibres.

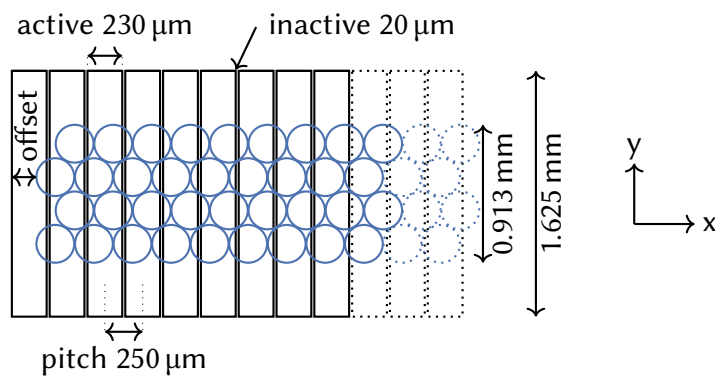


**Figure 9.6:** Front view of fibre ribbon (—) to SiPM column arrays (—) matching in the simulation framework. The fibres of the ribbon run along the z-direction.

edge is Gaussian distributed with a standard deviation<sup>3</sup> of 10  $\mu\text{m}$ , accounting for additional misalignment, and randomizing the sensor response. Photons which end up in the dead area between two columns are omitted. Table B.2 summarizes the numbering scheme for SiPM columns.

#### 9.2.4 THE PHOTON DISTRIBUTION OVER TIME

The SiPM response to all photons, potentially from multiple fibres, in one sensor column is dominated by the arrival time of the individual photons at the sensor. The detection time of a photon is derived from the interaction time of a particle with the detector, the decay constant of the scintillator, the scintillation photon's path length inside the fibre and the intrinsic SiPM time resolution. The sensor response time is determined by the ToA of the first photon inside the signal response time window at a given threshold.

#### PHOTON PRODUCTION TIME

For each photon, the scintillator's decay time, which corresponds to the photon's creation time  $\Delta t_{decay}$ , is sampled from an exponential distribution<sup>4</sup> with  $\tau_{decay}$ .

#### PATH LENGTH DISTRIBUTION

The photon's path length is difficult to access experimentally. Hence it is extracted from the dedicated fibre simulation (see chapter 8) and corresponds to geometrical considerations in combination with attenuation effects. Subsection 8.4.4 shows the distributions for perfectly smooth, round and square fibres. The relative path length  $f_{pathlength}$  of each photon, with respect to the interaction distance  $d_{interaction}$  from the fibre end, is sampled by a right-angled trapezoid distribution with relative path lengths from 1.00 to 1.13 and a linear probability decrease to 84 %. This neglects potential photons with long path lengths due to helical skew tracks. Due to the late arrival of these photons, they are of less relevance for the signal ToA determination. Furthermore, this simplified distribution disregards a peak in the distributions caused by the overlap of the photon path length distributions from core-cladding and cladding-cladding reflected rays.

The photon propagation time is given by

$$\Delta t_{propagation} = \frac{f_{pathlength} \cdot d_{interaction}}{c/n}, \quad (9.9)$$

where  $c/n$  is the speed of light in the medium.

---

<sup>3</sup>This alignment precision can be set in the configurations.

<sup>4</sup> $\tau_{decay} = 2.8$  ns for the used Kuraray SCSF-78 fibres.

### INTRINSIC SINGLE PHOTON TIME RESOLUTION (SPTR)

As described in subsection 5.2.4, typical SiPM sensors show SPTR of  $\sigma_{\text{sptr}}$  (see Table 5.1). Hence, the detection time of each photon is by convenience smeared by a Gaussian distribution with this width.

The detection time of a photon is given by

$$t_{\text{detection}} = t_{\text{interaction}} + \Delta t_{\text{decay}} + \Delta t_{\text{propagation}} + \Delta t_{\text{electronics delay}} \pm \text{measueremen} \Delta t_{\text{sptr}}. \quad (9.10)$$

#### 9.2.5 SENSOR AND READOUT ELECTRONIC RESPONSE

The response of the sensors and readout electronics to the photons is simulated in multiple steps. In a first step, SiPM dark counts and crosstalk between channels are added to each sensor. It is possible to simulate the electrical response of the sensors by summing a template single photon response waveform for each photon at its detection time  $t_{\text{detection}}$ . Figure B.6a shows the used template waveform and Figure B.6b shows an example event consisting of summed waveforms. This simulation of the full waveform is computationally expensive. Hence, in the baseline configuration, the ToA is determined by the detection time of the first photon passing the set threshold level. For a threshold level of 0.5 photoelectrons, this is the first detected photon, whereas for a threshold of 1.5 photoelectron the detection time of the second photon is selected.

Events within the ASIC's deadtime of 40 ns are merged and flagged as piled up. The advantage of the full waveform mode is that the influence of pileup to the ToA is modelled. Because of the small signals and usage of fast scintillators, this procedure is not required for the simulation of the fibre sub-detector.

### 9.3 SIMULATION SETTINGS AND VALIDATION

Whenever possible, the simulation settings are chosen according to measured values. Table 9.1 summarizes settings motivated by vendor specifications and measurements. The simulated number of photons and cluster size distributions with these unbiased settings agree well with measurements done with ribbons consisting of Kuraray SCSF-78MJ and NOL-11 fibres.

*Test beam-like* simulation conditions are compared to the DRS4 based test beam measurements to validate the simulation's settings. In the *test beam-like* simulation conditions, positively charged pions with a momentum of 160 MeV/c and isotropically distributed momentum direction are generated in the centre of the Mu3E experiment simulation. Only particles which cross the fibre ribbons in the ribbon centre within  $\pm 1$  cm around the centre and with angles below  $20^\circ$  with respect to the ribbon's normal are selected. The former guarantees constant attenuation and photon propagation distances. A variation of the propagation distance results in a smearing of the  $t_{\text{left}}-t_{\text{right}}$  distribution. The employed restriction of incident angles results in variations of path lengths below 6.5%. The photon yield is proportional to the deposited energy which in turn is proportional to the path length of a MIP in the active volume of a fibre. Hence, the variations in path length translate directly to variations in light yield.

## CHAPTER 9. THE SCINTILLATING FIBRE DETECTOR IN THE MU3E SIMULATION FRAMEWORK

**Table 9.1:** Simulation settings for round Kuraray SCSF-78MJ fibres and MuTRiG readout. The abbreviation *exp.* indicates that these values are obtained by measurements, whereas those labelled with *vendor* are references to data sheets.

setting		value		reference
scintillation decay time	$\tau_{\text{decay}}$	2.8	ns	Table 7.1 ( <i>vendor</i> )
photon yield	$Y$	8000	photon /MeV	Table 7.1 ( <i>vendor</i> )
fibres capture efficiency	$\varepsilon_{\text{capture}}$	5.4	%	subsection 4.2.1 ( <i>vendor</i> )
fibre attenuation length	$\Lambda_{\text{attenuation}}$	1.395	m	[80] ( <i>exp.</i> )
fibre crosstalk		2	%	[124] ( <i>exp.</i> )
SiPM PDE	$\varepsilon_{\text{pde}}$	40	%	section 5.3 ( <i>vendor</i> )
SiPM SPTR	$\sigma_{\text{sptr}}$	85	ps	Table 5.1 ( <i>exp.</i> )
SiPM channel crosstalk		4	%	Table 11.3 ( <i>exp.</i> )
SiPM pixel crosstalk		2	%	Table 11.3 ( <i>exp.</i> )
DAQ jitter	$\sigma_{\text{jitter}}$	200	ps	

### VALIDATION OF SIMULATED NUMBER OF PHOTONS PER PARTICLE CROSSING

Figure 9.7 shows the simulated sum of detected photons per ribbon side in a cluster induced by a single particle crossing. The distributions are fitted with the same model, a convolution of a Landau and a Poisson distribution, as described in Figure 7.3.4. To validate the simulation settings, the distribution from *test beam-like* simulation configuration is compared to the results obtained in the DRS4 based measurement in a test beam (see Figure 7.15). Their MPVs agree better than to 5 %, and the simulated and measured distributions roughly coincide. Furthermore, the simulated fibre ribbon efficiencies for *test beam-like* simulation configuration of  $(95.4 \pm 0.2) \%$  in an AND configuration,  $(95.8 \pm 0.2) \%$  in an OR configuration respectively, agree within 1.5 % with the measured values.

### VALIDATION OF DISTRIBUTION OF SIMULATED CLUSTER SIZES

Figure 9.8 shows the simulated cluster size distribution of clusters induced by a single particle crossing. The distributions are fitted with the same model as described above. The distribution from the *test beam-like* simulation configuration is compared to the result obtained in a DRS4 based measurement during a test beam (see Figure 7.14). The simulated cluster sizes, with no explicit tuning to this data set, yield a distribution with a 13 % reduced MPV but with a correct shape.

### VALIDATION OF SIMULATED TIME RESOLUTION

To reproduce the time resolution measured in test beams and in lab measurements an additional DAQ time jitter of 200 ps is added to the simulation. Figure 9.9 shows the resulting distribution of the cluster time difference  $t_{\text{left}} - t_{\text{right}}$  between the ribbon sides in a *lab-like*

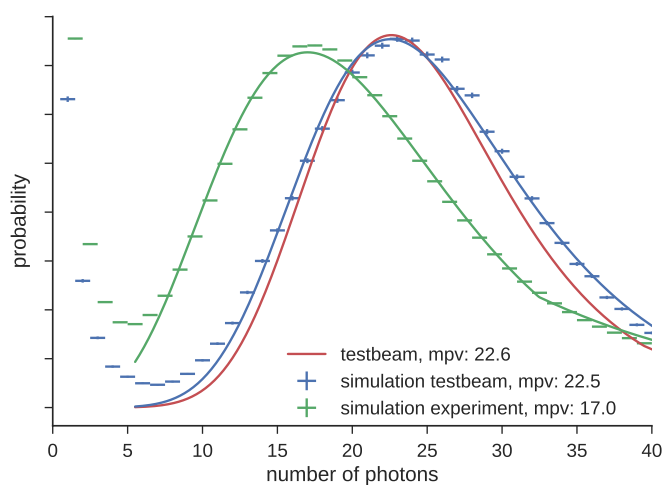


**Figure 9.7:** Simulated number of photons for *test beam-like* (—) and *experiment-like* (—) simulation configuration of one ribbon side. DRS4 based test beam measurement (—) of a 4 layer ribbon consisting of SCSF-78 fibres is shown for comparison.

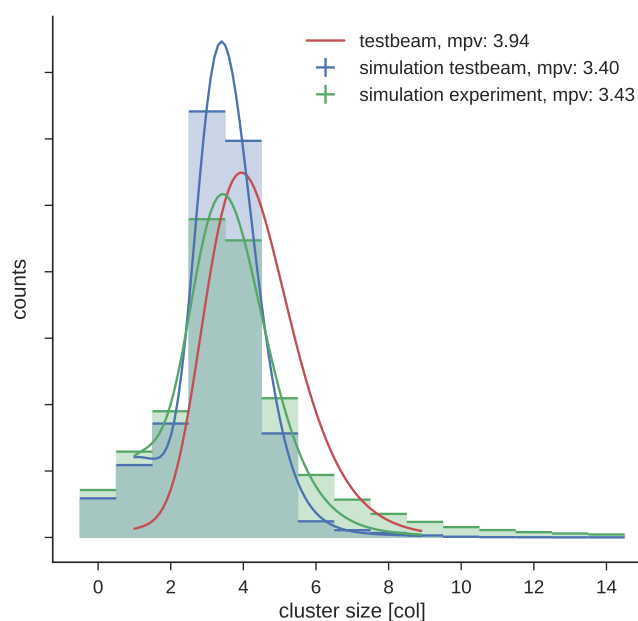


**Figure 9.8:** Simulated cluster size distribution for *test beam-like* (—) and *experiment-like* (—) simulation configuration of one ribbon side. DRS4 based test beam measurement (—) are shown for comparison.

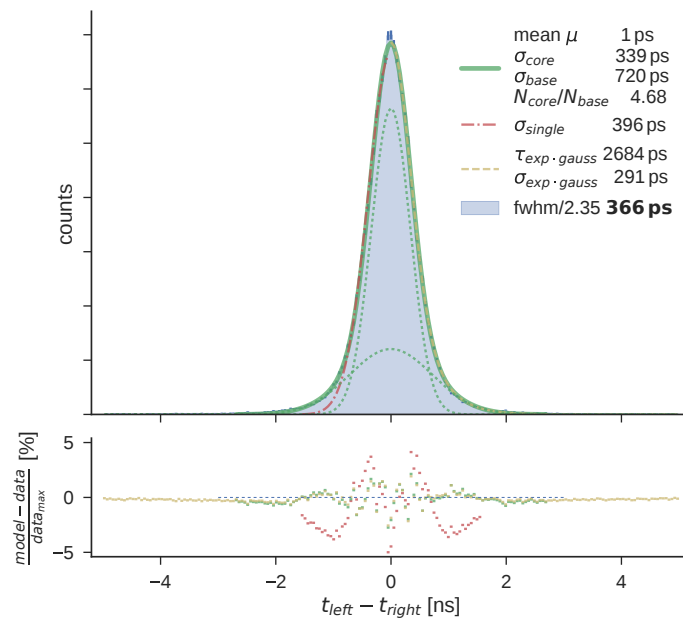


**Figure 9.9:** Simulated time resolution for *lab-like* particle crossings in a 4 layer ribbon consisting of round Kurary SCSF-78MJ fibres. *lab-like* simulation settings correspond to the irradiation of the ribbon by positrons from a  $^{90}\text{Sr}$  source at the fibre ribbon centre.

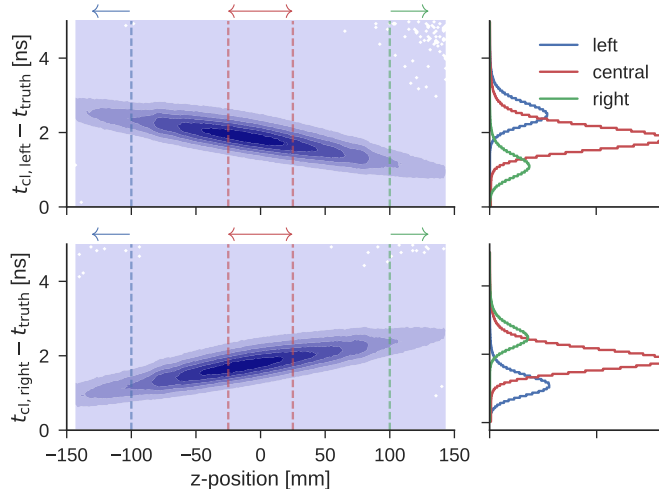


**Figure 9.10:** Simulated cluster time with respect to the Monte Carlo true interaction time of the particle with the scintillating fibres for both detector sides as a function of the true interaction position. On the right side, the projections of events in the centre (—) with  $|z| < 25$  mm, upstream (←) with  $z < -100$  mm and downstream (→) with  $z > 100$  mm are presented. Given the distance from interaction to the corresponding fibre end is known, the time of flight inside the fibres can be corrected for. Alternative, the time difference ( $t_{cl,left} - t_{cl,right}$ ) allows to determine the hit position along the fibre axis ( $z$ ).

simulation. This configuration differs from the *test beam-like* only by the type and energy of the emitted particles. Positrons from  $^{90}\text{Sr}$  decay with kinetic energies below 2 MeV are used. This corresponds to a pessimistic tuning to the lab measurement with MuTRiG (presented in chapter 11 and shown in Figure 11.24).

#### 9.4 SIMULATED PERFORMANCE OF THE SCINTILLATING FIBRE DETECTOR

The expected performance of the scintillating fibre detector is extracted from the simulation framework. The expected number of detected photons per ribbon side and cluster sizes are presented in Figure 9.7 and Figure 9.8 indicated as *simulation experiment* configuration.

The detection time at one side is given by

$$t_{\text{det}}(d) = t_{\text{particle}} + \Delta t_{\text{delay}} + \frac{d}{c/n}, \quad (9.11)$$

where  $d$  is the distance from the SiPM to the particle's interaction with the scintillating detector and  $c/n$  is the speed of light in the fibre core. Figure 9.10 shows the time resolution of the detector as a function of the particle incident position in beam ( $z$ ) direction for both ribbon sides.

Ab initio the particles incident position is not known. Their incident time is taken as the mean time of the two detector sides. Given a detector with length  $L$ , the distance from one

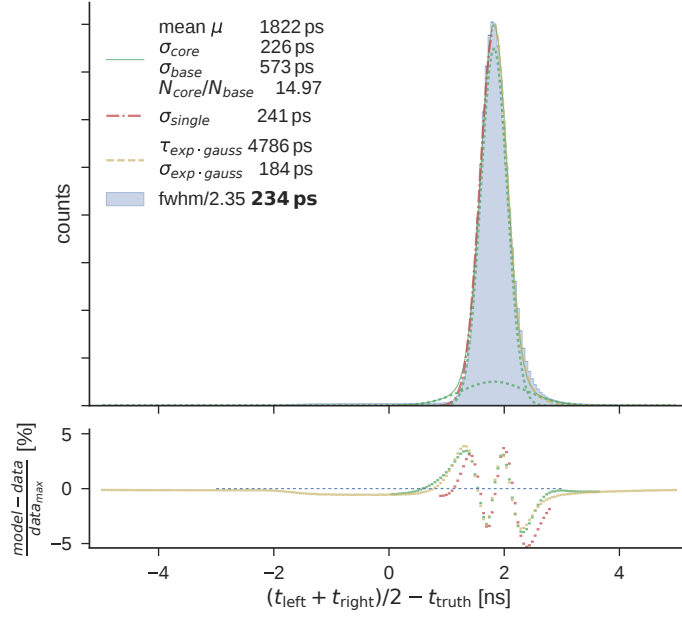


**Figure 9.11:** Simulated cluster mean time resolution as specified by Equation 9.12 with respect to the true interaction time. The offset  $\mu$  is the sum of the propagation time of the photons ( $\frac{L}{2c/n} \sim 0.8$  ns) and the simulated delay of the DAQ of 1 ns. Note the asymmetrical shape of the distribution.

side to the interaction position  $d$  cancels out:

$$t_{\text{det}}^{\text{particle}} = \frac{t_{\text{det, left}} + t_{\text{det, right}}}{2} = t_{\text{particle}} + \Delta t_{\text{delay}} \cdot \frac{\frac{d}{c/n} + \frac{L-d}{c/n}}{2} \quad (9.12)$$

$$= t_{\text{particle}} + \Delta t_{\text{delay}} + \frac{L}{2c/n} \quad (9.13)$$

Figure 9.11 shows the simulated time resolution extracted as stated above. If the particle's hit position is known, either from tracking or less precise from the time difference ( $t_{\text{left}} - t_{\text{right}}$ ) in the fibre detector itself, the propagation time can be corrected for  $t' = t_{\text{det}}^{\text{particle}} - \frac{d}{c/n}$ .

Figure 9.12 shows the modified, i.e. using the hit position information, distribution of the time difference ( $t'_{\text{left}} - t'_{\text{right}}$ ) and the time resolution of a single fibre ribbon side with respect to the true particle interaction time. The width of the two distributions scales with the expected factor of  $\sqrt{2}$ . Different than expected from previous studies (see [143]), it turns out, that as cluster time extraction from two linked clusters of opposite sides by  $\min(t_{\text{left}}, t_{\text{right}})$  performs worse than their mean time.

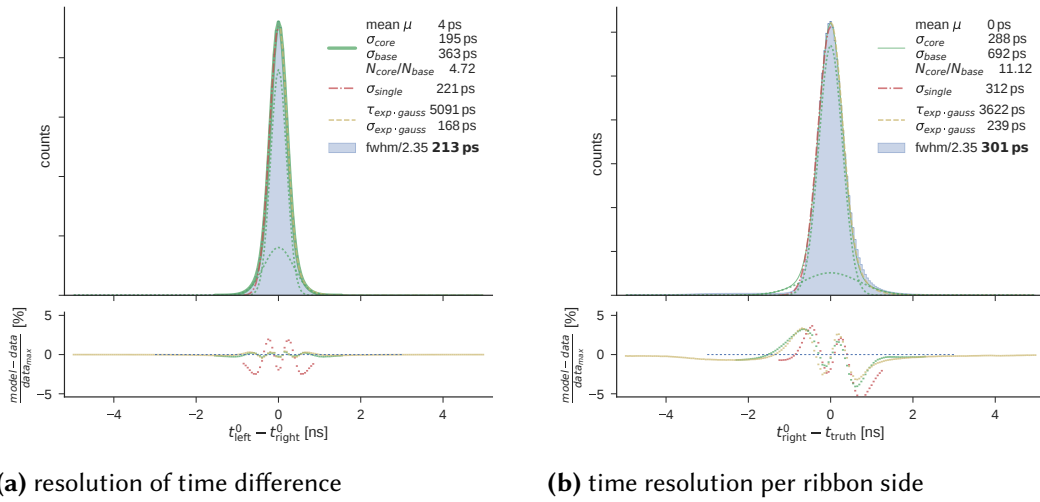


**Figure 9.12:** Simulated cluster time resolution which is corrected for the propagation time in the fibres. This correction requires the knowledge of the hit position along the beam line-direction ( $z$ ) from tracking. The extraction of the time resolution per ribbon side is only possible with this correction.



# 10

## Timing in the Reconstruction and Analysis Framework

The MU3E reconstruction framework consists of a triplet-based track finding algorithm (see subsection 2.4.3) and a vertex fit. They are used in different variations: online for event filtering and offline for analysis. The detector responses are grouped into frames based on their timestamps<sup>1</sup>. Out of all events within such a frame track candidates are built. Currently, reconstruction frames of 50 ns are used, which is roughly aligned to the silicon pixel's time resolution of  $\mathcal{O}(14\text{ ns})$ . The timing information from the fibre and tile detectors is linked only offline to the reconstructed tracks. It is available for suppression of combinatorial background and mis-reconstructed track candidates.

The linking of additional time information to reconstructed track candidates, which was developed in the scope of this thesis, is described in section 10.1. This is followed by a description of the vertexfit in section 10.2 which combines three track candidates to signal candidates. In particular the handling of the timing is described. The resulting impact of this additional time information on background suppression and rejection of mis-reconstructed track candidates, as well as the influence of the scattering in the sub-detector on the momentum resolution, are studied in this work and described in section 10.3.

### 10.1 TIME-TO-TRACK MATCHING

Additional time information from the scintillating fibre detector and the scintillating tile detector is assigned to track candidates after track finding. In the case of the scintillating fibre detector, firstly clusters are built per ribbon side which are merged from both sides in a second step. Thirdly, fibre detector clusters within a defined distance from a track candidate's extrapolated fibre detector crossing position are assigned to this track. The cluster time information is available in further analysis steps.

---

<sup>1</sup>Currently 8 ns timestamps are foreseen.

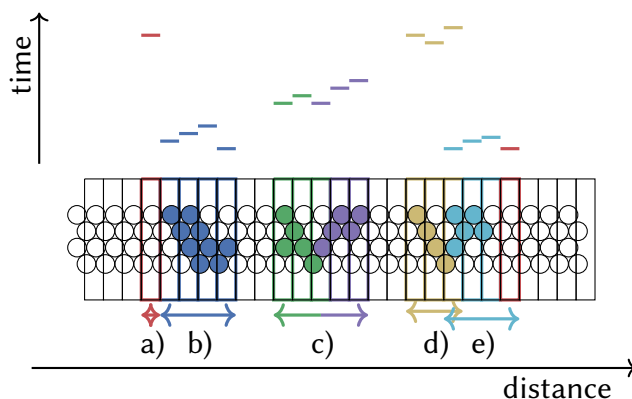


**Figure 10.1:** Sketch of firing fibres due to crossing particles and matching to SiPM column. The detection time in the individual columns is indicated in a vertical time-direction. Randomly firing cells due to dark count rates are added (—). The resulting clusters a)-e) are indicated at the bottom. Cluster a) is a single hit due to dark counts; b) is a ordinary cluster which is not merged with a) due to the time difference of the hits; Cluster c) is caused by pileup of two different particle crossings; The clusters d) and e) are separated due to the time difference of their hits, where cluster e) includes a dark count hit in a consecutive channel which shows a compatible time.

### 10.1.1 FIBRE DETECTOR HIT CLUSTERING

Due to potential clustering on FPGA level the fibre detector hits are built at a first step individual for the up- and downstream side. Only the data from one side is available on the experiment's front-end FPGAs. The MuTRIG-based DAQ provides 50 ps binned timestamps of photon detection time in the individual SiPM columns. No signal amplitude or charge information is used in the current design. Potentially, a flag indicating signals larger than a specified  $E$ -threshold will be available. Clusters are built out of hits in consecutive columns of the 128 channel SiPM array attached to one side of a fibre ribbon. The time span of a cluster, the time difference between the earliest and the latest hit, is limited to  $80 \text{ ns}^2$ . This default setting corresponds to all hits within one reconstruction frame of 50 ns. Figure 10.1 shows a sketch of potential cluster configurations. In a second step, the clusters from both sides are linked if at least one hit is inside the specified time window of the other and if the clusters have an overlap in  $\phi$ -position they span<sup>3</sup>.

### 10.1.2 FIBRE DETECTOR CLUSTER TO TRACK CANDIDATE MATCHING

Depending on the track candidate type, potentially one or two fibre detector clusters are assigned. The track candidates are grouped in three classes by the number of pixel tracking layers they contain hits in, as illustrated in Figure 10.2.

<sup>2</sup>Set by CLUSTER\_DT\_MAX.

<sup>3</sup>Specified by CLUSTER\_SIDE\_TOLERANCE.

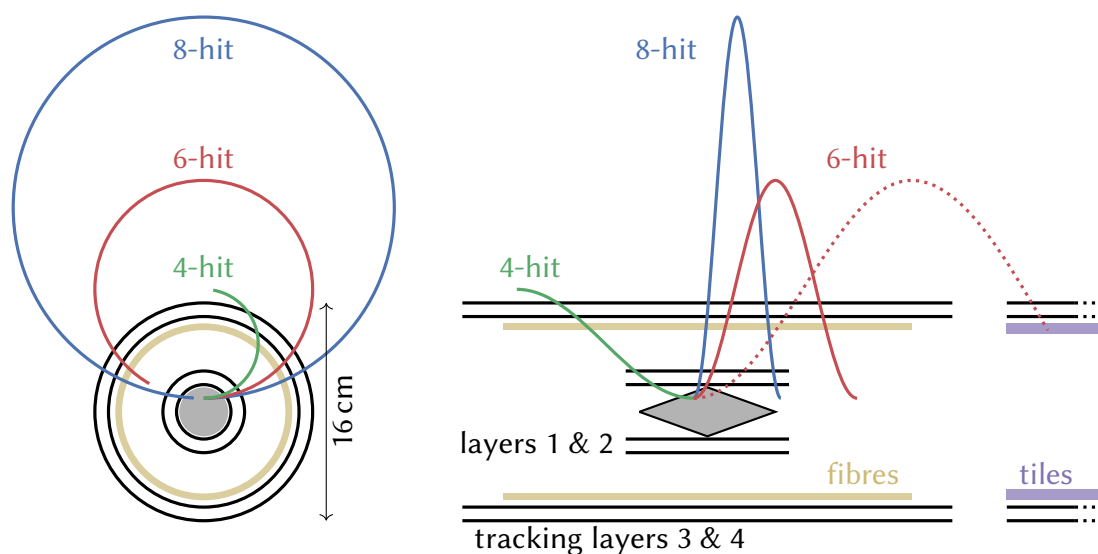


**Figure 10.2:** Track candidate classification by the number of pixel tracking layers they contain hits in into short 4-hit (→) and long 6-hit (→) and 8-hit (→) track candidates. A transverse (left) and longitudinal (right) cut through the detector is shown.

#### TRACK CANDIDATE CLASSIFICATION

**4-HIT TRACKS** All track candidates need to pass at least all four tracking layers once. Track candidates which are neither linked to another recurring 4-hit track candidate nor to recurring hit candidates in the outer detector barrels are in this category.

**6-HIT TRACKS** This category consists of 4-hit track candidates which are linked to two hits in the outer pixel layers. They are predominantly linked to hits in the outer detector barrels where the particles are stopped in the scintillating tile detector or the support structure, for example the beam pipe.

**8-HIT TRACKS** This category consists of two linked 4-hit tracks corresponding to recurring track candidates in the central detector barrel. Track candidates linked outside the outermost tracking layer are distinguished from the ones connected between two hits of the most central layer.

#### MATCHING TO TRACK CANDIDATE'S INTERSECTION WITH FIBRE DETECTOR

A track candidate is propagated to its first intersection with a plane at the centre of a fibre ribbon. All clusters with a size of at least two columns<sup>4</sup> within a distance of

$$d(n_{\text{cluster}}) = 500 \mu\text{m} + n_{\text{cluster}} \cdot \frac{250 \mu\text{m}}{4} \quad (10.1)$$

<sup>4</sup>Specified by LINK\_NH\_MIN.

## CHAPTER 10. TIMING IN THE RECONSTRUCTION AND ANALYSIS FRAMEWORK

**Table 10.1:** Scintillating fibre (top) and tile (bottom) detector’s time resolution of 4-, 6- and 8-hit tracks of all involved detector crossings at the hit position (pixel-layer) and propagated back to the first pixel layer. 6 and 8-hit tracks can comprise a first and a second fibre hit if at least one is present the mean time is built (combined). The efficiency states the fraction of track candidates of a given track type with timing from the considered detector crossing (combined corresponds to an OR condition).

class track type	crossing	time resolution $\sigma$ [ns]		efficiency [%] per track type
		at hit position	at first si layer	
4-hit tracks	first	$262.6 \pm 0.5$	$260.9 \pm 0.5$	94.1
6-hit tracks	first	$262.6 \pm 0.5$	$261.3 \pm 0.7$	97.1
	second	$271.8 \pm 1.5$	$270.7 \pm 1.3$	30.4
	combined		$205.1 \pm 1.0$	97.9
8-hit tracks	first	$264.7 \pm 1.6$	$262.8 \pm 1.5$	97.0
	second	$268.2 \pm 1.7$	$268.7 \pm 1.7$	94.1
	combined		$256.8 \pm 1.8$	99.0
6-hit tracks	only tile hit		$82.5 \pm 0.2$	
	combined tile & fibre hits		$82.3 \pm 0.1$	

are linked. 6-hit tracks are further propagated to a potential second intersection with the fibre detector. If such an intersection exists, the procedure described above is repeated for this detector crossing. 8-hit tracks consist of two linked 4-hit tracks; the matched fibre clusters from the individual short track candidates are linked to the long track.

### 10.1.3 PIXEL AND TILE DETECTOR TIME MATCHING

Each tracker hit also contains a timestamp from the MUPix sensors. The current sensor shows a time resolution of  $\mathcal{O}(14 \text{ ns})$  binned in timestamps of 8 ns. The tile detector, with a time resolution better than 50 ps provides timestamps from the same ASIC as the fibre detector with 50 ps bins. 6-hit track candidates are propagated to the tile detector surface at the outer detector barrels. The closest hit in a tile within  $\pm 2$  tiles in beam direction is linked to the candidate. All hits in the direct neighbours, as well as next-neighbours in the outward z-direction, are summed up. The mean time of all involved hits defines the time of the hit in the tile detector.

### 10.1.4 TRACK CANDIDATE TIMING

The time information of all linked detector hits of a track candidate is propagated back to the first hit  $t^{(1)}$  in the innermost silicon tracker layer. Later, once a vertex candidate is found, the track candidate is propagated back further to obtain the track’s vertex time  $t(v)$ . The candidate’s time is given by the weighted mean of all its hits in the pixel tracker, scintillating

**Table 10.2:** Default cuts applied to identify signal candidates. # stands for “number of”.

variable	cut value	comment
$\chi_{\text{vertex}}^2$	<35	3 degrees of freedom
$ \vec{p}_{eee}  =  \sum \vec{p}_i $	<10 MeV/c	
distance: $\vec{v}$ to target	<1 mm	closest approach
# crossed tracking layers	$\geq 6$	6- and 8-hit tracks
$\chi_{\text{timing}, t_s}^2$	<	no default yet

fibre and tile detector

$$\bar{t}^{(1)} = \frac{\sum_{i=1}^{\text{hits}} \frac{t_i^{(1)}}{\sigma_i^2}}{\sum_{i=1}^{\text{hits}} \frac{1}{\sigma_i^2}} \quad (10.2)$$

A constant time resolution  $\sigma_i$  per sub-detector hit is assumed. Table 10.1 summarizes the time resolution from the timing detectors for each track type (see subsection 10.1.2) for the individual, as well as combined, sub-detector crossings. The pixel timestamps are not used in the presented implementation for more than assigning the track candidates to the correct reconstruction frame.

## 10.2 VERTEXFIT: SIGNAL CANDIDATES

Out of all reconstructed tracks within a reconstruction frame, signal candidates are chosen and tested for a common vertex. Signal candidates consist of three tracks, two positively charged ( $e^+$ ) and one with negative electrical charge ( $e^-$ ). The curvature in the magnetic field determines a track candidate’s charge. A potential common vertex position  $\vec{v}$  is estimated by the minimization of the scattering angles at the first tracking layer given the reconstructed track momentum from the track finding algorithm described above. The scattering angle minimization utilises the following  $\chi^2$ -function:

$$\chi^2(\vec{v})_{\text{vertex}} = \sum_{i=1}^{\text{tracks}} \frac{\Phi_{\text{MS},i}(\vec{v})^2}{\sigma_{\phi,i}^2} + \frac{\Theta_{\text{MS},i}(\vec{v})^2}{\sigma_{\theta,i}^2} \quad (10.3)$$

The Multiple Scattering angles  $\Phi_{\text{MS}}$  and  $\Theta_{\text{MS}}$  follow the notation in Figure 2.6. The time of each track is propagated back from the innermost pixel layer ( $t^{(1)}$ ) to the time at the found vertex position  $t^{(v)}$ . In principle, the  $\chi^2$  could be extended by a time dimension to  $\tilde{v} = (\vec{v}, t^{(v)})$ .

### 10.2.1 SIGNAL CANDIDATE TIMING CUTS

Table 10.2 lists the default cuts a signal candidate fulfils; no default timing cuts exist yet. The time coincidence of signal candidates is estimated by two methods. The first uses the normal-

ized weighted variance for the times at  $\vec{v}$ :

$$\chi_{\text{timing}}^2(\vec{v}) = \frac{\sum_{i=1}^{\text{tracks}} \frac{(t_i^{(v)} - \bar{t}^{(v)})^2}{\sigma_i^2}}{\sum_{i=1}^{\text{tracks}} \frac{1}{\sigma_i^2}} \quad (10.4)$$

where  $\bar{t}^{(v)}$  is the weighted mean of the three tracks. The primary task of the timing cuts on track candidates is to suppress the dominant Bhabha background. Therefore a second method assuming Bhabha-like topologies is employed. The positron-electron pair with the smaller time difference is treated as the Bhabha pair ( $e_{\text{pair}}^+$ ,  $e_{\text{pair}}^-$ ) with

$$\sigma_{\bar{t}_{\text{pair}}}^2 = \frac{1}{\sigma_{e_{\text{pair}}^+}^2 + \sigma_{e_{\text{pair}}^-}^2} \quad (10.5)$$

$$\bar{t}_{\text{pair}} = \sigma_{\bar{t}_{\text{pair}}}^2 \left( \frac{t_{e_{\text{pair}}^+}}{\sigma_{e_{\text{pair}}^+}^2} + \frac{t_{e_{\text{pair}}^-}}{\sigma_{e_{\text{pair}}^-}^2} \right). \quad (10.6)$$

The time separation is given by

$$t_s = \left| \frac{t_{e^+} - \bar{t}_{\text{pair}}}{\sqrt{\sigma_{\bar{t}_{\text{pair}}}^2 + \sigma_{e^+}^2}} \right|. \quad (10.7)$$

Figure 10.3 shows the distribution of  $t_s$  for signal and Bhabha events.

### 10.3 IMPACT OF THE SCINTILLATING FIBRE DETECTOR

The time information from the scintillating fibre detector is used to suppress combinatorial background and to reject mis-reconstructed, predominantly wrong charge assignment, tracks. On the downside, the material of the fibre sub-detector with its radiation length of  $\sim 0.5\% X_0$  causes significant scattering which impacts the experiment's momentum resolution and reconstruction efficiency. For reference, the radiation length of a silicon tracking layer including support structure is projected to be about  $0.1\% X_0$  and  $0.15\% X_0$  for the Mylar target.

#### 10.3.1 BACKGROUND SUPPRESSION BY TIME INFORMATION

Different simulation modes are used to study the suppression of combinatorial background through the time information. The expected background topologies are needed to estimate the suppression by the timing cuts whereas signal-like events are required to study the inefficiencies added by this cuts. Default  $\mu \rightarrow eee$  signal like events are generated with decay products randomly distributed in the allowed phase space. Table 10.3 gives an overview of the abundance of the different track types in the different simulation modes.

**Table 10.3:** Abundance of different track types in different simulation modes: the actual muon decay is dominated by Michel decays,  $\mu \rightarrow eee$  signal decays and Bhabha background. *Rec* stands for reconstructed by the track finding algorithms and *cand* for tracks which are part of a signal candidate triplet which fulfils the cuts presented in Table 10.2.

track type	fraction [%]				
	Michel rec	$\mu \rightarrow eee$ rec	$\mu \rightarrow eee$ cand	Bhabha rec	Bhabha cand
4-hit tracks	24.7	25.1	20.1	26.0	24.2
6-hit tracks	65.4	65.0	68.2	63.9	60.6
8-hit tracks	9.9	9.9	11.7	10.1	15.2
tracks which reach the tiles	43.2	41.3	42.7	42.2	32.2

### SIMULATION OF COMBINATORIAL BACKGROUND FOR TIME SUPPRESSION STUDIES

The dominant combinatorial background consists of the superposition of a positron from a Michel decay which undergoes Bhabha scattering with an electron in the target material, with a second positron from another Michel decay. Besides the vectorial momentum ( $\sum \vec{p}_i = 0$ ), the energy ( $\sum E_i = m_\mu$ ) and spatial vertex constraints, the combinatorial background of this topology is additionally suppressed by the requirement of a time coincidence. It is assumed, that the time suppression factorizes from the other suppression factors. Hence topologies of Bhabha pairs in combination with a positron with a common vertex, and which also fulfil the momentum and energy signal candidate cuts shown in Table 10.2 are generated at a common vertex. Weighted events are used to speed up the simulation. The weight of an event is defined by the matrix element of the Bhabha scattering and the probability of the two Michel decays.

Time suppression of combinatorial background with the given event topology is studied through the random distribution of the decay time of the additional Michel positron,

### ACHIEVABLE BACKGROUND SUPPRESSION

Figure 10.3 shows the distribution of the time separation, as defined in Equation 10.7, for signal and Bhabha background events. Furthermore, a detector with a perfect Gaussian distributed times according to the resolutions and efficiencies stated in Table 10.1 and track abundance as summarized in Table 10.3 is simulated denoted by reference model. While the background events are distributed uniformly, the distribution of signal candidates peaks towards zero. Note that the distribution of events from the simulation framework shows a larger tail than the reference model caused by tails in the simulated time resolution distribution with respect to a Gaussian shape.

The tracker is assumed to provide time information precise enough to assign the hits to individual 50 ns reconstruction frames. In the presented studies no further time information from the pixel tracker is used. Figure 10.4a shows the signal selection efficiency of the timing cut and the Bhabha background suppression due to the additional time information from

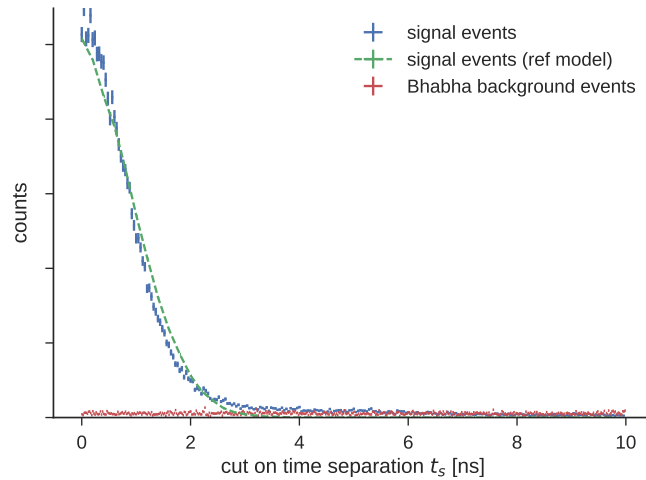


**Figure 10.3:** Distribution of the time separation  $t_s$  for signal (—, +) and Bhabha background (—, +) events. A reference model (---, +) with event times following perfectly Gaussian distribution shown for comparison. The signal events from the simulation framework (—, +) show larger tails than the reference model (---, +). The different distribution of signal and background events is used to distinguish them statistically.

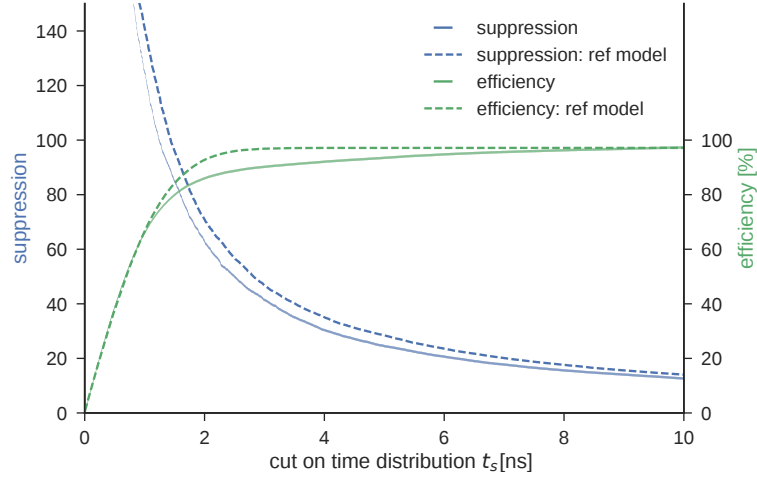
the scintillating fibre and tile detector. Only track candidates with all three tracks detected in the timing detectors are shown. Such track candidates are denoted as *timing required*. This requirement results in a loss of signal efficiency of 2.7 %. Figure 10.4 shows the achievable suppression of Bhabha background by time information as a function of the signal event selection efficiency. The suppression is displayed for *all* events and for *timing required* events where the inefficiency due to this requirement is taken into account. The same reference model as above is shown as comparison. The tails in the simulated event time distributions cause the suppression to be slightly smaller than in the reference model. The efficiency converges slower towards one. Furthermore, the results obtained by cutting on  $\chi_{\text{timing}}^2$ , as described in Equation 10.4, is shown. For Bhabha background, a cut on the time separation  $t_s$  performs better.

The working point of the time cut can be adjusted by the needs of an analysis, as the DAQ works independently of these cuts. At a signal selection efficiency of 80 % a Bhabha background suppression of  $\mathcal{O}(85)$  can be achieved.

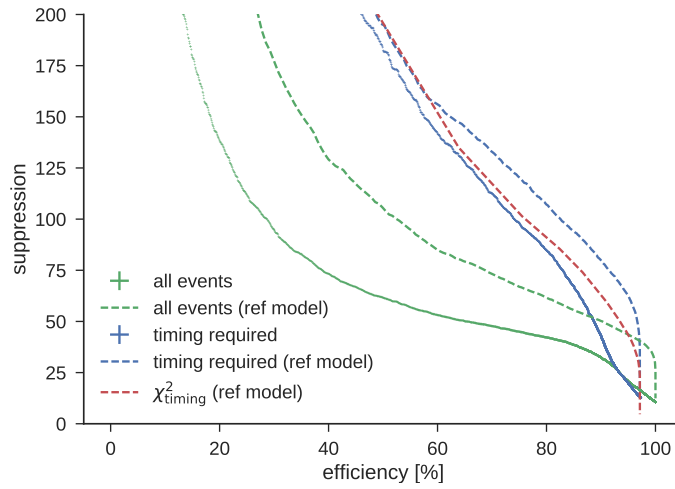
The performance of the individual sub-detectors, either fibre or tile, for the different cuts are illustrated in Figure 10.5a. In the presence of only the tile detector, significant suppressions are only achieved<sup>5</sup> if all three particles of a candidate end up in this sub-detector. Hence, the efficiency for long tracks reduces to  $(53\%)^3 \approx 15\%$ . In the sole presence of the fibre detector and perfectly Gaussian distributed event times the suppression at a given efficiency is reduced to  $(66.7 \pm 0.5)\%$ . Both timing detectors are required to achieve the presented suppressions.

---

<sup>5</sup>for cuts on  $t_s$ .

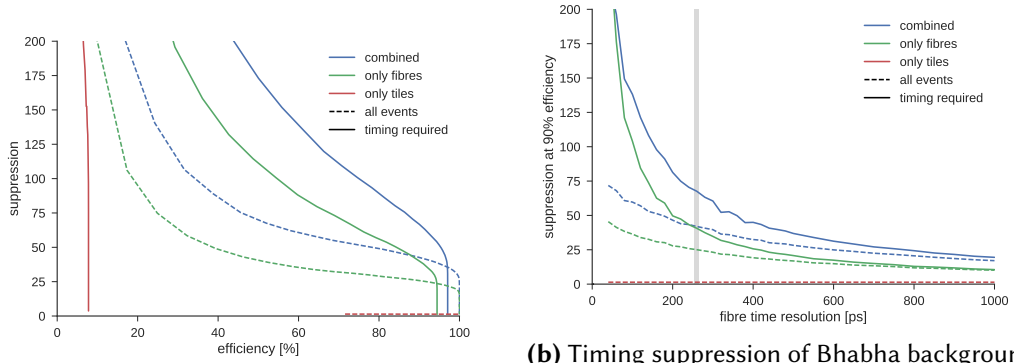


(a) Additional Bhabha background suppression factor due to the timing detectors and signal selection efficiency as a function of the cut on time separation  $t_s$ .



(b) Suppression versus efficiency for all track candidates ( $\rightarrow$ ) and with *required timing* ( $\leftarrow$ ) for all three tracks. Furthermore, the performance of a cut on  $\chi^2_{\text{timing}}$  ( $\dashrightarrow$ ) can be compared to the default cut on  $t_s$ .

**Figure 10.4:** Suppression of Bhabha background due to the time information from the fibre and tile sub-detectors in relation to the relative signal selection efficiency. The additional suppression within 50 ns reconstruction frames is presented. Either *all events* or only those candidates which all three tracks have a hit in the timing detectors (*timing required*) can be used. A reference model (*ref model*) as in Figure 10.3 is shown for comparison.



(a) Timing suppression of Bhabha background as a function of the relative selection efficiency of signal candidates.

(b) Timing suppression of Bhabha background at relative signal selection efficiency of 90 % as a function of the fibre detector's mean resolution. The expected resolution of 260 ps is highlighted.

**Figure 10.5:** Timing suppression of Bhabha background in the presence of only fibre detector (—), only the tile detector (—) and the combination of the two detectors (—) The dashed lines (---) show the suppressions if *all events* are used, whereas the solid lines (—) show the suppression if timing is required for all three tracks of a candidate (*timing required*). The here used reference model, where the event times are distributed according to a perfect Gaussian, yields upper limits.

The dependency of the suppression on the fibre detector's resolution at a relative signal selection efficiency of 90 % is illustrated in Figure 10.5b. Purely Gaussian time distributions are employed to obtain upper limits. Small improvements in the detectors time resolution show significant effect on the possible Bhabha background suppression.

### 10.3.2 MIS-RECONSTRUCTION IDENTIFICATION BY TIME INFORMATION

In addition to background suppression, the scintillating fibre detector provides an excellent tool to reject mis-reconstructed track candidates. In particular tracks with two crossings of a timing detector, either two times in the fibre detector or once in the fibre detector and once in the tile detector, can be efficiently rejected. This corresponds to almost all 6- and 8-hit tracks. The baseline configuration for the search for  $\mu \rightarrow eee$  requires three such "long" tracks. As an example, Figure 10.6 shows the path length of 8-hit tracks between two fibre crossings as a function of the measured time between them. These are tracks which recur into the central part. The different branches in the left plot correspond to the combination of different segments of recurling tracks. The branches with  $\Delta t_{\text{fibres}} < 0$  are assigned the wrong charge and hence the wrong rotation direction. Only the track candidates indicated in blue are correctly reconstructed; the tracks in the other branches correspond to mis-reconstructed track candidates. Most of them confuse recurling track segments. In the right plot, the velocity  $v = \text{distance}/\Delta t$  of the tracks in terms of the speed of light is shown. The different branches in the left plot correspond to the distinct peaks in this spectrum. The accurately reconstructed tracks are shown again in blue and peak at  $v = 1$ . By cutting on this reconstructed velocity

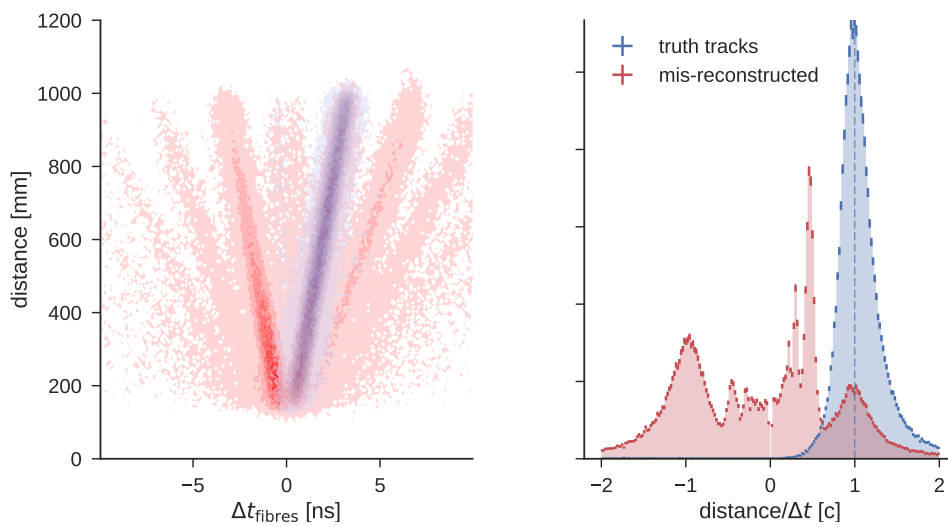
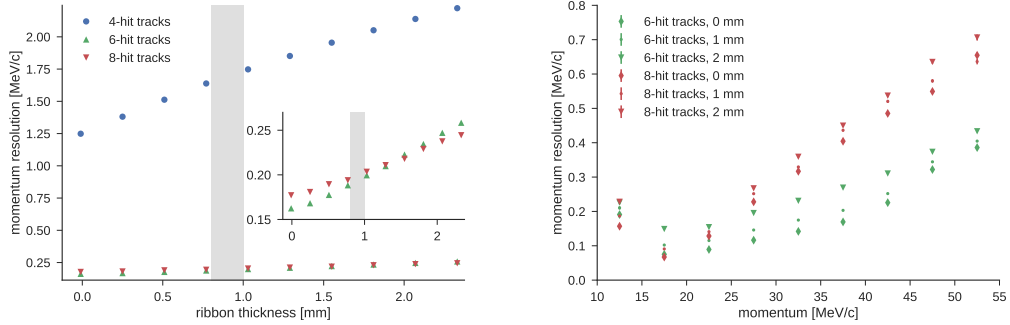


**Figure 10.6:** Correct (—) and mis-reconstructed (—) 8-hit track candidates with two hits in the fibre detector. The left plot shows the correlation between the length of the trajectory of a track candidate between the two fibre hits and the time difference between them. The different branches correspond to the combination of different segments of recurring tracks. The right plot shows the corresponding velocity of the track candidates  $v = \text{distance}/\Delta t$  in terms of speed of light  $c$ . The different branches in the left plot correspond to the peaks in this spectrum. Track candidates with  $\Delta t < 0$ , respectively  $v < 0$ , have a wrong charge assignment; hence the wrong rotation direction.



(a) Momentum resolution for single tracks as a function of fibre ribbon thickness. The targeted fibre ribbon thickness of  $\sim 0.9$  mm is highlighted.

(b) Momentum resolution of single tracks as a function of the particle momentum in the absence of a fibre detector, in the presence of a 1 mm and a 2 mm thick ribbon.

**Figure 10.7:** Momentum resolution of single track candidates grouped into 4-hit ( $\bullet$ ), 6-hit ( $\blacktriangle$ ) and 8-hit ( $\blacktriangledown$ ) tracks. The momentum resolution of long (6- and 8-hit) tracks is improved over short (4-hit) tracks due to their recurving. The effect of the fibre detector is more pronounced for 6-hit than 8-hit tracks.

$v$ , the correctly reconstructed tracks can be separated from the mis-reconstructed ones. Track candidates with a wrong charge assignment,  $\Delta t_{\text{fibres}} < 0$  or  $v < 0$ , are identified efficiently.

### 10.3.3 SCINTILLATING FIBRE DETECTOR IMPACT ON MOMENTUM RESOLUTION AND RECONSTRUCTION EFFICIENCY

The possibility of additional suppression of Bhabha background and rejection of mis-reconstructed track candidates due to the time information from the fibre detector comes with extra material in the experiments active volume. This material causes significant scattering which impacts the experiment's momentum resolution and reconstruction efficiency. Figure 10.7 shows the momentum resolution as a function of the fibre ribbon thickness. Motivated by the improved momentum resolution of long 6- and 8-hit tracks, due to their recurving, only such tracks are used in the default analysis. The effect of the additional material of the fibre detector is more pronounced for 6-hit than for 8-hit tracks. At a detector thickness of 0.9 mm, the momentum resolution of 6-hit track degrades by  $(31 \pm 1)$  keV/c, corresponding to  $(19.4 \pm 0.6)\%$ , whereas the resolution of 8-hit tracks degrades by  $(22 \pm 1)$  keV/c, corresponding to  $(12.2 \pm 0.6)\%$ .

The momentum resolutions of the single tracks combine to the resolution of invariant mass of a signal candidate  $m_{eee}$ . Figure 10.8 shows the resolution of  $m_{eee}$  and the relative reconstruction efficiency of signal events as a function of the fibre ribbon thickness. The relative reconstruction efficiency is stated with respect to the absence of the fibre sub-detector for signal selection as described in section 10.2. Only long tracks, e.g. 6- and 8-hit tracks, are used. The signal resolution and relative reconstruction efficiency show a linear behaviour in the ribbon thickness which is proportional to the scattering. For a fibre ribbon thickness of 0.9 mm,

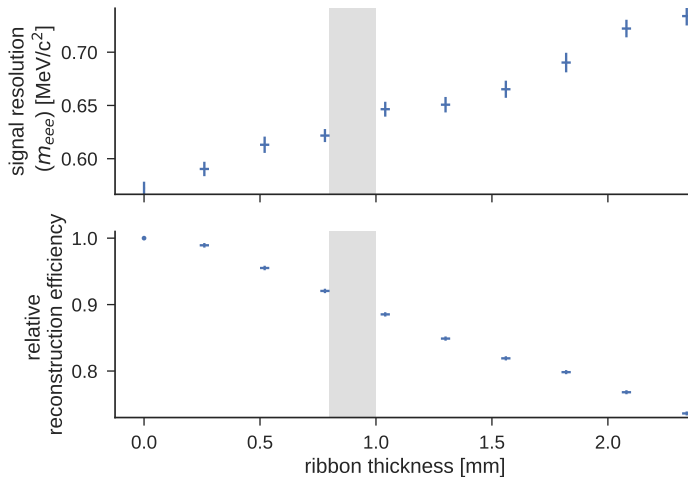


**Figure 10.8:** Signal resolution in terms of the invariant mass of the three tracks of a candidate  $m_{eee}$  (top) and the relative reconstruction efficiency (bottom) with respect to the absence of the fibre detector as a function of the fibre ribbon thickness. The planned ribbon thickness  $\sim 0.9$  mm is highlighted. The signal resolution is stated for signal selection as summarized in section 10.2.

the signal resolution degrades by  $(62 \pm 1) \text{ keV}/c^2$ , which corresponds to  $(10.8 \pm 0.2) \%$ .

Based on this studies, the upper limit of the fibre detector material budget of 1 mm plastic scintillator was set.



**Part IV**  
**DAQ and Integration**



# 11

## MuTRiG

The analogue SiPM signals from the fibre sub-detector are digitized by the custom mixed-mode ASIC MuTRiG developed by the Kirchhoff Institute for Physics at the University of Heidelberg in the scope of the Mu3E experiment. section 6.3 gives an detailed description of the ASIC.

In this chapter, the performance of prototypes described in chapter 7 is confirmed in a setup where the sensors are read out by MuTRiG. In a first part, this setup and DAQ system developed in the scope of this thesis to readout fibre ribbon prototypes with this ASIC are presented. Followed by an outline of the measurement and analysis procedure which can be understood as a user's guide. The performance of the fibre ribbon prototypes read out by MuTRiG ASIC, in the following also called simply MuTRiG, is discussed in the last part.

### 11.1 MuTRiG SETUP AND DAQ

The utilized MuTRiG setup is developed by KIP<sup>1</sup> at the University of Heidelberg, the same group that also designed the ASIC. More details can be found in [122, 144, 145]. To test the MuTRiG in the scope of the Mu3E scintillating fibre detector an adaptor to the same setup as used with the DRS4 readout (see chapter 7) was used.

A custom DAQ FPGA board, also developed at KIP, called FLYSPY is available. It provides a USB 2.0 based DAQ for STiC and MuTRiG comprising a CYPRESS EZ-USB FX2LPTM micro-controller. The acquisition rate with the default firmware is limited to  $\mathcal{O}(300 \text{ events/s})$ , which was increased up to  $\mathcal{O}(700 \text{ kevents/s})$  in the scope of this thesis. In principle it is possible to buffer the events on the FPGA, hence acquire data as long as this buffer is not full, followed by a longer readout cycle.

Since the data acquisition for the Mu3E scintillating fibre detector requires thresholds at the single photon level, the full SiPM dark rate needs to be digitized. This results in a few 100 kevents/s per channel. Furthermore, MuTRiG is designed to handle up to 1.1 Mevents/s per channel. The FLYSPY DAQ is not suited for such data rates. Hence, a MuTRiG DAQ utilizing

---

<sup>1</sup> Kirchhoff-Institute for Physics.

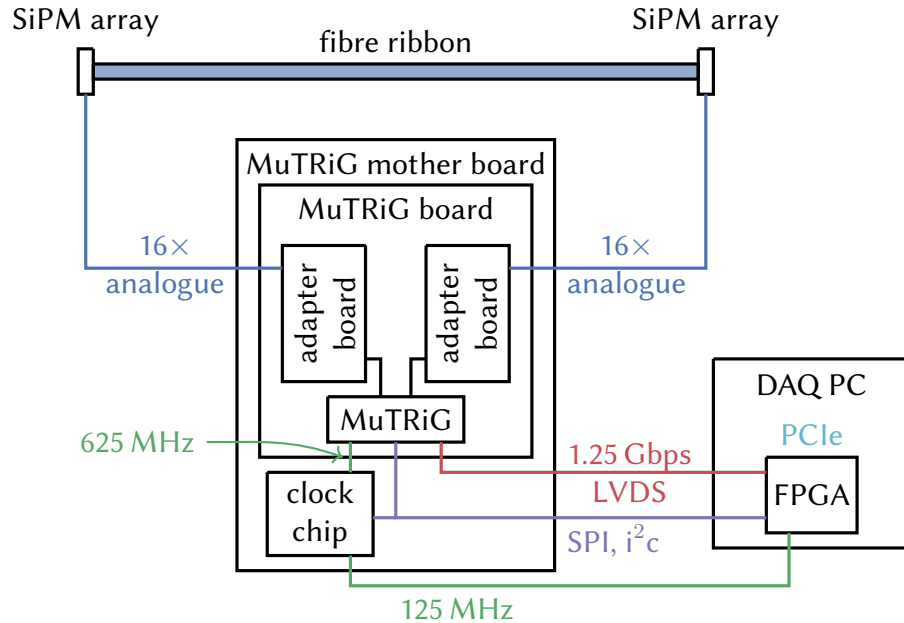


**Figure 11.1:** Diagram of the MuTRiG setup for fibre ribbon characterization. The analogue signals (—) from the SiPM arrays from both fibre ribbon sides are connected via adapter boards to the MuTRiG hosted by the MuTRiG board. The MuTRiG mother board provides the ASIC’s supplies including the 625 MHz (—) reference clocks. A 1.25 Gbps LVDS link (—) connects the chip with the FPGA which is located inside the DAQ computer. They communicate through a PCIe (—) interface. The FPGA provides SPI and I<sup>2</sup>C slow control for the readout ASIC and clock chip (—), as well as a 125 MHz system reference clock (—).

the collaboration’s Peripheral Component Interconnect Express (PCIe) based Direct Memory Access (DMA) developments has been realized in the scope of this thesis to read out fibre ribbon prototypes with MuTRiG at thresholds below one photoelectron. At the same time, this DAQ system is a foundation for the development of the scintillating fibre detector’s front end board firmware in the experiment. Thus, a MIDAS (see subsection 2.6.1) based approach was chosen because this system will be used by the Mu3E experiment.

An overview of the MuTRiG setup with the above described DAQ system is given in Figure 11.1. The analogue signals from SiPM arrays attached to both fibre ribbon sides are connected via adapter boards (see subsection 11.1.3) to the MuTRiG hosted on a carrier board. The MuTRiG mother board (see subsection 11.1.2) provides the ASIC’s supplies. The readout chip’s data and slow control links are connected to the FPGA which is located inside the DAQ computer. An PCIe interface is used for communication between them (see subsection 11.1.4).

### 11.1.1 MuTRiG ELECTRICAL CONNECTIVITY

The MuTRiG accommodates 161 pads on three edges which allows placing two ASICs next to each other. The pads divide into 72 for power and ground, 64 for the differential input

**Table 11.1:** Summary of all MuTRIG pads and their functionality. † In the next MuTRIG version it is foreseen to have one differential reset.

type	description	signal type	number of pads
power/ground	power 1.8 V analogue		11
	ground analogue		11
	power 1.8 V digital		23
	power 3.3 V digital		2
	ground analogue		25
signal	inputs (p)	single ended (p)	32
	inputs (n)	or differential	32
reference clocks	pll reference	LVDS, 625 MHz	2
	digital part	LVDS, 625 MHz	2
data links	data link	LVDS, 1.25 Gbit/s	2
slow control	chip reset†		1
	channel reset†		1
	chip select (cs)	SPI	1
	clock (sclk)	SPI	1
	data in (sdi)	SPI	1
	data out (sdo)	SPI	1
	CEC chip select (cec_cs)	SPI	1
	CEC data out(cec_sdo)	SPI	1
debug, monitor and filter	external trigger		1
	pll monitor		1
	analogue monitor		1
	2 × digital monitor	differential	4
	pll filter	differential	2

signals, 2 for the LVDS data output, 13 for slow control and 10 monitoring, debugging and filters. Table 11.1 summarises all available electrical connections.

### POWER

The supply voltages and grounds for the analogue and the digital part are separated to minimize noise in the input-stage from the digital partition. The analogue part works with a voltage of 1.8 V. The digital part needs supply voltages of 1.8 V and 3.3 V, where the latter is required for the LVDS drivers. The total power consumption in operational mode is measured to be  $(32 \pm 3)$  mW per channel. In a not configured state the ASIC's power consumption is roughly 10 % higher. Because of connections on the STiC and MuTRiG carrier boards, the measured current distributes between the two 1.8 V supplies, whereas the current in the digital 3.3 V supply is only 15 mA.

### REFERENCE CLOCKS

Two differential LVDS reference clocks need to be supplied. One is the reference clock for the chip's PLL which determines the timestamp bin size. The coarse counter is driven by the PLL reference clock's frequency. The TDC is designed for a frequency of 625 MHz. In case of the Mu3E experiment, this matches the experiment's base clock of 125 MHz from which the pixel timestamps are likewise derived. The second reference clock drives the ASIC's digital part.

### FAST DATA LINK

The data link operates at double data rate of the digital part's reference clock. It is designed for 1.25 Gbit/s. An excellent opening in the signal's eye diagram resulting in a Bit Error Rate (BER) below  $5.9 \cdot 10^{-15}$  was shown in [111, 145]. Furthermore, the link was operated up to 1.9 Gbit/s within the same BER performance.

### SLOW CONTROL

The slow control consists of the resets and the SPI interfaces for the configuration and CEC as described in subsection C.1.4. The SPI interface is designed for up to 20 MHz. The specified thresholds for input signals are  $U_{\text{low}}^{\text{in}} < 0.8$  V and  $U_{\text{low}}^{\text{in}} > 2.0$  V and for the output  $U_{\text{low}}^{\text{out}} < 0.4$  V and  $U_{\text{low}}^{\text{out}} > 2.4$  V. Tests with signals with a high level at 1.8 V were also successful. If no chip select is active<sup>2</sup>, the SPI data outputs are in a high impedance state to allow the use of common (sdo) lines by multiple slaves.

### MONITORING, DEBUGGING AND PLL FILTER

Various monitors and debug pads exist. An analogue monitor allows observing the analogue signal after the input stage at the amplification stage. The digital monitors provide access to

---

<sup>2</sup>active low.

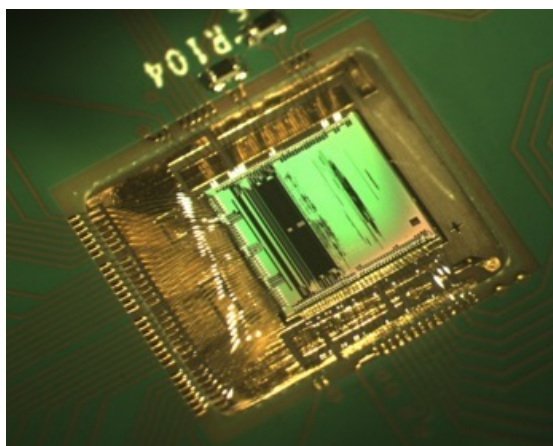


**Figure 11.2:** A wire bonded MuTRiG with a size of  $5\text{ mm} \times 5\text{ mm}$  on the cavity carrier board. From [145].

the differential  $T$ - and  $E$ -trigger signals. In the described setups, one of the two digital monitors is utilized to trigger the TDCs manually. An external filter network is added to the ASIC's PLL.

### 11.1.2 EVALUATION BOARDS

In the development setup produced at KIP to validate the ASIC functionality, the MuTRiG is hosted on a carrier board with only passive components. Two different sets of connectors can be used for input signals. Switching between these connectors is realized via  $0\ \Omega$  resistors. One is intended to connect to sensors, and the other is foreseen to mimic signals by injecting charge via a  $100\text{ pC}$  capacity into the positive inputs. The ASIC sits in a cavity and is wire bonded to two different PCB layers (see Figure 11.2). The chip is glob topped to improve the mechanical stability and simplify the cooling. This carrier board is connected to a motherboard.

#### THE MUTRIG MOTHERBOARD

Besides a connection to a MuTRiG carrier board, the motherboard developed at KIP provides all necessary supplies, data and slow control connections. Figure 11.3 shows the board with all its components.

**POWER** The motherboard is powered with  $12\text{ V}$ . The digital and analogue  $1.8\text{ V}$  are each generated by a DC-to-DC converter (GE PICOGLYNX) followed by an Low-DropOut (LDO) (MICREL MIC59300) regulator. An additional DC-to-DC converter (MURATA OKX-T/10) potentially powers the FLYSPY FPGA board and supplies another LDO (DIODES AP1086) providing  $3.3\text{ V}$  for MuTRiG and components on the motherboard.

**DAQ INTERFACE** The data and slow control connections can be switched between an interface to the FLYSPY FPGA board and an ALTERA High Speed Mezzanine Card (HSMC) interface

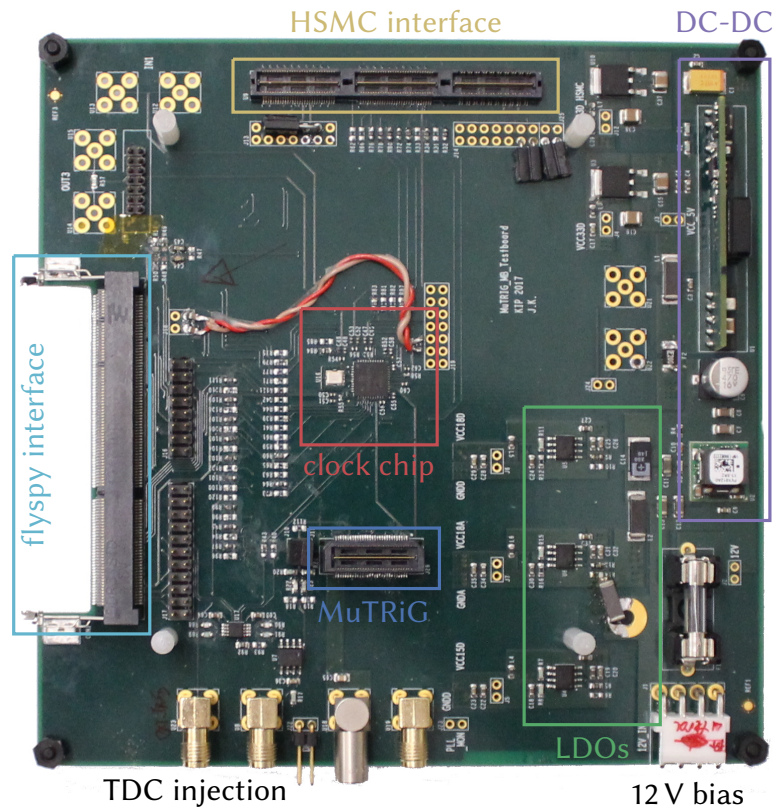


**Figure 11.3:** MuTRiG development board designed by KIP with: MuTRiG interface (←), the clock chip with its oscillator crystal (→), the ASIC bias LDOs (→) and DC-to-DC converters (→), and the two DAQ interfaces to the flyspy (←) and the HSMC (→) interface.

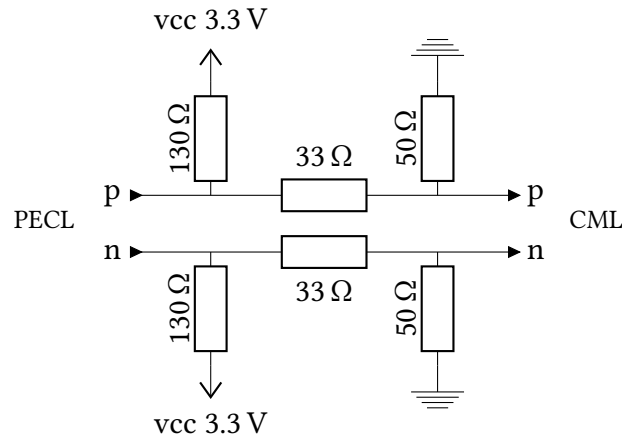


**Figure 11.4:** Resistor network to transform PECL signals into MuTRiG internal CML levels.

(SAMTEC ASP-122953). The fast LVDS data link is fanned out (ON NB6N14S) to both interfaces and to debug outputs. 0 Ω resistors switch the slow control signals.

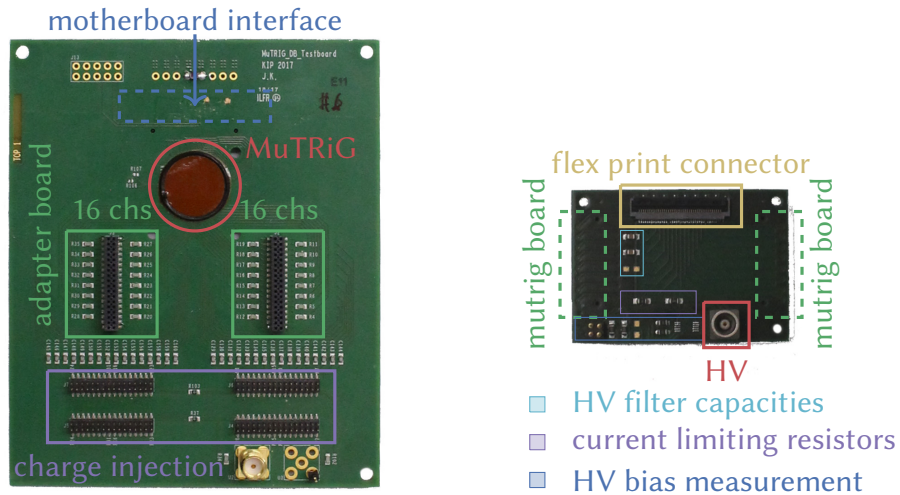
**CLOCK CHIP** MuTRiG's reference clocks are supplied by a clock multiplier chip (SILICON LABS SI5344) with a local crystal oscillator (KYOCERA CX3225SB). The clock chip's reference is provided either via the DAQ interface or external. The chip is configured by I<sup>2</sup>C interface.

**TDC INJECTION** To test the MuTRiG's PLL, the TDC can be triggered by an external signal connected to one of the digital monitors. This injection signal needs the MuTRiG internal Current Mode Logic (CML) signal levels, which requires differential signals between -1.8 V and 0.9 V. This is realised by a Transistor-Transistor Logic (TTL)-to-differential Positive Emitter-Coupled Logic (PECL) translator (MICREL SY100ELT22) followed by a resistor network, shown in Figure 11.4. In this way, it is possible to trigger the TDCs by a single-ended TTL pulse with an amplitude larger than 3 V.

### 11.1.3 RIBBON AND SENSOR CONNECTION

An adapter board, shown on Figure 11.5b, allows to couple the SiPM column arrays with their flex print as described in subsection 7.3.2 and shown in Figure 7.3 to the MuTRiG carrier board presented in Figure 11.5a. 32 channels on one of the four flex prints can be connected to the positive 32 channels of MuTRiG. This corresponds to half a sensor die or a quarter of an array. The negative channels from the differential input pairs are floating. Furthermore, the high voltage bias for half a sensor is provided through this adapter board and the flex print cables. The board hosts a 1 kΩ current limiting resistor and two filter capacitors (100 nC and 100 pC).

It is possible to connect only half the number of channels of one connector board to the MuTRiG. In this configuration, two adapter boards can be used to connect two different SiPM column arrays. 16 channels of each array are read out. This allows to read out a scintillating



(a) MuTRiG board developed at KIP hosting one ASIC. Two connectors, each for 16 channels, connect to the adapter board.

(b) The adapter board connects up to 32 SiPM column array channels single-ended to the MuTRiG board.

**Figure 11.5:** If only one of the two connectors of the adapter board is used, one adapter board can be used to read out two times 16 SiPM channels of two different SiPM arrays.

fibre ribbon with one SiPM column array per side, precisely as in the setup with the full waveform digitisation by the DRS4 readout (see subsection 7.3.2). The readout of 16 channels per side corresponds to an active width of the ribbon of  $\approx 4$  mm.

#### 11.1.4 PCIe BASED DATA ACQUISITION SYSTEM

A MuTRiG DAQ that allows to fully exploit the ASIC's rate capacities was developed in preparation for its integration into the experiment's framework. At the moment it bases on an Altera Stratix IV GX FPGA Development Kit (DK-DEV-4sGX230N) [146], which provides PCIe and HSMC interfaces. Later in the experiment, this functionality will be handled by the front-end FPGA board. The FPGA receives the 8b/10b encoded 1.25 Gbit/s LVDS based data stream, decodes it and pushes the single events by DMA based on PCIe interface into the DAQ computer's memory. Furthermore, the FPGA handles the ASIC's and clock chip's slow control. The system uses the MIDAS framework (see subsection 2.6.1).

#### FPGA AND FIRMWARE

The FPGA is controlled by a read-only register whose values are set by the DAQ computer. A second register, which can be written by the FPGA, is used for slow control information. Table C.3 summarizes the MuTRiG specific flags. Data transfer between the FPGA and the

**Table 11.2:** 8 byte data structure of DAQ's readout frames. *0s* means that all remaining bits are filled with zeros.

type	byte							
	0	1	2	3	4	5	6	7
header	01 + 0s	0x00cafe			0 + frame no		frame info	
data	1 + frame number		event data					
trailer	00 + frame no (14bits)		frame info		0x00	prbs err cnt	0x00	0s + crc error

host computer is realised via 1 GB of Random Access Memory (RAM), accessed by the FPGA through PCIe 2.0 based DMA. More details to the utilized PCIe interface and the DMA engine can be found in [73]. For the host computer read-only, a memory range is used for MuTRIG data transmission and read back of slow control settings. A second memory area is used to transfer slow control data from the host computer to the FPGA.

**THE DATA PATH** An Altera IP<sup>3</sup> core transceiver receives the 1.25 Gbit/s MuTRIG serial LVDS data stream, recovers the data clock by locking an internal PLL to it, aligns the phase according to comma control words (see Table C.2) and decodes the 8b/10b encoding. The latter deserializes the data stream to 1 byte words at the same time. A detailed description can be found in [147]. The transceiver status is stored in several flags in the FPGA's register.

The MuTRIG frames, as described in subsection C.1.5, are decomposed, and the extracted events in combination with the frame info are stored in a 16 events deep First In, First Out (FIFO) buffer. This buffer bridges between the clock domain recovered from the data streams and the PCIe domain. The FIFOFULL register flag maps the buffer status. The stored events are extended from 48 bits to 8 bytes by appending 15 bit frame number and prepending a 1. This flag indicates that these 8 bytes contain an event. If multiple ASICs are used, their address has to be added. Readout frames group events again, rimmed with 8 byte header and trailer. Table 11.2 shows an overview of the readout frame data structure. The header starts with its indicator 01 filled up with zeros followed by an alignment word 0x00cafe. It contains further the 15 bit frame number followed by 16 bit frame information which consists of 6 bits frame flags (see Table C.1.5) and 10 bits frame length. The trailer starts with the indicator 00 followed by 14 bits of the frame number. The frame is supplemented by the repetition of the frame info and a 1 byte Pseudo-Random Bit Stream (PRBS) error counter. This counter is used to validate MuTRIG's digital part with its PRBS debug mode. The last bit of the trailer indicates the occurrence of a frame Cyclic Redundancy Check (CRC) error.

If the slow control does not occupy the memory interface, controlled by the SLOW ENABLE register flag, the DMA engine pushes events from the FIFO buffer to the computer's memory.

<sup>3</sup>Intellectual Property.

**CHANNEL EVENT COUNTER** If the CEC readout is enabled by the CEC register flag, an SPI interface is used to map the CEC data (see subsection 6.3.3) to the read-only registers listed in Table C.3.

**SLOW CONTROL** The CONFIG, respectively CONFIG CLK register flags trigger the SPI MuTRIG and I<sup>2</sup>C clock chip configurations. The configuration data is loaded through the memory interface which has to be claimed by the slow control via the SLOW ENABLE register flag. The slow control read-back values are written to the corresponding positions in the read-only memory. The large size of configuration data motivated the use of the memory interface. The TIMEOUT register flag indicates a potential time-out of the I<sup>2</sup>C interface. After completed configuration, the CONFIG flags in the read-only registers are raised. Once the host system has released these flags in the command registers, the slow control finite state machine returns to its idle state. This hand-shake architecture guarantees the exclusive use of the memory interface.

The resets, chip and channel reset, (see subsection 6.3.4) are controlled by the RESET CHANNEL and the RESET CHIP register flags. A reset is issued, whenever a corresponding flag is raised and reset by the same hand-shake mechanism as described above. Differently, in the presence of a RESET CHANNEL HOLD flag, the channel reset is also held active. Synchronization of different ASICs and subsystems will be realised by this scheme.

The FPGA generates the 125 kHz base clock for the clock chip.

**DEBUG MODES: DUMMY** Different debug modes are available and controlled through the DUMMY flags. The MuTRIG configuration shift register can be mimicked, or artificial data can be fed into the data path in the FPGA.

#### MIDAS INTEGRATION

The MIDAS [74] framework combines run control, event building and logging, slow control and history systems with online monitoring and data analysis (see subsection 2.6.1). Therefore, the Mu3E experiment will also exploit this system. The framework handles Remote Procedure Calls (RPCs) between different systems locally or remotely in a network and manages shared buffers between, potentially multiple, different data producers and consumers. The Online Database (ODB) stores all variable experiment data. The presented MuTRIG MIDAS DAQ has proven to read and store the maximal data rate of one MuTRIG of 20.7 MHz PRBS-events efficiently. Note that the PRBS-events have a size of 48 bits, whereas the shortened *T*-events consist only of 28 bits what results in an event rate of 1.1 MHz/channel. A MIDAS based custom web application provides a Graphical User Interface (GUI) for the ASIC configuration.

**MIDAS FRONTEND** In the MuTRIG DAQ a single MIDAS frontend handles the configuration of the ASIC and the clock chip through the FPGA and further the readout of the DMA buffer. The events are copied, grouped by readout frames, to the buffers managed by MIDAS. Furthermore, the CEC values from the FPGA registers are copied periodically into a second buffer. These are two typical data producers. The MuTRIG configuration bit pattern is generated by the configuration settings stored in the ODB.

**MIDAS MuTRiG CONFIGURATION** The 1264 MuTRiG configuration values and 6 DAQ settings are stored and loaded from the ODB. The settings are structured in a *Daq*, a *Global*, a *Tdc* and *Channel* part. Figure C.3 shows the corresponding settings in the different panels. Whereas the first two parts exist only once, one *Tdc* group for each MuTRiG, respectively two *Tdc* groups for each STiC, are required. The *Channel* settings exist for each channel. The MIDAS based GUI for the ASIC configuration stores the local configuration in HTML5 web storage; it can be exported and imported into JSON<sup>4</sup> files. Table C.2 gives a more detailed GUI description.

**MIDAS DATA LOGGING AND ONLINE MONITOR** Standard MIDAS loggers are employed to write the events from the DAQ buffers to disk. The loggers write either the full data stream or only the CEC information in MIDAS' binary format. A ROOTANA<sup>5</sup> based analyzer decodes MuTRiG event data and provides histograms for online monitoring. A MIDAS custom web page can be used to include the online monitoring into the DAQ framework.

### 11.2 MEASUREMENT AND ANALYSIS PROCEDURE: A USER'S GUIDE

A typical MuTRiG measurement cycle for the Mu3E scintillating fibre detector consists out of the following steps. It starts with the determination and validation of the chip's PLL settings by triggering the TDC externally with a periodic signal. Only if the measured period matches, the MuTRiG data stream is meaningful. Secondly, the *T*-thresholds for each channel have to be determined by a threshold scan. This step is optionally followed by a gain uniformization between SiPM channels based on the DCR. The cycle ends with the actual data taking and analysis during which clusters are built.

To increase the time resolution, it is possible to correct offline for DNL of the fine counter bins and small channel dependent time offsets caused by the ASIC or due to signal path length differences.

#### 11.2.1 PLL VALIDATION

The STiC and MuTRiG internal PLL is configured by 9 Digital-to-Analogue Converter (DAC) settings where each consists of a value and a scale. Even though the PLL has proven to be very stable concerning temperature and reference voltages, a proper ASIC operation requires a correct lock of the VCO circuits. The PLL can lock at different discrete frequencies. This corresponds to a change of the time base which determines the timestamp's bin size.

#### PLL VALIDATION SETTINGS

The TDCs are triggered with an external periodic signal as described in Figure 11.1.2. A signal with a swing from 0 V to 3 V with a 50 % duty cycle is used. The external trigger through

---

<sup>4</sup>JavaScript Object Notation.

<sup>5</sup>An analysis package for MIDAS.

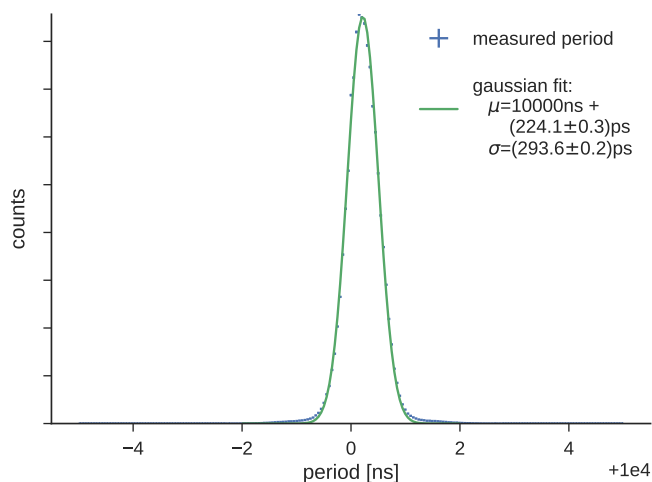


**Figure 11.6:** The measured period in a randomly picked channel (3) with a 100 kHz external TDC trigger. The x-axis shows the deviation around 10  $\mu$ s, corresponding to the period of the used 100 kHz pulse injection.

the digital monitor pads is enabled channel wise by switching off the DISABLE TDCTEST configuration bit. The energy validation has to be turned off by the global RECIEVE ALL bit to receive data. Since the external TDC trigger is combined with signals from the input stage comparators, these should be switched off. Table C.7 lists the used channel DAC settings.

With the energy validation switched off, an event contains the current timestamp as well as the previous one in the same channel (see. subsection C.1.3). The difference between the two timestamps<sup>6</sup> corresponds to the time difference between two consecutive events in a channel.

#### PLL VALIDATION MEASUREMENTS

The time difference of consecutive timestamps in a channel in the presence of a periodic external trigger have been measured for PLL validation. Figure 11.6 shows the fitted period distribution of a single, randomly chosen channel (3) at an external trigger frequency of 100 kHz. The applied PLL settings are summarized in Table C.6. Figure 11.7 shows in the top the relative trigger rate between channels. The trigger rate is very uniform at the  $7 \cdot 10^{-6}$  level.

The central Figure shows the period offset to the expected 10  $\mu$ s, corresponding to the applied 100 kHz trigger. The mean offset over all channels yields a frequency deviation of  $2.2 \cdot 10^{-5}$ . Note that the pulse generator's (KEITHLEY 3390) frequency resolution is 1  $\mu$ Hz, what corresponds to  $1 \cdot 10^{-11}$  at the used 100 kHz. The MuTRiG's reference clock frequency resolution is determined by the utilised crystal oscillator of the used clock chip (see Figure 11.1.2). The frequency tolerance is stated to be  $15 \cdot 10^{-6}$ . The measured deviation is of the same order of magnitude as the reference clock uncertainty. The periods measured in the

<sup>6</sup>usually the  $T_{\text{OT}}$ -like energy.

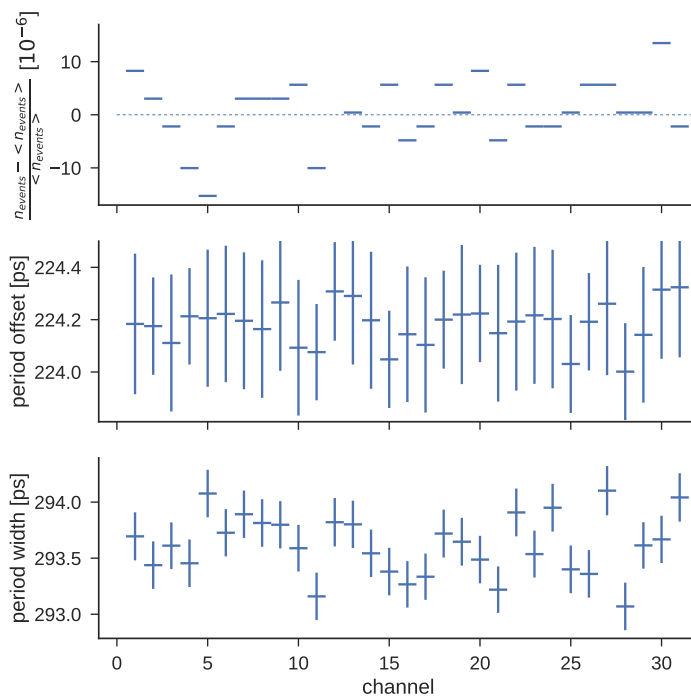


**Figure 11.7:** The relative trigger rate uniformity between all channels (top), the period offset from the expected 10 000 ns corresponding to the 100 kHz external TDC trigger (middle), and the widths of the period distribution per channel (bottom). The shown errors are derived by the MINUIT fitter.

different channels are very uniform, with a variation of  $\pm 79$  ps what corresponds to a  $7.9 \cdot 10^{-9}$  frequency level.

In the bottom of Figure 11.7 the period distributions widths of the different channels are shown. The widths of  $(293.6 \pm 0.3)$  ps are dominated by the rise time of the injected trigger. Hence, they correspond not to the intrinsic TDC jitter.

#### PLL VALIDATION: BLACK MAGIC TIPS & TRICKS

The lock of the PLL at wrong frequencies can usually be adjusted by changing the VNCODELAY and VNHITLOGIC DACs. Further sanity checks involve the check of uniformity in the fine and coarse counter distributions of all active channels. The non-uniform fine bin size results in a not flat distribution of fine counter values. However, the complete absence of specific bins or half of the distribution is a strong indication for an improperly configured TDC. The coarse counter distribution is supposed to be uniform. Spikes in arbitrary bins, in particular in the zero bin, indicate likewise improper configuration. This often comes along with some scattered period events which show up only in logarithmic scale. The latter issue can usually be solved by increasing the VNCNT DAC.

Furthermore, it is possible that the PLL locks successfully after a specific sequence of settings, but does not lock with the same parameters derived out of a different sequence. It has proven helpful to unlock it after two settings at test deliberately. This is achieved by setting the value and the scale of VNCNT to zero.

#### 11.2.2 THRESHOLD DETERMINATION

Once the chip's performance is validated, the  $T$ -thresholds are determined. This procedure applies only to the operation with disabled  $E$ -threshold validation. Due to the low number of photons, this is the case for the M $\mu$ 3E scintillating fibre detector but not for the scintillating tile detector or the operation with Lutetium-Yttrium Oxyorthosilicate ( $Lu_{2(1-x)}Y_{2x}SiO_5$ ) (LYSO) crystals in a PET application.

#### SENSOR BIASING: VOLTAGE AND CURRENTS

The SIPM DAC, which is available for each channel, allows adjusting the voltage at the ASIC's positive input terminal to which the sensors cathodes are connected (see subsection C.1.1). The potential at the input terminal is typically in a range 100 mV to 900 mV and it is not linear in the DAC value. Figure C.4 shows typical input voltages as a function of SIPM DAC values. This feature allows homogenizing the overvoltage of the different SIPM columns. The DCR, measured as the event rate at a specific threshold or as the current through one column, provides a suited handle for this task.

Table C.10 summarizes the measured currents through the biased sensors at different operation voltages in the absence and the presence of a beta source.

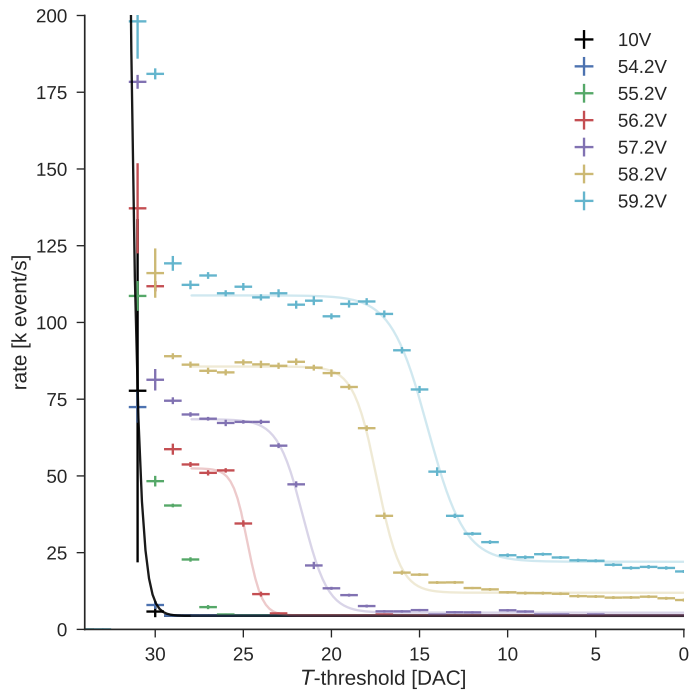


**Figure 11.8:** Measured event rate at different SiPM sensor bias voltages at TTHRESHOLD DAC *scale* 0 as a function of  $T$ -threshold of a randomly chosen channel (26). The step functions are fitted with sigmoid functions to determine the position of the step.

### *T*-THRESHOLD SCANS

The thresholds are determined through threshold scans with attached and biased sensors. Due to the sensors DCR behaviour, the measured rate as a function of the threshold yields a step function as shown in Figure 11.8 in section 5.2. The simplest method to determine the rate of each channel at a given threshold utilizes the CEC. This prevents huge amounts of data. Per threshold step the mean CEC value over 1 s is determined and plotted as a function of threshold DAC value. The *T*-threshold consists of 64 DAC values in 8 different scales and covers both signal polarities. Only the positive range is probed. Table C.8 lists the channel DAC settings used for the threshold scans. One scan is performed with a sensor bias below breakdown to determine the systems' noise, respectively the ASIC's baseline level.

Figure 11.8 shows a *T*-threshold scan of a randomly chosen channel (26) at *scale 0* at different SiPM bias voltages. Below breakdown, the baseline is determined, and potential system noise is measured. With increased bias voltage, the DCR increases which manifests in the increased level of the plateau. At the same time the gain increases, hence the larger signals shift the step function edge to larger amplitude, corresponding to smaller DAC values. Note that the stated voltages are applied with respect to ground. The potential at the positive MuTRiG input terminal can be adjusted and shows  $\mathcal{O}(0.5\text{ V})$  positive offset to ground. The DCR scans are fitted with a sigmoid function to determine the position of the edge.

### *T*-THRESHOLD RANGE

Based on the *T*-threshold scans, as shown in Figure 11.8, the possible dynamic range of MuTRiG in combination with the utilised sensor can be determined. Figure 11.9 shows in the top the edge positions of the DCR steps at different bias voltages in combination with the baseline level. The amplitude of one single photoelectron in DAC steps is given by the distance of the edges to the baseline. This is shown in the middle part. The dynamic range is approximately given by the available DAC settings above baseline divided by the above-stated amplitude. This is summarized in the bottom of Figure 11.9. Note the significant deviations between channels and that the linearity of the DAC values is only approximated.

***T*-THRESHOLD SCALE** The dynamic range of the *T*-threshold can in principle be adjusted with the DAC's scale. Figure 11.10 shows threshold scans of a randomly chosen channel (26) of a sensor biased with 56.2 V at all available DAC scales. In two scales, 3 and 7, no single photon step is present at all. It turns out that the dynamic range in the default baseline *scale 0* is maximized.

**INPUT BIAS** A second handle on the dynamic range is given by the constant current of the input stage controlled by the INPUTBIAS DAC which affects the gain. Figure 11.11 shows threshold scans of a randomly chosen channel (26) of a sensor biased with 56.2 V for different values of this DAC. The effect at small signals, as in case of the MU3E scintillating fibre detector, is minor.

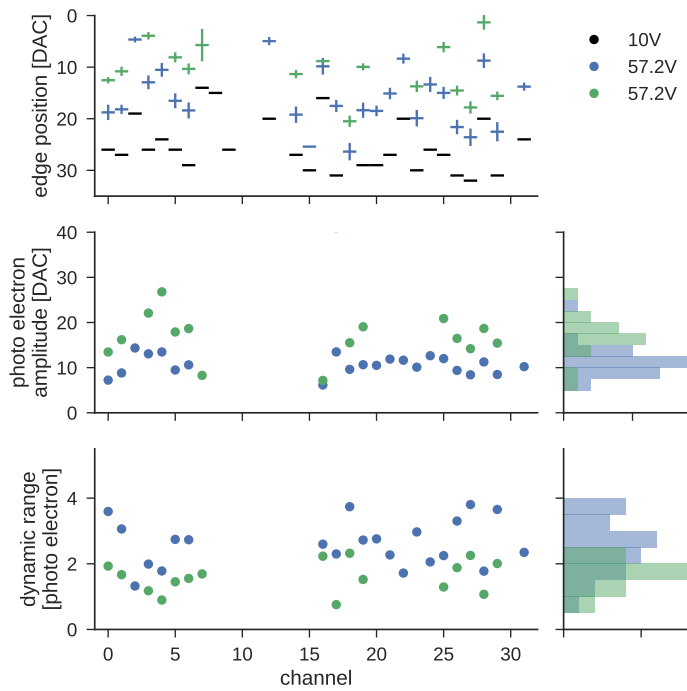


**Figure 11.9:** The position of the sub-breakdown 10 V (—), 57.2 V (—) and 59 V (—) edges (top). The amplitude of single photoelectrons in DAC steps is derived from the edge position differences (middle). The resulting dynamic range of MuTRIG with the utilized sensors (bottom). Channels 8 through 16 are missing in this measurement.

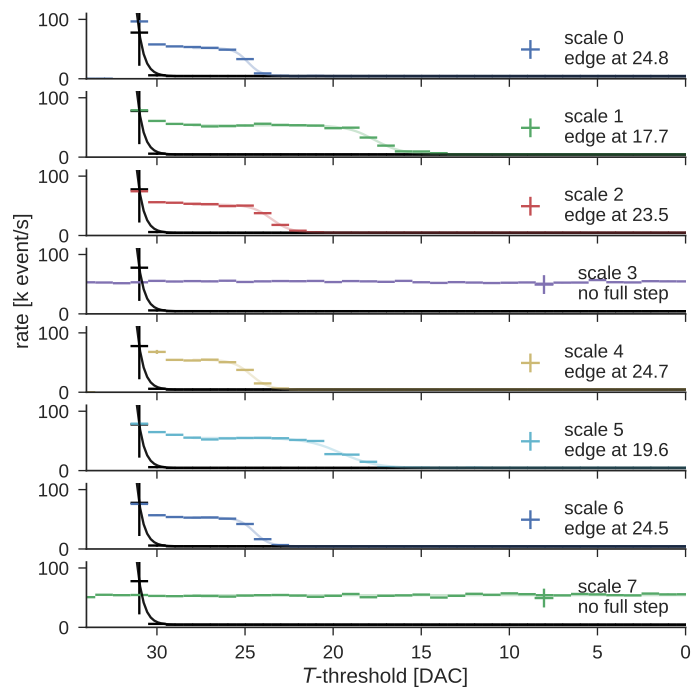


**Figure 11.10:** Measured event rate at a sensor bias of 56.2 V for all available DAC scales as a function of the  $T$ -threshold of a randomly chosen channel (26). *Scale 0* is used as the default baseline scale.

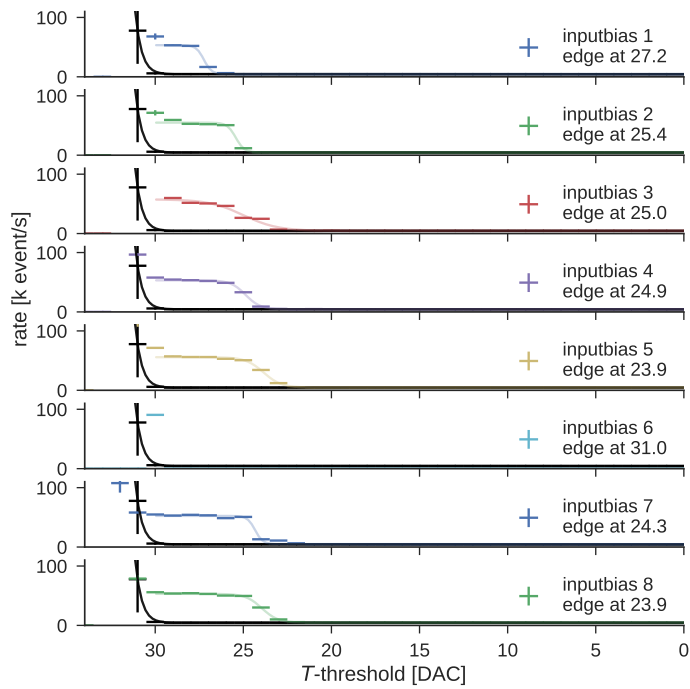


**Figure 11.11:** Measured event rate at a sensor bias of 56.2 V for different values of the INPUTBIAS DAC as a function of  $T$ -threshold of a randomly chosen channel (26). Input bias setting of 4 is the default baseline.

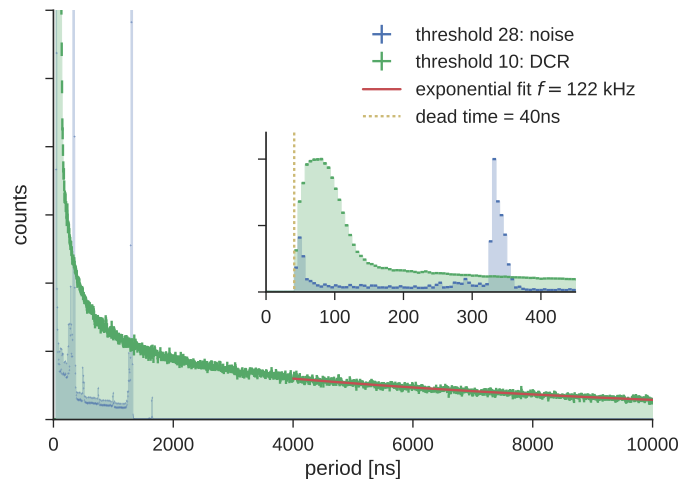


**Figure 11.12:** Period spectrum of a single channel connected to a SiPM array biased with 58.2 V at two different threshold DAC settings: a threshold of 28 ( $\rightarrow$ ) is in the noise whereas a threshold of 10 ( $\leftarrow$ ) corresponds to 0.5 photoelectron trigger level. An exponential fit of the distributions tail ( $\rightarrow$ ) allows the extraction of the DCR. Furthermore, the TDC dead time manifests in the spectrum's lower edge cutoff at 40 ns.

**SUMMARY** The presented consideration to the possible dynamic range of MuTRiG in combination with the employed SiPM column arrays yield the conclusion that at reasonable bias voltages (above 56.2 V) it is feasible to operate up to  $\approx 2$  photoelectron thresholds in all channels. The dynamic range of most channels is larger than this. But, the possible uniform threshold levels of all channels is dominated by the one with the minimal range. For high bias voltages ( $\approx 60.2$  V) the possible dynamic range is below 2 photoelectrons in the worst channels. This has to be considered especially in the scope of irradiated sensors which show significant DCR increase and potential raised pixel to pixel crosstalk.

### THRESHOLD VALIDATION

Based on the  $T$ -threshold scans the desired operation point is chosen. Typically, thresholds at 0.5 or 1.5 photoelectrons are chosen. These thresholds are validated by the period spectrum of each channel. Figure 11.12 shows an example of one channel with two different threshold settings with a SiPM array biased at 58.2 V. The threshold at a DAC value of 28 is below the amplitude of noise, respectively the ASIC's baseline. A few discrete frequencies dominate the spectrum. The noise in the presented example consists of two main contributions at frequencies of  $\approx 2.99$  MHz and  $\approx 766$  kHz. The period spectrum outside of the baseline at approximately 0.5 photoelectron at a DAC value of 10 is expected to be smooth. The presence of peaks is a strong indication of pick up of noise. An exponential fit of the distribution's tail yields the DCR at this threshold level. Furthermore, the TDC's dead time manifests itself the lower cut off of the period spectrum at 40 ns.

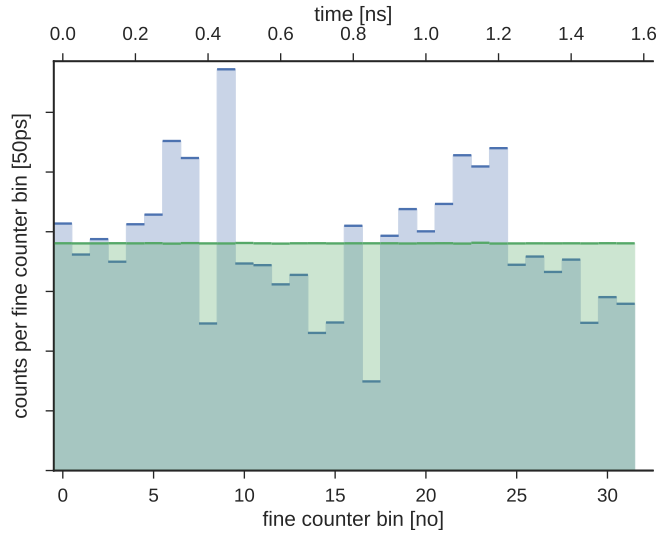


**Figure 11.13:** The fine counter bin distribution ( $\leftarrow$ ) caused by the non-uniform delays of the VCO delay stages. The DNL effects can be corrected for as shown in the time distribution ( $\rightarrow$ ) binned into the mean fine counter width of 50 ps.

### 11.2.3 CLUSTERING AND TIME RESOLUTION EXTRACTION

To compare the time resolution of scintillating fibre ribbon prototypes read out by the DRS4 with the same prototypes read out by MuTRiG, a very similar data processing is used. The main steps are the  $T_{0A}$  extraction for each channel, followed by clustering of neighbouring, coincident hits and the subsequent time resolution extraction and fitting from clusters.

In contrast to the DRS4 based measurement, the  $T_{0A}$  in MuTRiG is determined by the  $T$ -trigger level which yields the  $T_{0A}$  in the  $T$ -timestamps with respect to a common reset. No offline waveform processing and time extraction are required. Furthermore, MuTRiG is used without a global external trigger. Each channel is self-triggered by its  $T$ -threshold.

#### IMPROVED $T_{0A}$ : DNL CORRECTION

The  $T_{0A}$  is improved if the Differential Non-Linearity (DNL), as described in subsection 6.3.2, is corrected for. The integrated DNLs of all previous fine bins determines the correct time of an event with a specific fine counter value. The centre of the corresponding bin yields the corrected timestamp. Figure 11.13 shows the distribution of the raw and DNL-corrected bins of the fine counter. Due to the different fine counter bin widths, the uncertainties of the timestamps are a function of the fine counter bin.

As we demonstrated in [148], the fit's quality improves if each time difference is smeared out by its uncertainties to randomize these quantisation errors. This effect is of particular importance if time resolutions in the order of only a few fine counter bins,  $\mathcal{O}(100\text{ ps})$ , are extracted. Figure 11.14 shows an example time resolution of positron annihilation measured with  $3.1\text{ mm} \times 3.1\text{ mm} \times 12\text{ mm}$  LYSO crystals and the STiC ASIC.

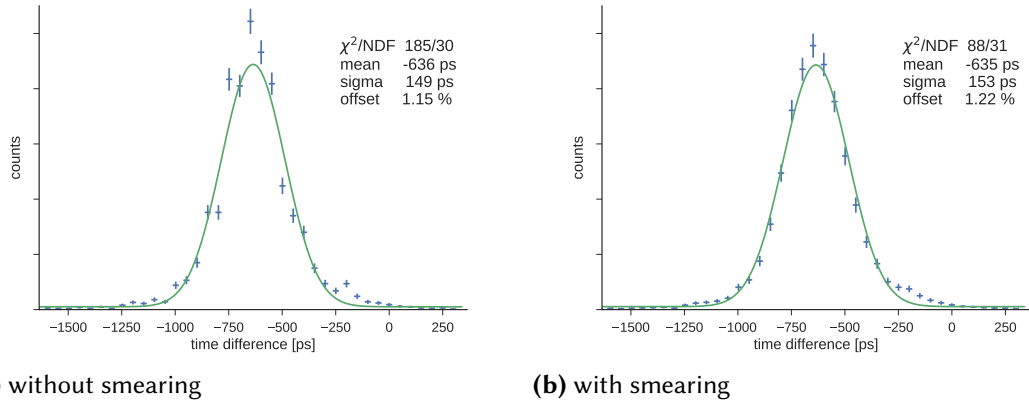


**Figure 11.14:** Time resolution of positron annihilation measured with  $3.1 \text{ mm} \times 3.1 \text{ mm} \times 12 \text{ mm}$  LYSO crystals and the STiC ASIC. From [148].

### CLUSTERING PROCEDURE

The clustering is realized in a multi-step approach. Firstly, events in coarse coincidence in time, within 20 ns, from all channels per side are built. In the presented setup, 16 channels are present per side. An event is added to a group if its time difference to any event already in the group is smaller than the coincidence window. Otherwise, a new group is built which contains this event. If a new event is within the time coincidence window to two existing group, they are merged. This is realized based on the  $12.6 \mu\text{s}$  long MuTRiG readout frames and leads to a set of groups, whose hits are all disjunct by at least the time coincidence window.

In a second step, clusters of adjacent channels are built based on these groups which contain all hits within the coincidence window of at least one other. If a channel is known to be not working, it is ignored, and clusters are built spanning it.

### TIME RESOLUTION EXTRACTION

The time resolution extraction from the clusters follows precisely the procedure described in Figure 7.3.4. The distribution of the differences of the smallest time of the clusters on both ribbon sides is considered.

To further improve the time resolution, a small channel by channel time offset can be corrected for. These offsets, in the order of  $\sqrt{\text{var}} = 140 \text{ ps}$  as shown in Figure 11.15, are constant between resets but show a slight DAC and bias voltage dependency. Unfortunately, the external triggering of the TDCs yields incompatible offsets, because only the digital signal part is involved. Therefore, they have to be extracted from the full chain with biased sensors for each used set of DAC settings, including  $T$ -threshold. This has the advantage, that different signal path lengths are corrected for at the same time.

In the presented analysis, the channel time offsets are extracted by two different methods. Firstly, the time difference of crosstalk events between neighbouring channels, as shown in Figure 11.17, can be utilized. Under the assumption that crosstalk, induced from one channel

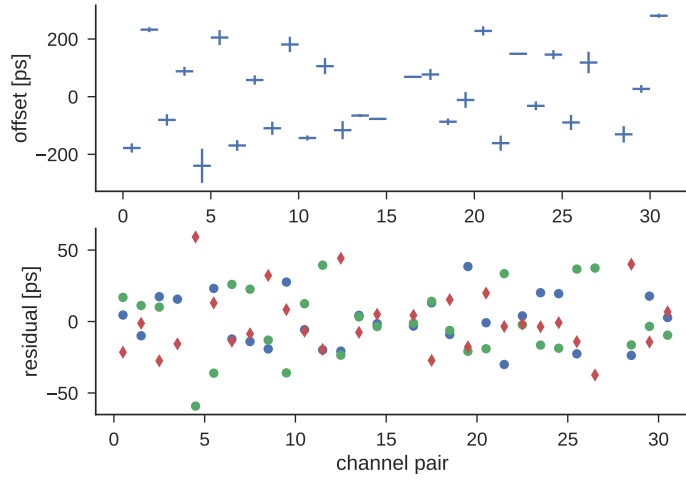


**Figure 11.15:** Measured time offsets between channels by crosstalk between channels (♦) and common coincidences to channels on the opposite fibre ribbon side (•, +). The bin centred at channel pair 0.5 corresponds to the pair 0-1.

to its neighbour, shows the same time constant as vice versa, the relative time offset of the neighbouring channel pair is extracted. It is given by the centre between the two crosstalk peak positions. Secondly, a signal in coincidence in the two adjacent channel to one reference channel of the other ribbon side can be utilized. Such coincidence signals can either be caused by passing particles at a well-defined position along the ribbon or crosstalk mediated by the fibres as described in Figure 11.3.2. The time offset of two neighbouring channels is given by the difference of the offsets to the third common channel on the other fibre ribbon side. Figure 11.15 summarizes the offsets extracted by both mentioned methods, where two opposite side channels per pair were used. The offset is determined by the mean of the three extracted values per channel. Their residuals show an Root Mean Square (RMS) of 18.5 ps, which is close to the fine bin resolution of  $50 \text{ ps}/\sqrt{12} \approx 14.4 \text{ ps}$ . The three extracted offsets are consistent with each other.

### 11.3 MUTRIG PERFORMANCE

The same setup as described in subsection 7.3.1 with the beam replaced by a 21 MBq  $^{90}\text{Sr}$  source with two 2 cm long collimators with an aperture with a diameter of 6.7 mm, respectively 2 mm, is used. The SiPM column arrays are connected to the MUTRIG setup, instead of to the amplifiers and DRS4 based DAQ, as described in subsection 11.1.3. A 4 layer SCSF-78 ribbon without additional  $\text{TiO}_2$  in the glue is used.

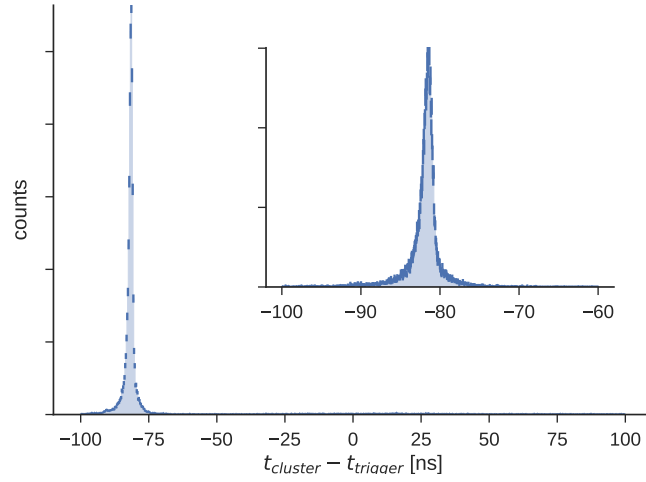


**Figure 11.16:** Time delay of the external trigger with respect to the corresponding clusters.

### 11.3.1 HIT VALIDATION BY THE EXTERNAL TRIGGER

One channel of the used setup, MuTRIG channel 10 corresponding to SiPM channel 27 is not connected to the input lines but is in principal functional. Hence the signal from the external trigger cross which consists of 1 mm scintillating fibres read out by PMTs is fed into this channel. This is realized by external NIM discriminator followed by AND coincidence of the crossed fibres. The NIM coincidence signal is converted into a TTL pulse which in turn is used to trigger the TDC of MuTRIG channel 10 through the motherboard's injection (see Figure 11.1.2). The described chain introduces a significant delay of signals from the external trigger with respect to the corresponding clusters. Figure 11.16 shows the coincidence spectrum. The external trigger validates clusters with a distance between  $-90$  ns to  $-75$  ns. The external trigger cross is used to ensure that the electrons from the beta decay fully penetrate the ribbon. Hence the non-radiative deposited energy is well under control (see Figure 7.6) and very similar to the test beam environment. The measured time resolution of all clusters and validated ones are consistent. In the presence of the  $^{90}\text{Sr}$  source a rate of 30 Hz is measured in the crossed fibres and a mean rate 67 kHz in the SiPM channels with an RMS of 14 kHz between them. The employed  $T$ -threshold settings at different sensor bias voltages are summarized in Table C.9.

### 11.3.2 COINCIDENCE BETWEEN CHANNELS

The time coincidence spectrum between individual channels without a source in place reveals crosstalk between sensor channels as well as crosstalk mediated by the fibres from one side of the fibre ribbon to the other. Figure 11.17 and Figure 11.18 show the effect of these types of crosstalk for two neighbouring SiPM channels of the same sensor and for two SiPM channels located on the opposite sides of the fibre ribbon. Both sensors are biased with 58.2 V. In the presence of the strong  $^{90}\text{Sr}$  source, a coincidence peak between the ribbon sides appears.

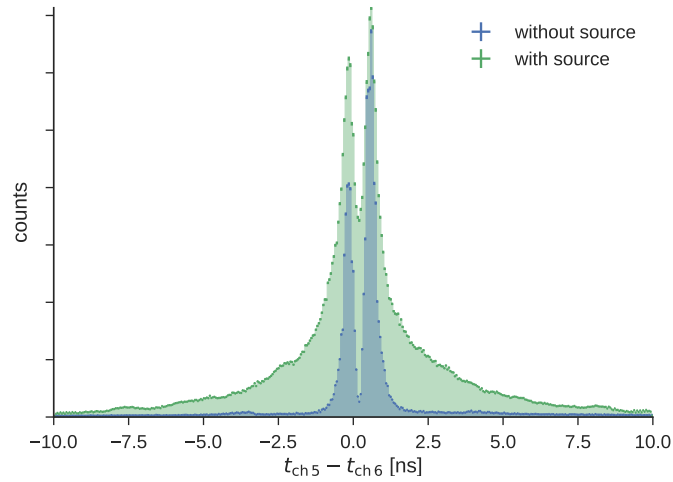


**Figure 11.17:** Coincidence events of two neighbouring SiPM channels (5 and 6) with a sensor biased at 58.2 V without (—) and with (—) the presence of the  $^{90}\text{Sr}$  source.

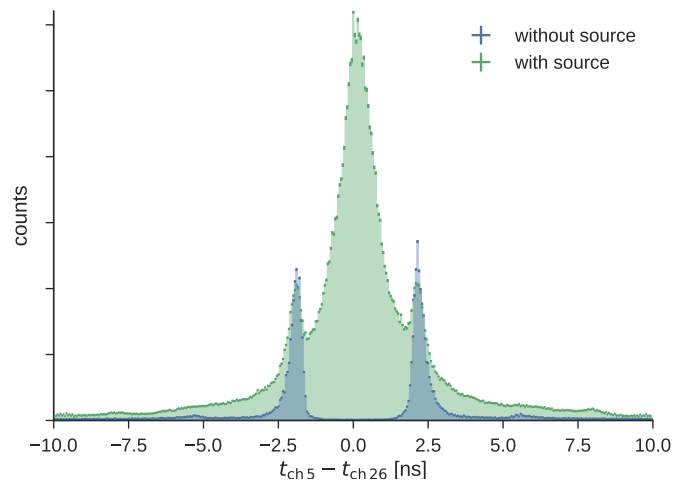


**Figure 11.18:** Coincidence events of SiPM channels (5 and 26) on the opposite side of the fibre ribbon. Both sensors are biased at 58.2 V. The coincidence spectrum without (—) and with (—) the presence of a  $^{90}\text{Sr}$  source are shown.

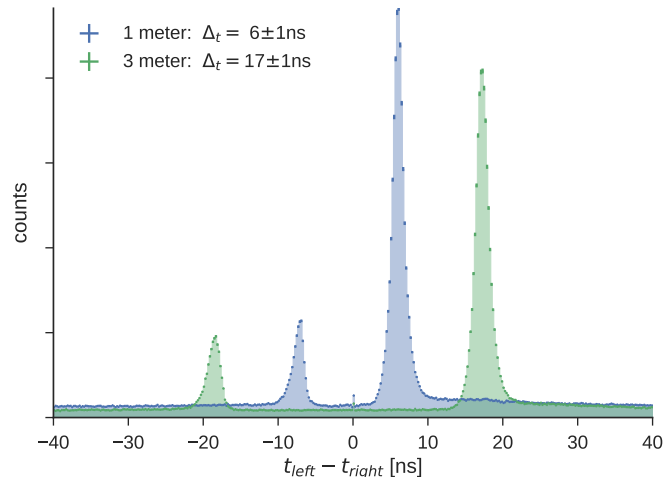


**Figure 11.19:** Crosstalk mediated by a single 1.5 mm thick round scintillating fibre of 1 m (—) and 3 m (—) length. Courtesy of J. Allenspach and T. Schmid.

Furthermore, adjacent channels are often part of the same cluster. Thus a coincidence peak manifests also between them.

### CROSTALK MEDIATED BY SCINTILLATING FIBRES

Crosstalk mediated by plastic fibres from one side to the other side of a ribbon has the same cause as crosstalk between SiPM pixels and channels (see subsection 5.2.3). A fraction of the infra-red photons emitted by the accelerated charge carriers of an avalanche couple into the fibres which guide them to the other side. Even though the fibres show a significant loss in the propagation of near infra-red photons, a few trigger avalanches in the attached SiPM channels on the opposite side. The time difference consists of a propagation term and a crosstalk time constant  $\mathcal{O}(1 \text{ ns})$ . The propagation term is determined by the speed of light in the fibre Polystyrene<sup>7</sup> core and the mean propagation length given by the photon's angle with respect to the fibre axis.

In a dedicated study with single round fibres with a diameter of 1.5 mm coupled to SiPMs<sup>8</sup> with an active area of  $1 \text{ mm} \times 1 \text{ mm}$ , this effect was confirmed by J. Allenspach and T. Schmid. The setup utilizes a pre-amplifier and a DRS4 based full waveform readout. Figure 11.19 shows the time difference between signals with an amplitude larger than 0.5 photo electrons for two different fibre lengths of 1 m and 3 m.

**Table 11.3:** Crosstalk measured in a fibre ribbon prototype. The mean value and standard deviation over all channels are stated.

bias voltage	crosstalk [%]			
	channel to channel		fibre mediated	
	mean	std	mean	std
57.2 V	2.7	2.2	1.3	1.0
58.2 V	3.2	1.9	1.8	1.5
59.2 V	4.0	2.5	2.5	1.9
60.2 V	4.5	2.6	3.1	2.1

### CROSSTALK RATES

Table 11.3 summarises the bias voltage dependent crosstalk rates extracted from the fibre ribbon prototype. The stated crosstalk probability is determined by the ratio of all events in coincidence with the corresponding partner normalized by the total number of events in this channel. For the mediated crosstalk, all events within  $\pm 6\sigma$  of a Gaussian fit of the corresponding time difference peak are used. For the channel by channel crosstalk, all events from the centre between the two respective crosstalk peaks up to  $\mu + 3\sigma$  outwards the distribution are used. The measurement is performed at  $(25.9 \pm 0.2)^\circ\text{C}$ .

#### 11.3.3 CLUSTER SIZES MEASURED WITH MUTRIG

Figure 11.20 shows the distribution of the cluster sizes measured with MuTRiG. Even though the distributions show a slightly different shape concerning the cluster size distributions obtained by the DRS4 based readout, their MPVs are very similar. The full waveform based measurement yields distribution of cluster sizes with MPV of  $3.27 \pm 0.01$  columns and  $3.24 \pm 0.01$  columns compared to 3.2 columns and 2.88 columns of the MuTRiG measurement. Note that in the MuTRiG measurement one channel on the right side is missing, what results in slightly reduced cluster sizes.

#### 11.3.4 TIME RESOLUTION MEASURED WITH MUTRIG

The cluster time resolution, extracted as described in Figure 11.2.3 and Figure 7.3.4, at different SiPM array bias voltages are summarized in Table 11.4. The extracted time resolutions for all clusters ( $cl \geq 1$ ) and for clusters consisting of at least two ( $cl \geq 2$ ) column hits per side are quoted. Figure 11.21 shows an example time difference distribution for clusters with a minimum size of 2, obtained with a sensor biased at 58.2 V. It agrees very well with the time resolution extracted by the DRS4 based DAQ of the same ribbon. For example, the FWHM/2.35

<sup>7</sup> $n_{\text{PS}} = 1.6$ .

<sup>8</sup>Hamamatsu S10362-11-050P.

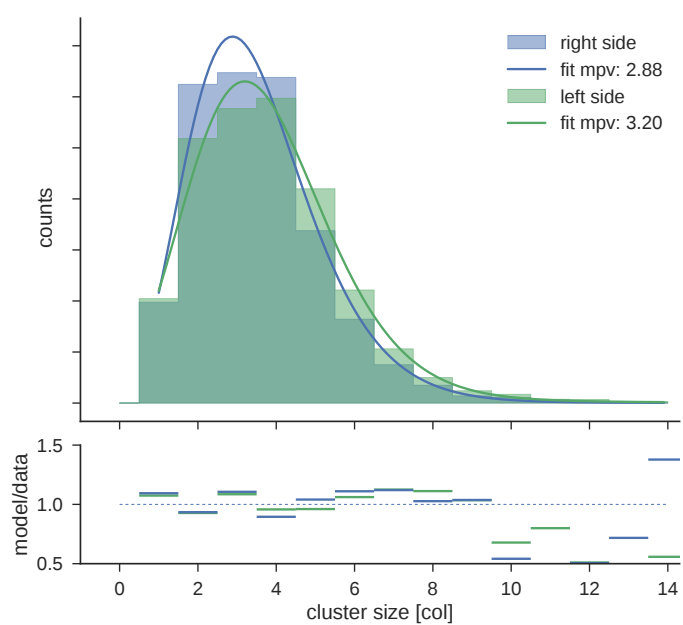


**Figure 11.20:** distribution of cluster sizes of a 4 layer SCSF-78 ribbon without additional  $\text{TiO}_2$  in the glue measured with MUTRIG. Note that on the right side one channel (27) is missing.

**Table 11.4:** Scintillating fibre prototype time resolutions at different sensor bias voltages for all clusters ( $cl \geq 1$ ) and for clusters consisting of at least two SiPM column hits per side ( $cl \geq 2$ ). Furthermore, the time resolution at different threshold levels is presented. If no  $\sigma_{\text{base}}$  is given, it converged to 1 ns used as lower bound to prevent dilution of  $\sigma_{\text{core}}$ . Fibre type 78 in the table corresponds to Kuraray SCSF-78, NOL to NOL-11.

ribbon type	layers	th [phe]	cl $\leq$	bias [V]	$\frac{\text{FWHM}}{2.35}$ [ps]	$\sigma_{\text{single}}$ [ps]	$\sigma_{\text{core}}, \sigma_{\text{base}}$ [ps]	$N_{\text{core}}/N_{\text{base}}$
78	4	0.5	1	57.2	$391 \pm 20$	$420 \pm 2$	$388 \pm 7, 1524$	16.14
78	4	0.5	1	58.2	$380 \pm 18$	$409 \pm 3$	$382 \pm 6, 2054$	19.60
78	4	0.5	1	59.2	$368 \pm 9$	$405 \pm 2$	$376 \pm 4, 3612$	19.79
78	4	0.5	1	60.2	$376 \pm 15$	$403 \pm 2$	$366 \pm 3, 1e5$	15.02
78	4	0.5	2	57.2	$379 \pm 18$	$398 \pm 2$	$373 \pm 4$	15.59
78	4	0.5	2	58.2	$366 \pm 13$	$389 \pm 3$	$366 \pm 5$	16.89
78	4	0.5	2	59.2	$358 \pm 7$	$386 \pm 2$	$366 \pm 7, 1101$	19.95
78	4	0.5	2	60.2	$366 \pm 14$	$385 \pm 2$	$368 \pm 8, 1642$	29.66
78	4	0.5	1	58.2	356	403	363	9.80
78	4	$\approx 1.0$	1	58.2	371	415	369	8.54
78	4	DAC 0	1	58.2	431	472	401	5.5
78	4	0.5	2	58.2	345	383	360	16.43
78	4	$\approx 1.0$	2	58.2	372	396	365	12.44
78	4	DAC 0	2	58.2	403	435	390	8.74
78	3	0.5	1	58.2	$413 \pm 13$	$456 \pm 1$	$409 \pm 5, 1674$	11.74
78	3	0.5	2	58.2	$374 \pm 19$	$385 \pm 2$	$363 \pm 4, 2792$	24.21
NOL	4	0.5	1	58.2	$381 \pm 4$	$424 \pm 1$	$385 \pm 4, 1000$	10.14
NOL	4	0.5	2	58.2	$360 \pm 17$	$367 \pm 2$	$353 \pm 6, 1081$	27.28

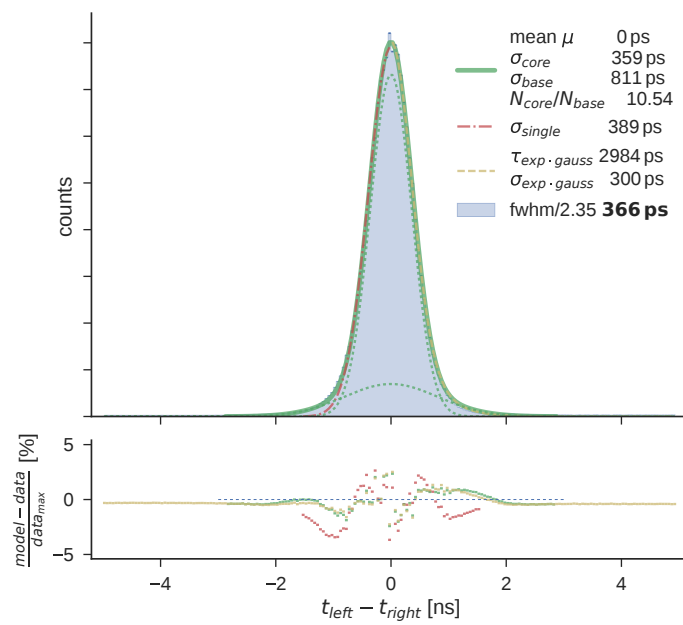


**Figure 11.21:** Time Resolution of a 4 layer SCSF-78 ribbon without additional  $\text{TiO}_2$  in the glue extracted from clusters with at least 2 active columns. No channel by channel time offset correction is applied.

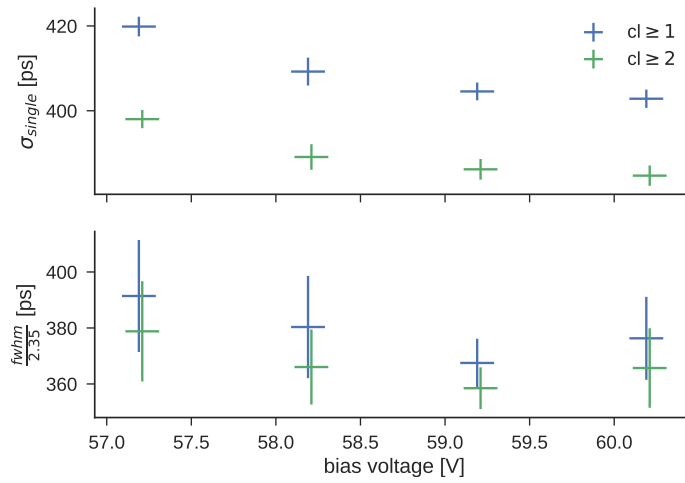


**Figure 11.22:** Measured time resolution as a function of the sensor’s bias voltage.

obtained in the MuTRIG measurement of  $(366 \pm 13)$  ps lies very well inside the uncertainty of  $(361 \pm 23)$  ps obtained in the full waveform test beam analysis.

#### BIAS VOLTAGE DEPENDENCY

A small improvement of the time resolution with increased SiPM bias voltage is observed. Figure 11.22 illustrates the effect which is of the order of  $\mathcal{O}(10)$  ps.

#### THRESHOLD DEPENDENCY

In addition to the time resolution at different bias voltages, Table 11.4 lists the time resolution at different threshold levels. In addition to the default 0.5 phe  $T$ -threshold level,  $\approx 1$  phe and all  $T$ -threshold DACs at a value of 0 are used. Increased thresholds worsen the time resolution.

#### POSITION DEPENDENCY

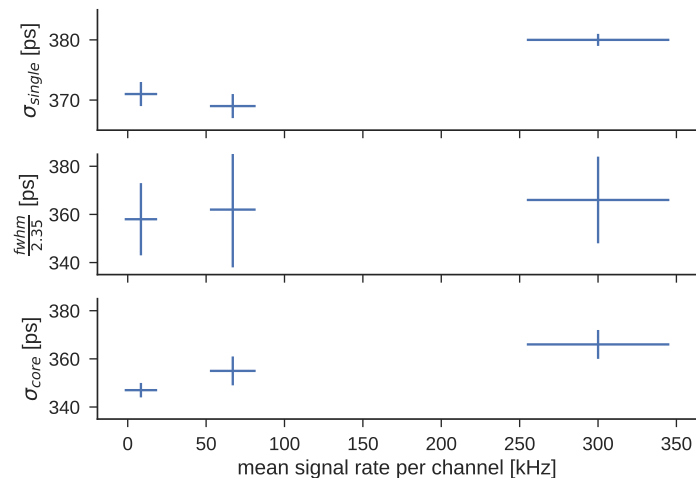
Table 11.5 lists the measured time resolution and the time offset of the time difference peak as a function of the source position along the fibre ribbon. A linear fit determines a propagation speed in the fibre ribbon of  $(0.255 \pm 0.003)c$ . The time resolution shows no source position dependency.

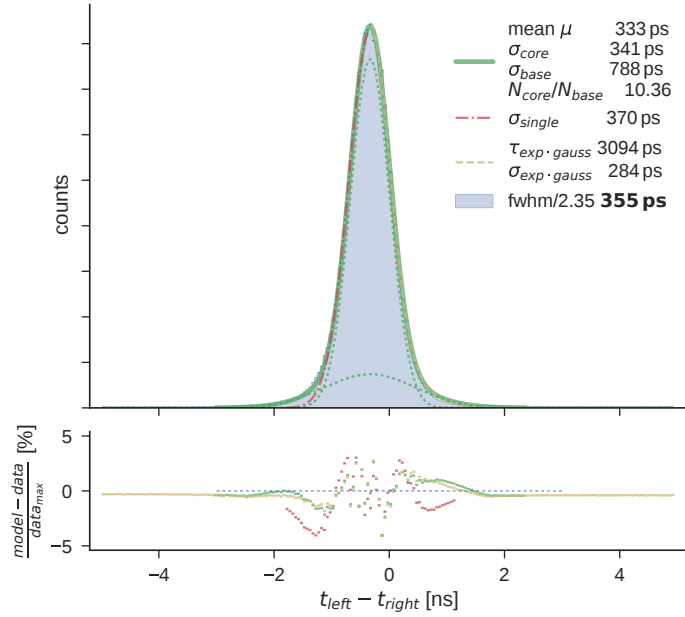
#### CHANNEL RATE DEPENDENCY

Figure 11.23 shows the cluster time resolution of clusters with at least two hits from a 4 layers NOL fibre ribbon prototype as a function the mean rate per MuTRIG channel caused by passing particles. The horizontal error bars correspond to the rate RMS between all channels. For such

**Table 11.5:** Time resolution and time difference offset for different source position along the fibre ribbon.

th [phe]	cl ≤	position [mm]	mean $\mu$ [ps]	$\frac{\text{FWHM}}{2.35}$ [ps]	$\sigma_{\text{single}}$ [ps]	$\sigma_{\text{core}}$ [ps]	$N_{\text{core}}/N_{\text{base}}$
0.5	1	0	-18	371	403	365	9.98
0.5	1	44	545	385	405	363	9.18
0.5	1	70	921	381	405	362	9.00
0.5	1	100	1275	366	402	364	10.15
0.5	2	0	-24	358	384	360	16.32
0.5	2	44	538	369	384	361	16.36
0.5	2	70	913	363	383	361	17.03
0.5	2	100	1267	355	380	361	20.36

**Figure 11.23:** Cluster time resolution of clusters with at least two columns extracted from a 4 layer NOL fibre ribbon prototype as a function of the mean rate per MUTRIG channel caused by passing particles. The horizontal error bars in rate correspond to the rate RMS between all channels.




**Figure 11.24:** Time resolution of a 4 layer SCSF-78 ribbon without additional  $\text{TiO}_2$  in the glue extracted from clusters with at least 2 active columns. Channel by channel time offsets are corrected for.

signal rates up to  $\approx 300$  kHz/channel no significant degradation of the time resolution is observed with the scintillating fibre detector prototypes. This behaviour differs from measurement for PET applications which utilize LYSO crystals. Due to the raised number of photons, about 1000, the increased SiPM signals lead to larger currents through the ASIC. A strong coincidence time resolution dependency on the channel rate in the order of 2 ps/kHz with an energy cut right below the Compton edge is observed [148]. This effect is believed to be caused by the internal feedback (see subsection C.1.1).

#### FURTHER IMPROVEMENTS

The cluster time resolution can be further improved by a channel by channel offset correction. This method is described in Figure 11.2.3. Figure 11.24 shows the improved result with respect to Figure 11.21. The improvement of  $\mathcal{O}(10$  ps) is negligible.

#### SUMMARY

The time resolutions of the fibre ribbon prototypes obtained by the digitization of the full waveform with a DRS4-based DAQ are reproduced by reading out the sensors with MuTRIG (see Table 11.4). The performance dependency on the sensor's bias voltage (see Figure 11.22),

threshold levels, particle crossing position (see Table 11.5) and event rates (see Figure 11.23) are presented. Up to an event rate of 300 kHz/channel no performance degradation is observed. Furthermore, a preliminary channel by channel calibration scheme based on crosstalk in the sensor arrays, as well as crosstalk which is mediated by the fibres between the two ribbon sides, is outlined.

# 12

## Mechanical and Electrical Integration

The sub-detector has to fit into the experiment's base structure, supplies and constraints from the silicon pixel tracker. In a first part, this chapter summarizes the mechanical constraints and requirements of the sub-detector. In a second part, a sub-detector integration concept including the electrical connectivity, the components of the readout board and detector cooling is proposed.

### 12.1 CONSTRAINTS AND REQUIREMENTS

The limited space for detector mechanical support structure and readout electronics is one of the main challenges of the M $\nu$ 3E fibre detector. Furthermore, also the volume available for supplies and signal lines is very restricted.

#### 12.1.1 THE AVAILABLE VOLUME

The cylindrically symmetric volume available for the fibre detector is constrained outwards by the third silicon tracking layer at a maximal radius of 67.5 mm, along the beam line by the supports of the same tracking layer which is separated by 330 mm, and towards the beam pipe by helium channels for the inner two tracking layers at a radius of 79.2 mm. Figure 12.1 gives an overview in the transverse plane. The stated numbers take on the one hand into account that the pixel sensors of the third tracking layers are shifted slightly inwards during pixel detector assembly. On the other hand, a roughly 5 mm wide helium channel is required between the fibre support and the tracking detector flanges. The separation of the two sub-detectors support structure allows the tracker support rings to move independently along the beam direction accommodating thermal expansion of this sub-detector.

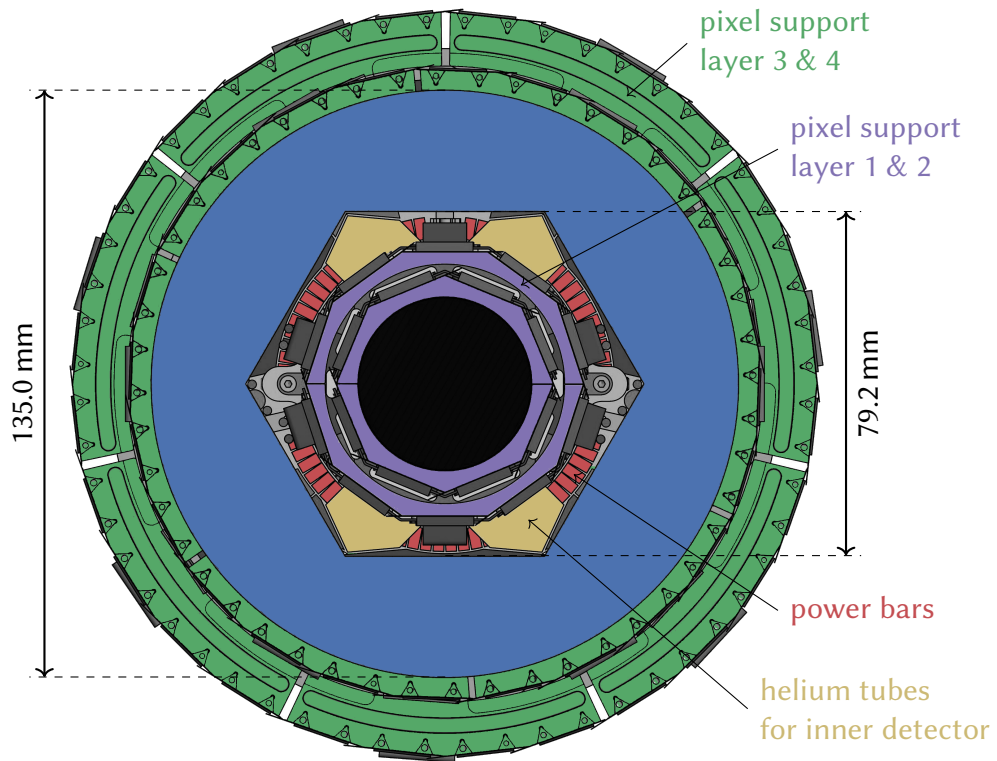


**Figure 12.1:** Transverse cut through the central part of the detector. The space available for the fibre detector and its support is indicated in blue (•). The volume is constrained by the third tracking layer indicated in green (•) and the helium supply tubes (•) shown in yellow for the inner detector region. Additionally, the support for the inner tracking layers (•) and the detector’s power bars (•) are highlighted in purple and red.

### 12.1.2 THE ENVIRONMENT OF THE DETECTOR

**TEMPERATURE** The sub-detector is surrounded by the helium atmosphere of the experiment at roughly atmospheric pressure. The operation temperature of the whole Mu3E experiment is still under investigation. It depends on the power consumption of the final MuPIX sensor and the details of the cooling concept. The overall operation temperature is expected to be above room temperature with a gradient along the beam direction of up to 40 celsius over the full third tracker layer in the central part with a length of 32 cm. The sub-detector is supposed to withstand temperatures up to a maximum of 80 °C without damage.

**HELIUM FLOW** The volume between the fibre detector and the third layer of the tracking detector is flushed with gaseous Helium for cooling of the silicon pixel sensors. A pressure difference of 3 mbar is expected over the full length of the fibre detector [75], corresponding to a helium flow speed of 5 m/s, respectively 1.2 m<sup>3</sup>/min.

**LIGHT TIGHT** The volume inside the magnet needs to be light tight. This means for example that LEDs have to be avoided and that light sources required for the alignment system are can be switched off.

### 12.1.3 MECHANICAL REQUIREMENTS

The mechanical and electrical design of the fibre detector must ensure simple radial access to the inner detector area. Furthermore, no access from the upstream nor the downstream side is possible during the sub-detector assembly. Hence, a design which allows mounting the detector from the radial direction is chosen.

### THERMAL EXPANSION OF FIBRE RIBBONS

Compensation of the thermal expansion of the fibre ribbons is required. Figure 12.2 shows the measured expansion of two prototypes, one with and one without additional TiO<sub>2</sub> in the glue, as a function of the ambient temperature. An expansion coefficient in the order of  $80 \cdot 10^{-6} /K$  is found. Over the full potential temperature range of up to 80 °C, this corresponds to an expansion of about 2 mm.

### COOLING REQUIREMENTS

The power dissipation in the SiPMs is, with below 5 mW per array, negligible. Due to the high ambient temperature, cooling will be required to ensure sensor operation around room temperature or below. This reduces significantly the DCR (see section 5.2).

The MuTRiG has a power consumption of about 30 mW per channel. This adds up to 60 W to 100 W per detector side if losses in local power regulators are taken into account. The helium cooling system cannot absorb this additional heat; another system with liquid coolant is required.

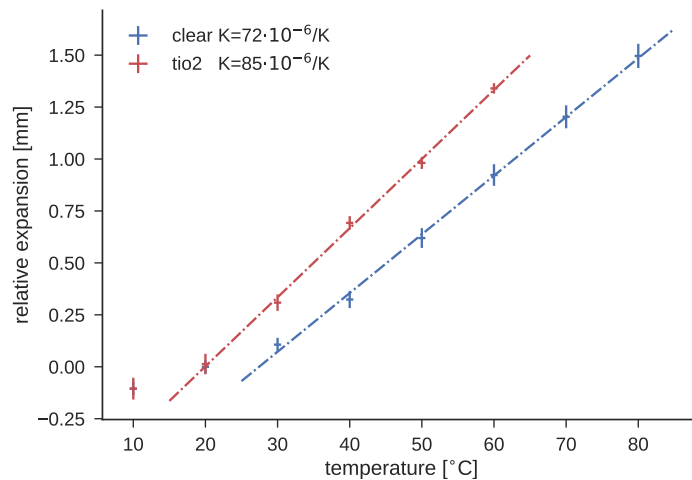


**Figure 12.2:** The relative expansion along the fibre direction of two 1.6 cm wide and 40 cm long fibre ribbon prototypes consisting of 4 layers 250  $\mu\text{m}$  thick round fibres with (*tio2*  $\rightarrow$ ) and without (*clear*  $\rightarrow$ ) additional  $\text{TiO}_2$  in the glue. Linear functions are fitted to the data; their slopes and the fibre total fibre length determine the thermal expansion coefficients  $K$ .

## 12.2 DETECTOR INTEGRATION CONCEPT

The fibre detector is divided into 6 modules which each consists of two ribbons as described in chapter 3. The  $(32.0 \pm 0.1)$  mm wide and  $(288.0 \pm 0.5)$  mm long fibre ribbons with one 128-channel SiPM column array (see section 5.2) attached to each side build the base unit of the detector. One side of such a module is shown in Figure 3.2. The sensors, shipped on a PWB which is soldered to a flex print cable, are fixed by three screws directly to the holding structure which is glued onto the fibre ribbons at both ends.

To reduce the ribbon's sag and compensate the thermal expansion each ribbon is spring-loaded individually. Figure 12.3 shows the sag of two prototypes, one with and one without additional  $\text{TiO}_2$  in the glue, as a function of the applied tension. The used ribbons are arched by the production procedure. This intrinsic tension results in an orientation dependent behaviour. For forces larger than 0.3 N a sag below 2 mm is observed which is believed to be sufficient for the sub-detector.

Two ribbons are attached to the same fibre support structure; they form one module. The two ribbons are offset with respect to each other along the beam direction by 4 mm to accommodate the sensors. On each side, the flex print cables from both sensors end at the bottom of the support structure, where they are connected to the scintillating fibre board (SCIFI BOARD). Figure 12.4 shows the spring loading of a ribbon on one side of a ribbon, a full module is shown in Figure 12.6. This modular design allows to test and characterize the full fibre ribbon-sensor assembly outside of the detector.

The modules are mounted radially onto fibre support rings which are fixed rigidly to the beam pipe. This is possible because the thermal expansion of the modules is handled by the

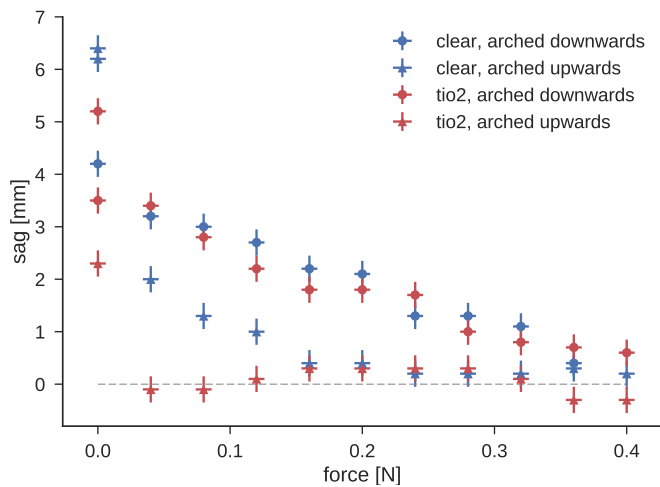


**Figure 12.3:** The sag at the centre of 40 cm long and 1.6 cm wide prototypes consisting of 4 layers of 250  $\mu\text{m}$  thick round fibres as a function of the applied force for tension. One ribbon is produced with ( $\rightarrow$ ) and one without ( $\leftarrow$ ) additional  $\text{TiO}_2$  in the glue. The ribbons are intrinsically arched, both orientations are shown (arched *downwards* and *upwards*). If no force is applied the sag depends on the way the ribbon is placed in the setup.

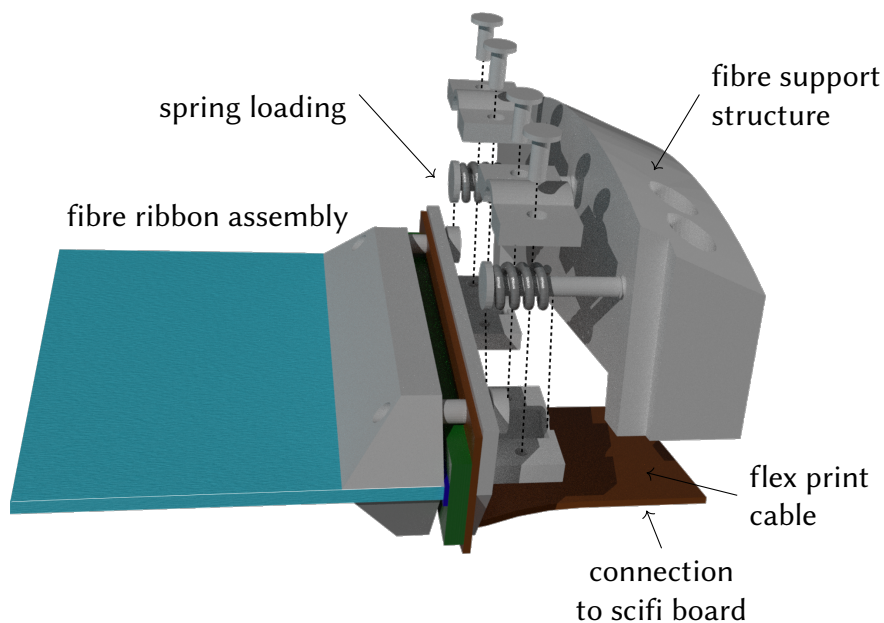


**Figure 12.4:** Spring loading of one fibre ribbon to the fibre support structure. One module comprises two ribbons. The flex print cable onto which the sensor is bonded ends at the bottom of the support. Figure 3.2 shows a more detailed view of the fibre ribbon assembly.

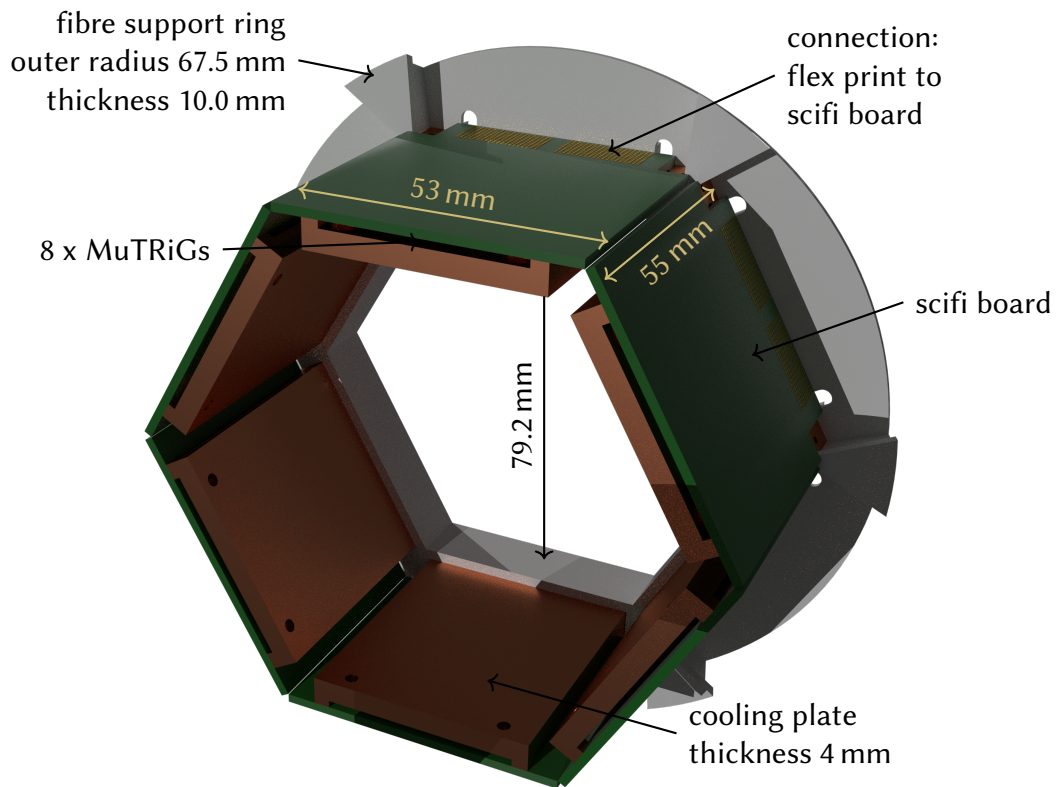


**Figure 12.5:** Fibre detector support ring with one electronic board (SCIFI BOARD) and cooling plate per module. The support ring backsides of both detector sides are separated by 330 mm.

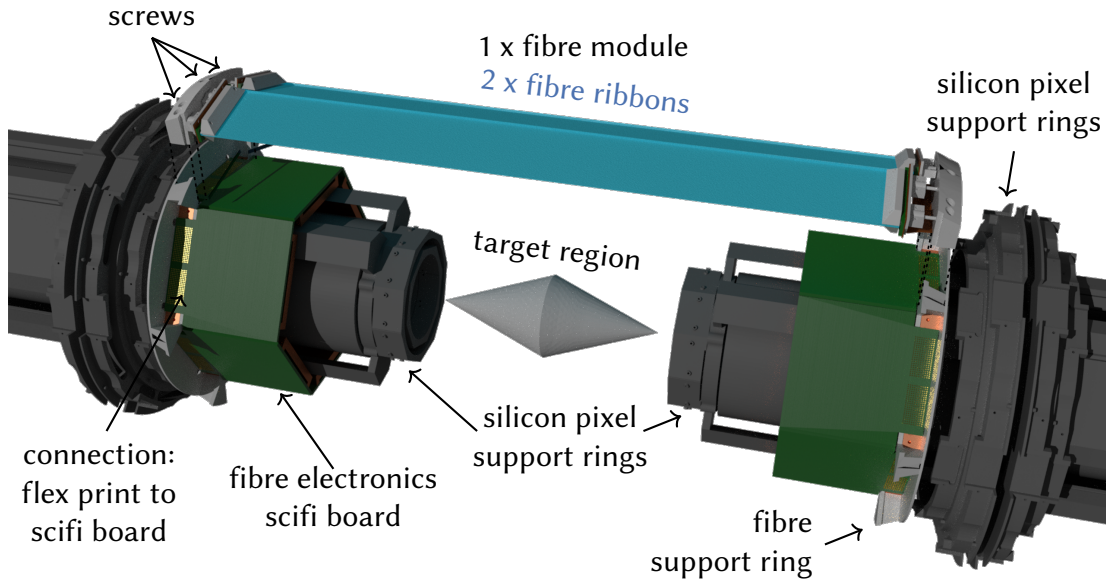


**Figure 12.6:** Radial insertion of one fibre module comprising two fibre ribbons. Two-dimensional connectors realise the electrical connection between the flex print cables and the SCIFI BOARDS.

individual spring loading of each ribbon. The support rings comprise one scintillating fibre readout board (SCIFI BOARD) per module per side, which host the readout ASICs. The boards are attached to liquid-cooled plates. Figure 12.5 shows the support ring of one side.

The electrical connection between the sensors and the readout electronics is realized through the flex print cables which end at the bottom of the module support structure. The flexibility is required to compensate for the distance difference caused by the spring loading. During radial module insertion onto the support rings a two-dimensional connector, called interposer, realizes the electrical connection between the flex print cables and SCIFI BOARD. Furthermore, the module support is thermally connected to the cooling plate. Figure 12.6 shows the radial insertion of a fibre module. Screws fasten the electrical connections and the module through holes in the module support exclusively from the radial direction.

Figure D.2 shows a picture of a 3d-printed model of the fibre detector integrated into the Mu3E experiment.

### 12.2.1 ELECTRICAL CONNECTION

The proposed mechanical design relies on the feasibility of the flex print cables for the analogue SiPM signals and their connection through the interposers to the SCIFI BOARD which has to be proven.

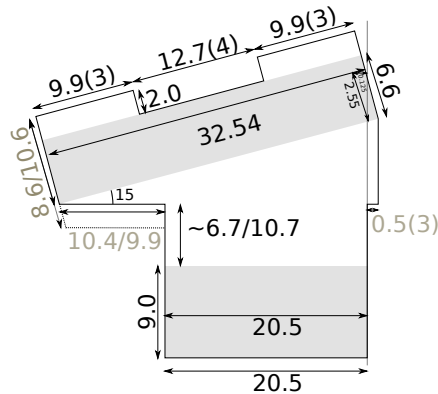


**Figure 12.7:** Dimensions of the flex print cables in the proposed design. The offset of the fibre ribbons along the beam direction of 4 mm require every second flex print cable to be longer. Furthermore, the two flex print cables of the two sensors of one side of the same module are mirrored.

## FLEX PRINT CABLES

The flex print cables connect the sensors, which are soldered to the cables, with the readout electronics. Their flexibility is required to account for the thermal expansion of the fibre ribbons. Common positive high voltage is applied at the SiPM's cathode which demands a filter as close to the sensors as possible. A sufficiently large capacity has to be placed on the flex print cable. The 128 single-ended SiPM signals are routed individually from the sensor through an interposer to the MuTRIG inputs. Furthermore, digital temperature sensors on the backside of the sensors allow monitoring the SiPM operation conditions. To minimise cross-talk from the steep rising edges of clock lines, I<sup>2</sup>C is waived and much slower and better to control one-wire sensors will be used. In total the flex print cables supply ground and high voltage bias, host filter capacities and one-wire temperature sensors and 128 single ended analogue signal lines. Low impedance is envisaged to guarantee good time resolution and fast recovery times. Cross-talk between signal lines from neighbouring SiPM channels could mimic the presence of clusters, therefore pollute the suppression of dark counts and increase the occupancy.

A density of  $\approx 4$  lines/mm is required to fit all 128 signal of one SiPM array into two signal layers. This leads to a feature size of  $\approx 125$   $\mu\text{m}$  if no ground lines are placed between two signal lines or  $\approx 60$   $\mu\text{m}$  if this is the case. The bending radius of a flex cable is in general twelve times the thickness. To achieve the required bending radius of below 2 mm the height of the flex cable at the bending zone has to be below 170  $\mu\text{m}$ . Figure 12.7 shows the outline of the flex print cable in the proposed design.

Different possible designs of micro strips and striplines are described in more detail in section D.1.

**Table 12.1:** Number of contacts of one flex print connection grouped by type. On interposer with  $10 \times 40$  contacts connects two flex print cables to one SCIFI BOARD.

type	number		
	domains	contacts per domain	total
SiPM signals	128	1	128
SiPM bias voltage	2	6	12
ground	1	54	54
$2 \times$ temperature sensors	$2 \times 3$	1	6
<b>total</b>			<b>200</b>

### THE INTERPOSERS

The proposed design utilizes a high-density two-dimensional connector. This allows module connection from purely radial direction. It is foreseen to use one Samtec ZA8 microarray with  $10 \times 40$  contacts per module per side. The pads of this connector have a pitch of 0.8 mm. The connector is specified up to rates above 9 GHz [149]. Table 12.1 lists the number of contacts grouped by type. One interposer connects two flex print cables of which each is connected to one 128-channel sensor. The bias voltages of the two dices of one sensor are separated (see section 5.3).

#### 12.2.2 THE READOUT BOARD: SCIFI BOARD

The scintillating fibre detector readout board (SCIFI BOARD) hosts the readout ASICs, provides the required supplies of these chips and provides slow control information, such as temperature and current monitoring. The flex print cables and the interposer connect  $2 \times 128$  SiPM channels to one board. Hence, 8 MuTRiG s, each with 32 channels, are required per module per side. The board has a maximal size of 53 mm  $\times$  55 mm. Table 12.2 gives an overview of the proposed components. This scheme allows connecting one SCIFI BOARD to one bank of the experiments front-end FPGA board. Note, that in principle multiple banks would be available.

### THE MuTRiG ASICs

Table 11.1 lists all MuTRiG<sup>1</sup> pads and their functionality. The ASICs are either wire bonded directly to the SCIFI BOARD and covered with glob-top or a similar technology to increase the mechanical stability or a packaging hosting two ASICs is used. The proposed packaging has a size of 17 mm  $\times$  17 mm with a 0.8 mm-pitch ball grid array. Note that due to the single-ended sensor readout scheme only one ASIC pad per channel needs to be connected. The readout ASICs dissipate in total 8-10 W per board. Hence they are located on the “bottom” side of the board facing the cooling plate.

<sup>1</sup>Of the first ASIC version.

**Table 12.2:** Proposed components on the SCIFI BOARD. *LV* stands for low voltage and *HV* for high voltage. The MuTRiG ASICs could be directly wire bonded or packed in pairs of two.

component	comment	area [mm <sup>2</sup> ]	number
MuTRiG		5.0 × 5.0	8
	wire bonded	~15 × 10	8
	packaging	17 × 17	4
LDO 1.8 V analogue	TPS7A830	3.5 × 3.5	2
LDO 1.8 V digital	TPS7A92	2.5 × 2.5	2
LDO 3.3 V digital	TPS7A92	2.5 × 2.5	1
current monitor, LV	LTC2991	4.0 × 3.0	2
voltage and current monitor, HV	LTC4151	3.0 × 3.0	2
temperature sensors			≥4
chip select (cs) multiplexing	MAX349	5.3 × 7.3	2
clock fan-out	SI53344	5.0 × 5.0	1
TDC injection	PL138-48	3.0 × 3.5	2
LVDS buffer	DS15BR400	5.0 × 5.0	2

#### VOLTAGE GENERATION AND MONITORING

The supply voltages of 1.8 V and 3.3 V for the MuTRiGs need to be generated from a common supply by the copper bar on the board. The LDO regulators listed in Table 12.2 are proposed for this task. Furthermore, the current of the ASIC is monitored by a current monitor with I<sup>2</sup>C interface. In addition to the power from the copper bars, high voltage, generated outside of the detector<sup>2</sup> is provided for each board. The voltage at the interposer and the current through the SiPM are monitored and read out through the common I<sup>2</sup>C bus.

#### ASIC SLOW CONTROL

The MuTRiG SPI slow control, including Channel Event Counter, is multiplexed to reduce the number of required signal lines between the SCIFI BOARD and the experiment's front-end FPGA board. All MuTRiG share a common SPI clock (sclk), data-in (sdi), data-out (sdo) and CEC data-out (cec\_sdo) lines. Two multiplexers switch the chip select signal for the slow control (cs) and the CEC (cec\_cs). The multiplexers themselves are also configured by SPI what requires an additional chip select (cs\_cs, cec\_cs\_cs) per such device.

#### CLOCK DISTRIBUTION

The experiment front-end FPGA board provide a reference selectively at 625 MHz. This clock needs to be distributed to the ASICs. A Low-jitter LVDS fanout clock buffer is utilized. The two

<sup>2</sup>probably inside the magnet.

reference clocks required by each MuTRiG, one for the digital part and one as the reference for the PLL, can be combined. If the utilized cables for the clock signals from the experiment front-end FPGA board to the SCIFI BOARD turn out not to be suited for the reference clock distribution at the described rate, the experiment's 125 MHz system clock could be used alternatively. This requires the replacement of the LVDS fanout clock buffer with a clock multiplier including a local oscillator<sup>3</sup>.

### MuTRiG TDC INJECTION

The external triggering of the TDC of the ASIC provides a useful tool for calibration and monitoring as described in subsection 11.1.2. To allow TDC injection triggered by LVDS signal from the front-end FPGA an LVPECL fanout buffer in combination with a resistor network is used as described in Figure 11.4.

### INTERFACE OF THE SCIFI BOARD

The experiments common front-end FPGA boards comprise 5 banks which each connects to 3 MuPIX sensors. Each bank connects 9 LVDS data links, additional 5 differential links for monitoring, clocks and fast resets and 3 differential links for chip configuration to LVDS up to 1.25 Gbps Serializer-Deserializer pairs (SERDES) of the Arria V FPGA. Furthermore, a configurable differential line from the experiments clock distribution is available. The possibility to connect three analogue temperature sensors which are connected to an ADC on the front-end board and an analogue pulse generation for injection in the pixel sensors are not used by the fibre detector. The presented SCIFI BOARD design allows to connect such boards to one bank of the experiment's front-end board. Table 12.3 summarizes the lines of this interface.

Due to bandwidth considerations (see section 2.6) only two SCIFI BOARDS are connected to one front-end board. This would in principle allow to use up to 2.5 banks per board. The here presented use of only one bank is motivated by the minimization of the number of cables between front-end board and SCIFI BOARD and might be adjusted in future.

### 12.2.3 THE DETECTORS COOLING

The cooling of the fibre sub-detector splits into two parts. Firstly, the system has to dissipate up to 100 W per side dissipated by the readout ASIC and LDOs. This is realised directly through the liquid-cooled plates below the SCIFI BOARDS. Secondly, the temperature of the SiPM sensors is required to be stabilized. Depending on the overall experiment temperature, which is expected to be high ( $>30^{\circ}\text{C}$ ), cooling is needed to operate them around or below room temperature.

---

<sup>3</sup>For example SI5345.

**Table 12.3:** The interface of the SCIFI BOARD to one bank of the front-end FPGA board and power distribution. The abbreviation *sensor temp* stands for the temperature sensors at the SiPMs on the backside of the flex print cables (see subsection 12.2.3). The *external trigger* line is optional. † The reset of the current MuTRIG comprises two single-ended signals. The next version will incorporate a single differential reset.

group	name	type	direction	rates	lines
reference clock	clk	LVDS	in	625 MHz	1 × 2
data	data	LVDS	out	1.25 Gpbs	8 × 2
slow control	sclk	SPI	in	20 MHz	1
	cs, cec_cs, cs_cs, cec_cs_cs	SPI	in	20 MHz	4
	sdi	SPI	in	20 MHz	1
	sdo, cec_sdo	SPI	out	20 MHz	2
	<b>total</b>	<b>SPI</b>		<b>20 MHz</b>	<b>7</b>
injection	inj	LVDS	in	$\mathcal{O}(100 \text{ kHz})$	1 × 2
I <sup>2</sup> C	scl, sda	I <sup>2</sup> C	inout	MHz	2
reset†	rst		in	sync. 125 MHz	1 × 2
sensor temp		1-wire	inout		2
<i>trigger</i>	<i>trg</i>		in		1
spare					2
<b>total</b>					<b>34</b>
power, ground	1.4 V to 6.5 V, <20 W		in		2
high voltage	~55 V		in		2

### LIQUID-COOLED PLATES

The major share of heat dissipation of the fibre detector is caused by the eight MuTRiG s and subordinately by the LDO regulators on the SCIFI BOARD. They are located at the bottom side of the board in direct contact with the copper cooling plates (see Figure 12.5).

Per side, six supply tubes with an inner diameter of  $\sim 3$  mm provide the liquid coolant. The liquid is passed through two modules in series. Simulations have shown that a water flow below 1 m/s corresponding to 0.3 L/min at an inlet temperature of  $10^\circ\text{C}$  is sufficient to keep the ASIC temperature low.

Under the very conservative assumption of a power dissipation of 24 W per package (2 MuTRiGs), corresponding to a factor 10 with respect to expectations, and a surrounding helium temperature of  $40^\circ\text{C}$ , the temperature of the package is below  $35^\circ\text{C}$ . The copper plate's temperature stabilizes at  $\sim 30^\circ\text{C}$ , and the water temperature at the outlet of the first cooled module is  $15^\circ\text{C}$ . Figure D.1 shows the equilibrium temperature of the system.

An Alternative cooling scheme where the ASICs are located on the top side of the SCIFI BOARD and are cooled from the bottom is also being considered. This is motivated by preliminary cooling tests performed on STiC ASIC in a packages, where the latter scheme performed better [150].

### TEMPERATURE STABILIZATION OF THE SENSORS

Two sensors at the backside of the flex print cable at the position where the sensors are soldered to monitor the temperature of the SiPMs. Depending on the experiment's operation temperatures and gradients over the central barrel, additional cooling is required. In this case, it is foreseen to build the fibre module support structure out of a well heat conducting material. The stiffener at the backside of the sensor assembly is connected flexibly and well heat conducting. The efficiency of this concept needs further investigation.



# 13

## DAQ

The trigger-less DAQ of the experiment is designed in such a way, that the information of the full detector of a time slice is available for online reconstruction (see section 2.6). Although the additional information from the timing detectors is not used for the online event reconstruction, the corresponding detector hits need to be assigned to the right reconstruction frame for potential event building and storage.

An overview of the experiment's DAQ is given section 2.6. This chapter firstly summarizes the expected data rates from the fibre sub-detector at different stages of the experiment's DAQ, followed by a discussion of the available and required link bandwidths.

### 13.1 THE EXPECTED DATA RATES

The analogue signals from one side of one module, two 128-channel SiPM column arrays are digitized on the SCIFI BOARD which hosts 8 MuTRiG ASICs. Each digitises 32 channels and is linked with one 8b/10b [121] encoded 1.25 Gbps link to the experiment front-end. The front-end decodes the timestamps from the ASICs, sorts the events and packages them for later merge with the data stream from all sub-detectors. Two 6.25 Gbps links connect each front-end board to the switching boards which combines the data streams and forwards it on a total of four 12.5 Gbps links to the filter farm.

#### 13.1.1 DATA RATES FROM THE SCIFI BOARD

Figure 13.1 shows the expected event rates caused by particles per readout channel, a SiPM column, of  $\mathcal{O}((619 \pm 20) \text{ kHz})$  ( $\mathcal{O}((504 \pm 15) \text{ kHz})$ ) for trigger levels at 0.5 photoelectrons (1.5 photoelectrons). The sensor's DCR, which depends on the sensors over-voltage, operation temperature and radiation dose (see section 5.2), has to be added to these numbers. It ranges from 50 kHz up to several hundred kHz. Operation at a trigger level above 1 photoelectron reduces the DCR considerably.

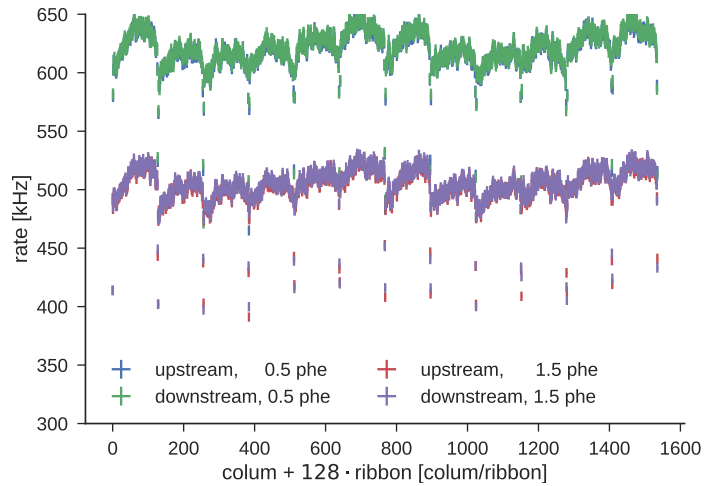


**Figure 13.1:** Expected rate per SiPM column at  $1 \cdot 10^8$  stopped muons per second at MuTRiG trigger level at 0.5 photoelectrons and 1.5 photoelectrons grouped into up- and downstream sensors. At the fibre ribbons edge, which coincides with the 128 channel sensor edge, the rate drops due to inefficiencies.

In the time mode of the MuTRiG, the events consist of 28 bits; for each MuTRiG readout ASIC a bandwidth of 670 Mbps (450 Mbps) after 8b/10b encoding at a trigger level of  $\sim 0.5$  photoelectrons ( $\sim 1.5$  photoelectrons), is required for events caused by crossing particles. Potential DCR has to be added. For each MuTRiG, one 1.25 Gbps 8b/10b encoded link to the experiment's front-end is available. At a trigger level of 0.5 photoelectrons, this allows for a DCR up to  $\sim 300$  kHz at this DAQ stage.

### 13.1.2 SORTING AND PACKAGING IN THE FRONT-END

On the experiment's front-end board the data stream from the individual MuTRiGs are time sorted, combined and prepared to be merged with the pixel and tile sub-detector data streams.

The time information needed for the sorting is obtained from the MuTRiG coarse counter which is encoded in a LFSR. Hence, this timestamps need to be decoded first.

Although the digitized hits of one SiPM channel are strictly time ordered, the different channels are not. Furthermore, the experiments data streams are merged based on the experiment frames which base on the 8 ns pixel timestamps. The MuTRiG timestamps of the timing detectors are based on 50 ps wide bins. Since the latter are not a two potency part<sup>1</sup> of the pixel timestamps, the mapping from MuTRiG timestamps to experiment frames (pixel timestamps) is non-trivial once the counter overflows. To simplify merging of the data streams and since the storage of events will be managed based on the experiment frames, a sorting based on pixel timestamps, as described in [151], is proposed.

<sup>1</sup>50 ps/8 ns=160.

**Table 13.1:** Proposed fibre sub-detector data format after the front-end board. The data stream is sorted and prepared to be merged to the pixel data stream based on 8 ns experiment frame counter values. It is transmitted in blocks of 128 such frames. The abbreviation *ts* stands for timestamp.

---

0	header word
1	block counter
2	FPGA internal <i>ts</i> (8 ns), bits 31 to 61
3	FPGA internal <i>ts</i> (8 ns), bits 0 to 30
4	FPGA internal MuTRiG <i>ts</i> (12.8 ns), bits 50 to , 80
5	FPGA internal MuTRiG <i>ts</i> (12.8 ns), bits 19 to 49
<i>ribbon header</i>	
j	ribbon (5 bits), N (7 bits), frame <i>ts</i> (10 bits), MuTRiG <i>ts</i> (10 bits: bits 9 to 18)
j + 1	<i>event data</i> (1/2 word)
...	column (7 bits), e-flag (1 bit), MuTRiG <i>ts</i> (8 bits: bits 0 to 8)
j + 1 + ceil(N/2)	
trailer word	

---

## MULTIPLEXING

One SCIFI BOARD is connected by eight 1.25 Gbps links to the experiment FPGA front-end board. The information of one SiPM hit is contained in 3.5 bytes (28 bits). The expected data rates allow multiplexing of four links if the sorting and storing runs at 125 MHz of the recovered byte-clock<sup>2</sup>. At double data rate, it is feasible to multiplex two times four links. This approach follows again the pixel sub-detector's design [151].

## DATA FORMAT OF THE PACKAGED DATA STREAM

The 8 ns timestamp-wise ordered fibre SiPM hits are read out out in blocks of 128 timestamps. Table 13.1 shows a potential structure of such a readout block in units of 32-bit words. It follows closely the proposed structure of the pixel sub-detector [151]. On the FPGA on the experiment's front-end boards two internal timestamp counters are present: a 62-bit frame counter, as well as a 60-bit MuTRiG counter which extends the 20-bit timestamps from the ASICs. The *ribbon header* and *event data* are only sent in the presence of events.

---

<sup>2</sup>This clock is synchronous to the individual de-serialized bytes of the 8b/10b encoded 1.25 Gbps links.

**Table 13.2:** Expected event rate and the required bandwidth per SCIFI BOARD and in total for different readout scenarios (modes). In the *raw events* mode, all hits are transmitted, whereas in the *clusters* mode the information content is reduced.

mode type	trigger [phe]	multiplicity	rate [MHz]		bandwidth [Gbps]	
			scifi board	total	scifi board	total
raw events	0.5	all	188	2256	6.17	73.99
raw events	1.5	all	161	1927	5.34	64.13
raw events	0.5	> 1	147	1768	3.56	42.75
raw events	1.5	> 1	126	1509	3.11	37.38
clusters	0.5	> 1	28	337	0.92	11.01
clusters	1.5	> 1	25	297	0.81	9.72

**Table 13.3:** The available bandwidth at the different DAQ stages in the baseline design. The total event rate is calculated based on the raw event size without any compression.

connection		bandwidth per link [Gbps]	event size [bit]	event rate per link [MHz]	number of links	total raw event rate [GHz]
from	to					
SCIFI BOARD	front-end	1.25	28	36	$12 \times 8$	3.46
front-end	switching	6.25	34	147	$6 \times 2$	1.76
switching	farm	12.5	34	294	$1 \times 4$	1.18

#### DATA FORMAT OF THE PACKAGED DATA STREAM IN THE PRESENCE OF CLUSTERING

Even though the use of the time information in the online reconstruction is not foreseen it could be provided. The online exploitation of hit information of the fibre sub-detector would require an online clustering. Only one MuTRiG timestamp is used per cluster. Table D.2 shows a potential structure of a readout block in the presence of online clustering. Note that the information content is reduced.

#### 13.1.3 EXPECTED FINAL DATA RATES

In both above mentioned cases, the streaming of raw events and in the presence of an online clustering, data from ribbons with a hit multiplicity below two could be rejected to suppress DCR and reduce the required bandwidth. Table 13.2 list the expected event rates and bandwidth requirements per SCIFI BOARD and in total for the different scenarios including trigger levels of  $\sim 0.5$  photoelectrons and  $\sim 1.5$  photoelectrons.

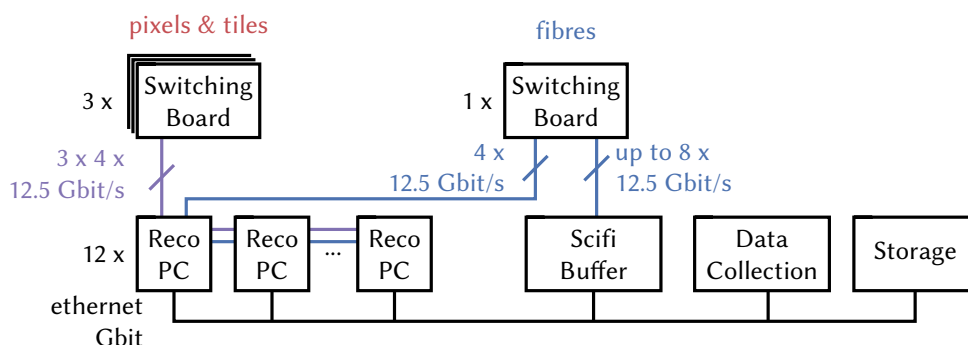


**Figure 13.2:** Alternative DAQ design with respect to Figure 2.7 if a bandwidth above 40 Gbps is required for the fibre sub-detector.

## 13.2 THE AVAILABLE LINK BANDWIDTH

Table 13.3 gives an overview of the available bandwidths in the different stages of the DAQ chain. Each MuTRiG is connected via 1.25 Gbps 8b/10b encoded LVDS link to the front-end board. With an event size of 28 bits, this allows a maximal event rate of 36 MHz per 32-channel ASIC. The 12 scifi boards host each 8 ASICs resulting in a total bandwidth of up to 3.46 GHz.

On the front-end board, the address of hits is extended by 7 bits, 4 bits for the board number (12) and 3 bits for the MuTRiG ASIC number (8). Since one of the 28 bits of the MuTRiG time event structure is not used (see section 6.3), this results in a new event size of at least 34 bits. Taking a link 8b/10b-encoding overhead of 25 % into account, this leads to maximal total event rate for raw events of 1.76 GHz, a reduction by a factor 2 with respect to the previous DAQ stage. The switching boards combine the data streams from all fibre detector front-ends. It is connected via  $4 \times 12.5$  Gbits links to the reconstruction farm. At this stage, the maximal available bandwidth for raw fibre detector hits is reduced again by a third to 1.18 GHz.

### 13.2.1 ALTERNATIVE DAQ SCHEME

In the presented DAQ scheme the number of four 12.5 Gbps links from the fibre switching board to the filter farm and in between the filter computer is a hard limit imposed by the deployed QSFP<sup>3</sup> connectors which provide 12 optical duplex lines. If a mode of operation is chosen which exceeds the available bandwidth, the data stream from the fibre detector could bypass the filter farm. This is possible because the time information is not required for the online reconstruction. In this scheme shown in Figure 13.2, all frames are sent to a dedicated unit (scifi buffer) which provides the event builder only with the frames requested. The decision which frames are stored is based on the online reconstruction running on the farm.

<sup>3</sup>Quad Small Form-factor Pluggable.



**Part V**

**Summary and Outlook**



# 14

## Summary and Outlook

In a first phase, the MU3E experiment aims to measure the rare cLFV decay  $\mu \rightarrow eee$  at an Single Event Sensitivity of  $2 \cdot 10^{-15}$ . Achieving this sensitivity requires a combination of high muon rates of up to  $1 \cdot 10^8$  stopped muons per second and a detector with excellent momentum, vertex and time resolution capable of handling the high particle rates. The scintillating fibre sub-detector shall provide a time resolution better than 350 ps of a traversing particle in the inner detector part with minimal momentum resolution degradation and very high efficiencies. This time resolution is required to suppress combinatorial background and reject mis-reconstructed track candidates who are mainly assigned the wrong charge.

An extensive fibre ribbon characterization campaign by the whole MU3E fibre group led to the choice of round, double-clad 250  $\mu\text{m}$  thick fibres from Kuraray of type SCSF-81MJ. Furthermore, novel NOL fibres are identified as a viable option for future detector upgrades. The performance of the latest prototypes is presented in chapter 7. At the same time, the fibre ribbon production and handling at the University of Geneva and at PSI improved, resulting in prototypes with even more improved performance.

The measured performance of the fibre ribbon prototypes coupled to the identical SiPM column arrays as will be used in the experiment are used to tune and validate the sub-detector response in the experiment's simulation framework (see chapter 9). This allows relating the measured prototype time resolution of a ribbon consisting of 4 fibre layers of  $\sigma_{(t_{\text{left}}-t_{\text{right}})} \approx \frac{\text{FWHM}}{2.35} = (361 \pm 23)$  ps to an overall sub-detector time resolution per crossing particle of  $\sigma_{\text{fibre}} = 234$  ps. This exceeds the requirements of better than 350 ps by a considerable fraction.

The integration of the time information from the fibre and tile sub-detectors in the reconstruction and analysis framework allows studying the expected combinatorial background suppression as a function of signal selection efficiency, as well as the rejection of mis-reconstructed track candidates which have mainly a wrong charge assignment (see chapter 10). At a signal selection efficiency of 90 %, a Bhabha-like combinatorial background suppression in the order of factor 70 is expected. The required suppression factor has to be determined once the amount of background in the experiment has been actually measured with the full detector.

The scintillating fibre ribbons are read out on both sides by SiPM column arrays from Hama-

matsu of type S13552-HRQ. The specific requirements and results from test measurements of detector components and simulation led to the development of a dedicated readout chip, the MuTRiG ASIC by KIP at the University of Heidelberg. This ASIC digitises the analogue signals from the SiPMs and provides a timestamp of the Time of Arrival in combination with a flag of signal amplitude threshold. It will handle rates up to 1.1 MHz per channel, of which up to 650 kHz are assumed to be caused by particles crossing the scintillating fibre detector. The feasibility of operating this ASIC at a single-photon level at rates up to 300 kHz/channel has been successfully demonstrated (see chapter 11). The results obtained by digitization of the full waveform are reproduced with the MuTRiG. The effect of different chip settings and operation conditions, such as sensor bias voltage, particle crossing position and particle rates, are investigated in detail and described herein. The DAQ developed for this purpose is the base for the sub-detector's readout integration into the whole experiment. It is integrated into the MIDAS framework.

Based on the experience with the STiC and MuTRiG ASICs, as well as with the fibre prototypes of the fibre sub-detector, a complete mechanical and electrical sub-detector integration scheme and DAQ integration into the Mu3E experiment is proposed in chapters 12 and 13.

#### 14.1 PROPOSED SENSOR AND MuTRiG OPERATION MODE

I suggest to operate the sensors of the fibre sub-detector at rather high bias voltages  $\mathcal{O}(59\text{ V})$ , corresponding to an overvoltage in the order of 6 V. This maximizes on the one hand side the time resolution (see Table 11.4) and simplifies, on the other hand, the usage of the MuTRiG  $E$ -flag due to the larger signal amplitudes. At this voltage and around room temperature, the sensor's DCR is in the order of 110 kHz per channel (see Figure 11.8) and shows a dark current of  $4.2\ \mu\text{A}$  per array. Note the strong dependency on the operation temperature. Preliminary irradiation studies with a similar sensor indicate a DCR increase at room temperature in the order of 1 MHz per channel per year of operation ( $\sim 100$  days) at a muon stopping rate of  $1 \cdot 10^8\ \text{Hz}$  (see section 5.4). Neither the MuTRiG ASIC nor the DAQ can handle these raw rates which occur at the end of one year of operation. In addition to lower operation temperatures, a  $T$ -threshold above 1.0 photoelectrons will be required. As shown in Figure 11.2.2, the dynamic range of the ASIC is about sufficient for such thresholds. Although operation at thresholds of 1.5 photoelectrons degrades the time resolution of the sub-detector in the order of 35 ps (see Table 11.4) it suppressed DCR significantly due to the low pixel-to-pixel crosstalk probability of the employed SiPM generation. I propose to use thresholds of 1.5 photoelectrons. Alternatively, the possibility of relying on the additional  $E$ -threshold of the ASIC could be investigated (see section 14.2). The effects on the overall efficiency need to be studied in more details (see section 14.2). If the raw event data only from SiPM arrays (4 MuTRiG) with more than one hit per 8 ns readout frame are transmitted, a raw bandwidth of 37.4 Gbps is required (see Table 13.2).

#### 14.2 OUTLOOK AND UPCOMING ISSUES

This thesis outlines a possible path towards the Mu3E scintillating fibre detector. The feasibility of using MuTRiG to digitise the signals from the SiPM arrays is demonstrated. There

are topics to be resolved in the next one to two years to be able to reach the event sensitivity mentioned above. These issues are the actual production of the twelve fibre ribbons and the production and integration of the readout electronics which includes the up-scaling from a single MuTRiG ASIC to a whole system comprising 96 chips and their operation inside the experiment's environment and DAQ system. These activities will be accompanied by the development of calibration and alignment procedures, also in the time domain.

In the following, three subjects for future development expanding the work presented in this theses are proposed.

#### FIBRE RIBBON EFFICIENCIES

More sophisticated efficiency measurements of the current and future fibre ribbon prototypes which are able to provide sub-fibre resolution would benefit the quality control of the fibre production as well as their extrapolated response in the experiment's simulation and reconstruction framework. The in chapter 7 presented extraction of efficiency in a pseudo-telescope configuration consisting of additional scintillators lacks precision and flexibility for different rotation angles and positions. An improved measurement utilizing several MuTRiG ASICs in combination with a MuPIX-telescope would be a valuable system integration test towards the final experiment.

#### IMPROVEMENT OF TIME-TO-TRACK LINKING IN THE RECONSTRUCTION FRAMEWORK

The above discussed improved measurements would also provide a handle to improve the simulated cluster size distribution described in chapter 9. In the current scheme, firstly stand-alone fibre detector clusters are built which are linked in a second step to reconstructed track candidates. Alternatively, a track candidate based linking scheme could be investigated. Such a scheme starts with the identification of all individual fibre hits compatible with track candidates, followed by time extraction of a detector crossing from the full available information which would include multiple fibre detector crossings as well as time information from the tile detector and all pixel hits. Such an algorithm could significantly increase the purity of the time determination and therefore decrease the distribution's tails. This leads to better suppression factors at higher signal selection efficiencies and likely to more efficient rejection of mis-reconstructed track candidates.

#### SUB-DETECTOR FIRMWARE DEVELOPMENT AND E-THRESHOLD VALIDATION

The proposed firmware functionalities in chapter 13 need to be integrated into the experiment's front end FPGAs and to be validated. Depending on the chosen operation modes an online clustering could become required. As already mentioned in section 14.1 the capability of the ASIC's  $E$ -threshold should be investigated in more detail. In contrast to the default chip operation with an enabled filter on the energy branch and moderate sensor overvoltage, the proposed operation at higher bias voltages in combination with an ASIC operation without the mentioned filter could provide sufficient  $E$ -threshold intrinsic and DAC-value resolutions.



# A

## Appendix A

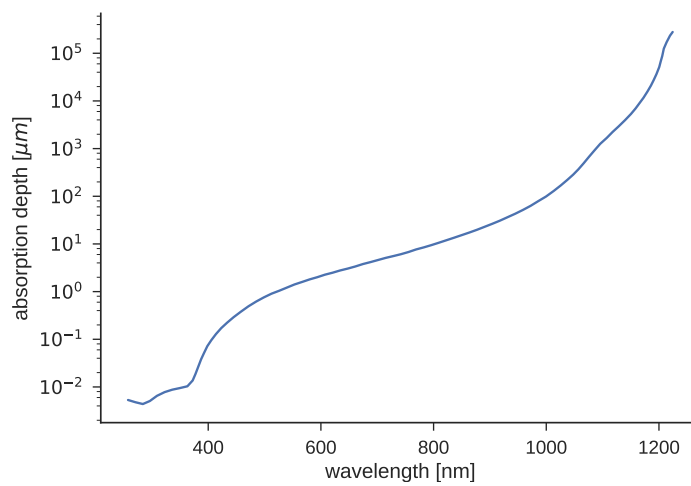
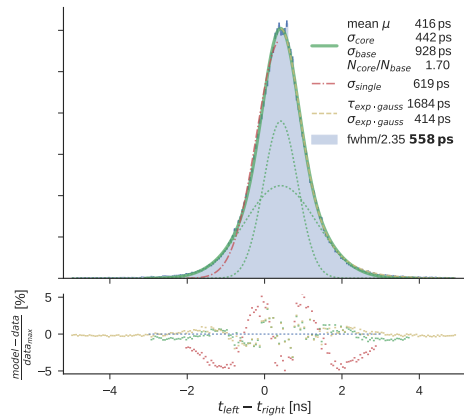
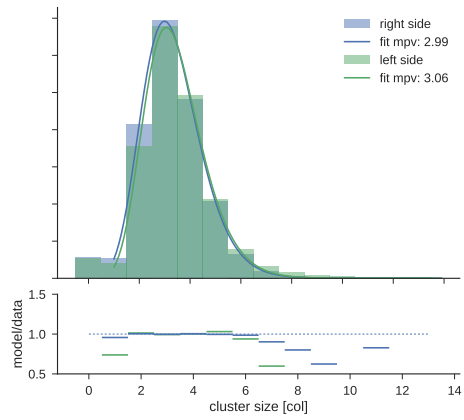


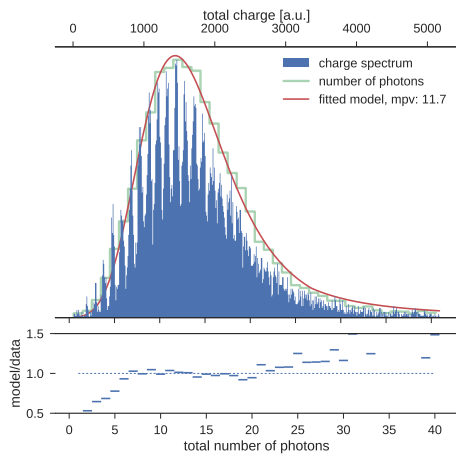
**Figure A.1:** Absorption depth in silicon as a function of wavelength from [152].



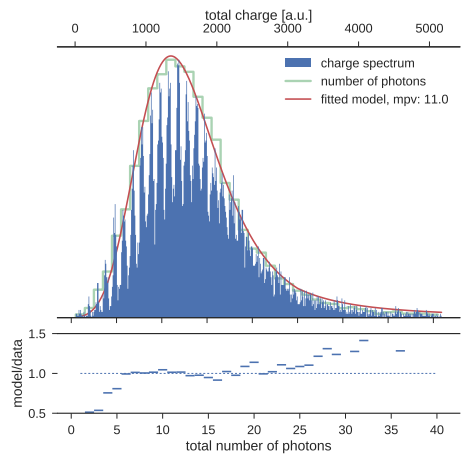
(a) Time Resolution



(b) Cluster Size

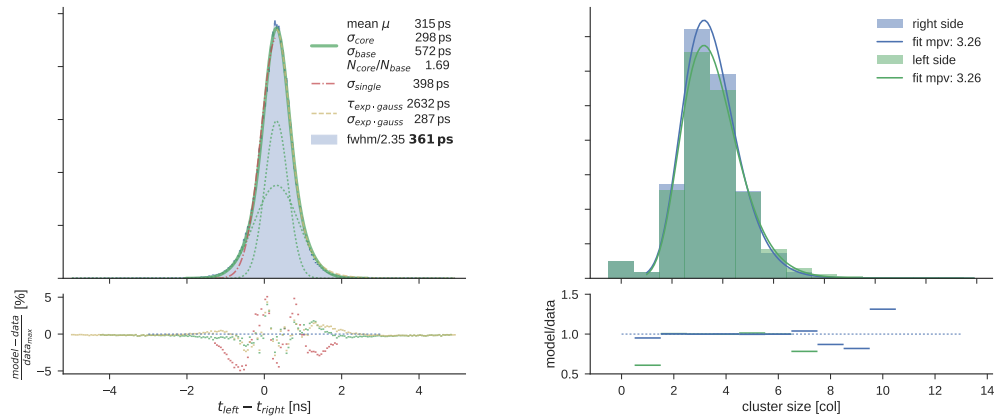


(c) Cluster Charge Left Side



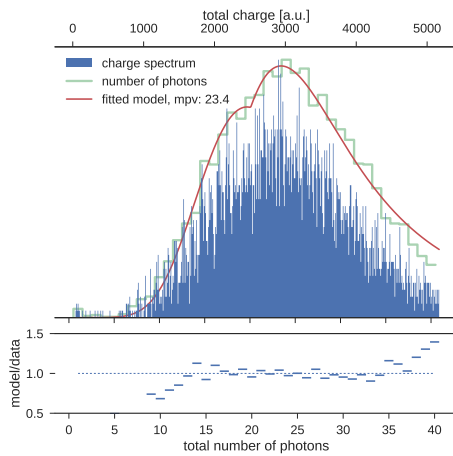
(d) Cluster Charge Right Side

**Figure A.2:** Characterization of fibre ribbon prototypes consisting of 4 layers of SCSF-81M] fibres with additional  $\text{TiO}_2$  2 in the glue as described in chapter 7.

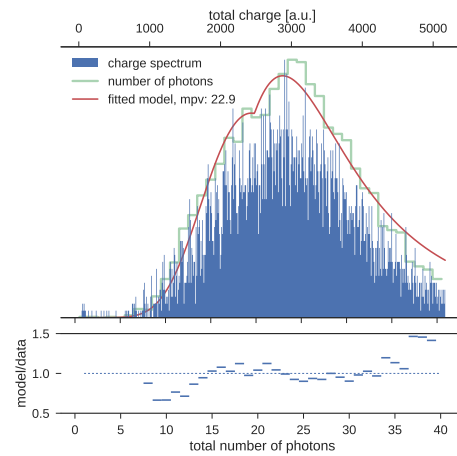


(a) Time Resolution

(b) Cluster Size

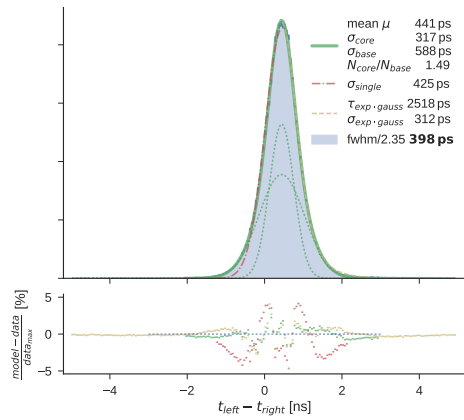


(c) Cluster Charge Left Side

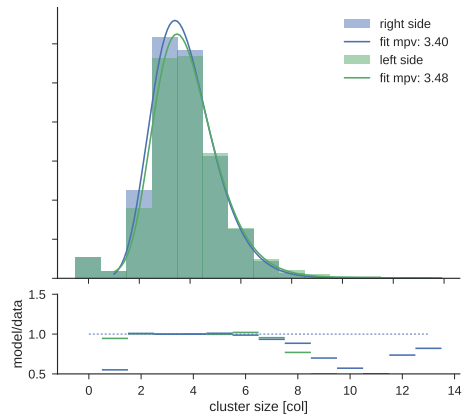


(d) Cluster Charge Right Side

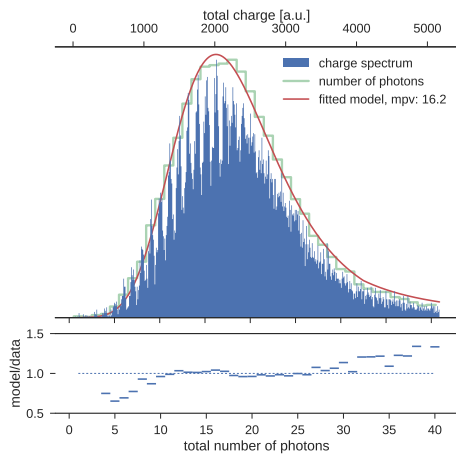
**Figure A.3:** Characterization of fibre ribbon prototypes consisting of 4 layers of SCSF-78MJ fibres with additional  $\text{TiO}_2$  in the glue as described in chapter 7.



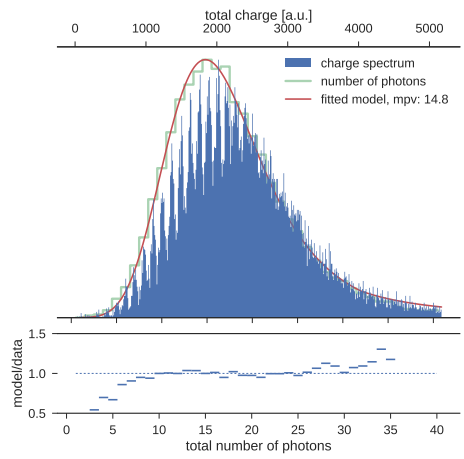
(a) Time Resolution



(b) Cluster Size

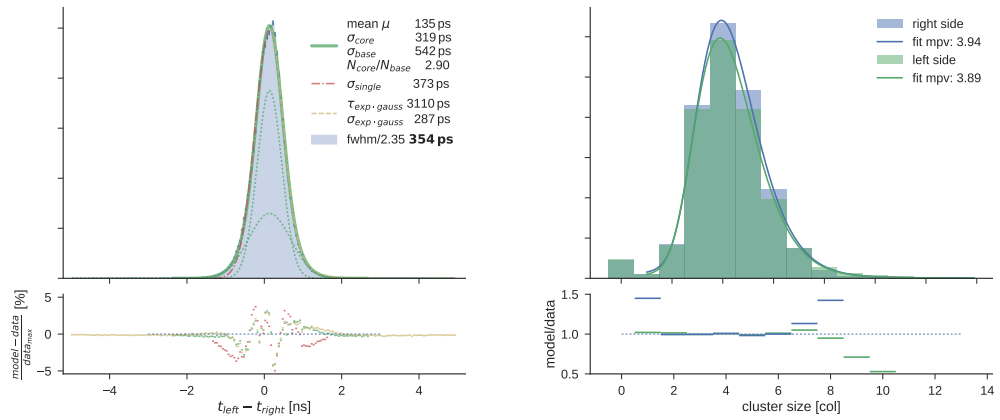


(c) Cluster Charge Left Side



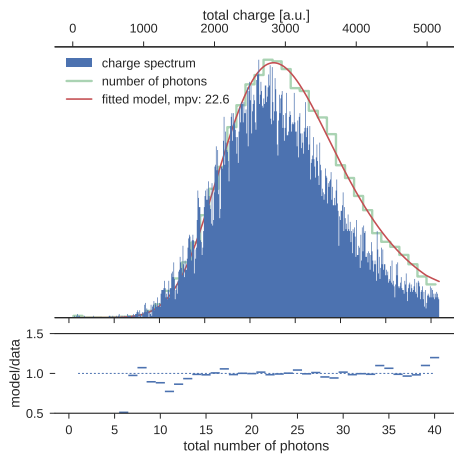
(d) Cluster Charge Right Side

**Figure A.4:** Characterization of fibre ribbon prototypes consisting of 3 layers of NOL-11 fibres with additional  $\text{TiO}_2$  2 in the glue as described in chapter 7.

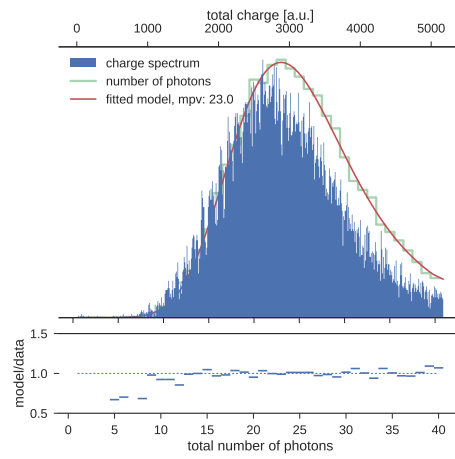


(a) Time Resolution

(b) Cluster Size

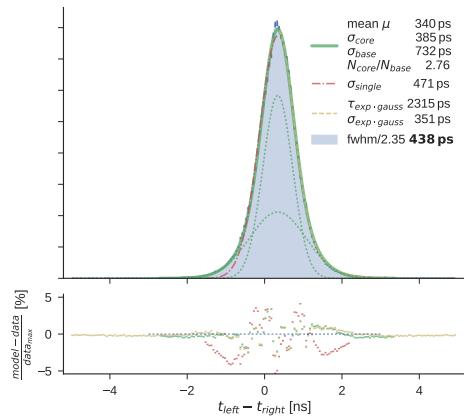


(c) Cluster Charge Left Side

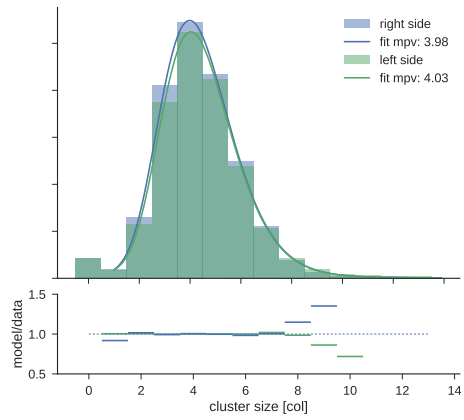


(d) Cluster Charge Right Side

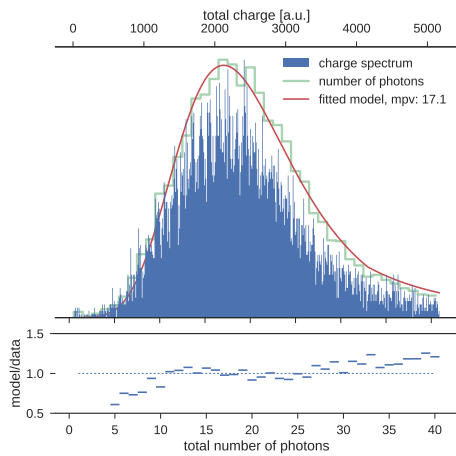
**Figure A.5:** Characterization of fibre ribbon prototypes consisting of 4 layers of NOL-11 fibres without additional  $\text{TiO}_2$  in the glue as described in chapter 7.



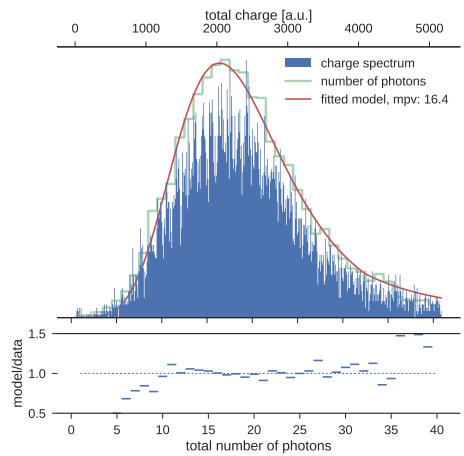
(a) Time Resolution



(b) Cluster Size

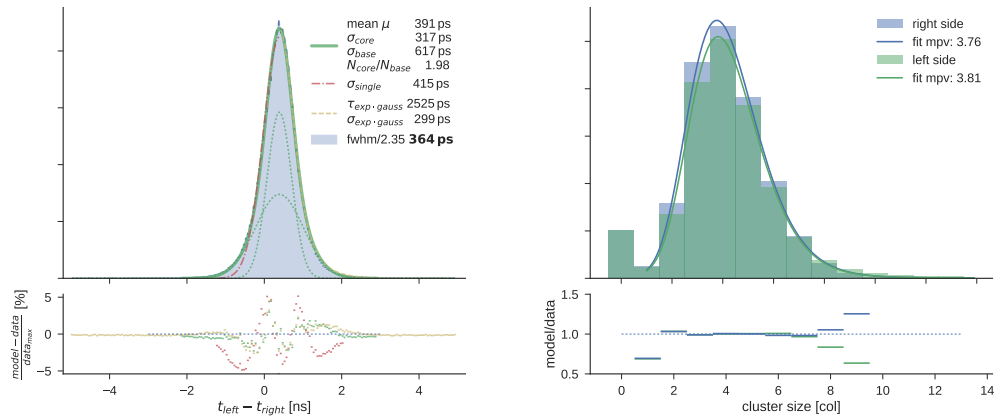


(c) Cluster Charge Left Side



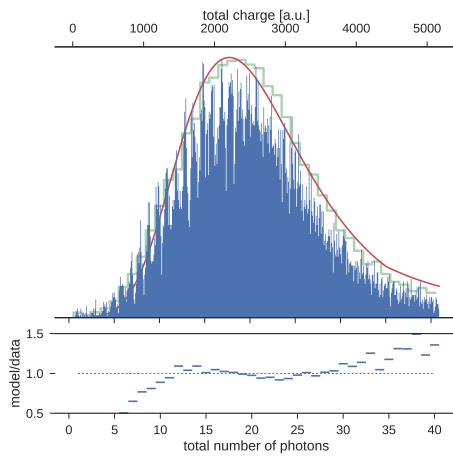
(d) Cluster Charge Right Side

**Figure A.6:** Characterization of fibre ribbon prototypes consisting of 4 layers of NOL-11 fibres which have been exposed to UV-light without additional  $\text{TiO}_2$  2 in the glue as described in chapter 7.

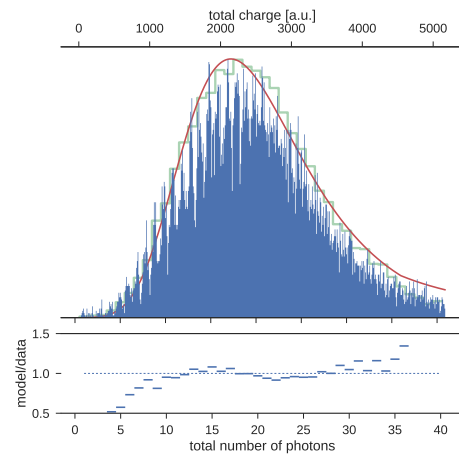


(a) Time Resolution

(b) Cluster Size

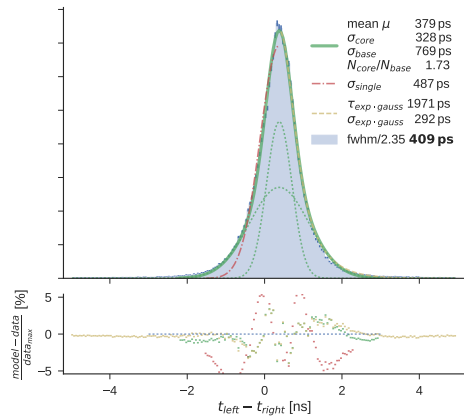


(c) Cluster Charge Left Side

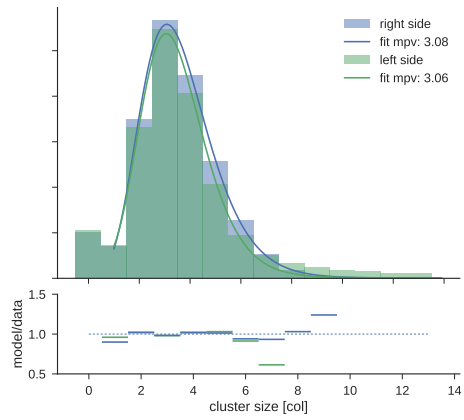


(d) Cluster Charge Right Side

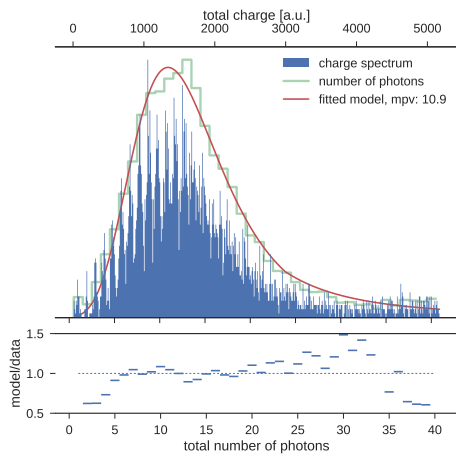
**Figure A.7:** Characterization of fibre ribbon prototypes consisting of 3 layers of NOL-11 fibres with additional  $\text{TiO}_2$  2 in the glue as described in chapter 7.



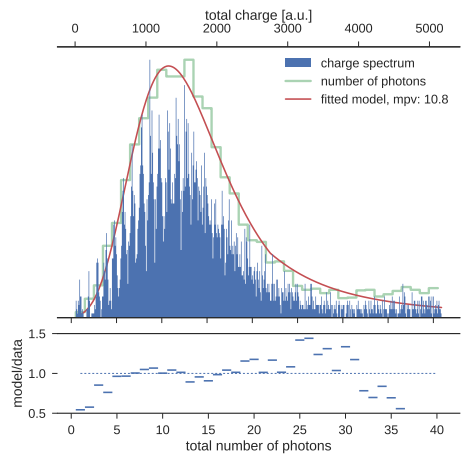
(a) Time Resolution



(b) Cluster Size

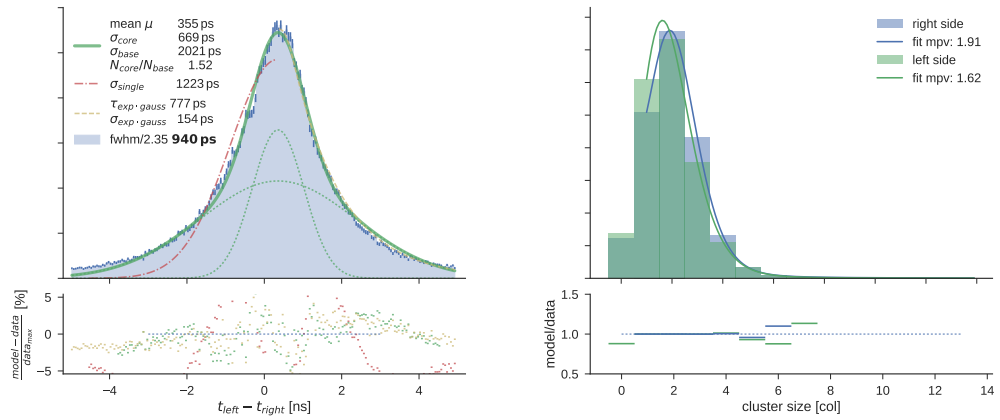


(c) Cluster Charge Left Side



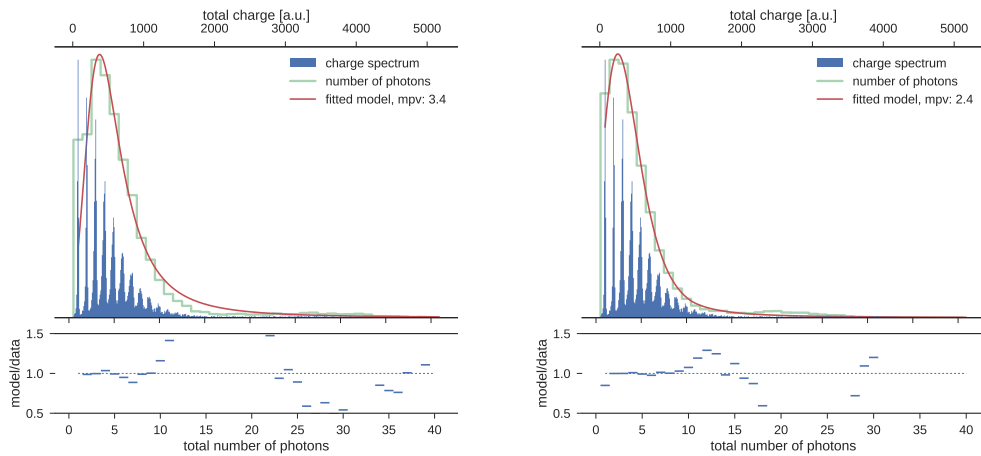
(d) Cluster Charge Right Side

**Figure A.8:** Characterization of fibre ribbon prototypes consisting of 2 layers of NOL-11 fibres with additional  $\text{TiO}_2$  2 in the glue as described in chapter 7.



(a) Time Resolution

(b) Cluster Size



(c) Cluster Charge Left Side

(d) Cluster Charge Right Side

**Figure A.9:** Characterization of fibre ribbon prototypes consisting of 4 layers of BCF-12 fibres with additional  $TiO_2$  2 in the glue as described in chapter 7.



material layers coating	nol11 3		nol11 2		nol11 4		bcf12 4	
	tio2	tio2	tio2	tio2	tio2	tio2	tio2	tio2
cl(n>0)	92.0 <sup>+0.06</sup> <sub>-0.06</sub>	95.4 <sup>+0.05</sup> <sub>-0.05</sub>	97.7 <sup>+0.03</sup> <sub>-0.03</sub>	95.4 <sup>+0.05</sup> <sub>-0.05</sub>	92.2 <sup>+0.06</sup> <sub>-0.06</sub>	96.7 <sup>+0.04</sup> <sub>-0.04</sub>	96.5 <sup>+0.04</sup> <sub>-0.04</sub>	
or phe≤1								
cl(n>0)	92.1 <sup>+0.07</sup> <sub>-0.07</sub>	95.5 <sup>+0.05</sup> <sub>-0.05</sub>	97.7 <sup>+0.04</sup> <sub>-0.04</sub>	95.5 <sup>+0.05</sup> <sub>-0.05</sub>	92.3 <sup>+0.07</sup> <sub>-0.07</sub>	96.7 <sup>+0.08</sup> <sub>-0.08</sub>	96.5 <sup>+0.07</sup> <sub>-0.07</sub>	
or ≤1.5 phe								
cl(n>0)	89.8 <sup>+0.07</sup> <sub>-0.07</sub>	94.5 <sup>+0.05</sup> <sub>-0.05</sub>	97.1 <sup>+0.04</sup> <sub>-0.04</sub>	94.2 <sup>+0.05</sup> <sub>-0.05</sub>	88.6 <sup>+0.07</sup> <sub>-0.07</sub>	90.2 <sup>+0.07</sup> <sub>-0.07</sub>	92.2 <sup>+0.06</sup> <sub>-0.06</sub>	
and phe≤1								
cl(n>0)	89.9 <sup>+0.07</sup> <sub>-0.07</sub>	94.5 <sup>+0.05</sup> <sub>-0.05</sub>	97.1 <sup>+0.05</sup> <sub>-0.05</sub>	94.3 <sup>+0.06</sup> <sub>-0.06</sub>	88.7 <sup>+0.07</sup> <sub>-0.07</sub>	90.3 <sup>+0.11</sup> <sub>-0.11</sub>	92.2 <sup>+0.11</sup> <sub>-0.11</sub>	
and ≤1.5 phe								
cl(n>1)	89.8 <sup>+0.07</sup> <sub>-0.07</sub>	94.4 <sup>+0.05</sup> <sub>-0.05</sub>	96.9 <sup>+0.04</sup> <sub>-0.04</sub>	94.1 <sup>+0.05</sup> <sub>-0.05</sub>	88.5 <sup>+0.07</sup> <sub>-0.07</sub>	84.5 <sup>+0.08</sup> <sub>-0.08</sub>	86.3 <sup>+0.08</sup> <sub>-0.08</sub>	
or phe≤1								
cl(n>1)	89.8 <sup>+0.07</sup> <sub>-0.07</sub>	94.5 <sup>+0.06</sup> <sub>-0.06</sub>	96.9 <sup>+0.07</sup> <sub>-0.07</sub>	94.1 <sup>+0.07</sup> <sub>-0.07</sub>	88.6 <sup>+0.07</sup> <sub>-0.07</sub>	84.5 <sup>+0.11</sup> <sub>-0.11</sub>	86.4 <sup>+0.11</sup> <sub>-0.11</sub>	
or ≤1.5 phe								
cl(n>1)	88.5 <sup>+0.07</sup> <sub>-0.07</sub>	93.1 <sup>+0.06</sup> <sub>-0.06</sub>	91.0 <sup>+0.06</sup> <sub>-0.06</sub>	88.4 <sup>+0.07</sup> <sub>-0.07</sub>	87.9 <sup>+0.07</sup> <sub>-0.07</sub>	46.5 <sup>+0.11</sup> <sub>-0.11</sub>	50.6 <sup>+0.11</sup> <sub>-0.11</sub>	
and phe≤1								
cl(n>1)	88.6 <sup>+0.09</sup> <sub>-0.09</sub>	93.2 <sup>+0.08</sup> <sub>-0.08</sub>	91.1 <sup>+0.11</sup> <sub>-0.11</sub>	88.5 <sup>+0.11</sup> <sub>-0.11</sub>	87.9 <sup>+0.08</sup> <sub>-0.08</sub>	46.6 <sup>+0.06</sup> <sub>-0.06</sub>	50.7 <sup>+0.07</sup> <sub>-0.07</sub>	
and ≤1.5 phe								
trg fb, cl(n>0)		99.9 <sup>+0.02</sup> <sub>-0.02</sub>		100.0 <sup>+0.01</sup> <sub>-0.01</sub>			99.9 <sup>+0.02</sup> <sub>-0.02</sub>	
or phe≤1								
trg fb, cl(n>0)		99.9 <sup>+0.02</sup> <sub>-0.02</sub>		100.0 <sup>+0.02</sup> <sub>-0.02</sub>			99.9 <sup>+0.17</sup> <sub>-0.17</sub>	
or ≤1.5 phe								
trg fb, cl(n>0)		99.8 <sup>+0.02</sup> <sub>-0.02</sub>		99.9 <sup>+0.02</sup> <sub>-0.02</sub>			96.5 <sup>+0.13</sup> <sub>-0.13</sub>	
and phe≤1								
trg fb, cl(n>0)		99.9 <sup>+0.04</sup> <sub>-0.04</sub>		99.9 <sup>+0.09</sup> <sub>-0.09</sub>			96.7 <sup>+0.34</sup> <sub>-0.34</sub>	
and ≤1.5 phe								
trg fb, cl(n>1)		99.8 <sup>+0.03</sup> <sub>-0.03</sub>		99.7 <sup>+0.04</sup> <sub>-0.04</sub>			91.2 <sup>+0.20</sup> <sub>-0.20</sub>	
or phe≤1								
trg fb, cl(n>1)		99.8 <sup>+0.06</sup> <sub>-0.06</sub>		99.8 <sup>+0.18</sup> <sub>-0.18</sub>			91.4 <sup>+0.35</sup> <sub>-0.35</sub>	
or ≤1.5 phe								
trg fb, cl(n>1)		98.6 <sup>+0.07</sup> <sub>-0.07</sub>		94.6 <sup>+0.16</sup> <sub>-0.16</sub>			54.9 <sup>+0.35</sup> <sub>-0.35</sub>	
and phe≤1								
trg fb, cl(n>1)		98.6 <sup>+0.18</sup> <sub>-0.18</sub>		94.7 <sup>+0.34</sup> <sub>-0.34</sub>			55.2 <sup>+0.23</sup> <sub>-0.23</sub>	
and ≤1.5 phe								
trg full, cl(n>0)		100.0 <sup>+0.01</sup> <sub>-0.01</sub>		100.0 <sup>+0.01</sup> <sub>-0.01</sub>			100.0 <sup>+0.01</sup> <sub>-0.01</sub>	
or phe≤1								
trg full, cl(n>0)		100.0 <sup>+0.01</sup> <sub>-0.01</sub>		100.0 <sup>+0.01</sup> <sub>-0.01</sub>			100.0 <sup>+0.02</sup> <sub>-0.02</sub>	
or ≤1.5 phe								
trg full, cl(n>0)		100.0 <sup>+0.01</sup> <sub>-0.01</sub>		100.0 <sup>+0.01</sup> <sub>-0.01</sub>			96.7 <sup>+0.17</sup> <sub>-0.17</sub>	
and ≤0.5 phe								
trg full, cl(n>0)		100.0 <sup>+0.04</sup> <sub>-0.04</sub>		100.0 <sup>+0.04</sup> <sub>-0.04</sub>			96.8 <sup>+0.46</sup> <sub>-0.46</sub>	
and ≤1.5 phe								
trg full, cl(n>1)		100.0 <sup>+0.01</sup> <sub>-0.01</sub>		100.0 <sup>+0.01</sup> <sub>-0.01</sub>			91.5 <sup>+0.26</sup> <sub>-0.26</sub>	
or ≤0.5 phe								
trg full, cl(n>1)		100.0 <sup>+0.02</sup> <sub>-0.02</sub>		100.0 <sup>+0.04</sup> <sub>-0.04</sub>			91.8 <sup>+0.47</sup> <sub>-0.47</sub>	
or ≤1.5 phe								
trg full, cl(n>1)		98.7 <sup>+0.09</sup> <sub>-0.09</sub>		98.7 <sup>+0.09</sup> <sub>-0.09</sub>			55.1 <sup>+0.47</sup> <sub>-0.47</sub>	
and ≤0.5 phe								
trg full, cl(n>1)		98.8 <sup>+0.26</sup> <sub>-0.26</sub>		98.8 <sup>+0.26</sup> <sub>-0.26</sub>			55.5 <sup>+0.32</sup> <sub>-0.32</sub>	
and ≤1.5 phe								

# B

## Appendix B

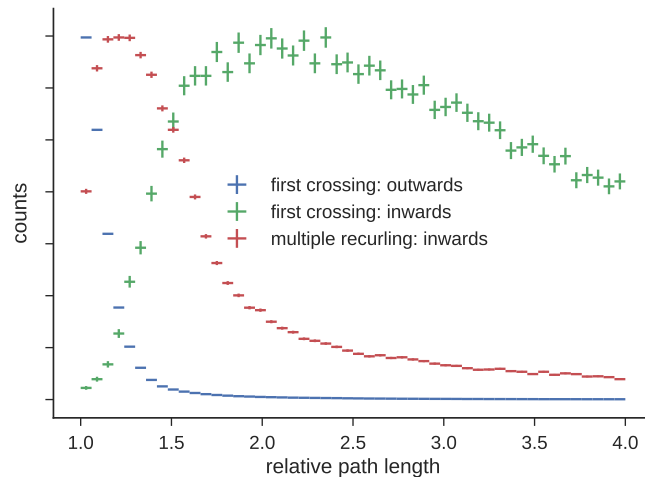
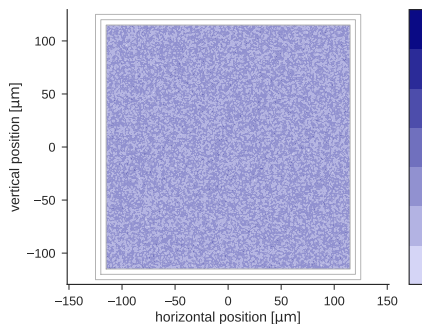
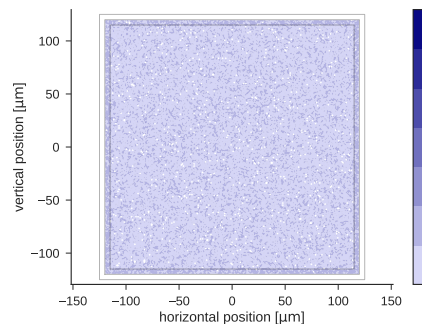


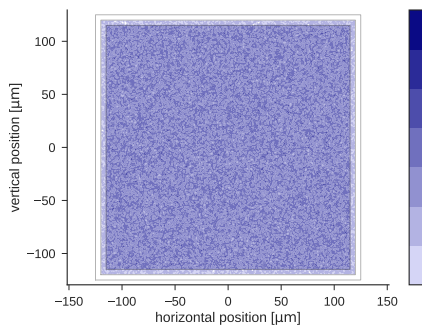
**Figure B.1:** Relative path length of particles in the scintillating fibre detector with respect to the detector's thickness of particles crossing the fibre detector at the first crossing outwards (—), at the first crossing inwards (—) and during all further recurlings (—).



**(a)** total reflection at first cladding



**(b)** total reflection at second cladding



**(c)** sum of (a) and (b)

**Figure B.2:** Simulated photon exit position in perfect 250 μm thick double clad square fibres.

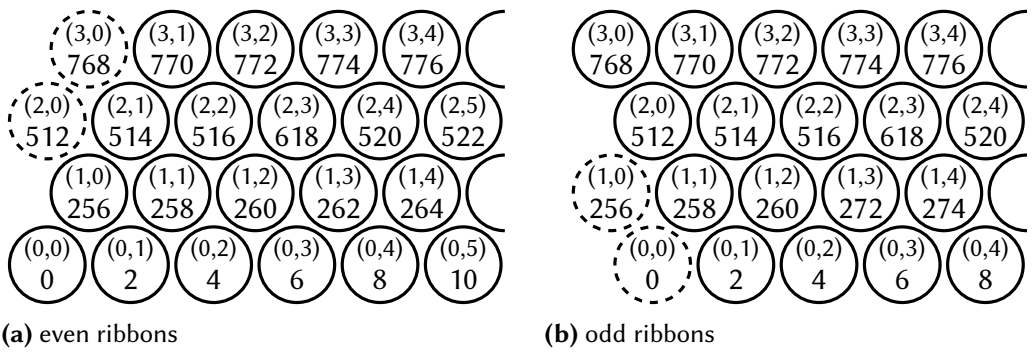


**Figure B.3:** Numbering scheme of the scintillating fibres in the GEANT4 simulation. If the *trapezium* edge mode is chosen, the dashed fibres are omitted.

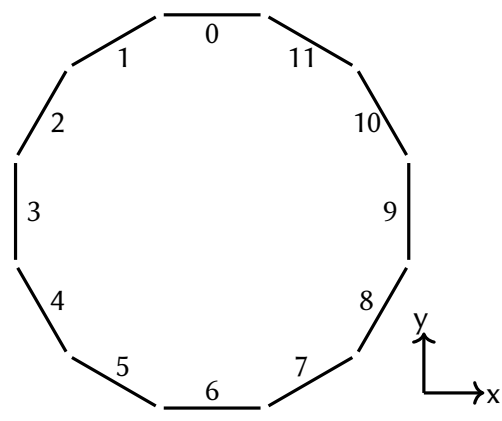


**Figure B.4:** Numbering scheme of the fibre ribbons in the GEANT4 simulation.

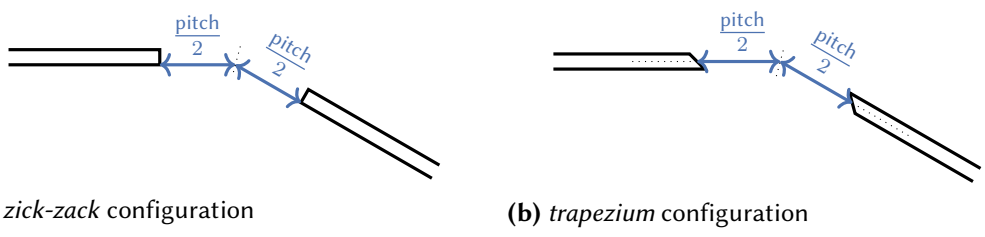


**Figure B.5:** Distance between fibre ribbons in the simulation framework.

**Table B.1:** Baseline scintillating fibre detector settings in the GEANT4 simulation framework. For values specifying lengths, the values are given in units of mm.

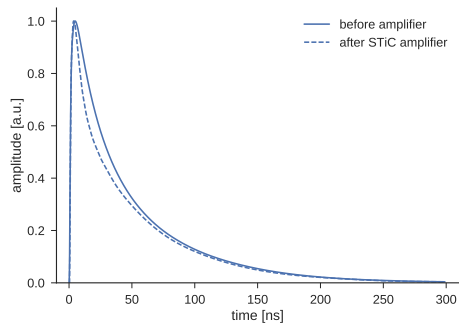
setting	value
fibre	
square	false
diameter	0.250
length	287.75
alCoating	0.000
refractiveIndex	1.59
deadWidth	0.005
nLayers	4
maxFibresPerLayer	126
ribbons	
n	12
pitch	0.18
geometry	0 ( <i>zick-zack</i> )
rOffset	0.0

**Table B.2:** Numbering scheme of signals in the SiPM column arrays in the GEANT4 simulation.

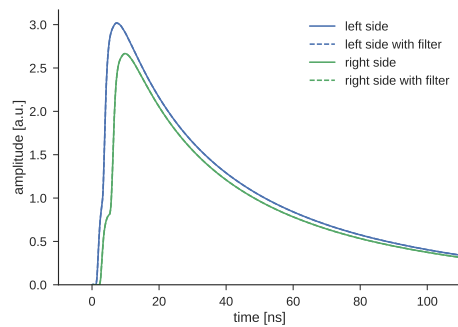
field	bits	number of bits	information
col	0-6	7	column
mppcId	0	1	side ( <i>0: for <math>z &gt; 0</math></i> )
mppcId	1-5	5	ribbon
timestamp	0-19	20	<i>T</i> -timestamp
timestamp	20	1	reserved: <i>E</i> -flag

**Table B.3:** Numbering scheme of scintillating fibres and fibre ends in the GEANT4 simulation.

bits	number of bits	information
0	1	side ( <i>0: for <math>z &gt; 0</math></i> )
1- 7	6	fibre number in layer
8-10	3	layer
11-15	5	ribbon



**(a)** Waveform of a single SiPM pixel. Waveforms obtained from Kirchhoff-Institute for Physics (KIP) at University of Heidelberg.



**(b)** The resulting waveforms on the left (←) and right (→) ribbon side.

**Figure B.6:** Simulated waveforms of a single SiPM pixel (a) before any amplifier (—) and after the STiC amplifier (---) right before the ASIC's comparator. The detector response consists of a sum of multiple single photon waveforms (b).



# C

## Appendix C

### C.1 MuTRiG

#### C.1.1 ANALOGUE FRONT-END

This description follows [144]. The analogue front-end is implemented fully differential to suppress common mode noise. It allows for a differential or single-ended connection scheme of detectors and positive as well as negative signal polarities. The ASIC's input-stage consists of two symmetrical structures; one half is shown in Figure C.1, connected to the positive and negative terminals.

The utilized common gate amplifier stages provide high bandwidth and low input impedance. An input transistor is biased by a constant current source controlled by a DAC (INPUTBIAS). The transconductance  $g_m$  of this resistor determines the input impedance which is proportional to

$$R_{\text{input}} = \frac{1}{g_m}, \quad g_m = \frac{2I_D}{V_{GS} - V_{th}} \quad (\text{C.1})$$

where  $I_D$  is the drain current and the denominator term the overdrive, the difference between the voltage between gate and source  $V_{GS}$ , and the threshold voltage  $V_{th}$ . Hence, an increase of the constant current in this transistor decreases the input impedance. Input impedances of less than  $50 \Omega$  can be achieved [144].

The voltage at the positive input terminal can be adjusted by a DAC (SIPM) which controls the input transistor's gate voltage. Since the current through the transistor is proportional to  $(V_{GS} - V_{th})$  in the saturation region, a change of the gate voltage at a constant current results in a change in the terminal voltage. This results in a tunable range from 100 mV to 900 mV (see Figure C.4) with respect to ground. An offset of the terminal voltage changes the bias voltage applied at an attached sensor.

The input-stage provides two outputs for a timing and an energy branch. These output voltages are stabilized by a low-frequency feedback from the timing path controlled by another

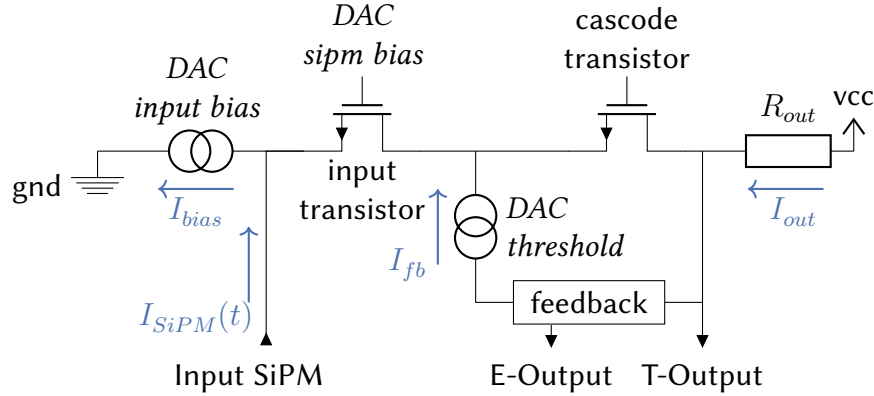


**Figure C.1:** Simplified diagram of one half of the symmetric STiC and MuTRiG input-stage. The analogue input signal ( $\rightarrow$ ) is amplified, copied and shaped by the analogue input stage of the ASIC. The discrimination of this output signal ( $\rightarrow$ ) resulting in the  $T$ - and  $E$ -triggers ( $\rightarrow$ ) is presented. Adapted from [144].

DAC (TTHRESHOLD) which at the same time defines the level of the  $T$ -threshold. An additional cascode transistor is used to increase the output's impedance.

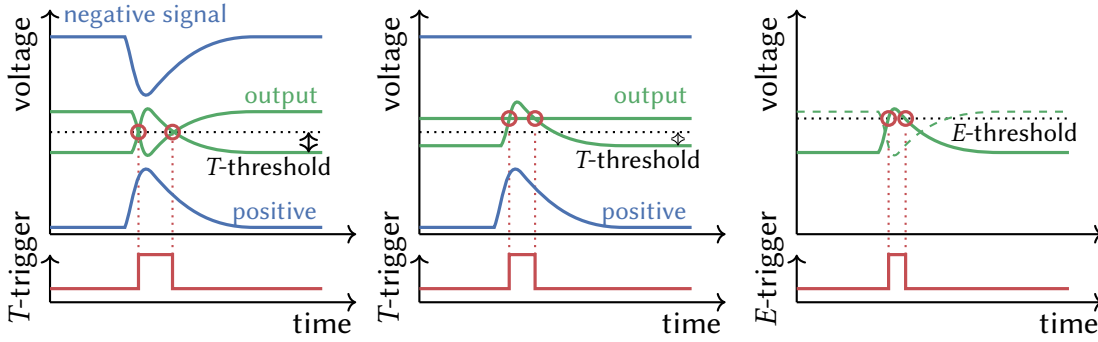
In the presence of an input current  $I_{SiPM}(t)$ , this current provides the constant bias current  $I_{bias}$ . It substitutes the current through the right part of the diagram in Figure C.1, this part is off. Its recovery time is linear to the discharge time of the detector's capacity by the constant current  $I_{bias}$ . This effect is exploited to linearise the ToT measurement. In the case of the MU3E fibre detector the energy threshold, required for the extraction of the ToT, are not used.

### C.1.2 TRIGGER UNITS

In the time branch, the differential signal from the positive and negative halves of the input-stages are amplified by three subsequent high bandwidth differential amplification stages. The output of the first stage is used for the feedback. The feedback current, tuned by the TTHRESHOLD DAC, determines the voltage difference between the two polarities' output signals. Figure C.2 illustrates the subsequent trigger generation for differential and single-ended operation modes. Note that the trigger edge can be changed by DAC-setting; hence this scheme allows for signals of both polarities.

The energy branch, which is utilized at most to generate a flag in the MU3E fibre detector, exploits only one of the polarities. A DAC allows switching between the positive and negative signal. In contrast to the time branch, the signal is compared to a threshold voltage tuned by TTHRESHOLD DAC. Note that the  $T$ -threshold, which acts on the common feedback, affects the absolute value of the  $E$ -threshold. As long as the current from the detector's capacity discharge substitutes the bias current  $I_{bias}$  the energy output is set to  $vcc$ , hence the trigger stays on. The input-stage  $E$ -output falls below threshold upon its recovery. As mentioned before, this leads to a partial linearization of the ToT.

A switchable filter reduces the noise in the  $E$ -branch for better energy resolution. However,



(a)  $T$ -threshold: differential      (b)  $T$ -threshold: single-ended      (c)  $E$ -threshold

**Figure C.2:** STiC and MuTRiG  $T$  (a,b) and  $E$  (c) trigger scheme for differential (a) and single-ended (b) operation modes. (a) and (b) adapted from [144].

at the same time the signal amplitude in this branch is reduced.

## HIT LOGIC

In order to digitise the  $T$ oA and  $T$ oT in a single TDC, the two triggers from the  $T$ - and  $E$ -branch are merged with an XOR. This yields two pulses with rising edges aligned to the rising edge at the  $T$ -threshold and to the falling edge of the  $E$ -threshold. The signal's fast rise time ensures on the one side that the time difference of these two edges is a good proxy for the  $T$ oT. On the other side, this would result in very short XOR outputs from the  $T$ -thresholds. To guarantee a minimal trigger pulse width, the  $E$ -trigger is delayed and put in coincidence with itself before it is fed into the XOR logic. This conserves the falling edge position of the  $E$  threshold. Besides the new trigger edge time, also the state of the delayed  $E$ -trigger is stored to discriminate between  $T$  and  $E$  times. In case of the energy timestamps, the delayed trigger is always on.

### C.1.3 EVENT BUILDING AND ARBITRATION

The event building is realized in two registers  $R1$  and  $R2$ . With each new timestamp from the TDC, the timestamps are shifted through these. If the  $E$ -flag is high, which means that the current timestamp is from the falling edge of the  $E$ -threshold, the hit is validated, and an event is built. Such an event consists of  $E$ -timestamp in  $R1$  and  $T$ -timestamp in  $R2$ .

The validation by the energy threshold can be overridden by a configuration bit (RECEIVE ALL). In this mode, utilized for the Mu3E fibre detector, an event is built for each timestamp. Now, a full event contains the current and the previous timestamp of this channel.

In MuTRiG, the number of events per channel per millisecond is stored in a latched counter, the CEC, which can be accessed by the slow control interface (see subsection C.1.4).

The event data is stored in channel groups in four Level 1 (L1 FIFO) buffers before they are combined in a shared Level 2 (L2) FIFO buffer. The L1 buffers employ a priority arbitration based

**Table C.1:** Event data format at transmission for STiC and MuTRiG. The table specifies which information is stored in which event bits.

ASIC mode	channel	time			energy			Flag	total
		Coarse	Fine	Bad	Coarse	Fine	Bad		
STiC	47-42	40-26	25-21	41	19-5	25-21	20		<b>48</b>
MuTRiG long	47-43	41-27	26-22	42	20-6	5-1	21	0	<b>48</b>
MuTRiG short	26-22	20-6	5-1	21				0	<b>27</b>

on the channel number whereas the L2 buffers use a fair round robin algorithm [144]. In case of STiC the L1 buffer combines 16 channels, one MuTRiGL1 buffer is assigned to 8 channels. Furthermore, MuTRiG allows validating the event data in the L1 buffers by an optional external trigger. The two FIFOs buffers with size of  $4 \times 624$  byte, 1536 byte respectively, are implemented in static RAM.

#### C.1.4 SLOW CONTROL

The two ASICs, STiC and MuTRiG, are configured by a SPI interface. This interface consists of a clock (sclk), a chip select (cs) which is active low, a data in (sdi) and a data out (sdo) line. The clock and data lines can be shared by multiple ASICs, called slaves. The configuration bit pattern is clocked into a shift register through SPI. The register's last element is put on data out, which allows to read back the previous configuration. At the rising edge of the cs, which turns off the SPI interface, the current shift register state is latched to the active chip configuration. This prevents undesired chip states during configurations. The configuration pattern of STiC is 4657 bits long, in MuTRiG it consists of 2358 bits.

#### CHANNEL EVENT COUNTER

In MuTRiG, an additional slow control interface allows to read out the CEC. This interface shares a common clock (sclk) with the configuration slow control and furthermore consists of a dedicated chip select (cec\_cs) and CEC data out (cec\_sdo). The serial data stream starts with an 8 bit header ( $0 \times 28$ ) followed by 13 bits, one overflow bit plus a 12 bit counter value per channel, starting at channel 31 descending. This sums up to a total of 53 bytes and allows to count rates up to 4.095 MHz per channel.

#### C.1.5 DATA TRANSMISSION AND FRAMES

The STiC and MuTRiG data transmission is frame based. The frame structure of the two ASICs differs.

**Table C.2:** 8b/10b control words utilized in MuTRIG.

Usage	K word	8 bits	10 bits RD=-1	10 bits RD=+1
comma	K.28.5	0xBC	001111 1010	110000 0101
header	K.28.0	0x1C	001111 0100	110000 1011
trailer	K.28.4	0x9C	001111 0010	110000 1101

## STiC

The digital part of STiC runs at 160 MHz. Every 1024 clock cycles a frame is composed and the present data in the L2 buffer is transmitted via an 8b/10b [121] encoded 160 MHz LVDS link. This corresponds to a frame length of 6.4  $\mu$ s. If more data is present in the buffer, the frame is extended.

## MuTRIG

In MuTRIG, the digital part is driven by a 625 MHz reference clock, and the 8b/10b encoded LVDS link runs at a double data rate of 1.25 GHz. A frame is generated every 12.3  $\mu$ s in normal mode and every 7.2  $\mu$ s in the *T*-mode [145]. Frames are not extended. The employed 8b/10b encoding ensures DC balancing of the links and introduces at the same time a dedicated set of control and alignment (comma) words [121]. Furthermore, it introduces a basic error detection which allows essential link quality monitoring. Only three (K.28.1, K.28.5, K.28.7) out of the twelve control words consist of a bit pattern that also never occurs across word boundaries. Table C.2 summarizes the control words used by MuTRIG.

Each new frame starts with a 5 byte header beginning with the header comma word (K.28.0), followed by two bytes containing a 16 bit frame number, 6 bit frame flags followed by 10 bit frame length, corresponding to the number of events included in this frame. The frame flags field contains the following settings and status flags:

- **generate idle** sends comma words between frames
- **fast mode** outputs only the *T*-timestamp and *E*-flag
- **prbs** debug option to test the serial links with a PRBS
- **single prbs** use only one prbs event per frame
- **fifo full** L2 fifo buffer is full
- **0** constant bit

**EVENT STRUCTURE** The header is followed by the number of events specified in the header. In the normal (long) mode, one event is 6 byte long. The 27 bit short events, which omit the *E*-timestamp, are appended by a zero bit to be contained precisely in 3.5 bytes. A second event starts at the fifth bit of the fourth byte. This allows fitting two short events into 7 bytes which keeps every second event byte-aligned. This simplifies data handling significantly because the 8b/10b encoding strongly favours data handling on the one-byte level.

**EVENT TRAILER** The event trailer consists of three bytes. The trailer control word (K.28.4) followed by two CRC bytes. A 16 bit CRC with the generator polynomial 0x18005 is calculated over the whole event starting after the header control word and appended to the event. If the same CRC is calculated over an entire received event, it has to yield the magic number 0x7ff2.

## C.2 DAC SETTINGS

**Table C.3:** MuTRiG specific registers in the FPGA.

name	description	register	bit
<b>commands</b>			
CONFIG	requests mutrig configuration	0x07	0
CONFIG CLK	requests clock chip configuration	0x07	1
SLOW ENABLE	enables slow control access to memory	0x07	16
CEC ENABLE	enables readout of CEC	0x07	30
DUMMY	switches on dummy configuration	0x07	17
DUMMY DATA ENABLE	switches on dummy data	0x07	18
DUMMY DATA FAST	switches on dummy data in short mode	0x07	19
DUMMY DATA CNT	number of dummy data per frame	0x07	20 - 29
<b>status</b>			
TIMEOUT	indicates I <sup>2</sup> C timeout	0x07	2
SYNC	receiver sync, no errors detected	0x08	0
SIGNAL	transceiver detected signal amplitude	0x08	0
PLL	transceiver PLL locked to data stream	0x08	3
FREQ	transceiver locked on data recovered clock	0x08	4
FIFOFULL	event buffering FIFO full	0x08	5
<b>Channel Event Counter</b>			
CEC	CEC data	0x10 to 0x23	
<b>resets</b>			
RESET SLOW	resets slow control	0x01	2
RESET CHANNEL	MuTRiG channel reset	0x01	3
RESET CHANNEL HOLD	holds channel reset	0x01	4
RESET CHIP	MuTRiG chip reset	0x01	5
RESET REC	receiver reset	0x01	6
RESET CEC	CEC reset	0x01	7



Figure C.3: MIDAS based MuTRIG Configuration GUI. Standard settings for operation for the scintillating fibre detector are shown.

**Table C.4:** First part of MIDAS based MuTRiG configuration GUI settings.

settings	panel	description
<b>DAQ settings</b>	1	ODB values which are loaded to eponymous FPGA registers to control debug modes.
<i>DUMMY CONFIG</i>	1	enables configuration shift register imitation on FPGA
<i>DUMMY DATA</i>	1	enables injection of pseudo data stream into the data path on the FPGA
<i>DUMMY FAST</i>	1	enables the generation of pseudo data in 'fast' format, only used if <i>DUMMY DATA</i> is active
<i>DUMMY DATA NUM</i>	1	number of injected events per frame, only used if <i>DUMMY DATA</i> is active
<b>Global settings</b>	1	Combination of DAQ settings and MuTRiG digital part configuration
<i>Num Asics</i>	1	number of used ASICs in the DAQ
<i>Num Channels</i>	1	Number of channels per ASIC. 32 for MuTRiG, 64 for STiC
<i>EXT TRG</i>		
<i>EXT TRG OFFSET</i>	1	configuration of external trigger
<i>EXT TRG ENDT</i>		
<i>EXT TRG ENDT SIGN</i>		
<i>LVDS VCM</i>	1	
<i>LVDS BIAS</i>		
<i>MS LIMITS</i>	1	
<i>PRBS</i>	1	enables PRBS generation in MuTRiG digital part
<i>PRBS SINGLE</i>	1	only one PRBS event per frame
<i>RECV ALL</i>	1	switch off <i>E</i> -threshold validation of events
<i>GEN IDLE</i>	1	enables comma word in LVDS data stream
<i>SHORT</i>	1	enables short event mode, only <i>T</i> -timestamps and <i>E</i> -flags are transmitted
<i>DIS COARSE</i>		
<i>PLL COARSE</i>	2	
<i>PLL ENVMON</i>		
<b>PLL settings</b>	2	Configuration values for ASIC's PLL. For MuTRiG one and for STiC two PLLs are present.
<i>AMON</i>		
<i>DMON1</i>	2	channel selection for the different monitor outputs
<i>DMON2</i>		

**Table C.5:** Second part of MIDAS based MuTRiG configuration GUI settings.

settings	area	description
<b>Channel settings</b>	<b>3</b>	ASIC configuration per channel
<i>Channel</i>	<b>3.1</b>	select displayed channel
<i>TTHRESH</i>	<b>3.1</b>	<i>T</i> -threshold
<i>ETHRESH</i>	<b>3.1</b>	<i>E</i> -threshold, used for event validation if <i>RECV ALL</i> is off, otherwise for <i>E</i> -flag
<i>MASK</i>	<b>3.1</b>	mask active channel
<i>mask</i>	<b>3.1</b>	masks all channels
<i>unmask</i>	<b>3.1</b>	unmasks all channels
<i>copy to</i>	<b>3.1</b>	copies selected settings of active channel to channels specified in the text field. <i>thrs</i> selects only the threshold settings (3.1) whereas <i>set</i> selects in addition all channel settings (3.2).
<i>SIPM</i>	<b>3.2</b>	controls input terminal potential (see subsection C.1.1)
<i>INPUTBIAS</i>	<b>3.2</b>	controls input stage constant current source
<i>POLE</i>	<b>3.2</b>	controls pole-zero like signal shaping
<i>DISABLE TDCTEST</i>	<b>3.2</b>	disables the external trigger of TDC
<i>S SWITCH</i>	<b>3.2</b>	enables capacity to ground on negative input terminal
<i>ENERGY C EN</i> <i>ENERGY R EN</i>	<b>3.2</b>	enables RC-filter in the energy branch
<i>DELAY</i>	<b>3.2</b>	delay of output of the discriminated <i>T</i> -threshold comparator output before the XOR (see Figure C.1.2)
<i>EDGE</i>	<b>3.2</b>	discriminator edge selection
<i>AMON, DMON</i>	<b>3.2</b>	monitor settings
<i>ASIC</i>	<b>4</b>	select active ASIC
<i>Set ODB</i>	<b>4</b>	stores current local settings in the ODB
<i>config ASIC</i>	<b>4</b>	configures the ASIC. If a run is active the DAQ is interrupted.
<i>Save config</i>	<b>4</b>	stores the local configuration in JSON file
<i>Load config</i>	<b>4</b>	loads configuration set from a JSON file
<i>Reset Histograms</i>	<b>4</b>	resets the online monitoring histograms
<i>Run Threshold Scan</i>	<b>4</b>	Performs a threshold scan of all channels with the current settings. The <i>T</i> -threshold start, stop, step size and time per step are configurable.

**Table C.6:** TDC DAC values used for all presented MuTRiG measurements.

DAC	value	scale	DAC	value	scale
<i>VNPFC</i>	8	3	<i>VNCnt</i>	40	3
<i>VNVCBuffer</i>	0	0	<i>VND2C</i>	31	3
<i>VNPCP</i>	24	3	<i>VNHitLogic</i>	32	3
<i>VNCntBuffer</i>	7	3	<i>VNVCODelay</i>	10	3
<i>LATCHBIAS</i>	1800				

**Table C.7:** Channel DAC settings for TDC injection.

DAC	value	scale	DAC	value	scale
<i>TTHRESH</i>	0	0	<i>S SWITCH</i>	false	
<i>ETHRESH</i>	255		<i>DELAY</i>	false	
<i>MASK</i>	false		<i>POLE_EN_N</i>	false	
<i>SIPM</i>	0	0	<i>ENERGY_C_EN</i>	false	
<i>INPUTBIAS</i>	0	0	<i>ENERGY_R_EN</i>	false	
<i>POLE</i>	0	0	<i>SENSING_HIGH_R</i>	false	
<i>AMPCOM</i>	0	0	<i>EDGE</i>	false	
<i>CML</i>	0	0	<i>EDGE_CML</i>	false	
<i>AMON CTRL</i>	0		<i>DMON_ENA</i>	false	
<i>COMP SPI</i>	0		<i>AMON_EN_N</i>	false	
<i>DISABLE TDCTEST</i>	false		<i>DMON_SW</i>	false	

**Table C.8:** Standard channel DAC settings used for *T*-threshold scans and data taking.

DAC	value	scale	DAC	value	scale
<i>TTHRESH</i>	X	0	<i>S SWITCH</i>	false	
<i>ETHRESH</i>	0		<i>DELAY</i>	true	
<i>MASK</i>	false		<i>POLE_EN_N</i>	false	
<i>SIPM</i>	15	0	<i>ENERGY_C_EN</i>	false	
<i>INPUTBIAS</i>	4	0	<i>ENERGY_R_EN</i>	false	
<i>POLE</i>	63	0	<i>SENSING_HIGH_R</i>	false	
<i>AMPCOM</i>	0	2	<i>EDGE</i>	true	
<i>CML</i>	8	0	<i>EDGE_CML</i>	false	
<i>AMON CTRL</i>	0		<i>DMON_ENA</i>	false	
<i>COMP SPI</i>	0		<i>AMON_EN_N</i>	false	
<i>DISABLE TDCTEST</i>	true		<i>DMON_SW</i>	false	

APPENDIX C. APPENDIX C

**Table C.9:**  $T$ -threshold DAC values for different sensor bias voltages. Channel 10 is used to inject the signal from the external trigger.

channel	57.2 V	58.2 V	59.2 V	60.2 V	channel	57.2 V	58.2 V	59.2 V	60.2 V
0	20	18	17	14	16	10	10	10	10
1	21	20	19	17	17	26	27	28	29
2	11	9	3	3	18	31	30	30	30
3	18	16	15	12	19	26	24	20	18
4	19	18	17	17	20	38	37	35	32
5	21	19	17	16	21	24	22	20	18
6	25	23	21	20	22	17	14	13	10
7	18	12	10	5	23	26	25	25	24
8	5	5	5	5	24	20	18	15	10
9	17	10	10	10	25	23	22	19	17
10	0	0	0	0	26	27	26	25	22
11	17	15	10	10	27	29	28	27	26
12	18	17	15	15	28	14	12	10	9
13	28	27	26	23	29	26	24	20	15
14	22	21	20	20	30	29	25	23	20
15	21	20	19	18	31	16	10	10	10

**Table C.10:** Sensor bias currents at different operation voltages in the absence and the presence of a beta source in 32 channels. Fibre type 78 in the table corresponds to Kuraray SCSF-78.

ribbon type	layers	source	bias voltage [V]	current [ $\mu$ A]
78	4	-	10.0	<0.01
78	4	-	57.2	1.6
78	4	-	58.2	2.8
78	4	-	59.2	4.2
78	4	-	60.2	6.6
78	4	1 collimator	57.2	7.5
78	4	1 collimator	58.2	11.0
78	4	1 collimator	59.2	14.9
78	4	1 collimator	60.2	21.1
78	3	1 collimator	58.2	8.0
NOLL	4	-	58.2	2.8
NOLL	4	2 collimators	58.2	3.0
NOLL	4	1 collimator	58.2	11.2
NOLL	4	no collimator	58.2	40.3

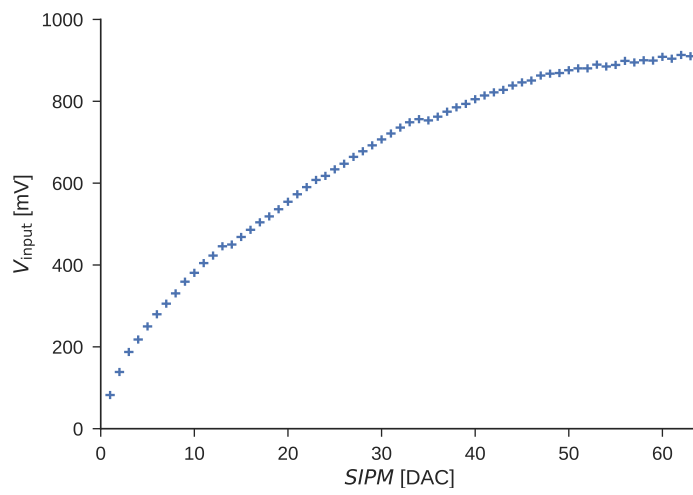


**Figure C.4:** STiC input terminal voltage as a function of the applied *SIPM* DAC value for scale 0. Measurement performed by KIP.



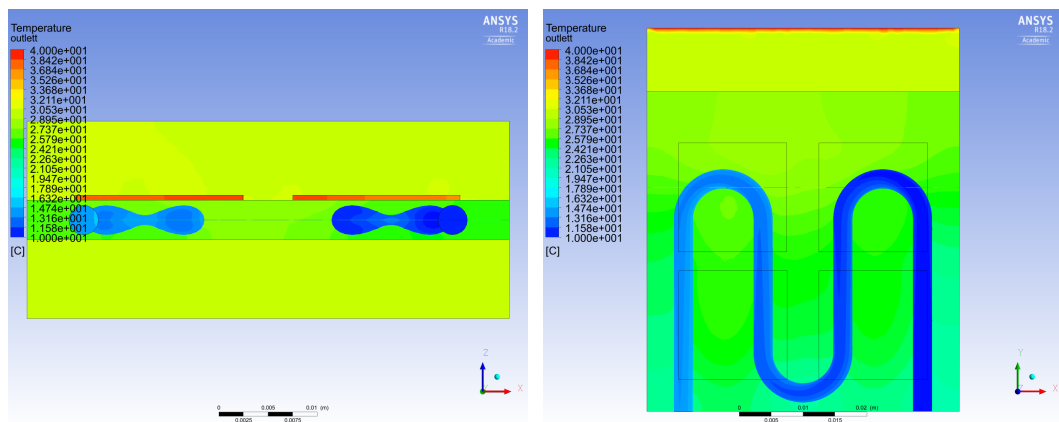
# D

## Appendix D

### D.1 FLEX PRINT CABLE OPTIMIZATION

Different possible flex print designs are investigated exploiting an electromagnetic field solver using Finite Difference Time Domain (FDTD) method [153]. In this method, Maxwell's equations are discretized on a grid by finite differences approximations to spacial and time partial derivatives. The electric and magnetic field components are solved alternately for all volumes in an iterative process. The advance of time domain simulation is that a wide frequency range is covered with a single simulation. Based on scattering parameters, which describe the behaviour of an electrical network as a function of the excitation frequency, the response to a typical SiPM current signal with a rise time of 1 ns and decay time of 10 ns is extracted. Figure D.3 shows these parameters for a 60  $\mu\text{m}$  feature size strip line and Figure D.4 the response in the time domain. An input impedance of 50  $\Omega$  at the MuTRIG side is assumed. The inactive SiPM channels are model with an overall lumped capacity of 2.664 pC and an internal resistance of 4.7 k $\Omega$ . This corresponds to the values stated in the CORSI model of the used sensors (see 5.2). Figure D.5 shows the schematic view of the simulation setup. The far-end cross-talk (*FEXT*), at the ASIC side, is extracted in terms of current in port 3 caused by the signal injection in port 1:  $FEXT = \frac{I_{31}}{I_{in}}$ .

The employed simulation model was validated concerning near-end crosstalk and impedance against the results of a study comparing further six different simulation tools [154]. The two compared designs are a strip line and a microstrip with a length of 25.4 mm, equal line width and separation of 127  $\mu\text{m}$  and a copper trace thickness of 18  $\mu\text{m}$ . The substrate with a thickness of 76  $\mu\text{m}$  for the microstrip design and 152  $\mu\text{m}$  for the strip lines, has a dielectric constant of 4. All ports have an impedance of 50  $\Omega$ . The near-end cross-talk is compared by  $k_b = \frac{V_{31}}{V_{in}}$  where  $V_{31}$  is the induced voltage in port 3 by excitation of port 1. The simulated cross-talk of 4.2 % and impedance of 48.4  $\Omega$  of microstrips agrees within the quoted uncertainties of  $(4.4 \pm 0.5)$  % crosstalk and  $(49.1 \pm 0.7)$   $\Omega$  impedance. The same is true for the stripline



(a) cut in transverse plane

(b) cut in longitudinal plane

**Figure D.1:** Simulated temperature equilibrium in the fibre detector cooling plates and  $\mu$ TRIG packagings. A very pessimistic power dissipation of 24 W per package and a helium atmosphere of 40 °C is assumed. The plates are cooled by a water flow of 1 m/s with a temperature of 10 °C at the inlet. Radial symmetrical boundary conditions are applied.



**Figure D.2:** 3d-printed model of the mechanical integration of the scintillating fibre detector into the  $\mu$ 3E experiment.

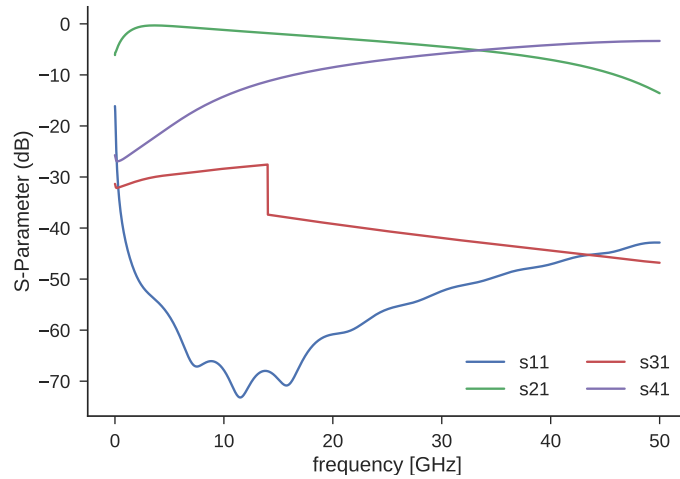


**Figure D.3:** The scattering parameters of a  $60\ \mu\text{m}$  feature size  $25\ \text{mm}$  long microstrip with a  $25\ \mu\text{m}$  thick substrate. The microstrip is excited at position 1 (1), the four shown parameters describe the response the far-end of the excited line (2), at the near-end of a neighbouring victim line (3) and at the far -end of the same line (4).

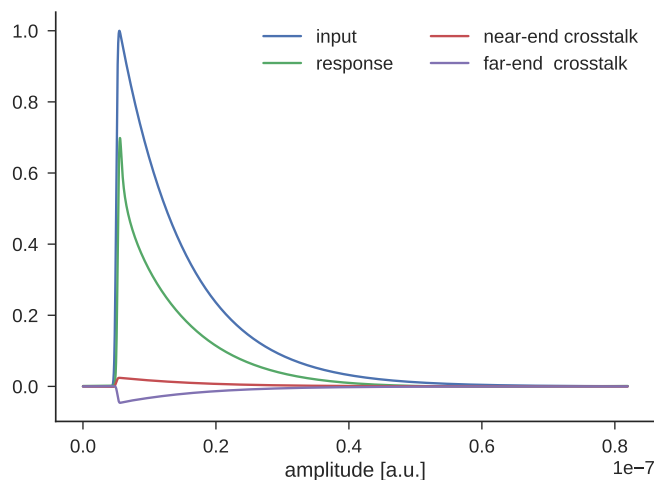


**Figure D.4:** Simulated response of an  $60\ \mu\text{m}$  feature size  $25\ \text{mm}$  long microstrip with an  $25\ \mu\text{m}$  thick substrate to a typical SiPM signal (1). The response on the far-end of the signal line (2), the near-end (3) and far-end crosstalk (4) in a neighbouring victim line are shown.

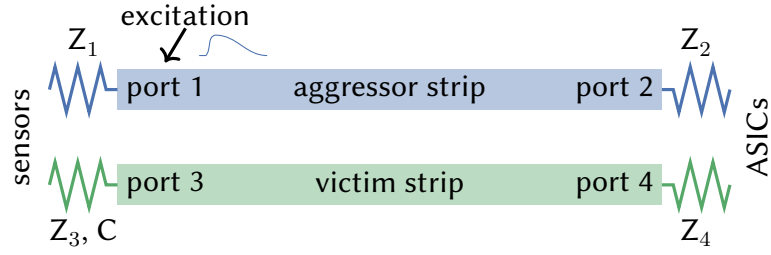


**Figure D.5:** Schematic view of the simulated transmission lines.

design, where the simulated cross-talk of 7.0 % is consistent with  $(6.6 \pm 0.5) \%$ , and the simulated impedance of  $43.6 \Omega$  is consistent with  $(43.0 \pm 0.7) \Omega$ .

To fit all 128 signal of one SiPM array into two signal layers, a density of  $\approx 4$  lines/mm is required. This leads to a feature size of  $\approx 125 \mu\text{m}$  if no ground lines are placed between two signal lines or  $\approx 60 \mu\text{m}$  if this is the case. The bending radius of a flex cable is in general twelve times the thickness. To achieve the required bending radius of below 2 mm the height of the flex cable at the bending zone has to be below  $170 \mu\text{m}$ . This is possible with a stack of three  $8 \mu\text{m}$  to  $12 \mu\text{m}$  thick copper layers and  $25 \mu\text{m}$  Kapton dielectric cores or with five copper layers with  $12 \mu\text{m}$  thick dielectrics.

Microstrips, consisting of conducting strips separated by a dielectric substrate from a common ground plane, could be used in a three layer design. Strip lines, comprising conducting stripes sandwiched between two ground planes, would require five copper layers. Table D.1 summarises the results for the different possible flex designs along with a cross-talk estimate given by the following approximations. An estimation for crosstalk dependent on the substrate thickness  $H$  and the strip width distance  $S$  is provided in Equation D.1 for strip lines and in Equation D.2 for microstrips.

$$\epsilon_{cross-talk}^{stripline} = \frac{1}{1 + \left(\frac{S}{H/4}\right)^4} \quad (\text{D.1})$$

for not too short tracks ( $\sim 3 \text{ cm}$ ) and signal rise times below 1 ns.

$$\epsilon_{cross-talk}^{microstrip} = \frac{1}{\left(1 + \frac{S}{H}\right)^2} \quad (\text{D.2})$$

**Table D.1:** Summary of simulated crosstalk behaviour of different flex print cable configurations.

type	width		trace		distance	substrate		impedance		crosstalk	
	$[\mu\text{m}]$	$[\mu\text{m}]$	thickness	$[\mu\text{m}]$		thickness	$[\mu\text{m}]$	FDTD	approx	FDTD	approx
micro strip	60	12	8	12	$1 \times 60$	25	48	42	4.6	14.8	
micro strip	60	8	8	8	$1 \times 60$	25	48	43	4.6	14.8	
micro strip (2l)	60	8	8	8	$1 \times 60$	25	48	43	4.6	14.8	
micro strip	60	8	8	8	$3 \times 60$	25	48	43	1.1	1.9	
micro strip	60	8	8	8	$1 \times 60$	12	41	27	0.3	3.9	
micro strip	60	8	8	8	$3 \times 60$	12	42	27	0.1	0.4	
micro strip	120	8	8	8	$1 \times 120$	25	42	27	0.7	0.4	
micro strip	120	8	8	8	$1 \times 120$	12	38	16	0.2	1.0	
stripline	60	12	8	12	$1 \times 60$	25	40	20	3.7	4.2	
stripline	60	8	8	8	$1 \times 60$	25	40	20	3.7	4.2	
stripline	60	8	8	8	$1 \times 60$	12	36	3	1.9	1.1	
stripline	60	8	8	8	$3 \times 60$	25	30	20	0.5	0.5	
stripline	60	8	8	8	$3 \times 60$	12	37	3	0.9	0.1	
stripline	120	8	8	8	$1 \times 120$	25	39	3	0.8	0.1	
stripline	120	8	8	8	$1 \times 120$	12	42	-15	0.3	0.3	

**Table D.2:** Proposed data format of the front-end board from the fibre sub-detector in the presence of online clustering on the FPGA. The abbreviation *ts* stands for timestamp.

---

0	header word
1	FPGA internal <i>ts</i> (8 ns), bits 31 to 61
2	FPGA internal <i>ts</i> (8 ns), bits 0 to 30
3	FPGA internal MuTRiG <i>ts</i> (12.8 ns), bits 50 to , 80
4	FPGA internal MuTRiG <i>ts</i> (12.8 ns), bits 19 to 49
5	block counter, ribbon side (1 bit)
5 + j	<i>event data</i> ribbon (4 bits), column (7 bits), number of columns (6 bits), frame <i>ts</i> (7 bits), MuTRiG <i>ts</i> (8 bits)
6 + N	trailer word

---

# Acknowledgments

I would like to thank Christoph Grab for giving me the opportunity to realize my PhD in his group embedded in the MU3E collaboration. I am grateful for his guidance, freedom and great trust he has shown me. A sincere thank goes to Niklaus Berger for his support to realize this thesis. I thank Klaus Kirch for being my co-examiner.

I am thankful to all the members of the MU3E scintillating fibre group. Without your collaboration, this thesis would not have been possible. Thanks to Roman Gredig who taught me the correct handling of radioactive sources and so much more. I am convinced he will be “forever young”. Thank you Antoaneta Damyanova for our excellent collaboration during many testbeam nights and Sandro Bravar for the many good discussions about the future of our field. Thanks for providing me with fibre ribbon prototypes. I would like to also thank Angela Papa, Giada Rutar, Peter Robmann, Malte Hildebrandt and David Miranda.

Furthermore, I would like to express my thank to the whole MU3E collaboration which became my academic family over the last years. Your spirit and enthusiasm motivated me over the entire time of my PhD. I like to thank Alexandr Kozlinskiy for the patience he has shown me with the software framework. A special thank goes to the group from the KIP institute: Patrick Eckart, Huangshang Chen, Vera Stankova, Yonatan Munwes and Wei Shen. It was always a great pleasure to work with you all. Thank you for all the support you provided me with respect to the ASICs as well as concerning sub-detector integration.

The people at our office and floor, Gaël, Luca, Vittorio, Lukas, Christian, Micha, Diego, Pirmin, Maren, Daniele, Joosep, Lukas, Felix, Malte, Philipp and Jan, and many other people from the institute, made it a real pleasure to work at ETH. There is a lot of technical and administrative staff at the institute that makes science possible. Many thanks for your help and support, Rosa, Bettina, Gabriele, Gaby, Caroline, Bruno, Patrick, Ulf, Sandro, Werner, Robert. I like to express special thanks to Chiara Casella who taught me much more beyond the operation of SiPM sensors and Alexander Howard who always is willing to help with his calm and smart way. I thank Lukas Gerritzen not only for joining our project but also for all the stimulating discussion and critical questions.

With his view from outside physics, Tobias Rommel helped me to put things into relation.



# Acronyms

<b>SM</b>	Standard Model of Particle Physics	<b>ASIC</b>	Application-Specific Integrated Circuit
<b>LFV</b>	Lepton Flavour Violation	<b>NIEL</b>	non-ionizing energy loss
<b>cLFV</b>	Charged Lepton Flavour Violation	<b>PKA</b>	Primary Knock-on Atom
<b>BSM</b>	Beyond Standard Model	<b>FDTD</b>	Finite Difference Time Domain
<b>EFT</b>	Effective Field Theory	<b>PMT</b>	Photomultiplier Tube
<b>RGE</b>	Renormalization-Group Evolution	<b>APD</b>	Avalanche Photo Diode
<b>PSI</b>	Paul Scherrer Institute	<b>PDE</b>	Photon Detection Efficiency
<b>TRIUMF</b>	Tri University Meson Facility	<b>DCR</b>	Dark Count Rate
<b>BNL</b>	Brookhaven National Laboratory	<b>SPTR</b>	Single Photon Time Resolution
<b>FNAL</b>	Fermi National Accelerator Laboratory	<b>FWHM</b>	Full Width at Half Maximum
<b>J-PARC</b>	Japan Proton Accelerator Research Complex	<b>PET</b>	Positron Emission Tomography
<b>SES</b>	Single Event Sensitivity	<b>TDC</b>	Time-to-Digital Converter
<b>C.L.</b>	confidence level	<b>DAC</b>	Digital-to-Analogue Converter
<b>NLO</b>	Next-to-Leading Order	<b>ToA</b>	Time of Arrival
<b>IC</b>	Internal Conversion	<b>ToT</b>	Time over Threshold
<b>NOL</b>	Nanostructured Organosilicon Luminophore	<b>VCO</b>	Voltage Controlled Oscillator
<b>SiPM</b>	Silicon Photomultiplier	<b>LFSR</b>	Linear Feedback Shift Register
<b>PCB</b>	Printed Circuit Board	<b>DNL</b>	Differential Non-Linearity
<b>DRS4</b>	Domino Ring Sampler	<b>FIFO</b>	First In, First Out
<b>VME</b>	Versa Module Europa	<b>SPI</b>	Serial Peripheral Interface
<b>PLL</b>	Phase Locked Loop	<b>CEC</b>	Channel Event Counter
<b>ADC</b>	Analog to Digital Converter	<b>LVDS</b>	Low Voltage Differential Signalling
<b>MIP</b>	Minimum Ionizing Particle	<b>CRC</b>	Cyclic Redundancy Check
<b>DAQ</b>	Data Acquisition System	<b>FPGA</b>	Field Programmable Gate Array
<b>NIM</b>	Nuclear Instrumentation Module	<b>DMA</b>	Direct Memory Access
		<b>PCIe</b>	Peripheral Component

APPENDIX D. APPENDIX D

---

	Interconnect Express	<b>PRBS</b>	Pseudo-Random Bit Stream
<b>MIDAS</b>	Maximum Integrated Data Acquisition System	<b>RPC</b>	Remote Procedure Call
<b>BER</b>	Bit Error Rate	<b>ODB</b>	Online Database
<b>HSMC</b>	High Speed Mezzanine Card	<b>GUI</b>	Graphical User Interface
<b>LDO</b>	Low-DropOut	<b>BADGE</b>	Bisphenol-A-diglycidylether
<b>CML</b>	Current Mode Logic	<b>CMOS</b>	Complementary Metal-Oxide-Semiconductor
<b>TTL</b>	Transistor-Transistor Logic	<b>LED</b>	Light Emitting Diode
<b>PECL</b>	Positive Emitter-Coupled Logic	<b>RAM</b>	Random Access Memory
<b>LYSO</b>	Lutetium-Yttrium Oxyorthosilicate ( $Lu_{2(1-x)}Y_{2x}SiO_5$ )	<b>CMBL</b>	Compact Muon Beam Line
<b>RMS</b>	Root Mean Square	<b>HV-MAPS</b>	High-Voltage Monolithic Active Pixel Sensor
<b>MPV</b>	Most Probable Value	<b>PWB</b>	Printed Wiring Board
		<b>MS</b>	Multiple Scattering

# List of Figures

1.1	SM diagram of $\mu \rightarrow e\gamma$ including neutrino oscillation. . . . .	4
1.2	EFT dipole and four-lepton operator bounds by $\kappa$ LFV experiments. . . . .	6
2.1	IC branching ratio as a function of missing energy. . . . .	13
2.2	Invariant mass and opening angle of Bhabha pairs from Michel muon decay positron and electron at rest. . . . .	15
2.3	The MU3E detector components. . . . .	16
2.4	Particle trajectories in a transverse detector cut. . . . .	18
2.5	The beamline used for the MU3E experiment. . . . .	20
2.6	Triplet fit: two helices fitted to a one triplet of pixel hits. . . . .	22
2.7	The experiment's DAQ system. . . . .	24
3.1	Scattering at the fibre detector as a function crossing particle's momentum. . . . .	28
3.2	Fibre ribbon coupling to SiPM arrays. . . . .	29
3.3	One fibre module inside the experiment's support structure. . . . .	29
3.4	Transverse projection of particles crossing angles of the fibre ribbons as a function of the incident position along the beam-direction. . . . .	30
3.5	Longitudinal projection of particles crossing angles of the fibre ribbons as a function of the incident position along the beam-direction. . . . .	31
3.6	Total and transverse momentum distribution of particles crossing the fibre detector. . . . .	32
3.7	Number of recurling particles in the fibre detector. . . . .	32
3.8	Vertex distribution of particles passing the fibre detector. . . . .	33
4.1	Chemical structure of scintillation molecules. . . . .	38
4.2	Energy levels of $\pi$ -electron energy levels scintillating material. . . . .	38
4.3	Fibres as photon guides due to internal total reflection. . . . .	40
4.4	Capture of scintillation photons in cladded fibres. . . . .	41
5.1	Diode $I$ - $V$ diagram. . . . .	44
5.2	Doping and electric field structure in PIN diodes and APDs. . . . .	44
5.3	Structure of a typical SiPM pixel. . . . .	46
5.4	SiPM's DCR versus threshold. . . . .	48
5.5	SiPM equivalent circuit. . . . .	50
5.6	Hamamatsu S13552-HRQ SiPM column array. . . . .	51
5.7	Damage function of electrons and expected particle energy spectrum in the fibre detector's SiPM. . . . .	53
5.8	Particle incident angles in the fibre sub-detector SiPMs, . . . . .	53

## LIST OF FIGURES

---

5.9	DCR as a function of 1 MeV neutron equivalent fluence. . . . .	55
6.1	Sketch of the STiC and MuTRiG functionality . . . . .	59
7.1	Emission spectrum of differen fibres. . . . .	66
7.2	Path lengths in different fibre ribbons configurations. . . . .	68
7.3	Image of a SiPM array on a flex print cable. . . . .	70
7.4	Image of fibre ribbon prototype. . . . .	72
7.5	Setup for fibre ribbon prototype characterisation. . . . .	73
7.6	Electrons energy deposition in plastic scintillators at different kinetig energies. . . . .	74
7.7	An exemplary multi-photon waveform. . . . .	76
7.8	An exemplary baseline waveform and its calibration. . . . .	77
7.9	Particle type identification by time of flight. . . . .	78
7.10	Waveforms in neighbouring sensor channels in the presence of crossing particles. . . . .	79
7.11	Charge versus amplitude of SiPM signals. . . . .	80
7.12	Cluster time difference between the two fibre ribbon sides. . . . .	82
7.13	Stability of the time resolution over time. . . . .	84
7.14	Cluster size in the SiPM column arrays. . . . .	85
7.15	Spectrum of charge and number of photons. . . . .	86
7.16	Stability over time of clusters and number of detedted photons. . . . .	88
7.17	Time resolution and efficiency of the different prototypes as a function of light yield for the different fibre prototypes. . . . .	91
7.18	Efficiencies of the different fibre ribbon prototypes in different configurations. . . . .	93
8.1	Light intensity profile at 7 mm from the fibre end. . . . .	97
8.2	Simulated photon exit position in double clad round fibres. . . . .	98
8.3	Simulated distribution of photon exit angles. . . . .	99
8.4	Simulated distribution of scintillation photon path lengths. . . . .	100
9.1	Transverse cut of the fibres detector in the simulation framework. . . . .	102
9.2	The shape of the fibre detector in the experiment's simulation framework. . . . .	102
9.3	Alternative parametrizations of photon yield as a function of interaction distance and deposited energy. . . . .	105
9.4	Simulated number of photons per fibre tuned to a square fibres prototype. . . . .	106
9.5	Horizontal distribution of photons on a sensor plane. . . . .	107
9.6	Fibre ribbon to sensor matching. . . . .	107
9.7	Simulated number of photons. . . . .	111
9.8	Simulated cluster size distribution. . . . .	111
9.9	Simulated time resolution for <i>lab-like</i> particle crossings. . . . .	112
9.10	Simulated cluster time as a function of interaction position along the ribbon. . . . .	113
9.11	Simulated cluster mean time resolution. . . . .	114
9.12	Simulated cluster time resolution corrected for the propagation time. . . . .	115
10.1	Sketch of fibre hit clustering. . . . .	118

10.2	Track candidate classification. . . . .	119
10.3	Distribution of the time separation for signal and background events. . . . .	124
10.4	Suppression of Bhabha background and the relative signal selection efficiency. . . . .	125
10.5	Timing suppression of Bhabha background by the different sub-detectors and as a function of the fibre detector's time resolution. . . . .	126
10.6	Rejection of mis-reconstructed track candidates by multiple fibre detector hits. . . . .	127
10.7	Momentum resolution of single track candidates. . . . .	128
10.8	Signal resolution and the relative reconstruction efficiency as a function of the fibre ribbon thickness. . . . .	129
11.1	Diagram of the MuTRiG setup for fibre ribbon characterization. . . . .	134
11.2	Picture of a MuTRiG wire bonded MuTRiG. . . . .	137
11.3	Image of the MuTRiG development board. . . . .	138
11.4	Resistor network to transform PECL signals into MuTRiG internal CML levels. . . . .	139
11.5	Image of the adapter board to connect SiPM arrays to MuTRiG. . . . .	140
11.6	Period of a PLL validation measurements. . . . .	144
11.7	PLL uniformity over all channels. . . . .	145
11.8	$T$ -threshold scan at different sensor bias voltages. . . . .	147
11.9	$T$ -threshold uniformity over different channel. . . . .	149
11.10	$T$ -threshold scans for all available DAC scales. . . . .	150
11.11	$T$ -threshold scans for different INPUTBIAS DAC settings. . . . .	151
11.12	Comparison of the period spectrum for sensor's DCR and noise. . . . .	152
11.13	The effect of the DNL correction on the fine counter. . . . .	153
11.14	Time resolution of positron annihilation to illustrate the effect of dithering. . . . .	154
11.15	Time offset between MuTRiG channels. . . . .	155
11.16	Time delay of the external trigger. . . . .	156
11.17	Coincidence of two neighbouring SiPM channels. . . . .	157
11.18	Coincidence of two SiPM channels on opposite sides of the ribbon. . . . .	157
11.19	Crosstalk mediated by fibres. . . . .	158
11.20	Distribution of cluster sizes measured by MuTRiG. . . . .	160
11.21	Time Resolution of fibre prototype extracted with MuTRiG. . . . .	162
11.22	Time resolution as a function of the bias voltage. . . . .	163
11.23	Time resolution as a function of rate. . . . .	164
11.24	Optimised time resolution of a fibre ribbon prototype. . . . .	165
12.1	Transverse cut through the central part of the detector. . . . .	168
12.2	Thermal expansion of fibre ribbons. . . . .	170
12.3	The sag of fibre ribbons as a function of tension. . . . .	171
12.4	Spring loading of the fibre ribbons. . . . .	171
12.5	Fibre detector support ring. . . . .	172
12.6	Radial insertion of one fibre module. . . . .	173
12.7	Dimensions of the flex print cables. . . . .	174
13.1	Expected event rates per sensor channel. . . . .	182

## LIST OF FIGURES

---

13.2	Alternative DAQ design increasing the bandwidth for the fibre detector. . . . .	185
A.1	Absorption depth in silicon as a function of wavelength. . . . .	194
A.2	SCSF-81MJ, TiO <sub>2</sub> 2, 4 layers . . . . .	195
A.3	SCSF-78MJ, TiO <sub>2</sub> 2, 4 layers . . . . .	196
A.4	NOL-11, TiO <sub>2</sub> 2, 3 layers . . . . .	197
A.5	NOL-11, no TiO <sub>2</sub> 2, 4 layers . . . . .	198
A.6	NOL-11, no TiO <sub>2</sub> 2, 4 layers . . . . .	199
A.7	NOL-11, TiO <sub>2</sub> 2, 3 layers . . . . .	200
A.8	NOL-11, TiO <sub>2</sub> 2, 2 layers . . . . .	201
A.9	BCF-12, TiO <sub>2</sub> 2, 4 layers . . . . .	202
B.1	Path length of photons in scintillating fibre ribbons. . . . .	206
B.2	Simulated photon exit position in square fibres. . . . .	206
B.3	Numbering scheme of the fibres in the main simulation framework. . . . .	207
B.4	Numbering scheme of the fibre ribbons in the GEANT4 simulation. . . . .	207
B.5	Distance between fibre ribbons in the simulation framework. . . . .	207
B.6	Waveforms which can be used for the digitization of signals of the fibre detector in the simulation framework. . . . .	209
C.1	Simplified diagram of the STiC and MuTRiG input-stage. . . . .	212
C.2	STiC and MuTRiG trigger scheme. . . . .	213
C.3	MIDAS based MuTRiG Configuration GUI . . . . .	218
C.4	STiC input terminal voltage as a function of the applied <i>SIPM</i> DAC value. . . . .	223
D.1	Simulated temperature equilibrium in the fibre detector cooling plates. . . . .	226
D.2	3d-printed model of the mechanical integration of the fibre detector. . . . .	226
D.3	The scattering parameters of microstrip flex print cable design. . . . .	227
D.4	Simulated response of an microstrip flex print cable design. . . . .	227
D.5	Schematic view of the simulated transmission lines. . . . .	228

# List of Tables

1.1	Current $\text{eLFV}$ muon decays upper limits. . . . .	7
1.2	Projected sensitivities of future muon $\text{eLFV}$ experiments. . . . .	8
3.1	Expected rates in the fibre detector. . . . .	31
4.1	Capture efficiency of round and square fibres. . . . .	41
5.1	SiPM properties, their dependencies and typical values. . . . .	49
5.2	Characteristics of used SiPM column arrays. . . . .	52
6.1	Overview of ASICs for SiPM readout. . . . .	58
7.1	Scintillating fibre properties. . . . .	67
7.2	Ribbon fill factors of different configurations. . . . .	67
7.3	Overview of scintillating fibre prototypes. . . . .	69
7.4	Jitter performance of the DRS4 based DAQ . . . . .	76
7.5	Time resolution at different thresholds and discrimination schemes. . . . .	83
7.6	Summary of properties of the different fibre ribbon prototypes. . . . .	90
9.1	Simulation settings for round Kuraray SCSF-78MJ fibres and MuTRiG readout. The abbreviation <i>exp.</i> indicates that these values are obtained by measurements, whereas those labelled with <i>vendor</i> are references to data sheets. . . . .	110
10.1	Timing detector's time resolution per track type. . . . .	120
10.2	Default cuts applied to identify signal candidates. . . . .	121
10.3	Track abundance in different simulation modes. . . . .	123
11.1	Summary of all MuTRiG pads and their functionality . . . . .	135
11.2	Data structure of DAQ's readout frames. . . . .	141
11.3	Crosstalk in the fibre ribbon prototype . . . . .	159
11.4	Fibre ribbon prototype time resolution at different bias voltages. . . . .	161
11.5	Time resolution as a function of position along the ribbon. . . . .	164
12.1	Number of contacts of one flex print connection grouped by type. . . . .	175
12.2	Proposed components on the SCIFI BOARD. . . . .	176
12.3	The interface of the SCIFI BOARD. . . . .	178
13.1	Proposed data format after sorting. . . . .	183
13.2	Expected event rate and the required bandwidth. . . . .	184

## LIST OF TABLES

---

13.3	The available bandwidth at the different DAQ stages. . . . .	184
A.1	Detailed overview of efficiencies of different fibre ribbon prototypes. . . . .	203
B.1	Default settings for the fibre detector in the simulation framework. . . . .	208
B.2	Numbering scheme of SiPM column hits in the simulation framework. . . . .	208
B.3	Numbering scheme of scintillating fibres and fibre ends in the GEANT4 simulation. . . . .	208
C.1	Event data format at transmission for STiC and MuTRiG . . . . .	214
C.2	8b/10b control words utilized in MuTRiG. . . . .	215
C.3	MuTRiG specific registers in the FPGA. . . . .	217
C.4	MIDAS based MuTRiG configuration GUI settings . . . . .	219
C.5	MIDAS based MuTRiG configuration GUI settings . . . . .	220
C.6	TDC DAC values used for all presented MuTRiG measurements. . . . .	221
C.7	Channel DAC settings for TDC injection. . . . .	221
C.8	Standard channel DAC settings. . . . .	221
C.9	T-threshold DAC values. . . . .	222
C.10	Sensor bias currents at different operation voltages. . . . .	222
D.1	Summary of simulated crosstalk behaviour of different flex print cable configurations. . . . .	229
D.2	Proposed data format in an online clustering scheme. . . . .	230

# Bibliography

- [1] F. Zwicky, “Die Rotverschiebung von extragalaktischen Nebeln,” *Helv. Phys. Acta*, vol. 6, pp. 110–127, 1933, [Gen. Rel. Grav.41,207(2009)]. doi:10.1007/s10714-008-0707-4.
- [2] P. A. R. Ade *et al.* [Planck Collaboration], “Planck 2015 results. xiii. cosmological parameters,” *Astron. Astrophys.*, vol. 594, A13, 2016. doi:10.1051/0004-6361/201525830.
- [3] A. D. Sakharov, “Violation of CP Invariance, C Asymmetry, and Baryon Asymmetry of the Universe,” *Pisma Zh. Eksp. Teor. Fiz.*, vol. 5, pp. 32–35, 1967, [Usp. Fiz. Nauk161,61(1991)]. doi:10.1070/PU1991v034n05ABEH002497.
- [4] T. Mori and W. Ootani, “Flavour violating muon decays,” *Prog. Part. Nucl. Phys.*, vol. 79, pp. 57–94, 2014. doi:10.1016/j.pnpnp.2014.09.001.
- [5] Y. Fukuda *et al.* [Super-Kamiokande], “Evidence for oscillation of atmospheric neutrinos,” *Phys. Rev. Lett.*, vol. 81, pp. 1562–1567, 1998. doi:10.1103/PhysRevLett.81.1562.
- [6] Q. R. Ahmad *et al.* [SNO], “Measurement of the rate of  $\nu_e + d \rightarrow p + p + e^-$  interactions produced by  $^8B$  solar neutrinos at the Sudbury Neutrino Observatory,” *Phys. Rev. Lett.*, vol. 87, 071301, 2001. doi:10.1103/PhysRevLett.87.071301.
- [7] K. Eguchi *et al.* [KamLAND], “First results from KamLAND: Evidence for reactor anti-neutrino disappearance,” *Phys. Rev. Lett.*, vol. 90, 021802, 2003. doi:10.1103/PhysRevLett.90.021802.
- [8] B. Pontecorvo, “Electron and Muon Neutrinos,” *Sov. Phys. JETP*, vol. 10, pp. 1236–1240, 1960, [Zh. Eksp. Teor. Fiz.37,1751(1959)].
- [9] L. Calibbi and G. Signorelli, “Charged Lepton Flavour Violation: An Experimental and Theoretical Introduction,” *Riv. Nuovo Cim.*, vol. 41, no. 2, 1, 2018. doi:10.1393/ncr/i2018-10144-0.
- [10] M. Blanke *et al.*, “Charged Lepton Flavour Violation and (g-2)(mu) in the Littlest Higgs Model with T-Parity: A Clear Distinction from Supersymmetry,” *JHEP*, vol. 05, 013, 2007. doi:10.1088/1126-6708/2007/05/013.
- [11] M. Kakizaki, Y. Ogura, and F. Shima, “Lepton flavor violation in the triplet Higgs model,” *Phys.Lett.*, vol. B566, pp. 210–216, 2003. doi:10.1016/S0370-2693(03)00833-5.

## BIBLIOGRAPHY

---

- [12] Y. Okada, K. Okumura, and Y. Shimizu, “ $\mu \rightarrow e\gamma$  and  $\mu \rightarrow 3e$  processes with polarized muons and supersymmetric grand unified theories,” *Phys.Rev.*, vol. D61, 094001, 2000. doi:10.1103/PhysRevD.61.094001.
- [13] H. Borgohain and M. K. Das, “Lepton number violation, lepton flavor violation, and baryogenesis in left-right symmetric model,” *Phys. Rev.*, vol. D96, no. 7, 075021, 2017. doi:10.1103/PhysRevD.96.075021.
- [14] J. Bernabeu, E. Nardi, and D. Tommasini, “ $\mu - e$  conversion in nuclei and  $Z'$  physics,” *Nucl. Phys.*, vol. B409, pp. 69–86, 1993. doi:10.1016/0550-3213(93)90446-V.
- [15] A. Crivellin *et al.*, “Renormalisation-group improved analysis of  $\mu \rightarrow e$  processes in a systematic effective-field-theory approach,” *JHEP*, vol. 05, 117, 2017. doi:10.1007/JHEP05(2017)117.
- [16] R. Kitano, M. Koike, and Y. Okada, “Detailed calculation of lepton flavor violating muon electron conversion rate for various nuclei,” *Phys. Rev.*, vol. D66, 096002, 2002, [Erratum: *Phys. Rev.D*76,059902(2007)]. doi:10.1103/PhysRevD.76.059902.
- [17] A. Crivellin *et al.*, “Complementarity in lepton-flavour violating muon decay experiments,” in *18th International Workshop on Neutrino Factories and Future Neutrino Facilities Search (NuFact16) Quy Nhon, Vietnam, August 21-27, 2016*, arXiv:1611.03409.
- [18] S. H. Neddermeyer and C. D. Anderson, “Note on the Nature of Cosmic-Ray Particles,” *Phys. Rev.*, vol. 51, pp. 884–886, May 1937. doi:10.1103/PhysRev.51.884.
- [19] E. P. Hincks and B. Pontecorvo, “On the absence of photons among the decay products of the 2.2 microsecond meson,” *Canadian Journal of Research*, vol. 28a, no. 1, pp. 29–43, 1950. doi:10.1139/cjr50a-002.
- [20] B. Aubert *et al.* [BaBar Collaboration], “Searches for Lepton Flavor Violation in the Decays  $\tau^\pm \rightarrow e^\pm\gamma$  and  $\tau^\pm \rightarrow \mu^\pm\gamma$ ,” *Phys.Rev.Lett.*, vol. 104, 021802, 2010. doi:10.1103/PhysRevLett.104.021802.
- [21] B. Aubert *et al.* [BaBar Collaboration], “Search for Lepton Flavor Violating Decays  $\tau^\pm \rightarrow \ell^\pm\pi^0, \ell^\pm\eta, \ell^\pm\eta'$ ,” *Phys. Rev. Lett.*, vol. 98, 2007. doi:10.1103/PhysRevLett.98.061803.
- [22] K. Hayasaka *et al.* [Belle Collaboration], “Search for Lepton Flavor Violating  $\tau$  Decays into Three Leptons with 719 Million Produced  $\tau^+\tau^-$  Pairs,” *Phys. Lett.*, vol. B687, pp. 139–143, 2010. doi:10.1016/j.physletb.2010.03.037.
- [23] Y. Miyazaki *et al.* [Belle Collaboration], “Search for lepton flavor violating  $\tau^-$  decays into  $\ell^-\eta, \ell^-\eta'$  and  $\ell^-\pi^0$ ,” *Phys. Lett.*, vol. B648, pp. 341–350, 2007. doi:10.1016/j.physletb.2007.03.027.

- [24] Y. Miyazaki *et al.* [Belle Collaboration], “Search for Lepton-Flavor-Violating tau Decays into a Lepton and a Vector Meson,” *Phys. Lett.*, vol. B699, pp. 251–257, 2011. doi:10.1016/j.physletb.2011.04.011.
- [25] V. Khachatryan *et al.* [CMS Collaboration], “Search for lepton flavour violating decays of the Higgs boson to  $e\tau$  and  $e\mu$  in proton-proton collisions at  $\sqrt{s} = 8$  TeV,” *Phys. Lett.*, vol. B763, pp. 472–500, 2016. doi:10.1016/j.physletb.2016.09.062.
- [26] A. M. Sirunyan *et al.* [CMS Collaboration], “Search for lepton flavour violating decays of the Higgs boson to  $\mu\tau$  and  $e\tau$  in proton-proton collisions at  $\sqrt{s} = 13$  TeV,” *JHEP*, vol. 06, 001, 2018. doi:10.1007/JHEP06(2018)001.
- [27] A. M. Baldini *et al.* [MEG Collaboration], “Search for the lepton flavour violating decay  $\mu^+ \rightarrow e^+ \gamma$  with the full dataset of the MEG experiment,” *Eur. Phys. J.*, vol. C76, no. 8, 434, 2016. doi:10.1140/epjc/s10052-016-4271-x.
- [28] U. Bellgardt *et al.* [SINDRUM Collaboration], “Search for the Decay  $\mu^+ \rightarrow e^+ e^+ e^-$ ,” *Nucl.Phys.*, vol. B299, 1, 1988. doi:10.1016/0550-3213(88)90462-2.
- [29] C. Dohmen *et al.* [SINDRUM II], “Test of lepton flavor conservation in  $\mu \rightarrow e$  conversion on titanium,” *Phys. Lett.*, vol. B317, pp. 631–636, 1993. doi:10.1016/0370-2693(93)91383-X.
- [30] J. Kaulard *et al.* [SINDRUM II Collaboration], “Improved limit on the branching ratio of  $\mu^- \rightarrow e^+$  conversion on titanium,” *Physics Letters B*, vol. 422, pp. 334–338, Mar. 1998. doi:10.1016/S0370-2693(97)01423-8.
- [31] W. Honecker *et al.* [SINDRUM II Collaboration], “Improved limit on the branching ratio of  $\mu \rightarrow e$  conversion on lead,” *Phys. Rev. Lett.*, vol. 76, pp. 200–203, Jan 1996. doi:10.1103/PhysRevLett.76.200.
- [32] W. H. Bertl *et al.* [SINDRUM II Collaboration], “A Search for muon to electron conversion in muonic gold,” *Eur.Phys.J.*, vol. C47, pp. 337–346, 2006. doi:10.1140/epjc/s2006-02582-x.
- [33] A. Baldini *et al.*, “MEG Upgrade Proposal,” *e-Print*, Jan. 2013, arXiv:1301.7225.
- [34] A. Blondel *et al.* [Mu3e Collaboration], “Research Proposal for an Experiment to Search for the Decay  $\mu \rightarrow eee$ ,” *e-Print*, Jan. 2013, arXiv:1301.6113.
- [35] H. Natori, “DeeMe experiment - An experimental search for a mu-e conversion reaction at J-PARC MLF,” *Nuclear Physics B - Proceedings Supplements*, vol. 248-250, no. Supplement C, pp. 52 – 57, 2014, 1st Conference on Charged Lepton Flavor Violation. doi:10.1016/j.nuclphysbps.2014.02.010.
- [36] R. Abramishvili *et al.* [COMET Collaboration], “COMET Phase I Technical Design Report,” KEK, Tech. Rep., 2016, Online: [http://comet.kek.jp/Documents\\_files/PAC-TDR-2016/COMET-TDR-2016\\_v2.pdf](http://comet.kek.jp/Documents_files/PAC-TDR-2016/COMET-TDR-2016_v2.pdf).

## BIBLIOGRAPHY

---

- [37] L. Bartoszek *et al.* [Mu2e Collaboration], “Mu2e Technical Design Report,” *e-Print*, 2014, arXiv:1501.0524.
- [38] R. J. Barlow, “The PRISM/PRIME project,” *Nucl. Phys. Proc. Suppl.*, vol. 218, pp. 44–49, 2011. doi:10.1016/j.nuclphysbps.2011.06.009.
- [39] G. Cavoto *et al.*, “The Quest for  $\mu \rightarrow e\gamma$  and its Experimental Limiting Factors at Future High Intensity Muon Beams,” *e-Print*, 2017, arXiv:1707.01805.
- [40] S. L. Glashow, D. Guadagnoli, and K. Lane, “Lepton Flavor Violation in  $B$  Decays?” *Phys. Rev. Lett.*, vol. 114, 091801, 2015. doi:10.1103/PhysRevLett.114.091801.
- [41] J. P. Lees *et al.* [BaBar Collaboration], “Measurement of an Excess of  $\bar{B} \rightarrow D^{(*)}\tau^-\bar{\nu}_\tau$  Decays and Implications for Charged Higgs Bosons,” *Phys. Rev.*, vol. D88, no. 7, 072012, 2013. doi:10.1103/PhysRevD.88.072012.
- [42] S. Hirose *et al.* [Belle Collaboration], “Measurement of the  $\tau$  lepton polarization and  $R(D^*)$  in the decay  $\bar{B} \rightarrow D^*\tau^-\bar{\nu}_\tau$ ,” *Phys. Rev. Lett.*, vol. 118, no. 21, 211801, 2017. doi:10.1103/PhysRevLett.118.211801.
- [43] R. Aaij *et al.* [LHCb Collaboration], “Measurement of the ratio of branching fractions  $\mathcal{B}(\bar{B}^0 \rightarrow D^{*+}\tau^-\bar{\nu}_\tau)/\mathcal{B}(\bar{B}^0 \rightarrow D^{*+}\mu^-\bar{\nu}_\mu)$ ,” *Phys. Rev. Lett.*, vol. 115, no. 11, 111803, 2015, [Erratum: *Phys. Rev. Lett.*115,no.15,159901(2015)]. doi:10.1103/PhysRevLett.115.159901.
- [44] Y. Amhis *et al.*, “Averages of  $b$ -hadron,  $c$ -hadron, and  $\tau$ -lepton properties as of summer 2016,” *Eur. Phys. J.*, vol. C77, no. 12, 895, 2017. doi:10.1140/epjc/s10052-017-5058-4.
- [45] D. Buttazzo *et al.*, “B-physics anomalies: a guide to combined explanations,” *JHEP*, vol. 11, 044, 2017. doi:10.1007/JHEP11(2017)044.
- [46] R. Aaij *et al.* [LHCb Collaboration], “Test of lepton universality using  $B^+ \rightarrow K^+\ell^+\ell^-$  decays,” *Phys. Rev. Lett.*, vol. 113, 151601, 2014. doi:10.1103/PhysRevLett.113.151601.
- [47] M. Bordone, G. Isidori, and A. Pattori, “On the Standard Model predictions for  $R_K$  and  $R_{K^*}$ ,” *Eur. Phys. J.*, vol. C76, no. 8, 440, 2016. doi:10.1140/epjc/s10052-016-4274-7.
- [48] R. Aaij *et al.* [LHCb Collaboration], “Test of lepton universality with  $B^0 \rightarrow K^{*0}\ell^+\ell^-$  decays,” *JHEP*, vol. 08, 055, 2017. doi:10.1007/JHEP08(2017)055.
- [49] R. Aaij *et al.* [LHCb Collaboration], “Differential branching fractions and isospin asymmetries of  $B \rightarrow K^{(*)}\mu^+\mu^-$  decays,” *JHEP*, vol. 06, 133, 2014. doi:10.1007/JHEP06(2014)133.

- 
- [50] R. Aaij *et al.* [LHCb Collaboration], “Angular analysis and differential branching fraction of the decay  $B_s^0 \rightarrow \phi\mu^+\mu^-$ ,” *JHEP*, vol. 09, 179, 2015. doi:10.1007/JHEP09(2015)179.
- [51] G. W. Bennett *et al.* [Muon g-2 Collaboration], “Final report of the E821 muon anomalous magnetic moment measurement at BNL,” *Phys. Rev. D*, vol. 73, 072003, Apr 2006. doi:10.1103/PhysRevD.73.072003.
- [52] J. Grange *et al.* [Muon g-2 Collaboration], “Muon (g-2) Technical Design Report,” *e-Print*, 2015, arXiv:1501.06858.
- [53] A. Antognini *et al.*, “Proton structure from the measurement of 2s-2p transition frequencies of muonic hydrogen,” *Science*, vol. 339, no. 6118, pp. 417–420, 2013. doi:10.1126/science.1230016.
- [54] J. C. Bernauer *et al.* [A1 Collaboration], “High-precision determination of the electric and magnetic form factors of the proton,” *Phys. Rev. Lett.*, vol. 105, 242001, Dec 2010. doi:10.1103/PhysRevLett.105.242001.
- [55] C. G. Parthey *et al.*, “Improved Measurement of the Hydrogen  $1S - 2S$  Transition Frequency,” *Phys. Rev. Lett.*, vol. 107, 203001, Nov 2011. doi:10.1103/PhysRevLett.107.203001.
- [56] C. Patrignani *et al.* [Particle Data Group], “Review of Particle Physics,” *Chin. Phys.*, vol. C40, no. 10, 100001, (2016) and 2017 update.. doi:10.1088/1674-1137/40/10/100001.
- [57] P. J. Mohr, D. B. Newell, and B. N. Taylor, “CODATA Recommended Values of the Fundamental Physical Constants: 2014,” *Rev. Mod. Phys.*, vol. 88, no. 3, 035009, 2016. doi:10.1103/RevModPhys.88.035009.
- [58] V. Tishchenko *et al.*, “Detailed Report of the MuLan Measurement of the Positive Muon Lifetime and Determination of the Fermi Constant,” *e-Print*, 2012, arXiv:1211.0960.
- [59] C. Patrignani *et al.* [Particle Data Group], “Review of Particle Physics,” *Chin. Phys.*, vol. C40, no. 10, 100001, (2016) and 2017 update., MUON DECAY PARAMETERS, Revised September 2013 by W. Fetscher and H.-J. Gerber (ETH Zurich).. doi:10.1088/1674-1137/40/10/100001.
- [60] Y. Kuno and Y. Okada, “Muon decay and physics beyond the standard model,” *Rev. Mod. Phys.*, vol. 73, pp. 151–202, 2001. doi:10.1103/RevModPhys.73.151.
- [61] W. H. Bertl *et al.* [SINDRUM Collaboration], “Search for the Decay  $\mu^+ \rightarrow e^+e^+e^-$ ,” *Nucl. Phys.*, vol. B260, pp. 1–31, 1985. doi:10.1016/0550-3213(85)90308-6.

## BIBLIOGRAPHY

---

- [62] M. Fael and C. Greub, “Next-to-leading order prediction for the decay  $\mu \rightarrow e(e^+e^-)\nu\bar{\nu}$ ,” *Journal of High Energy Physics*, vol. 2017, no. 1, 84, Jan 2017. doi:10.1007/JHEP01(2017)084.
- [63] G. Pruna, A. Signer, and Y. Ulrich, “Fully differential nlo predictions for the rare muon decay,” *Physics Letters B*, vol. 765, pp. 280 – 284, 2017. doi:10.1016/j.physletb.2016.12.039.
- [64] R. R. Crittenden, W. D. Walker, and J. Ballam, “Radiative decay modes of the muon,” *Phys. Rev.*, vol. 121, pp. 1823–1832, Mar 1961. doi:10.1103/PhysRev.121.1823.
- [65] A. M. Baldini *et al.* [MEG], “Measurement of the radiative decay of polarized muons in the MEG experiment,” *Eur. Phys. J.*, vol. C76, no. 3, 108, 2016. doi:10.1140/epjc/s10052-016-3947-6.
- [66] V. L. Highland, “Some practical remarks on multiple scattering,” *Nuclear Instruments and Methods*, vol. 129, no. 2, pp. 497 – 499, 1975. doi:10.1016/0029-554X(75)90743-0.
- [67] N. Berger *et al.*, “A New Three-Dimensional Track Fit with Multiple Scattering,” *Nucl. Instrum. Meth.*, vol. A844, 135, 2017. doi:10.1016/j.nima.2016.11.012.
- [68] F. A. Berg, “CMBL - A High-Intensity Muon Beam Line & Scintillation Target with Monitoring System for Next-Generation Charged Lepton Flavour Violation Experiments,” Ph.D. dissertation, ETH Zurich, 2017. doi:10.3929/ethz-b-000213470.
- [69] J. Hammerich and L. Huth, “Mupix 8 results,” in *DPG Frühjahrstagung 2018*, Würzburg, Germany, March. 19-23 2018.
- [70] H. Augustin *et al.*, “Efficiency and timing performance of the MuPix7 high-voltage monolithic active pixel sensor,” *Nucl. Instrum. Meth.*, vol. A902, pp. 158–163, 2018. doi:10.1016/j.nima.2018.06.049.
- [71] M. Kiehn, “Pixel Sensor Evaluation and Track Fitting for the Mu3e Experiment,” Ph.D. dissertation, Heidelberg University, 2016. doi:10.11588/heidok.00020493.
- [72] P. Eckert, “The Mu3e Tile Detector,” PhD thesis, Heidelberg University, 2015. doi:10.11588/heidok.00018763.
- [73] D. vom Bruch, “Pixel Sensor Evaluation and Online Event Selection for the Mu3e Experiment,” Ph.D. dissertation, Ruperto-Carola-University of Heidelberg, 2017. doi:10.11588/heidok.00023689.
- [74] S. Ritt, P. Amaudruz, and K. Olchanski, “Maximum Integration Data Acquisition System,” 2001.
- [75] D. Wiedner and F. Meier [Mu3e Collaboration], “Mu3e review at PSI BVR,” February 2018, internal Document.

- [76] J. Birks, *The Theory and Practice of Scintillation Counting*, ser. International series of monographs on electronics and instrumentation. Pergamon Press, 1964. doi:10.1016/C2013-0-01791-4.
- [77] R. Gredig, “Scintillating Fiber Detector for the Mu3e Experiment,” Ph.D. dissertation, University of Zurich, Faculty of Science, 2016. doi:10.5167/uzh-127074.
- [78] Wikipedia contributors, “Wikipedia: Benzene,” accessed: 2018-05-03.
- [79] O. Borshchev *et al.*, “Development of a New Class of Scintillating Fibres with Very Short Decay Time and High Light Yield,” *Journal of Instrumentation*, vol. 12, no. 05, P05013, 2017. doi:10.1088/1748-0221/12/05/P05013.
- [80] D. L. Medina Miranda [Mu3e Collaboration], private communication, March 2018.
- [81] *Scintillation Materials*, Kuraray, 2014.
- [82] S. Piatek, “Physics and operation of the mppc silicon photomultiplier,” <https://hub.hamamatsu.com/jp/en/technical-note/sipm-physics-operation/index.html>, 2014, accessed: 2018-03-09.
- [83] S. Piatek, “A technical guide to silicon photomultipliers (sipm),” [https://www.hamamatsu.com/us/en/community/optical\\_sensors/articles/technical\\_guide\\_to\\_silicon\\_photomultipliers\\_sipm/index.html](https://www.hamamatsu.com/us/en/community/optical_sensors/articles/technical_guide_to_silicon_photomultipliers_sipm/index.html), 2017, accessed: 2018-03-09.
- [84] SensL, “An Introduction to the Silicon Photomultiplier (Rev. 6.0),” <https://www.sensl.com/downloads/ds/TN%20-%20Intro%20to%20SPM%20Tech.pdf>, 2017, accessed: 2018-06-09.
- [85] V. Golovin and V. Saveliev, “Novel type of avalanche photodetector with Geiger mode operation,” *Nuclear Instruments and Methods in Physics Research A*, vol. 518, pp. 560–564, Feb. 2004. doi:10.1016/j.nima.2003.11.085.
- [86] R. Mirzoyan, R. Kosyra, and H.-G. Moser, “Light emission in Si avalanches,” *Nuclear Instruments and Methods in Physics Research Section A: Accelerators, Spectrometers, Detectors and Associated Equipment*, vol. 610, no. 1, pp. 98 – 100, 2009. doi:10.1016/j.nima.2009.05.081.
- [87] M. V. Nemallapudi *et al.*, “Single photon time resolution of state of the art SiPMs,” *JINST*, vol. 11, no. 10, P10016, 2016. doi:10.1088/1748-0221/11/10/P10016.
- [88] Y. Munwes *et al.*, “Single photon time resolution with silicon photomultipliers using the STiC readout chip,” in *2015 IEEE Nuclear Science Symposium and Medical Imaging Conference (NSS/MIC)*, Oct 2015, pp. 1–4. doi:10.1109/NSSMIC.2015.7581738.

## BIBLIOGRAPHY

---

- [89] F. Corsi *et al.*, “Modelling a silicon photomultiplier (SiPM) as a signal source for optimum front-end design,” *Nuclear Instruments and Methods in Physics Research Section A: Accelerators, Spectrometers, Detectors and Associated Equipment*, vol. 572, no. 1, pp. 416 – 418, 2007, frontier Detectors for Frontier Physics. doi:10.1016/j.nima.2006.10.219.
- [90] Hamamatsu, “SPICE model based on CORSI model,” August 2017.
- [91] K. Axel *et al.* [LHCb Collaboration], “Characterisation of the Hamamatsu MPPC multichannel array for the LHCb SciFi Tracker v.11.2016,” EPFL, Tech. Rep., 2017, Online: <http://lphe.epfl.ch/publications/2017/LPHE-2017-001.pdf>.
- [92] F. Hönniger, “Radiation damage in silicon,” Ph.D. dissertation, Universität Hamburg, 2007.
- [93] J. Lindhard *et al.*, “Integral equations governing radiation effects. (notes on atomic collisions, iii),” *Kgl. Danske Videnskab., Selskab. Mat. Fys. Medd.*, vol. Vol: 33: No. 10, 1 1963.
- [94] M. Boschini, P. Rancoita, and M. Tacconi, “SR-NIEL Calculator: Screened Relativistic (SR) Treatment for Calculating the Displacement Damage and Nuclear Stopping Powers for Electrons, Protons, Light- and Heavy- Ions in Materials (version 3.9.5),” 2014, [online]: available at INFN sez. Milano-Bicocca, Italy [2018, March]: <http://www.sr-niel.org/>.
- [95] C. Xu *et al.*, “Influence of X-ray Irradiation on the Properties of the Hamamatsu Silicon Photomultiplier S10362-11-050C,” *Nucl. Instrum. Meth.*, vol. A762, pp. 149–161, 2014. doi:10.1016/j.nima.2014.05.112.
- [96] Y. Qiang *et al.*, “Radiation Hardness Tests of SiPMs for the JLab Hall D Barrel Calorimeter,” *Nucl. Instrum. Meth.*, vol. A698, pp. 234–241, 2013. doi:10.1016/j.nima.2012.10.015.
- [97] P. Bohn *et al.*, “Radiation damage studies of silicon photomultipliers,” *Nuclear Instruments and Methods in Physics Research A*, vol. 598, pp. 722–736, Jan. 2009. doi:10.1016/j.nima.2008.10.027.
- [98] S. Sanchez Majos, P. Achenbach, and J. Pochodzalla, “Characterisation of radiation damage in silicon photomultipliers with a Monte Carlo model,” *Nucl. Instrum. Meth.*, vol. A594, pp. 351–357, 2008. doi:10.1016/j.nima.2008.06.021.
- [99] T. Tsang *et al.*, “Neutron radiation damage and recovery studies of SiPMs,” *Journal of Instrumentation*, vol. 11, no. 12, P12002, 2016. doi:10.1088/1748-0221/11/12/P12002.
- [100] M. Cordelli *et al.*, “Neutron irradiation test of Hamamatsu, SensL and AdvanSiD UV-extended SiPMs,” *JINST*, vol. 13, no. 03, T03005, 2018. doi:10.1088/1748-0221/13/03/T03005.

- 
- [101] S. Baccaro *et al.*, “Irradiation study of UV Silicon Photomultipliers for the Mu2e Calorimeter,” *JINST*, vol. 12, no. 02, C02022, 2017. doi:10.1088/1748-0221/12/02/C02022.
- [102] T. Harion *et al.*, “STiC: a mixed mode silicon photomultiplier readout ASIC for time-of-flight applications,” *Journal of Instrumentation*, vol. 9, no. 02, C02003, 2014. doi:10.1088/1748-0221/9/02/C02003.
- [103] H. Chen *et al.*, “Mutrig: a mixed signal silicon photomultiplier readout asic with high timing resolution and gigabit data link,” *Journal of Instrumentation*, vol. 12, no. 01, C01043, 2017. doi:10.1088/1748-0221/12/01/C01043.
- [104] I. Sacco, P. Fischer, and M. Ritzert, “PETA4: a multi-channel TDC/ADC ASIC for SiPM readout,” *JINST*, vol. 8, C12013, 2013. doi:10.1088/1748-0221/8/12/C12013.
- [105] C. Piemonte *et al.*, “Performance of FBK SiPMs coupled to PETA3 readout ASIC for PET application,” *Nucl. Instrum. Meth.*, vol. A 718, 345, 2013. doi:10.1016/j.nima.2012.10.012.
- [106] I. Sacco, “Development of highly integrated PET/MR detector modules,” Ph.D. dissertation, Ruperto-Carola University of Heidelberg, 2016. doi:10.11588/heidok.00022239.
- [107] S. Ahmad *et al.*, “Triroc: A multi-channel sipm read-out asic for pet/pet-tof application,” *Nuclear Science, IEEE Transactions on*, vol. 62, no. 3, pp. 664–668, June 2015. doi:10.1109/TNS.2015.2397973.
- [108] M. Rolo *et al.*, “A 64-channel ASIC for TOFPET applications,” *IEEE Nuclear Science Symposium and Medical Imaging Conference Record (NSS/MIC)*, pp. 1460–1464, 2012. doi:10.1109/NSSMIC.2012.6551353.
- [109] A. D. Francesco *et al.*, “TOFPET2: a high-performance ASIC for time and amplitude measurements of SiPM signals in time-of-flight applications,” *Journal of Instrumentation*, vol. 11, no. 03, C03042, 2016. doi:10.1088/1748-0221/11/03/C03042.
- [110] K. Briggel *et al.*, “KLauS: an ASIC for silicon photomultiplier readout and its application in a setup for production testing of scintillating tiles,” *JINST*, vol. 9, C02013, 2014. doi:10.1088/1748-0221/9/02/C02013.
- [111] Z. Yuan *et al.*, “KLauS4: A Multi-Channel SiPM Charge Readout ASIC in 0.18 $\mu$ m UMC CMOS Technology,” *PoS*, vol. TWEPP-17, 030, 2017. doi:10.22323/1.313.0030.
- [112] M. Bagliesia *et al.*, “A custom front-end ASIC for the readout and timing of 64 SiPM photosensors,” *Nuclear Physics B (Proc. Suppl.)* 215, 2011. doi:10.1016/j.nuclphysbps.2011.04.049.

## BIBLIOGRAPHY

---

- [113] M. Bouchel *et al.*, “SPIROC (SiPM Integrated Read-Out Chip): dedicated very front-end electronics for an ILC prototype hadronic calorimeter with SiPM read-out,” *Journal of Instrumentation*, vol. 6, no. 01, C01098, 2011. doi:10.1109/NSSMIC.2007.4436519.
- [114] F. Corsi *et al.*, “BASIC: an 8-channel Front-end ASIC for Silicon Photomultiplier Detectors,” *IEEE Nuclear Science Symposium Conference Record*, pp. 1082–1087, 2009. doi:10.1109/NSSMIC.2009.5402431.
- [115] J. Castilla *et al.*, “Evaluation of the FlexToT ASIC on the Readout of SiPM Matrices and Scintillators for PET,” *IEEE Nuclear Science Symposium and Medical Imaging Conference (NSS/MIC)*, 2013. doi:10.1109/NSSMIC.2013.6829206.
- [116] J. Fleury *et al.*, “Petiroc, a new front-end ASIC for time of flight application,” *IEEE Nuclear Science Symposium and Medical Imaging Conference Record (NSS/MIC)*, pp. 1–5, 2013. doi:10.1109/NSSMIC.2013.6829018.
- [117] J. Fleury *et al.*, “Petiroc and Citiroc: front-end ASICs for SiPM read-out and ToF applications,” *JINST*, vol. 9, no. 01, C01049, 2014. doi:10.1088/1748-0221/9/01/C01049.
- [118] F. Anghinolfi *et al.*, “NINO: An Ultrafast Low-Power Front-End Amplifier Discriminator for the Time-of-Flight Detector in the ALICE Experiment,” *IEEE transactions on nuclear science*, vol. 51, 2004. doi:10.1109/TNS.2004.836048.
- [119] E. Auffray *et al.*, “A Comprehensive and Systematic Study of Coincidence Time Resolution and Light Yield Using Scintillators of Different Size, Wrapping and Doping,” *IEEE Nuclear Science Symposium Conference Record*, 2011. doi:10.1109/NSSMIC.2011.6154402.
- [120] S. Ritt, “Design and performance of the 6 GHz waveform digitizing chip DRS4,” in *2008 IEEE Nuclear Science Symposium Conference Record*, Oct 2008, pp. 1512–1515. doi:10.1109/NSSMIC.2008.4774700.
- [121] A. X. Widmer and P. A. Franaszek, “A DC-Balanced, Partitioned-Block, 8B/10B Transmission Code,” *IBM Journal of Research and Development*, vol. 27, 440, 1983. doi:10.1147/rd.275.0440.
- [122] M. Ritzert, “Development and Test of a High Performance Multi Channel Readout System on a Chip with Application in PET/MR,” Ph.D. dissertation, Universität Heidelberg, 2014. doi:10.11588/heidok.00017092.
- [123] *Scintillation Products*, Saint-Gobain Crystals, 2014.
- [124] G. Rutar, “In Search of Charged Lepton Flavor Violating Decays at PSI,” Ph.D. dissertation, ETH Zurich, 2017. doi:10.3929/ethz-b-000174750.
- [125] A. Papa and A. Damyanova [Mu3e Collaboration], private communication, Dec. 2017.

- [126] A. Damyanova, “Development of a Scintillating Fibre Detector for the Mu3e Experiment,” Ph.D. dissertation, University of Geneva, in preparation.
- [127] K. Axel, H. Guido, and O. Girard [LHCb Collaboration], “Characterisation of the Hamamatsu MPPC multichannel array for the LHCb SciFi Tracker v.9.2014,” EPFL, Tech. Rep., 2015, Online: <http://lphe.epfl.ch/publications/2015/LPHE-2015-001.pdf>.
- [128] K. Axel *et al.* [LHCb Collaboration], “Characterisation of the Hamamatsu MPPC multichannel array for the LHCb SciFi Tracker v.12.2015,” EPFL, Tech. Rep., 2016, Online: <http://lphe.epfl.ch/publications/2016/LPHE-2016-001.pdf>.
- [129] NA61/SHINE Collaboration, “Status report to the proposal SPSC-P-330: Report from the NA61/SHINE experiment at the CERN SPS,” European Laboratory for Particle Physics, Tech. Rep., 2016, Online: <https://cds.cern.ch/record/2222876/files/SPSC-SR-197.pdf>.
- [130] A. Damyanova and A. Bravar, “Scintillating fiber detectors for precise time and position measurements read out with Si-PMs,” *Nucl. Instrum. Meth.*, vol. A845, pp. 475–480, 2017. doi:10.1016/j.nima.2016.06.088.
- [131] A. Papa, G. Cavoto, and E. Ripiccini, “Feasibility study of an active target for the MEG experiment,” *Nucl. Phys. Proc. Suppl.*, vol. 248-250, pp. 121–123, 2014. doi:10.1016/j.nuclphysbps.2014.02.023.
- [132] E. Ripiccini, “An active target for the MEG experiment,” Ph.D. dissertation, Rome U., 2015, Online: <http://inspirehep.net/record/1494142/files/Ripiccini.pdf>.
- [133] M. Berger *et al.*, “(2005), ESTAR, PSTAR, and ASTAR: Computer Programs for Calculating Stopping-Power and Range Tables for Electrons, Protons, and Helium Ions (version 2.0.1),” [online] National Institute of Standards and Technology, Gaithersburg, MD, 2005, available: <http://physics.nist.gov/Star> [2018, February 8].
- [134] “piM1 beam line,” [http://aea.web.psi.ch/beam2lines/beam\\_pim1.html](http://aea.web.psi.ch/beam2lines/beam_pim1.html).
- [135] R. Gilman *et al.* [MUSE Collaboration], “Technical Design Report for the Paul Scherrer Institute Experiment R-12-01.1: Studying the Proton “Radius” Puzzle with  $\mu p$  Elastic Scattering,” *e-Print*, 2017, arXiv:1709.09753.
- [136] F. James, *Statistical Methods In Experimental Physics*, 2nd ed. World Scientific Publishing, 11 2006. doi:10.1142/6096.
- [137] S. Agostinelli *et al.*, “Geant4 – a simulation toolkit,” *Nucl. Instr. Meth.*, vol. A 506, no. 3, pp. 250 – 303, 2003. doi:10.1016/S0168-9002(03)01368-8.
- [138] J. Allison *et al.*, “Geant4 developments and applications,” *IEEE Trans. Nucl. Sci.*, vol. 53, 270, 2006. doi:10.1109/TNS.2006.869826.
- [139] J. Allison *et al.*, “Recent developments in Geant4,” *Nuclear Instruments and Methods in Physics Research Section A: Accelerators, Spectrometers, Detectors and Associated Equipment*, vol. 835, pp. 186 – 225, 2016. doi:10.1016/j.nima.2016.06.125.

## BIBLIOGRAPHY

---

- [140] M. Janecek and W. W. Moses, “Simulating scintillator light collection using measured optical reflectance,” *IEEE Transactions on Nuclear Science*, vol. 57, no. 3, pp. 964–970, June 2010. doi : 10 . 1109 / TNS . 2010 . 2042731 .
- [141] M. Deckenhof, “Simulation of Scintillating Fibres in Geant4,” *LHCb-PUB*, 2014, Online: <https://cds.cern.ch/record/1662547/files/LHCb-PUB-2014-023.pdf>.
- [142] Mu3e Collaboration, “Technical Design of the Phase I Mu3e Experiment,” in preparation.
- [143] N. Bocherens, “Clustering and Track Matching Studies for the Mu3e Scintillating Fibre Detector,” Master’s thesis, ETH Zurich, Department of Physics, 2016.
- [144] T. Harion, “The STiC ASIC High Precision Timing with Silicon Photomultipliers,” Ph.D. dissertation, Universität Heidelberg, 2015. doi : 10 . 11588 / heidok . 00019194 .
- [145] H. Chen, “A Silicon Photomultiplier Readout ASIC for the Mu3e Experiment,” Ph.D. dissertation, Universität Heidelberg, 2018. doi : 10 . 11588 / heidok . 00024727 .
- [146] Altera Corporation, *Stratix IV GX FPGA Development Board - Reference Manual*, 9th ed., 2012.
- [147] S. Corrodi, “Fast Optical Readout of the Mu3e Pixel Detector,” Master’s thesis, ETH Zurich, Department of Physics, 2014, Online: <https://www.psi.ch/mu3e/ThesesEN/MasterCorrodi.pdf>.
- [148] R. Becker *et al.*, “Studies of the high rate coincidence timing response of the STiC and TOFPET ASICs for the SAFIR PET scanner,” *Journal of Instrumentation*, vol. 11, no. 12, P12001, 2016. doi : 10 . 1088 / 1748 - 0221 / 11 / 12 / P12001 .
- [149] Samtec, “High speed characterization report,” Samtec Inc., Tech. Rep., 2014, Online: [http://suddendocs.samtec.com/testreports/hsc-report-sma\\_za8-xx-2-1mm-x-10-2\\_web.pdf](http://suddendocs.samtec.com/testreports/hsc-report-sma_za8-xx-2-1mm-x-10-2_web.pdf).
- [150] V. K. Stankova [Mu3e Collaboration], personal communication, Kirchhoff-Institute for Physics at University of Heidelberg.
- [151] A.-K. Perrevoort, “Sensitivity Studies to New Physics in the Mu3e Experiment and Development of Firmware for the Front-End of the Mu3e Pixel Detector,” Ph.D. dissertation, Ruperto-Carola-University of Heidelberg, 2018. doi : 10 . 11588 / heidok . 00024585 .
- [152] SensL, “Introduction to sipm: Technical note,” <https://www.sensl.com/downloads/ds/TN%20-%20Intro%20to%20SPM%20Tech.pdf>, Feb 2017, rev. 6.0.
- [153] T. Liebig, openems - open electromagnetic field solver. General and Theoretical Electrical Engineering (ATE), University of Duisburg-Essen.
- [154] G. Narula and E. Bogatin, “Field solvers for transmission line analysis: How similar are they?” *Printed Circuit Design and Fab*, Nov 2015.

